WestVirginiaUniversity
THE RESEARCH REPOSITORY @ WVU

Graduate Theses, Dissertations, and Problem Reports

2022

Modeling and Optimization of a Novel Chilled Ammonia Absorption Process and Amine-Appended Metal-Organic Frameworks for CO2 Capture

Ryan Keith Hughes
rkhughes@mix.wvu.edu

Follow this and additional works at: https://researchrepository.wvu.edu/etd

Recommended Citation

Hughes, Ryan Keith, "Modeling and Optimization of a Novel Chilled Ammonia Absorption Process and Amine-Appended Metal-Organic Frameworks for CO2 Capture" (2022). *Graduate Theses, Dissertations, and Problem Reports*. 11552.
https://researchrepository.wvu.edu/etd/11552

This Dissertation is protected by copyright and/or related rights. It has been brought to you by the The Research Repository @ WVU with permission from the rights-holder(s). You are free to use this Dissertation in any way that is permitted by the copyright and related rights legislation that applies to your use. For other uses you must obtain permission from the rights-holder(s) directly, unless additional rights are indicated by a Creative Commons license in the record and/ or on the work itself. This Dissertation has been accepted for inclusion in WVU Graduate Theses, Dissertations, and Problem Reports collection by an authorized administrator of The Research Repository @ WVU. For more information, please contact researchrepository@mail.wvu.edu.

Modeling and Optimization of a Novel Chilled Ammonia Absorption Process and Amine-Appended Metal-Organic Frameworks for CO_2 Capture

Ryan Hughes

Dissertation Submitted to the Benjamin M. Statler College of Engineering and Mineral Resources at West Virginia University

In partial fulfillment of the requirements for the degree of Doctor of Philosophy in Chemical Engineering

Debangsu Bhattacharyya, Ph.D., Chair
Fernando V. Lima, Ph.D.
Jianli Hu, Ph.D.
David Mebane, Ph.D.
Benjamin Omell, Ph.D.

Department of Chemical and Biomedical Engineering
Morgantown, West Virginia,
2022

Keywords: carbon capture, ammonia, metal-organic framework, absorption, adsorption, parameter estimation, uncertainty quantification, Bayesian inference, isotherm modeling, kinetic modeling, fixed bed, moving bed, process modeling, optimization, economic optimization

Copyright 2022 Ryan Hughes

Abstract

Modeling and Optimization of a Novel Chilled Ammonia Absorption Process and Amine-Appended Metal-Organic Frameworks for CO_2 Capture

Ryan Hughes

Post-combustion capture is one of the leading technologies for CO_2 abatement from anthropogenic sources which have contributed significantly to the rise of atmospheric greenhouse gases [1]. Specifically, solvent-based capture post-combustion processes are the industry standard but can suffer drawbacks such as high energy penalties and corrosion. In this work, two possible improvements are investigated which have been recently proposed in the literature. The first is aqueous ammonia as a capture solvent which has been shown to have several advantages including, but not limited to, a lower regeneration energy [2]. The second is a novel solid sorbent, an amine-appended metal-organic framework (MOF). The MOF exhibits several promising attributes, namely, a step-shaped adsorption isotherm which leads to lower working capacities and lower regeneration energies when compared to traditional solid sorbents [3]. The overall goal of this work is to develop rigorous mathematical models which can be used for process design and economic evaluation of these technologies.

First, an integrated mass transfer model is developed for the chilled ammonia process (CAP). This model is developed using a simultaneous regression approach that has been recently proposed in the literature with parameter estimation performed using data from a pilot plant source and wetted-wall column. The optimally estimated parameters are shown to have a lower prediction error to validation data than parameters found in literature. The integrated mass transfer model is then used to develop a model for a novel chilled ammonia process. The process includes a NH_3 abatement system which utilizes a reverse osmosis membrane to aid in separation and reduce the energy penalty. Simulation of the process shows that the membrane can significantly reduce the energy requirement of the reboiler, condenser, and cooler in the abatement section. Uncertainty of the estimated mass transfer parameters is quantified using a fully Bayesian approach which is demonstrated to show a significant reduction in the prediction uncertainty of key process indicators.

Second, isotherm and kinetic models are developed for amine-appended MOFs, dmpn-Mg_2(dobpdc) and Mg_2(dobpdc)(3-4-3). The step-shaped adsorption isotherms exhibited by these MOFs present a modeling challenge since many of the traditional isotherm models are unable to capture step transitions. Three isotherm models are examined in this work, a weighted dual-site Langmuir model found in literature, a dual-site Sips model developed in this work, and an extended weighted Langmuir model also developed in this work. Parameter estimation is performed using available isotherm data and it is shown that the models are able to predict the CO_2 adsorption data well. A kinetic model is then developed using a linear driving force for mass transfer which does an excellent job at predicting time dependent TGA data. An additional goal of this work is development of a chemistry-based model for functionalized solid sorbents that aims to capture the underlying adsorption reaction mechanisms which are not typically considered in solid sorbent modeling. As part of this model, optimal reaction set selection is performed since the reaction pathways for dmpn-Mg_2(dobpdc) are still relatively unknown. Parameter estimation is performed, and it is found that the chemistry-based model significantly outperforms the Sips isotherm model with regards to prediction error and other model building criteria. To aid in the evaluation of the commercial feasibility of the MOF, equation-oriented mathematical models for a fixed bed contactor and moving bed contactor are developed. The contactors are then to simulate industrial scale CO_2 capture process for coal based and NGCC based flue gas. Using developed cost models, techno-economic analysis and optimization of these processes is then performed and it is found that efficient thermal management can make these MOFs viable alternatives for CO_2 capture processes.

Acknowledgements

First, I would like to specifically thank my family for their support. To my mom and dad, for their love and encouragement throughout my entire life. To my wife Abbey, for her love and for being by my side throughout this journey. To my best friends Dax and Ellie, for keeping me company while working from home and reminding me to actually go outside and take them on a walk.

I would also like to extend my deepest gratitude to my advisor Dr. Debangsu Bhattacharyya. I am thankful he believed in me and gave me the opportunity to continue my education. His insight, attention to detail, and thoroughness amazes me, and it has been a pleasure to learn from him.

I am thankful for my committee members Dr. Fernando Lima, Dr. Jianli Hu, Dr. David Mebane, and Dr. Benjamin Omell for their knowledge and allowing me to present my research to them. I would also like to thank Michael Matuszewski for his ideas and support in my research. I would like to mention the group at Lawrence Berkeley National Laboratory for their support and discussion of amine-appended MOFs.

I would also like to take the time to mention and thank my friends, colleagues, and staff in the Chemical and Biomedical Engineering Department at West Virginia University. I would like to mention Goutham Kotamreddy for his help and insight during my research, especially when it came time to troubleshoot Aspen simulations. The rest of Dr. Bhattacharyya's research group have also been helpful to my research, especially Josh Morgan, Anderson Chinen, and Eli Hedrick.

I would like to acknowledge the financial support from the CCSI^2 program funded through the U.S. DOE (contract# 379419).

Table of Contents

Cover i

Abstract iv

Acknowledgements iv

Table of Contents v

List of Figures vii

List of Tables xii

1. Introduction 1
   - 1.1. Aqueous Ammonia 1
   - 1.2. Amine-appended Metal-organic Frameworks 2
   - 1.3. Research Objectives 3
2. Development of a Chilled Ammonia Absorption Process 5
   - 2.1. Introduction 5
   - 2.2. Modeling of a NH_3-CO_2-H_2O Absorption System 8
   - 2.3. Integrated Mass Transfer Model 10
   - 2.4. Chilled Ammonia Absorption Process 19
   - 2.5. Uncertainty Quantification 27
   - 2.6. Conclusions 35
3. Isotherm and Kinetic Models for dmpn–Mg_2(dobpdc) and Mg_2(dobpdc)(3-4-3) 37
   - 3.1. Introduction 37
   - 3.2. Isotherm Model Development 39
   - 3.3. Kinetic Model Development 48
   - 3.4. Conclusions 50
4. Chemistry-based Modeling for Functionalized Solid Sorbents 51
   - 4.1. Introduction 51
   - 4.2. Chemistry Model Equations 54
   - 4.3. Reaction Set Selection and Parameter Estimation 60
   - 4.4. Results 63
   - 4.5. Conclusions 71
5. Fixed Bed Contactor Modeling 73
   - 5.1. Introduction 73
   - 5.2. Fixed Bed Modeling Equations 74

5.3. Fixed Bed Model Validation and Parameter Estimation 82
5.4. Thermal Management Studies 86
5.5. Conclusions 88
6. Moving Bed Contactor Modeling 90
6.1. Introduction 90
6.2. Moving Bed Modeling Equations 92
6.3. Modeling Results 97
6.4. Conclusions 102
7. Techno-economic Analysis and Optimization of Amine-Appended MOF Capture Processes 103
7.1. Analysis of dmpn-Mg_2(dobpdc) for Coal-based Capture 103
7.1.1. Cost Model 104
7.1.2. Fixed Bed TSA Process 105
7.1.3. Moving Bed TSA Process 119
7.2. Analysis of Mg_2(dobpdc)(3-4-3) for NGCC-based Capture 137
7.2.1. Cost Model 137
7.2.2. Fixed Bed TSA Process 139
7.2.3. Conclusions 150
8. Final Remarks and Future Work 152
Appendix 156
Appendix A: CAP Process Modeling 156
Appendix B: Isotherm and Kinetic Modeling of dmpn-Mg2(dobpdc) 162
Appendix C: Chemistry-based Modeling for Functionalized Solid Sorbents 167
Appendix D: Contactor and Process Modeling 168
Appendix E: Presentations and Publications 171
References 174

List of Figures

Figure 2.1: Model performance using regressed parameters obtained from the WLS estimator vs. experimental data for (top) packed absorber columns [14] and (bottom) WWC [2] 18

Figure 2.2: Simplified process flow diagram for the base case CAP 19

Figure 2.3: Simplified process flow diagram for the CAP with membrane-assisted NH_3 abatement section 24

Figure 2.4: Sensitivity of membrane H_2O removal to required membrane area and energy requirement of the NH_3 stripper reboiler 25

Figure 2.5: Retentate mole fraction varying along the normalized length (0 = feed flow inlet) of the membrane 25

Figure 2.6: Impact of membrane H_2O removal on the energy requirements of the NH_3 abatement system 26

Figure 2.7: UQ methodology flow diagram 29

Figure 2.8: MARS response surface validation using 10-fold cross validation (R^2=0.98). (Left) Error histogram and (Right) parity plot comparing CO_2 capture predictions 30

Figure 2.9: Single parameter marginal probability density functions for prior and posterior distributions 31

Figure 2.10: Two-parameter prior (left) and posterior (right) probability distributions 32

Figure 2.11: Comparison of stochastic model generated using posteriors to experimental data. Experimental data presented with error bars representing ±1 standard deviation included in reporting of the data [14]. 33

Figure 2.12: Probability density function of CO_2 capture percentage for operating conditions corresponding to experimental test ID 30 (Table A.1) 33

Figure 2.13: Stochastic model results for energy requirements [MJ/kg CO_2] of important equipment in the membrane-assisted CAP process generated using the posteriors. Results also generated considering 60% membrane water removal. 95% Confidence Intervals: [$2.88 \leq CO_2$ Stripper Reboiler ≤ 2.99], [$1.00 \leq NH_3$ Stripper Reboiler ≤ 1.07], [$2.44 \leq CO_2$ Lean Solvent Chiller ≤ 2.55] 34

Figure 3.1: Experimental CO_2 adsorption isotherms for dmpn–Mg_2(dobpdc) at the indicated temperatures (colored symbols) and fits (colored lines) using a dual-site Sips isotherm model (upper) and a weighted dual-site Langmuir isotherm model (lower). 45

Figure 3.2: Model validation results for the dual-site Sips model (upper) and weighted dual-site Langmuir model (lower). Experimental CO_2 adsorption data for dmpn–Mg_2(dobpdc) at 80 and 90 °C are shown as colored symbols and fits to the data are shown as colored lines 45

Figure 3.3: Experimental CO_2 adsorption isotherms for Mg_2(dobpdc)(3-4-3) at the indicated temperatures (colored symbols) and fits (colored lines) using the extended weighted Langmuir model 47

Figure 3.4: Experimental data for time-dependent CO_2 adsorption in dmpn−Mg_2(dobdc) (colored symbols) and fits obtained using the linear driving force kinetic model (RMSE = 0.025). 49

Figure 4.1: Structure of ammonium carbamate chains (a) and mixed product of carbamate and carbamic acid (b). Carbamate chain formation shown using generic diamine and dmpn-Mg_2(dobpdc) shown in mixed structure figure [30]. 56

Figure 4.2: Integer sensitivity results for model selection. AIC for varying combinations of chain formation reactions. Minimal AIC (-3418) is at N=2, M=1 (red bar)............ 63

Figure 4.3: Parameter estimation results for N=2 and M=1 for linear pressure scale (left) and logarithmic pressure scale (right). Symbols represent experimental data and lines represent model prediction. 65

Figure 4.4: Optimal chemistry model (N=2, M=1) prediction of validation data. Symbols represent experimental data and lines represent model prediction. 66

Figure 4.5: Chemistry model heat of adsorption as a function of loading and temperature......... 67

Figure 4.6: Loadings [mol/kg] of the species present in the optimal chemistry model (N=2, M=1). Left) Unreacted diamine (Am). Right) Adsorbed phase free CO_2 ($CO2*$)............ 68

Figure 4.7: Prediction of chemisorbed CO_2 loading and chemisorbed product distribution. Top) Total chemisorbed CO_2 loading. Dashed line represents the maximum achievable loading (QAm). Bottom) Fraction of chemisorbed CO_2 contained in cooperatively adsorbed species *B*. 69

Figure 4.8: Left) Prediction of physisorbed CO_2 loading and right) fraction of total loading which is physisorbed............ 71

Figure 5.1: Diagram of a fixed bed reactor............ 76

Figure 5.2: Comparison of breakthrough model prediction (black trace) and experimental breakthrough data (blue trace). The normalized outlet concentration, C/C_0, represents the concentration of gas phase CO_2 exiting the bed relative to gas phase CO_2 entering the bed (root mean squared error = 0.051). 84

Figure 5.3: Fit of the Mg_2(dobpdc)(3-4-3) heat of adsorption surrogate model. Open circles represent fitting data and solid line represents model prediction. 84

Figure 5.4: Comparison of Mg_2(dobpdc)(3-4-3) breakthrough model prediction (black trace) and experimental breakthrough data (blue trace). The normalized outlet concentration, F/F_0, represents the concentration of gas phase CO_2 exiting the bed relative to gas phase CO_2 entering the bed............ 86

Figure 5.5: Modeled breakthrough curves for isothermal and adiabatic case studies discussed in the text. The normalized outlet concentration C/C_0 represents the concentration of gas phase CO_2 exiting the bed relative to gas phase CO_2 entering the bed. Vertical lines correspond to the breakthrough times for each scenario. 87

Figure 5.6: Dynamic loading (upper) and temperature (lower) profiles at the entrance, middle, and exit of the bed for the adiabatic case study. 88

Figure 6.1: Diagram of a moving bed reactor (Kim *et al.*, 2016) [85] 92

Figure 6.2: Adsorber steady-state response to a 50% decrease in solids flow. z/L represents the normalized length of the bed with 0 corresponding to the bottom of the bed. 99

Figure 6.3: Desorber steady-state response to a +/-50% change in solids flow. z/L represents the normalized length of the bed with 0 corresponding to the bottom of the bed. 99

Figure 6.4: Adsorber lean loading input disturbance. 100

Figure 6.5: Dynamic adsorber response of instantaneous CO_2 capture (left) and rich CO_2 loading (right). 100

Figure 6.6: Desorber rich solids temperature input disturbance. 101

Figure 6.7: Dynamic desorber response of lean CO_2 loading (left) and gas phase CO_2 mole fraction of the exit gas (right). 101

Figure 7.1: Configuration steps for the basic TSA process (upper) and the modified TSA process (lower). 107

Figure 7.2: Simplified diagram of the parallel bed configuration used in modeling the basic TSA cycle. A process that uses *n* beds is shown, with dashed lines representing the possibility of introducing more beds. 107

Figure 7.3: Equivalent annual operating cost (EAOC) versus flue gas residence time for the basic dmpn-Mg_2(dobpdc) TSA process (upper) and the modified dmpn-Mg_2(dobpdc) TSA process (lower). Different colored data points indicate cost variations resulting from changing the bed temperature and flue gas temperature at the beginning of the adsorption step. The horizontal line in both plots represents the EAOC for the state-of-the-art MEA system as discussed in the text. 110

Figure 7.4: Profiles for breakthrough time vs. residence time for the modified TSA process and basic TSA process for dmpn-Mg_2(dobpdc). 111

Figure 7.5: Basic dmpn-Mg_2(dobpdc) fixed bed TSA dynamic profiles 112

Figure 7.6: Modified dmpn-Mg_2(dobpdc) fixed bed TSA dynamic profiles 113

Figure 7.7: EAOC versus flue gas residence time for the basic dmpn-Mg_2(dobpdc) TSA process (red) and modified dmpn-Mg_2(dobpdc) TSA process (black) assuming 35% practical heat recovery (upper) and 85% heat recovery (lower). The horizontal line represents the EAOC for the state-of-the-art MEA system. 115

Figure 7.8: EAOC versus flue gas residence time for varying costs of MOF particles ($/kg) of the modified process with practical heat recovery. 116

Figure 7.9: Temperature and loading axial profiles at the end of the adsorption step for the basic and modified TSA processes. 118

Figure 7.10: Moving bed TSA process 121

Figure 7.11: Moving bed EAOC versus lean sorbent loading. 122

Figure 7.12: Moving Bed EAOC versus lean sorbent loading for 85% heat recovery between lean/rich sorbent stream. 123

Figure 7.13: Capital cost uncertainty effect on moving bed EAOC. The base case (solid blue line) corresponds to a lean solids temperature of 25 °C and 85% heat recovery 124

Figure 7.14: Moving bed EAOC versus lean sorbent loading for high pressure adsorber scenarios at 25°C lean sorbent temperature. 125

Figure 7.15: Effect of MOF particle cost uncertainty on moving bed process economics......... 126

Figure 7.16: Moving bed optimization results for varying MOF price and lifespan................. 130

Figure 7.17: Adsorber Moving Bed Profile Plots. Top) Gas phase CO_2 mole fraction. Middle) Solids phase CO_2 loading. Bottom) Temperature profiles for gas phase, solid phase, heat transfer fluid, and tube wall. X axis is normalized axial distance along the reactor with 0 being the bottom of the moving bed and 1 being the top. 132

Figure 7.18: Desorber Moving Bed Profile Plots. Top) Gas phase CO_2 mole fraction. Middle) Solids phase CO_2 loading. Bottom) Temperature profiles for gas phase, solid phase, heat transfer fluid, and tube wall. 132

Figure 7.19: Capital cost uncertainty analysis for optimal Version 2 moving bed cases. Dashed lines represent a +/- 50% change in capital costs 134

Figure 7.20: Configuration and steps of the TSA process for the Mg_2(dobpdc)(3-4-3)............ 140

Figure 7.21: Simplified diagram of the Mg_2(dobpdc)(3-4-3) TSA capture process.................. 141

Figure 7.22: Simplified diagram for Mg_2(dobpdc)(3-4-3) optimization framework................. 142

Figure 7.23: Mg_2(dobpdc)(3-4-3) Fixed Bed TSA Optimization Results: Costing Breakdown 144

Figure 7.24: Impact of heat recovery for Mg_2(dobpdc)(3-4-3) TSA Process. MEA value taken from Du *et. al.* [121] and NETL report value taken from James *et. al.* [119]. 145

Figure 7.25: Sensitivity of Mg_2(dobpdc)(3-4-3) TSA economics to MOF price. MEA value taken from Du *et. al.* [121] and NETL report value taken from James *et. al.* [119]. 146

Figure 7.26: High Temperature Optimization Results for Mg_2(dobpdc)(3-4-3) TSA Process: Costing Breakdown.. 148

Figure 7.27: Heat recovery sensitivity for high temperature Mg_2(dobpdc)(3-4-3) TSA process. MEA value taken from Du *et. al.* [121] and NETL report value taken from James *et. al.* [119]. 149

Figure 7.28: MOF price sensitivity for high temperature Mg_2(dobpdc)(3-4-3) TSA process. MEA value taken from Du *et. al.* [121] and NETL report value taken from James *et. al.* [119]......... 149

Figure A.1: Model performance using regressed parameters obtained from Hampel's estimator vs. experimental data for (left) packed absorber columns (Qi *et al.,* 2013) and (right) WWC (Puxty *et al.,* 2010)... 157

Figure A.2: Model performance using regressed parameters obtained from Logistic estimator vs. experimental data for (left) packed absorber columns (Qi *et al.,* 2013) and (right) WWC (Puxty *et al.,* 2010) 157

Figure A.3: Simplified diagram of the RO membrane 158

Figure A.4: Residual Plots for the dual-site Sips isotherm model (left) and weighted dual-site Langmuir isotherm model (right).. 166

Figure A.5: Experimental CO_2 adsorption isotherms for dmpn–Mg_2(dobpdc) at the indicated temperatures (colored symbols) and fits using a dual-site Sips isotherm model (colored lines). Pressure is shown on a linear scale. The right plot shows an expanded view of the experimental and fit data at 100, 110, and 120 °C.. 166

Figure A.6: Experimental CO_2 adsorption isotherms for dmpn–Mg_2(dobpdc) at the indicated temperatures (colored symbols) and fits using a weighted dual-site Langmuir isotherm model (colored lines). Pressure is shown on a linear scale. The right plot shows an expanded view of the experimental and fit data at 100, 110, and 120 °C. 167

Figure A.7: Steady-state moving bed adsorber profiles for base case operating conditions. 169

Figure A.8: Steady-state moving bed desorber profiles for base case operating conditions. 169

Figure A.9: Surrogate model for Blower Equipment Costs. 170

Figure A.10: Surrogate model for inlet flue gas compression work. 171

List of Tables

Table 2.1: Operating conditions for pilot plant and WWC data sources 15

Table 2.2: Simultaneous regression results, parameter sets... 17

Table 2.3: CAP design specifications and operating conditions.. 21

Table 2.4: Base case simulation results 22

Table 2.5: Base case energy requirements [MJ/kg CO_2] 23

Table 2.6: Regression confidence intervals of parameters included in the UQ framework 29

Table 3.1: Fit parameters determined using the weighted dual-site Langmuir model for CO_2 adsorption in dmpn–Mg_2(dobpdc). 46

Table 3.2: Fit parameters determined using the dual-site Sips model for CO_2 adsorption in dmpn–Mg_2(dobpdc) 46

Table 3.3: Root mean squared errors determined for the dual-site Sips and weighted dual-site Langmuir model fits.. 46

Table 3.4: Fit parameters determined using the extended weighted Langmuir model for CO_2 adsorption in Mg_2(dobpdc)(3-4-3). 47

Table 3.5: Fitted parameters for linear driving force kinetic model 49

Table 4.1: Estimated parameters for N=2 and M=1 65

Table 4.2: Comparison of chain length estimations for varying MOFs and methods. 70

Table 5.1: dmpn-Mg_2(dobpdc) fixed bed reactor model constants... 82

Table 5.2: Mg_2(dobpdc)(3-4-3) fixed bed reactor model constants... 82

Table 5.3: Experimental breakthrough conditions used to collect data to validate the dmpn-Mg_2(dobpdc) fixed bed model. 83

Table 5.4: Estimated parameters for Mg_2(dobpdc)(3-4-3) heat of adsorption surrogate model... 85

Table 5.5: Experimental breakthrough conditions used to collect data to validate the Mg_2(dobpdc)(3-4-3) fixed bed model. 85

Table 5.6: Mg_2(dobpdc)(3-4-3) fixed bed parameter estimation results...................................... 86

Table 5.7: Process conditions for thermal management case studies. 88

Table 6.1: Base case design and operating conditions for moving bed modeling studies............ 98

Table 7.1: Utility prices used in dmpn-Mg_2(dobpdc) costing model....................................... 105

Table 7.2: Important variables for the fixed bed TSA process configuration. 109

Table 7.3: Breakdown of step times and number of beds of the optimal scenarios for the basic and modified dmpn-Mg_2(dobpdc) TSA processes.. 112

Table 7.4: Breakdown of contributing costs to the equivalent annual operating cost ($Million/year) of the optimal scenarios for the basic and modified dmpn-Mg_2(dobpdc) TSA processes. 113

Table 7.5: Breakdown of contributing costs to the EAOC ($Million/year) for the heat recoveries considered in this work. Cases presented correspond to the optimal scenarios for the basic and modified TSA processes. 115

Table 7.6: Best case EAOC ($Million/year) breakdown for best moving bed cases with different heat recoveries. 123

Table 7.7: EAOC ($Million/year) breakdown for optimal high-pressure cases with different heat recoveries. 125

Table 7.8: Reactor breakdown for the best moving bed cases with different adsorber pressures 125

Table 7.9: MOF price and particle lifespan for moving bed optimization cases 129

Table 7.10: Moving bed optimization results for each particle cost uncertainty case. 131

Table 7.11: Cost breakdown [$million/year] for each moving bed optimization case. 131

Table 7.12: EAOC values for varying MOF capture processes, lifespans, and prices. 135

Table 7.13: Utility prices used in Mg_2(dobpdc)(3-4-3) costing model 139

Table 7.14: Mg_2(dobpdc)(3-4-3) Fixed Bed TSA Optimization Results: Decision Variables ... 143

Table 7.15: Mg_2(dobpdc)(3-4-3) Fixed Bed TSA Optimization Results: Costing Variables 144

Table 7.16: High Temperature Optimization Results for Mg_2(dobpdc)(3-4-3) TSA Process: Decision Variables 147

Table 7.17: High Temperature Optimization Results for Mg_2(dobpdc)(3-4-3) TSA Process: Costing Variables 148

Table A.1: Pilot plant regression and validation cases (Data from Qi *et al*., 2013) 156

Table A.2: Hydrated ionic radius 160

Table A.3: Solute permeability constants 161

Table A.4: Fit of traditional isotherms to dmpn-Mg_2(dobpdc) data 162

Table A.5: Reaction Set Selection Results 167

1. Introduction

The Intergovernmental Panel on Climate Change report states increasing greenhouse gas levels in the atmosphere have played a key role in the upward trend of the earth's average temperature over the last century [1]. The report also states that emissions from anthropogenic sources have played the largest part of these increasing gas levels with CO_2 emissions from fossil fuel burning power plants accounting for nearly 80% of the increase [1]. To reduce CO_2 emissions, post-combustion capture (PCC) of CO_2 is one of the leading technologies since these systems can be retrofitted to existing plants without major changes to the process [2,4]. Typically, CO_2 from a flue gas source is absorbed using aqueous chemical solvents at near ambient conditions and then regenerated to create a stream of high purity CO_2 [5]. Monoethanolamine (MEA) is the most common solvent for PCC and while it has excellent steady-state [6] and dynamic performance [7], it can invoke a high energy penalty. In this research two potential PCC processes- one using an aqueous chilled ammonia solvent and another using a functionalized metal organic framework (MOF) solid sorbent being developed by UC, Berkeley will be investigated.

1.1. Aqueous Ammonia

Aqueous ammonia is an alternative solvent with advantages including lower energy requirements for regeneration, high CO_2 loading, and absence of oxidative degradation which can cause corrosion for solvents like MEA [2,8]. However, one key disadvantage of aqueous ammonia is the high volatility which results in ammonia slip from the absorber. Two typical methods, pursued separately and concurrently, are operating the absorber at low temperatures to reduce vapor pressure and inclusion of a water wash section to recover solvent after the absorber. The low temperature process is known as the chilled ammonia process (CAP). The CAP technology has been studied through several lab scale tests, pilot plant trials, and model evaluation [2,9–16]. There are also several studies on the water wash method focusing on NH_3 abatement and recycling [17–20].

Both the CAP and water wash methods can lead to a total process energy requirement larger than that of CO_2 regeneration in traditional MEA systems [18,19]. Chilling the system to very low operating temperatures does not only lead to a large energy penalty, but it leads to higher capital cost. In addition, there is also possibility of solids formation that can cause an increase in the viscosity causing higher pressure drop and in the worst case, solids precipitation leading to transport problems. A collaborated study between General Electric (earlier Alstom Power) and the U.S. Department of Energy focused on the use of a reverse osmosis membrane to aid in the separation of the ammonia from the wash water in a CAP configuration [21]. The study mentioned the possible advantages of a membrane present in the abatement section, but the results are not public.

1.2. Amine-appended Metal-organic Frameworks

Another alternative to chemical solvents that is being investigated for PCC is the use of solid sorbents. Specifically, porous coordination solids known as metal–organic frameworks (MOFs) have emerged as promising candidates for carbon capture [22–24]. Composed of metal ions or clusters connected via organic linkers, these materials possess large internal surface areas and highly tunable pore structures and surface chemistries. In particular, it has been shown by the researchers at UC, Berkeley that appending alkyldiamines at the open metal sites in the framework Mg_2(dobpdc) (dobpdc^{4-} = 4,4′-dioxidobiphenyl-3,3′-dicarboxylate) results in powerful new adsorbents for CO_2 capture under a range of conditions relevant to coal [3,25–27] and natural gas flue gas [28,29]. These amine-appended MOFs exhibit much higher working capacities than traditional adsorbents and have the potential to exhibit lower regeneration energies than both leading amine-based solvents and traditional adsorbents as a result of their step-shaped CO_2 adsorption. This unique behavior arises due to an unprecedented mechanism wherein CO_2 inserts into the metal amine bond to form chains of ammonium carbamate [25] or carbamic acid [30] pairs that propagate down the framework channels. Accordingly, negligible CO_2 uptake occurs until a certain threshold pressure or temperature (under isothermal or isobaric conditions, respectively), beyond which point the material exhibits a sharp increase in gas uptake until it is nearly saturated with CO_2. In addition to this unprecedented adsorption behavior, these diamine-appended MOFs exhibit excellent long-term stability and maintain affinity for CO_2 under humid conditions, both desirable attributes for CO_2 capture [26]. Importantly, it is possible to tune the CO_2 adsorption step pressure or temperature simply by changing the structure of the appended diamine [27]. Many of the diamine-appended frameworks studied to date exhibit a low step pressures around 1 mbar of CO_2, however, and this strong adsorption can result in high regeneration temperatures [3]. Recently, the framework dmpn–Mg_2(dobpdc) (dmpn = 2,2-dimethyl-1,3-diaminopropane) was found to exhibit step-shaped adsorption at ~15 mbar CO_2 and 40 °C and nearly complete desorption at 100 °C as well as extended cycling stability under humid conditions. These properties render dmpn–Mg_2(dobpdc) a promising candidate for CO_2 capture from pulverized coal fired power plants. Additionally, a novel tetraamine-appended MOF, Mg_2(dobpdc)(3-4-3), has been presented and identified as a candidate for PCC from NGCC power plants in part due to characteristics such as CO_2 adsorption capacity for concentrations as low as parts per million and remarkable stability under conditions relevant for NGCC flue gas capture [29]. Notably, this class of tetraamine-appended MOFs exhibit a two-step adsorption isotherm which is theorized to be due to a cooperative adsorption mechanism which forms ammonium-carbamate chains.

1.3. Research Objectives

The objectives of this research are focused on modeling support for carbon capture systems. The main focuses of the research can be separated into two parts: application of new model development techniques to an ammonia absorption system and model development for a novel amine-appended metal organic framework. To accomplish the objectives of this work, Aspen Plus, Aspen Custom Modeler (ACM), Matlab, The Framework for Optimization, Quantification of Uncertainty, and Surrogates (FOQUS), and Python/Pyomo are the main modeling/optimization platforms used. The main objectives are as follows:

- Development of a novel chilled ammonia absorption process using a simultaneous regression approach
- Uncertainty quantification of the chilled ammonia process

- Development of isotherm and kinetic models for dmpn-Mg_2(dobpdc) and Mg_2(dobpdc)(3-4-3)
- Development of a chemistry-based model for functionalized solid sorbents with application to dmpn-Mg_2(dobpdc)
- Development of fixed bed contactor models for dmpn-Mg_2(dobpdc) and Mg_2(dobpdc)(3-4-3)
- Development of a moving bed contactor model for dmpn-Mg_2(dobpdc)
- Techno-economic analysis of coal-based capture processes for dmpn-Mg_2(dobpdc) using fixed bed and moving bed contactors
- Techno-economic analysis of a NGCC-based capture process for Mg_2(dobpdc)(3-4-3) using fixed bed contactors

2. Development of a Chilled Ammonia Absorption Process

In this chapter, a rigorous, rate-based model for a chilled ammonia CO_2 absorption process is developed and presented. Mass transfer and kinetic reaction parameters are optimally estimated using a simultaneous regression approach which incorporates wetted wall column and pilot plant data. A model of a membrane-assisted chilled ammonia process was developed for reducing the energy penalty in the NH_3 abatement section where a reverse osmosis membrane is used to aid in the separation of ammonia from the wash water. A fully Bayesian approach is used for quantifying the uncertainty of the selected parameters. Forward uncertainty quantification is then used to investigate how the uncertainty in the selected parameters affects key performance indicators.

The contents of this Chapter are published in the following peer-reviewed journal article:

Hughes, R.; Kotamreddy, G.; Bhattacharyya, D.; Omell, B.; Matuszewski, M. Modeling and Bayesian Uncertainty Quantification of a Membrane-Assisted Chilled Ammonia Process for CO_2 Capture. *Ind. Eng. Chem. Res.* **2022**, *61* (11), 4001–4016. https://doi.org/10.1021/acs.iecr.1c04601.

2.1. Introduction

Experimental studies of CO_2 in aqueous ammonia have been present since Pinsent *et al.* [31] studied the reaction kinetics of the system. They present kinetic model parameters which are still used by the majority of modeling studies found in literature today. Recently, experimental work of multiple scales has been focused on evaluating ammonia specifically as a PCC solvent. Puxty *et al.* [2] perform wetted wall column (WWC) experiments to study the CO_2 absorption rate into aqueous ammonia, and Qi *et al.* [14], Yu *et al.* [16], and Li *et al.* [17] present pilot plant scale data for a PCC plant using aqueous ammonia.

Numerous modeling studies focusing on ammonia as a PCC solvent are also present in the literature. Que and Chen[32] develop an electrolyte-NRTL thermodynamic model by regressing parameters using vapor-liquid equilibrium (VLE) data, heat capacity data, speciation data, and solubility data for the NH_3-CO_2-H_2O system over various temperature ranges. This electrolyte-NRTL model is available as a built-in library model in Aspen Plus. Other sources focus on rate-based process modeling of an ammonia absorption system which are generally more accurate when compared to equilibrium-based models for reactive absorption processes [10,13,14,33]. However, these rate-based studies use generalized correlations and parameters for many of the mass transfer submodels that have been obtained for different type of liquid-gas system or different type of packing. Some of the authors of these studies show that these models can reasonably replicate experimental data [10,14,33], but such parameters are likely to be suboptimal since they strongly depend on the specific reactive absorption technology and packing type [34–36]. To the best of the author's knowledge there is no paper in the open literature that has estimated both the liquid and gas side mass transfer coefficients as well as the interfacial area for a tower using CAP. In addition, typically the parameters are estimated for one specific sub-model at a time or sequentially one after another. However, such a sequential approach can lead to a sub-optimal set of parameters since both liquid and gas side mass transfer take place simultaneously with the chemical reactions for reactive solvent systems. The typical approach to get around this problem is to use data from targeted experiments that try to capture the effect of the desired mechanism. Such experiments are conducted in wetted wall columns or packed towers in operating conditions to achieve the desired outcomes. Another approach is to 'trust' parameters for one or more models while estimating the parameters of other models. Yet, another approach is to use the data from a nonreactive system to estimate the parameters for the mass transfer models. However, several limitations exist for these methods of a traditional sequential approach. One limitation is that the errors in estimates of the model parameters that are either directly taken from the literature or obtained from one step in the sequential approach gets propagated to the next step thus leading to the loss in the optimality. Another limitation is that the sequential approach assumes that the parameters estimated using the data from one scale, say the WWC, or one system, say the non-reactive system, are also the best estimate for other scales, say a packed tower. However, there are considerable differences in the operating regimes and characteristics between these scales or systems that cause differences in the hydrodynamics and physical and chemical properties affecting the wettability, reactivity, and flow non-idealities. Therefore, a model and its parameters that can adequately capture the mass transfer characteristics of a surrogate system or can capture the physics at a given scale may not be optimal for the system at a different scale or for the true system at the same scale. A recent literature source has proposed a simultaneous parameter estimation approach where parameters for the kinetic and mass transfer model parameters are simultaneously estimated using data from multiple scales such from WWC, and packed beds of different sizes and configuration [37]. The parameter estimates from the simultaneous regression approach are optimal for the data from all spatial scales. The sequential estimates of parameters are optimal for the data from the specific spatial scale used for estimating those and therefore not necessarily optimal for the data from all spatial scales. In that paper, the approach when applied to an MEA system was found to be more predictive than the conventional sequential approaches. In this work, the simultaneous approach is extended to the CAP system.

Uncertainty in model parameters is unavoidable so quantifying these uncertainties is desired for developing predictive models. When these parametric uncertainties are propagated through the process models, quantified uncertainties of the key performance measures can be obtained. This information is valuable for commercialization efforts supported by limited operational experience such as those for novel CO_2 capture technologies. Previous work by some of the authors of this paper has focused on uncertainty quantification (UQ) of properties models [38], vapor-liquid equilibrium model [39], mass transfer and hydraulic models [37]. These parametric uncertainties when propagated through the process model led to superior prediction of the key performance measures such as the CO_2 capture in the absorber, CO_2 loading in the regenerator, and temperature profile in the absorber and stripper for a large-scale pilot plant in comparison to the deterministic model [6]. However, those papers have focused on MEA-H_2O-CO_2 systems. To the best of our knowledge, there is no work to date on uncertainty quantification for CAP systems in the open literature. Here we extend our previous approach and apply it to the CAP system.

For Bayesian uncertainty quantification, a large number of samples needs to be drawn from the distributions of all uncertain parameters and then propagated through the sub-model/model. When there are a large number of uncertain model parameters and the sub-model/model is complex such as those for the membrane-assisted CAP system, uncertainty propagation can be highly computationally expensive. For reducing the computational expense, typically a reduced model is used [6,37], but computational expense can remain prohibitive for especially large problems. If the sensitivity to a given parameter is low in the space of the experimental data, then the Bayesian inference yields little information about the uncertainty of that parameter. Thus, such parameters can be excluded from UQ without losing any value practically.

2.2. Modeling of a NH_3-CO_2-H_2O Absorption System

2.2.1. Chemistry Modeling. The model is developed using Aspen Plus. The following reactions are included in the chemistry model of the NH_3-CO_2-H_2O system in Aspen Plus:

$$2H_2O \overset{K_{eq,1}}{\longleftrightarrow} H_3O^+ + OH^- \quad (2.1)$$

$$NH_3 + H_2O \overset{K_{eq,2}}{\longleftrightarrow} NH_4^+ + OH^- \quad (2.2)$$

$$CO_2 + 2H_2O \overset{K_{eq,3}}{\longleftrightarrow} H_3O^+ + HCO_3^- \quad (2.3)$$

$$NH_3 + HCO_3^- \overset{K_{eq,4}}{\longleftrightarrow} H_2O + NH_2COO^- \quad (2.4)$$

$$HCO_3^- + H_2O \overset{K_{eq,5}}{\longleftrightarrow} H_3O^+ + CO_3^{2-} \quad (2.5)$$

$$NH_4HCO_3(s) \overset{K_{eq,6}}{\longleftrightarrow} NH_4^+ + HCO_3^- \quad (2.6)$$

Reaction (2.6) is included to account for the possibility of the precipitation of NH_4HCO_3 at low temperatures and high CO_2 loadings. Aspen solids handling includes the solid species in the tower mass balance but its effect on transport equations or hydrodynamics is ignored. Several authors have determined equilibrium constants for reactions (2.1)-(2.6) by using the experimental data [13,14]. Que and Chen [32] compared the equilibrium constants obtained using the experimental data with those obtained by using the Gibbs free energy in the corresponding reactions and found that both approaches agree very well with each other. In this work, the equilibrium constants are calculated from the Gibbs free energy change of those reactions.

The following reactions are included under ‘Reactions’ in the RadFrac model of ASPEN Plus:

$$H_3 + H_2O \leftrightarrow NH_4^+ + OH^- \tag{R1}$$

$$2H_2O \leftrightarrow H_3O^+ + OH^- \tag{R2}$$

$$HCO_3^- + H_2O \leftrightarrow H_3O^+ + CO_3^{2-} \tag{R3}$$

$$CO_2 + OH^- \rightarrow HCO_3^- \tag{R4}$$

$$HCO_3^- \rightarrow CO_2 + OH^- \tag{R5}$$

$$NH_3 + CO_2 + H_2O \rightarrow H_2NCOO^- + H_3O^+ \tag{R6}$$

$$H_2NCOO^- + H_3O^+ \rightarrow NH_3 + CO_2 + H_2O \tag{R7}$$

$$NH_4HCO_3(s) \leftrightarrow NH_4^+ + HCO_3^- \tag{R8}$$

Reactions (R1)-(R3) are equilibrium reactions that were previously included in the chemistry model, reactions (R4)-(R7) are kinetically controlled reactions, and reaction R8 is salt precipitation which was also previously included in the chemistry model. For the kinetically controlled reactions, a general power law expression is used:

$$r = k\exp\left(-\frac{E}{RT}\right)\prod_{i=1}^{M} C_i^{\nu_i} \tag{2.7}$$

The concentration basis used is molarity, and parameter values *k* and *E* are based of the work of Pinsent *et al.* [31].

2.2.2. Thermodynamic Modeling. For the VLE model, the electrolyte non-random two-liquid (eNRTL) model is used for the liquid phase while the perturbed chain-statistical associating fluid theory (PC-SAFT) is used for the vapor phase. The model parameters are taken from the work of Que and Chen [32]. The eNRTL model is used to calculate enthalpy and entropy departure for the non-ideal NH_3-CO_2-H_2O system [13]. CO_2, NH_3, and N_2 are assumed to follow the Henry's law while H_2O is assumed to follow the Raoult's law for VLE calculations. Que and Chen [32] regress VLE model parameters using the VLE data, heat capacity data, speciation data, and solubility data for the NH_3-CO_2-H_2O system over various temperature ranges. The model fit was found to be adequate and therefore no update to the VLE model parameters was made. The Clarke model is used to calculate the liquid molar volume, with regression done against experimental data for the quadratic mixing rule parameter for NH_3 and H_2O [40]. Again, the model fit was found to be accurate, and no updates were made.

2.2.3. Transport Properties. For liquid viscosity, the Jones-Dole model is used to calculate the corrected liquid viscosity for the NH_3-CO_2-H_2O system. The Onsager-Samaras model is used to calculate liquid surface tension. The Riedel electrolyte correction model is used to calculate thermal conductivity, and the Nernst-Hartley model is used to calculate binary diffusivity [32]. The model fit was found to be adequate, and no updates were made.

2.2.4. Mass Transfer Models. A rate-based tower model is used to simulate the absorber and wetted wall column. The rate-based model in Aspen Plus utilizes the two-film model. For the absorber model, the Billet and Schultes [41] correlation was used for mass transfer coefficients. The gas- and liquid-side mass transfer coefficient correlations are shown in Eqs. (2.8) and (2.9), respectively. The Tsai [42] model (Eq. (2.10)) was used for interfacial area calculation, and the Chilton-Colburn J-factor analogy [43] was used to model heat transfer. The Billet and Schultes correlation [41] as well as Chilton-Colburn [43] correlation are available in ASPEN Plus. The Tsai model [42] is implemented through a Fortran user model. The Billet and Schultes correlations and the Tsai model are considered for regression in the integrated mass transfer model. The WWC model was set up similar to the absorber model, but a fixed value is used for the interfacial area. A Fortran user model is used for this specification.

$$k_G = D_G C_G \left(\frac{a}{d_H}\right)^{0.5} Sc^{0.333} \left(\frac{u_G \rho_G}{a \mu_G}\right)^{0.75} \sqrt{\frac{1}{\varepsilon - h_L}} \tag{2.8}$$

$$k_L = C_L \left(\frac{g \rho_L}{\mu_L}\right)^{0.167} \left(\frac{D_L}{d_H}\right)^{0.5} \left(\frac{u_L}{a}\right)^{0.333} \tag{2.9}$$

$$a_h = A_1 \left[\frac{\rho_L}{\sigma} g^{1/3} \left(\frac{u_L A}{L_P}\right)^{4/3}\right]^{A_2} \tag{2.10}$$

2.3. Integrated Mass Transfer Model

As previously mentioned, an integrated mass transfer model is developed using a simultaneous regression approach. Traditional approaches attempt to solve this problem sequentially by estimating one set of parameters at a single scale and then applying them to the subsequent scales where estimation of additional parameters is performed. For example, applying mass transfer models fitted to WWC data to larger equipment types to estimate parameters for interfacial area. As stated earlier in this work, the goal of the simultaneous regression approach is to obtain parameter estimates which are better representative of the physics and chemistry over a large scale of operating regimes and therefore have better predictive capability. An important aspect of this approach is that the solution to the simultaneous regression approach may not result in a better fit to the experimental data used in regression, but it should never give a poorer fit than the model developed by the traditional regression approach. This is due to the parameters found by the sequential approach being present in the search space for the simultaneous optimization problem. Additionally, total estimation errors for a sequential approach and a simultaneous approach can be the same if the same data is used for regression in both cases. Therefore, the models developed from both approaches should be evaluated using their predictive capability to data that has not been used for model development in either approach. Simultaneous regression involves parameter estimation using data from multiple experimental scales and can be represented for *n* scales using Eq. (2.11).

$$\begin{aligned}\min_{\theta_1,\theta_2,\dots,\theta_n}\ & \left(y_{1,\text{model}} - y_{1,\text{exp}}\right)'\Sigma^{-1}\left(y_{1,\text{model}} - y_{1,\text{exp}}\right) \\ & + \left(y_{2,\text{model}} - y_{2,\text{exp}}\right)'\Sigma^{-1}\left(y_{2,\text{model}} - y_{2,\text{exp}}\right) + \dots \\ & + \left(y_{n,\text{model}} - y_{n,\text{exp}}\right)'\Sigma^{-1}\left(y_{n,\text{model}} - y_{n,\text{exp}}\right)\end{aligned}$$

s.t. (2.11)

$$f_1(\eta_1, u, \theta_1) = 0$$
$$f_2(\eta_2, u, \theta_1, \theta_2) = 0$$
$$\vdots$$
$$f_n(\eta_n, u, \theta_1, \theta_2, \dots, \theta_n) = 0$$

$$g_1(\eta_1, u, \theta_1) \le 0$$
$$g_2(\eta_2, u, \theta_1, \theta_2) \le 0$$

$$\vdots$$

$$g_n(\eta_n, u, \theta_1, \theta_2, \ldots, \theta_n) \leq 0$$

$$y_1 = h_1(\eta_1, u)$$

$$y_2 = h_2(\eta_2, u) \qquad \text{(2.11 cont.)}$$

$$\vdots$$

$$y_n = h_n(\eta_n, u)$$

$$\min(u_{\mathrm{L}1}, u_{\mathrm{L}2}, \ldots, u_{\mathrm{L}n}) \leq u \leq \max(u_{\mathrm{U}1}, u_{\mathrm{U}2}, \ldots, u_{\mathrm{U}n})$$

$$y_{\mathrm{L}1} \leq y_1 \leq y_{\mathrm{U}1}$$

$$y_{\mathrm{L}2} \leq y_2 \leq y_{\mathrm{U}2}$$

$$\vdots$$

$$y_{\mathrm{L}n} \leq y_n \leq y_{\mathrm{U}n}$$

In Eq. (2.11), f and g represent equality constraints (mass balances, energy balances, etc.) and inequality constraints, respectively. y represents a measured variable with lower and upper bounds y_L and y_U, u represents input variables bounded between u_L and u_U, η represents process variables, and θ represents model parameters to be estimated. For this work, n=2 and uses WWC and pilot plant data from available literature sources.

An issue facing this work is that existing commercial process simulation software, such as Aspen Plus, cannot perform the simultaneous parameter estimation due to how the software is organized. For large experimental data sets, parameter estimation can also become computationally expensive and more than most process simulators can handle. To perform this simultaneous optimization problem, MATLAB is used for optimization by interfacing it with Aspen Plus for reading from and writing to the Aspen Plus model. The regression is done with data that can in general contain gross errors in laboratory, bench-scale, and pilot plant data. Presence of gross errors in the experimental data can contaminate the parameter estimates if generalized least squares estimates are used [44–47]. Thus, it is desired that the parameter estimates be robust to the uncertainties in the experimental data. Therefore, in addition to the weighted least squares (WLS) estimate, two robust estimation approaches using Hampel's redescending M-estimator and Logistic estimator are used. The general and respective objective functions are shown in Eqs. (2.12)-(2.15). The traditional WLS function is shown in Eq. (2.13), Hampel's estimator is shown in Eq. (2.14), and the Logistic estimator is shown in Eq. (2.15). Hampel's estimator is a piecewise function which remains constant at large values of the error function and renders the optimization insensitive to changes or improvements in the error function in this range. A similar phenomenon occurs for the Logistic estimator at large values of the error function. This error structure can be beneficial when data points that contain gross errors are essentially omitted from the optimization problem, but significant information can be lost if this occurs to data without gross error. Therefore, the adequateness of these parameter estimates should be evaluated using validation data not seen in the parameter estimation. Özyurt and Pike [48] give an in-depth look at the derivation and intricacies of these estimators. Tuning constants for the estimators are as follows; a_H=1.35, b_H=2.7, c_H=5.4, and c_{Lo}=0.602 [48]. Each estimator is only a function of the error function, ϵ_i, shown in Eqs. (2.16)-(2.17) for the absorber (corresponding to the pilot plant data) and WWC data, respectively. Since the derivative information is not available from Aspen plus, a derivative free approach is used in MATLAB for optimal parameter estimation. The problem is solved using the 'fminsearch' function in MATLAB which utilizes the Nelder-Mead algorithm [49].

$$\min \ \frac{1}{N_{abs}}\sum_{i=1}^{N_{abs}}\left[\mathrm{E}^*\left(\epsilon_{i,abs}\right)\right]+\frac{1}{N_{WWC}}\sum_{i=1}^{N_{WWC}}\left[\mathrm{E}^*\left(\epsilon_{i,WWC}\right)\right], \qquad \mathrm{E}^*\in\left[\mathrm{WLS,\ Hampel's,\ Logistic}\right] \tag{2.12}$$

$$\mathrm{WLS}(\epsilon_i)=\frac{1}{2}\epsilon_i^2 \tag{2.13}$$

$$\text{Hampel's}(\epsilon_i) = \begin{bmatrix} \frac{1}{2}\epsilon_i^2, \quad 0 \le |\epsilon_i| \le a_H \\ a_H|\epsilon_i| - \frac{1}{2}{a_H}^2, \quad a_H < |\epsilon_i| \le b_H \\ a_H b_H - \frac{{a_H}^2}{2} + (c_H - b_H)\frac{{a_H}^2}{2}\left[1 - \left(\frac{c_H - |\epsilon_i|}{c_H - b_H}\right)^2\right], \quad b_H < |\epsilon_i| \le c_H \\ a_H b_H - \frac{{a_H}^2}{2} + (c_H - b_H)\frac{{a_H}^2}{2}, \quad c_H < |\epsilon_i| \end{bmatrix} \tag{2.14}$$

$$\text{Logistic}(\epsilon_i) = 2\ln\left(1 + \exp\left(\frac{\epsilon_i}{c_{\text{Lo}}}\right)\right) - \left(\frac{\epsilon_i}{c_{\text{Lo}}}\right) \tag{2.15}$$

$$\epsilon_{i,abs} = \frac{\text{Capture}_{CO_2,exp,i} - \text{Capture}_{CO_2,pred,i}}{\bar{\sigma}_{abs,i}} \tag{2.16}$$

$$\epsilon_{i,WWC} = \frac{\text{ExitFlow}_{CO_2,exp,i} - \text{ExitFlow}_{CO_2,pred,i}}{\bar{\sigma}_{WWC,i}} \tag{2.17}$$

More details and explanations on the development of the simultaneous regression approach can be found in Chinen *et al.* [37].

As previously mentioned, WWC data and pilot plant data available in the literature were used to develop the integrated mass transfer model. Australia's Commonwealth Scientific and Industrial Research Organization (CSIRO) commissioned a post-combustion capture plant using aqueous NH_3 at the Munmorah power station, with the goal of addressing the knowledge gap in the performance and operation of an ammonia solvent capture system [14,16,17]. The absorption section consists of two absorbers operated in series with intercooled semi-rich solvent. More information on the absorber towers and configuration used for modeling can be found in Qi *et al.* [14]. Experimental WWC data is taken from Puxty *et al.* [2]. Table 2.1 lists the range of operating conditions used in the experimental trials for both data sources.

Table 2.1: Operating conditions for pilot plant and WWC data sources

Pilot Plant (Qi *et al.* [14])	**Value Range**
Lean Solvent NH_3 content [wt %]	[1.9-5.8]
Lean Solvent CO_2 Loading [mol CO_2/mol NH_3]	[0.22-0.41]
Lean Solvent Flow Rate [L/min]	[67-134]
Flue Gas Flow Rate [kg/h]	[632-916]
Flue Gas CO_2 content [vol %]	[7.6-10.9]
Rich Solvent CO_2 Loading [mol CO_2/mol NH_3]	[0.30-0.46]
CO_2 Capture Percentage	[48.6-91.3]
WWC (Puxty *et al.* [2])	**Value Range**
Lean Solvent NH_3 content [wt %]	[0.01-0.11]
Lean Solvent CO_2 Loading [mol CO_2/mol NH_3]	[0.0-0.8]
Lean Solvent Flow Rate [L/min]	0.220
Gas Flow Rate [L/min]	[3-5]
Gas CO_2 content [vol %]	[0-19.7]

A total of 14 pilot plant trials were considered in this work, 11 were used for regression and 3 were used for model validation. Table A.1 in the Appendix lists which were used for regression and which were used for validation along with the operating conditions for each case.

Reaction parameters (E and k) correspond to the reaction rate equation (Eq. (2.7)) for the kinetically controlled reactions (R4)-(R7) presented in Section 2.2. C_L and C_G are parameters for the mass transfer coefficient model (Eqs. (2.8) and (2.9)), and A_1 and A_2 are for the interfacial mass transfer area model (Eq. 2.10). Table 2.2 also provides a comparison of initial and estimated values using the simultaneous optimization approach for the three estimators used. All initial values were reported in the literature for the respective models. For every parameter set, objective function (Eq. 2.12) values calculated for each estimator are also calculated using the regression data and presented in Table 2.2. As expected, the objective function value for a specific estimator is minimized when that same estimator is considered in the optimization problem. For example, the minimum WLS objective function value of 9.31 corresponds to the parameter set that was obtained using a WLS estimator in the optimization problem. Similar results are seen for Hampel's estimator and Logistic estimator. Table 2.2 also presents the root mean square error (RMSE) for the model prediction to the 3 validation data points which is data that was not seen in the parameter estimation. The parameter set found using the WLS estimator shows a reduction in the RMSE of 10.3% when compared to the literature values. Parameter sets found using Hampel's estimator and Logistic estimator show an increase in RMSE of 9.9% and 4.6%, respectively. When comparing changes of the estimated parameter values, the WLS estimator also results in parameters that are much closer to the literature values than the other estimators as would be expected since the literature estimates were obtained using WLS. For the WLS estimator, parameters related to the mass transfer coefficients (C_L, C_G, A_1, and A_2) were the most affected by the regression, while the parameter related to the reaction kinetics remained largely unchanged. Figure 2.1 shows parity plots for the prediction of the models using regressed parameters obtained from the WLS estimator to the experimental data for the pilot plant absorber and WWC. Similar plots for Hampel's estimator and Logistic estimator can be found in the Appendix. For other studies completed in this work, parameters values obtained from regression using the WLS estimator are treated as the baseline value. Nevertheless, parameter estimates obtained from the robust estimators in this section give an initial guess for the uncertainty bounds of each parameter and therefore serve as an *a priori* estimate to avoid contamination of the UQ results in this work.

Table 2.2: Simultaneous regression results, parameter sets

Parameter/ Metric	Literature Values	Literature Source	Estimator Used in the Optimization Problem		
			WLS	***Hampel's***	***Logistic***
E_4 [cal/mol]	13249	(Pinsent *et al.*, 1956)	13358	17633	11915
E_5 [cal/mol]	29451		27627	37640	40613
E_6 [cal/mol]	11585		10856	11153	10993
E_7 [cal/mol]	17203		17753	16742	29780
k_4 [s^{-1}]	4.32E+13		5.03E+13	2.90E+13	7.01E+13
k_5 $\left[mol^2 \cdot L^{-2} \cdot s^{-1}\right]$	2.38E+17		2.36E+17	1.68E+17	3.61E+17
k_6 [s^{-1}]	1.35E+11		1.35E+11	2.08E+11	1.69E+11
k_7 $\left[mol^2 \cdot L^{-2} \cdot s^{-1}\right]$	2.14E+21		2.35E+21	8.71E+20	3.65E+21
C_L [-]	1.44	(Billet and Schultes, 1993)	1.60	1.512	1.089
C_G [-]	0.336		0.374	0.534	0.586
A_1 [-]	1.34	(Tsai *et al.*, 2010)	0.72	0.731	0.593
A_2 [-]	0.116		0.128	0.125	0.099
WLS Objective	36.41		**9.31**	11.99	11.63
Hampel's Objective	5.84		4.08	**3.45**	3.46
Logistic Objective	14.57		8.27	8.21	**8.13**
Validation Data RMSE [CO_2 Capture Percentage]	5.14		**4.61**	5.65	5.38

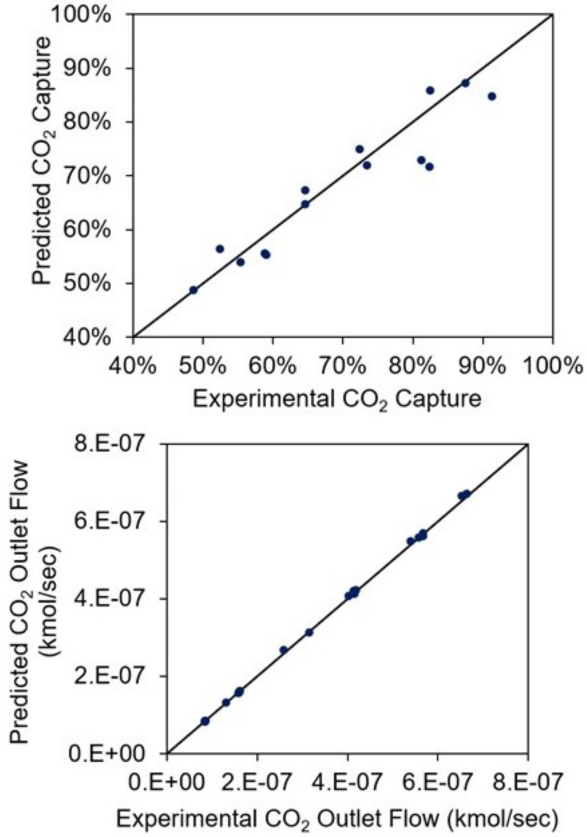

Figure 2.1: Model performance using regressed parameters obtained from the WLS estimator vs. experimental data for (top) packed absorber columns [14] and (bottom) WWC [2]

2.4. Chilled Ammonia Absorption Process

2.4.1. Base Case.

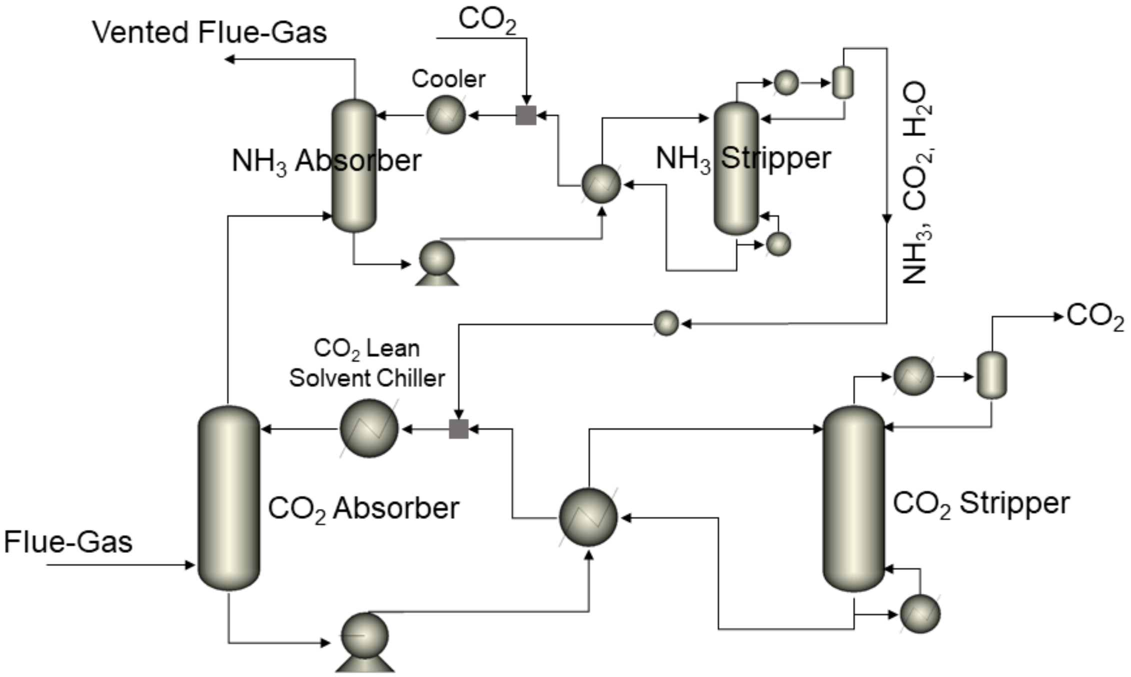

Figure 2.2: Simplified process flow diagram for the base case CAP

Figure 2.2 shows a process flow diagram for the base case CAP. Flue gas is absorbed by low temperature aqueous ammonia in the CO_2 absorber, and the CO_2 rich aqueous ammonia is regenerated at higher temperatures and pressures in the CO_2 stripper. Before re-entering the top of the CO_2 absorber, the regenerated aqueous ammonia is cooled to the low temperatures typical for the CAP system in the lean solvent chiller. The flue gas that exits the top of the CO_2 absorber enters the NH_3 absorber where excess ammonia is absorbed so that ammonia levels in the vented flue gas are below emission standards. The NH_3 rich water stream that exits the bottom of the NH_3 absorber is regenerated at higher temperatures and pressures in the NH_3 stripper. Vapor product from the ammonia stripper which contains the ammonia captured in the NH_3 absorber, along with additional water and CO_2, is recycled back to the aqueous ammonia solvent in the CO_2 absorption section. Before the lean wash water is sent back to the NH_3 absorber column, it is dosed with a small amount of CO_2 to help increase the NH_3 loading capacity. This is based on the work of Zhang and Guo [20] which found that this approach can significantly reduce the water circulation rate. For both the CO_2 absorption section and the NH_3 abatement section, heat between the cool, rich solvent stream and the hot, lean solvent stream is recycled in cross exchangers. One important aspect of the base case modeling is choosing important process parameters that can be fixed for the simulation, such as flue gas flow and composition, lean NH_3 weight percentage, and lean CO_2 loading. This study borrows from multiple studies performed in the literature which have evaluated process conditions that minimize important metrics such as energy consumption or emissions. Flue gas composition for a post-combustion capture system was taken from Modekurti *et al*. [50]. The flue gas is assumed to be available from a direct contact cooler where its temperature is reduced to 7 °C as a low inlet flue gas temperature is desired for the CAP system [10]. NH_3 concentration in the lean solvent is an important variable to reduce NH3 loss. Based on the work of Jilvero *et al*. [11], a NH_3 weight percentage of 10% and a CO_2 loading of 0.25 were used to keep NH_3 loss in an acceptable range. Lean solvent temperature is set at 10 °C to achieve the low absorber temperatures needed for the CAP similar to other studies on the CAP system [10,11]. CO_2 purity for the stream that exits the top of the CO_2 stripper was designed for 0.95 which is similar for other modeling studies found in literature [10]. In addition to the absorption process, the abatement system also has many important process parameters. These parameters also include lean solvent concentration, loading, temperature, pressure, as well as acceptable NH_3 levels in the vented flue gas. The design specification for the NH_3 concentration in the vented and cleaned flue gas can vary widely depending on the local emission standards. Zhang and Guo [20] performed a review of government standards for NH_3 emissions for various countries and designed the abatement section to reduce the vented NH_3 to a flow of 1.85 kg/h and concentration of 1.6 ppmv which is far below the emission standards of most countries, if not all. Li *et al*. [17] and Mathias *et al*. [18] designed for concentrations of <25 ppm and 10 ppm, respectively. In this work, the abatement system is designed to obtain a vented NH_3 concentration of 10 ppm. Zhang and Guo [20] performed an optimization of the composition and temperature of the lean abatement system water. A list of design specifications for the absorber and abatement system is shown in Table 2.3.

Table 2.3: CAP design specifications and operating conditions

CO_2 Absorption Section	
Flue Gas Flow Rate [kg/s]	55.45
Flue Gas CO_2 Content [mol fraction]	0.132
Flue Gas H_2O Content [mol fraction]	0.055
Flue Gas N_2 Content [mol fraction]	0.813
Flue Gas Inlet Temperature [°C]	7
CO_2 Capture Level	90%
Lean Solvent Temperature [°C]	10
Lean NH_3 fraction [mass fraction]	0.10
Lean Loading [mol CO_2/mol NH_3]	0.25
CO_2 Product Stream Purity [mass fraction]	0.95
CO_2 Absorber Height [m]	35
CO_2 Stripper Height [m]	20
CO_2 Stripper Pressure [bar]	10
NH_3 Abatement Section	
Vent Gas NH_3 Concentration [ppm]	10
Lean Wash Temperature [°C]	25
Lean Wash NH_3 Concentration [mol/L]	0.02
Lean Wash CO_2 Loading [mol CO_2/mol NH_3]	1.2
Regenerated H_2O content [mass fraction]	0.05
NH_3 Absorber Height [m]	15
NH_3 Stripper Height [m]	15
NH_3 Stripper Pressure [bar]	2.5

Table 2.4 shows results of important operating conditions for the simulation of the base case CAP system. These variables were calculated to achieve the design metrics listed in Table 2.3. The L/G ratio was adjusted to achieve the 90% CO_2 capture, and the CO_2 stripper conditions are needed to regenerate the CO_2 captured in absorber while maintaining the purity in the CO_2 product stream. The ammonia slip fraction from the absorber listed in Table 2.4 is much higher than the required emissions set by many countries and highlights the need for the NH_3 abatement section. Similar to the L/G ratio in the CO_2 absorption section, the lean wash water flow was adjusted to reduce the NH_3 content in the vented flue gas to 10 ppm according to the emission criterion for design.

Table 2.4: Base case simulation results

CO_2 Absorption/Stripping Section	
Liquid-to-Gas (L/G) Ratio [mass basis]	3.83
Ammonia Slip from CO_2 Absorber [kg/sec]	1.40
Ammonia Slip Fraction from CO_2 Absorber [ppm]	5.31×10^4
Solvent Rich Loading [mol CO_2/mol NH_3]	0.49
CO_2 Stripper Reboiler Temperature [°C]	138
CO_2 Stripper Condenser Temperature [°C]	87
CO_2 Stripper Reflux Ratio [mol basis]	0.22
NH_3 Abatement Section	
Lean Wash Water Flow [kg/sec]	68.5
NH_3 Stripper Reboiler Temperature [°C]	127
NH_3 Stripper Condenser Temperature [°C]	68
NH_3 Stripper Reflux Ratio [mol basis]	2.36

Table 2.5 shows the energy requirements for the base case CAP represented in terms of energy per mass of CO_2 absorbed by the entire capture system. Performance of post-combustion capture processes are typically measured by the energy requirements of reboilers since steam extracted from the main power plant is used to supply the energy and this extraction can heavily affect the overall process economics. Regeneration energies for an aqueous ammonia capture process found in the literature can vary depending on the operating conditions (chilled process vs. higher temperature process) and simulation type (equilibrium-based vs. rate-based) considered for the study. For the CO_2 adsorption section, the reboiler energy requirement of 2.92 MJ/kg CO_2 is slightly lower than other values reported in literature for rate-based simulations (3.05 [20], 3.15-3.42 [10]). Mathias *et al.* [18] and Niu *et al.* [19] report lower values of 2.29 and 1.29 MJ/kg CO_2, respectively, which are generated using equilibrium-based simulations that do not account for kinetic limitations. For the NH_3 abatement section, the reboiler energy requirement of 1.89 MJ/kg CO_2 is significantly lower than 5.43 MJ/kg CO_2 reported by Zhang & Guo, but similar to the values of 2.38 and 1.70 MJ/kg CO_2 reported by Mathias *et al.* and Niu *et al.,* respectively [18–20]. The reboiler energy requirement for the CO_2 stripper of the CAP is lower than regeneration energies for a traditional MEA process reported in the literature (3.2 – 5.5 MJ/kg CO_2 [51,52]). However, when the reboiler energy requirement for the NH_3 stripper is considered, the reboiler energy requirement for the entire capture process shows a 33% increase when

compared to a traditional MEA system. The CO_2 stripper condenser, NH_3 stripper condenser, and NH_3 lean solvent cooler operate at temperatures (≥ 25˚C) for which cooling water can be used to remove the required heat and will be less significant in the overall process economics when compared to the CO_2 lean solvent chiller. The energy required by the chiller is slightly larger than the energy requirement reported in the study performed by Hanak *et al.*, 1.34 – 1.92 MJ/kg CO_2 [10].

Table 2.5: Base case energy requirements [MJ/kg CO_2]

Reboilers	
CO_2 Stripper Reboiler	2.92
NH_3 Stripper Reboiler	1.89
	4.81
Condensers/Coolers/Chillers	
CO_2 Stripper Condenser	0.33
CO_2 Lean Solvent Chiller	2.48
NH_3 Stripper Condenser	1.28
NH_3 Lean Solvent Cooler	0.34
	4.43

2.4.2. Membrane-Assisted CAP

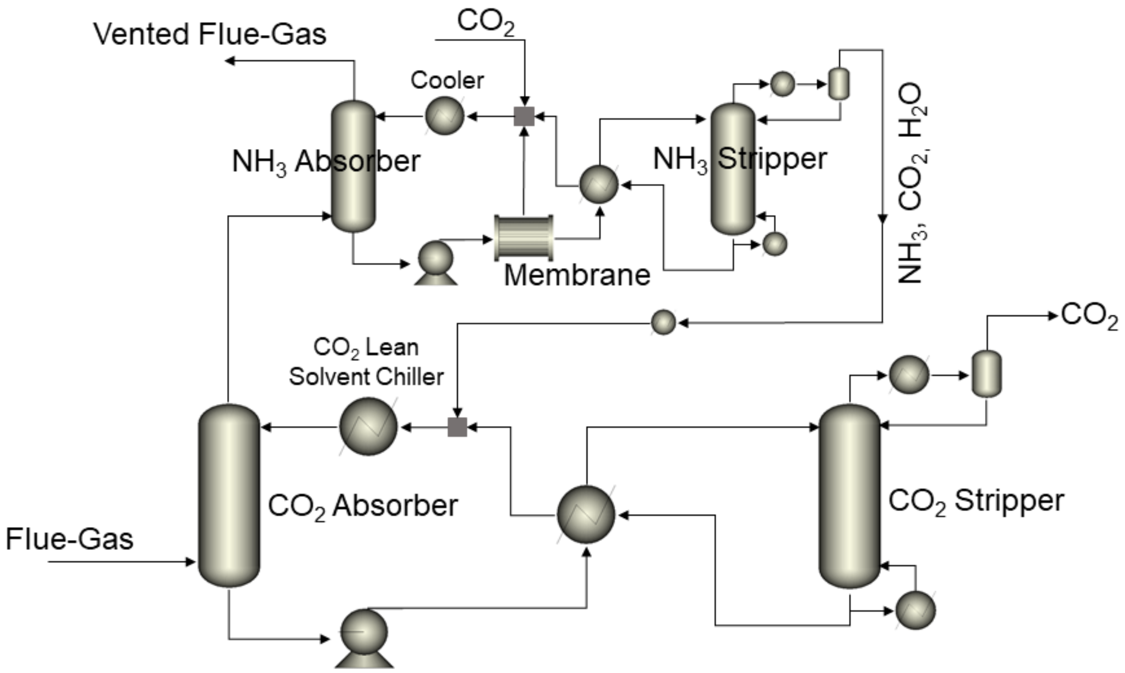
Vented Flue-Gas
CO_2
Cooler
NH_3 Absorber
NH_3 Stripper
Membrane
NH_3, CO_2, H_2O
CO_2
CO_2 Lean
Solvent Chiller
CO_2 Absorber
CO_2 Stripper
Flue-Gas

Figure 2.3: Simplified process flow diagram for the CAP with membrane-assisted NH_3 abatement section

Figure 2.3 shows the membrane-assisted CAP. This process expands upon the base case and implements a reverse osmosis membrane in the NH_3 abatement section to reduce the load in the NH_3 stripper. This work considers a reverse osmosis membrane which is assumed to follow the solution diffusion mechanism with properties and dimensions taken from those publicly available for cellulose acetate membranes. The model is capable of predicting the permeate flowrate and concentration profiles along the length of the membrane but is not developed as a part of this work and is instead included in the Appendix as a reference. The membrane is located in the ammonia rich water wash stream that exits the NH_3 absorber and separates high purity water from the stream therefore resulting in a lower total flow to the NH_3 stripper which reduces the energy required to regenerate the wash stream. For the membrane-assisted process, the design specifications listed in Table 2.3 are still satisfied.

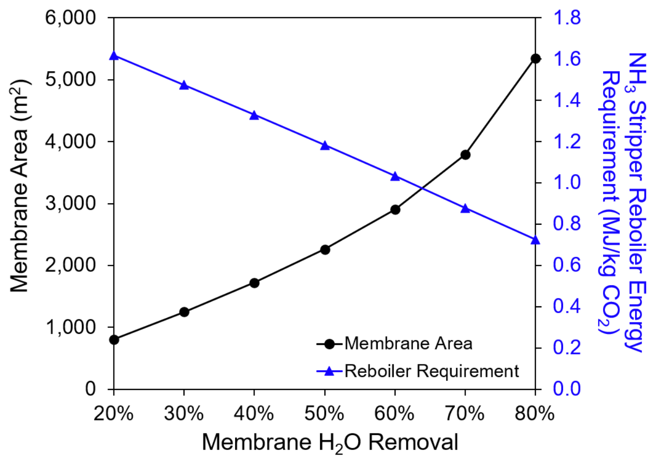

Figure 2.4: Sensitivity of membrane H_2O removal to required membrane area and energy requirement of the NH_3 stripper reboiler

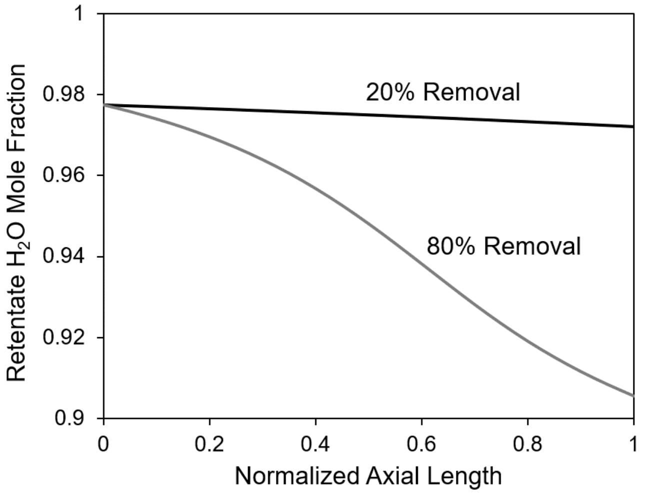

Figure 2.5: Retentate mole fraction varying along the normalized length (0 = feed flow inlet) of the membrane

To investigate the possible reduction in energy requirements that can be obtained with a membrane-assisted CAP, a sensitivity study was performed for the response of the energy requirements to varying amounts of water removed from the NH_3-rich solvent stream. Figure 2.4 shows the response of the required membrane area and the regeneration duty of the NH_3 stripper to the change in water removal. As expected, the stripper duty monotonically decreases with the increase in the extent of water removal thus resulting in a decrease in the operating cost. However, the required membrane area shows a steeper increase as the water capture increases thus obviously affecting the capital cost. Figure 2.5 shows the profiles of the mole fraction of water in the retentate for membrane water removal values at the upper and lower bound of the range considered in this work. For 20% water removal, the mole fraction remains largely unchanged from the membrane inlet value while a steady decrease along the membrane can be seen for 80% removal. This decrease in driving force, coupled with the larger amount of water separated in the membrane, result in the exponential increase in required membrane area as seen in Figure 2.4.

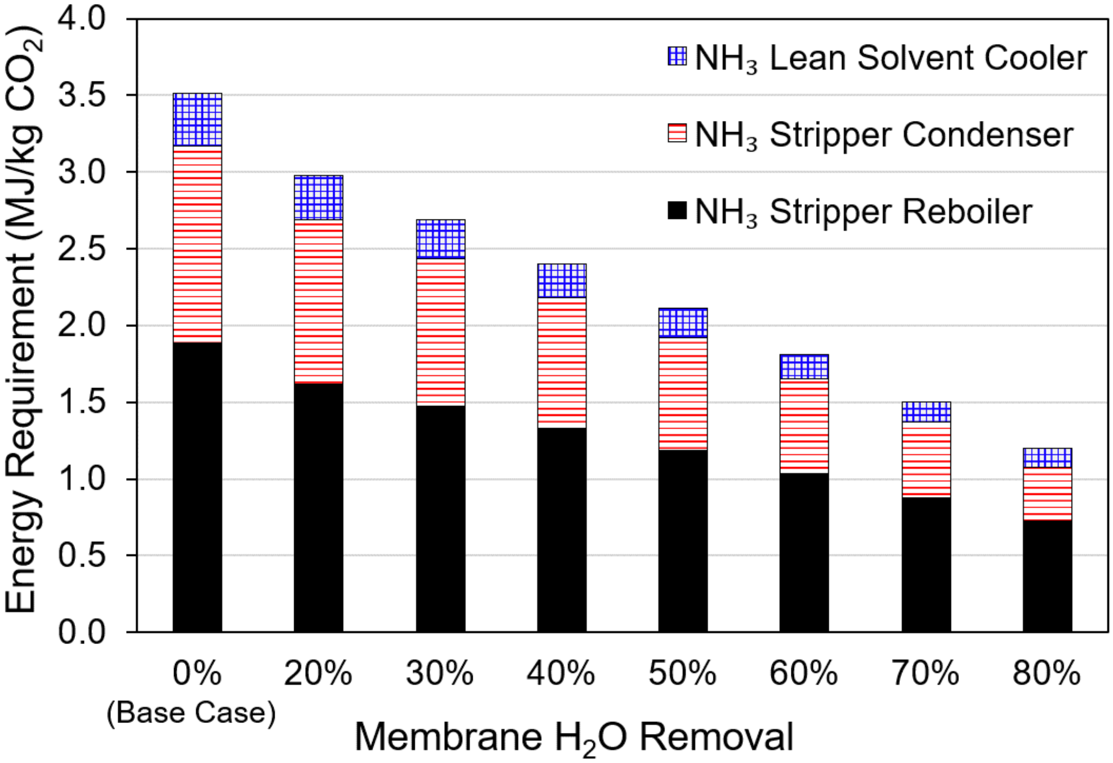

Figure 2.6: Impact of membrane H_2O removal on the energy requirements of the NH_3 abatement system

Figure 2.6 shows how the reboiler, cooler, and condenser duties in the NH_3 abatement section are reduced with increasing water removal by the membrane. When no water is removed (0%) the results correspond to the base case results shown in Table 2.4 and Table 2.5. Economic studies will be required to find the optimal membrane size by evaluating the tradeoff between increasing capital costs for the membrane and reduction in operating costs of the NH_3 stripper. For comparison, if a water removal of 60% is considered, which can be typical for large systems [53,54], the NH_3 stripper reboiler energy requirement is reduced to 1.03 MJ/kg CO_2 which is a 45% reduction from the base case. With this reduction in the NH_3 reboiler, the total system reboiler energy requirement is reduced to 3.95 MJ/kg CO_2, an 18% reduction from the base case.

Similarly, the combined duties of the condenser and cooler will decrease by 52% when compared to the base case. For the studies performed in this section, membrane water removal had no effect on the reboiler and condenser duties in the CO_2 stripper. Flow changes in the stream that exits from the top of the NH_3 stripper and is recycled back into the CO_2 absorption section has the potential to affect the duty of the CO_2 lean solvent chiller. However, since the amount of NH_3 regenerated and the composition of water in this recycle stream are maintained for these studies, the change in chiller duty is minimal (<1%) for all the cases in Figure 2.6.

2.5. Uncertainty Quantification

This work follows an uncertainty quantification methodology that was described in several previous works [37–39].

Deterministic models can be summarized as the model output (ϕ) being a function of a set of model parameters (θ) and predictor variables (x) as shown below

$$\varphi = F(x, \theta) \tag{2.18}$$

The model parameters are found using a parameter estimation method, which results in a single point for each parameter that best fits to experimental data. Once the deterministic model is developed, a stochastic model can be created by considering a distribution of the model parameters rather than single point estimates. These stochastic models can generate distributions of important process performance measures which are key in quantifying model uncertainties. In the Bayesian inference process, experimental data is used to develop more informed parameter distributions, known as posterior distributions.

The Bayesian inference process requires a large number of model evaluations and can be computationally expensive for chemical process models and large numbers of uncertain parameters subjected to the inference process. Also, the usefulness of the information generated during the Bayesian inference process is expected to be very little when the model sensitivity to the parameter of interest is low. Therefore, parameters were eliminated from the Bayesian process based on their 95% confidence intervals obtained from the regression performed in this work. Parameters in which zero was included in the confidence interval were removed individually from the stochastic model in a stepwise manner until no parameters remained that fit this criterion. Then, a reduced order model is developed and denoted as

$$\varphi \sim F^*(x, \theta) \tag{2.19}$$

The reduced order model is created by sampling from the input space of the parameters and predictor variables, then using a curve fitting method to map the inputs to the model output. In this work, multivariate adaptive regression splines (MARS)[55] is used to develop the response surface model. Cross validation is used to evaluate if the MARS model is representative of the actual model and to avoid overfitting.

Once the response surface model is developed, the posterior distribution, $\pi(\tilde{\theta}|Z)$, is computed by

$$\pi(\tilde{\theta}|Z) \propto P(\tilde{\theta}) L(Z|\tilde{\theta}) \tag{2.20}$$

$P(\tilde{\theta})$ represents the prior distribution of the parameters and is developed using prior knowledge of the parameters. For this work, a normal distribution with standard deviations obtained from the confidence intervals is used as the prior distributions for the parameters. For the joint prior parameter distributions, all parameters are assumed to be independent. The likelihood function, $L(Z|\tilde{\theta})$, measures how well the response surface matches the experimental data. The likelihood function used in this work is given by

$$L(Z|\tilde{\theta}) = \exp\left(-0.5 \sum_{j=0}^{M} \frac{\left[F^*(\tilde{x}_j, \tilde{\theta}) - Z_j(\tilde{x}_j)\right]^2}{M\sigma_j^2}\right) \tag{2.21}$$

Previous literature works have been performed to evaluate the accuracy and computational expensiveness of UQ propagation methods which have found Monte Carlo methods generally outperform other methods in both of these areas [56,57]. In this work, optimal selection of the UQ propagation method is not performed. The Markov Chain Monte Carlo (MCMC) method is used to calculate the posterior distribution, and the Gibbs sampling method is used to perform the parameter search. This Bayesian inference process results in an updated posterior distribution, $\pi(\tilde{\theta}|Z)$, given as a set of sample points. This problem was solved using The Framework for

Optimization, Quantification of Uncertainty, and Surrogates (FOQUS) toolset [58]. The main steps of this UQ methodology are highlighted in Figure 2.7. Again, more information on this methodology can be found in previous works [37–39].

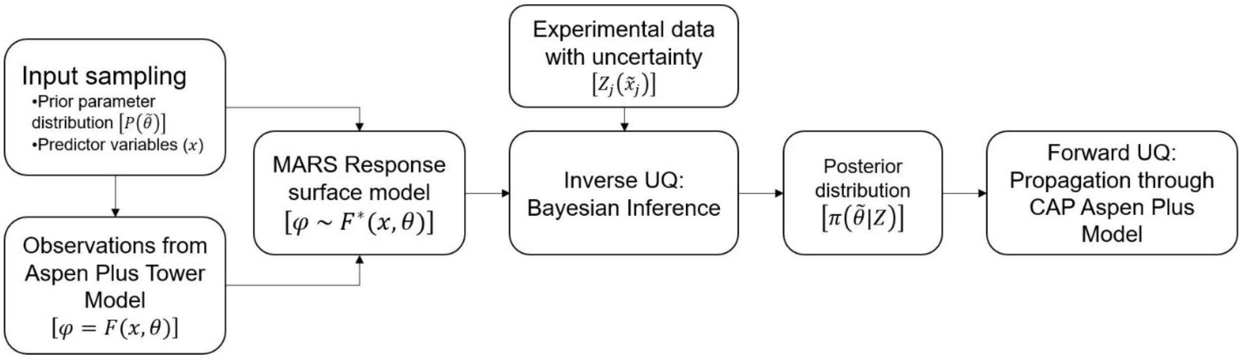
Input sampling
•Prior parameter distribution $[P(\tilde{\theta})]$
•Predictor variables (x)
Observations from Aspen Plus Tower Model $[\varphi = F(x,\theta)]$
MARS Response surface model $[\varphi \sim F^{*}(x,\theta)]$
Experimental data with uncertainty $[Z_j(\tilde{x}_j)]$
Inverse UQ: Bayesian Inference
Posterior distribution $[\pi(\tilde{\theta}|Z)]$
Forward UQ: Propagation through CAP Aspen Plus Model

Figure 2.7: UQ methodology flow diagram

2.5.1. Inverse UQ using Bayesian Inference

Table 2.6: Regression confidence intervals of parameters included in the UQ framework

	95% Confidence Interval	
Parameter	**Lower**	**Upper**
E_6 [cal/mol]	10559	11153
E_7 [cal/mol]	5726	29780
A_1 [-]	0.593	0.847

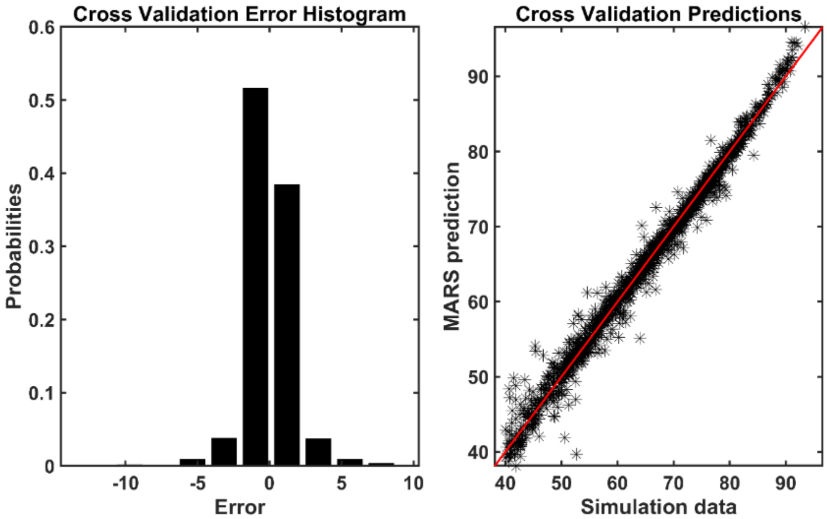

Figure 2.8: MARS response surface validation using 10-fold cross validation (R^2=0.98). (Left) Error histogram and (Right) parity plot comparing CO_2 capture predictions

Table 2.6 shows the parameters included in the UQ framework after downselection and their respective confidence intervals which were obtained from the regression done in this work including the robust estimates as mentioned earlier. The sensitivity of the priors to the results of the Bayesian inference process were tested by changing the variance of the priors and minimal changes were seen. Figure 2.8 shows the quality of the response surface model used in the Bayesian inference process, which was developed using simulation data generated from sampling of the parameter input space as well as operating conditions spanned by the experimental pilot plant data. Figure 2.8 shows that the error of the response surface model is centered around zero, and the large majority of the points in the parity plot lie near the diagonal which, along with a high R^2 value, indicates that the surrogate model is able to accurately represent the packed tower model in the space of parameters and operating conditions considered.

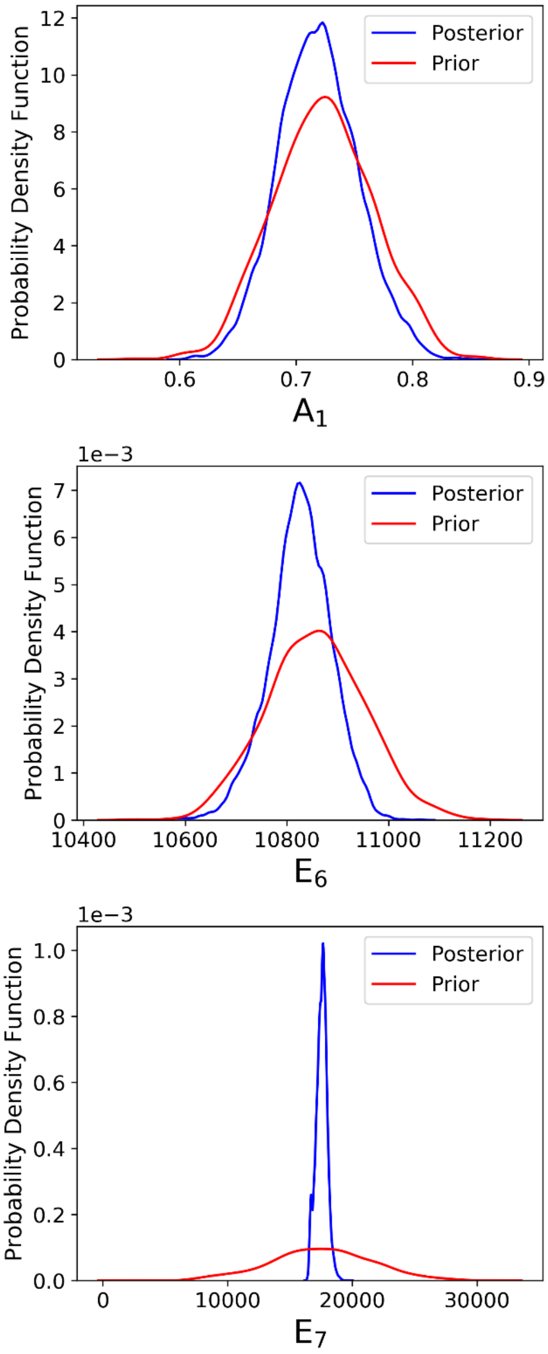

Figure 2.9: Single parameter marginal probability density functions for prior and posterior distributions

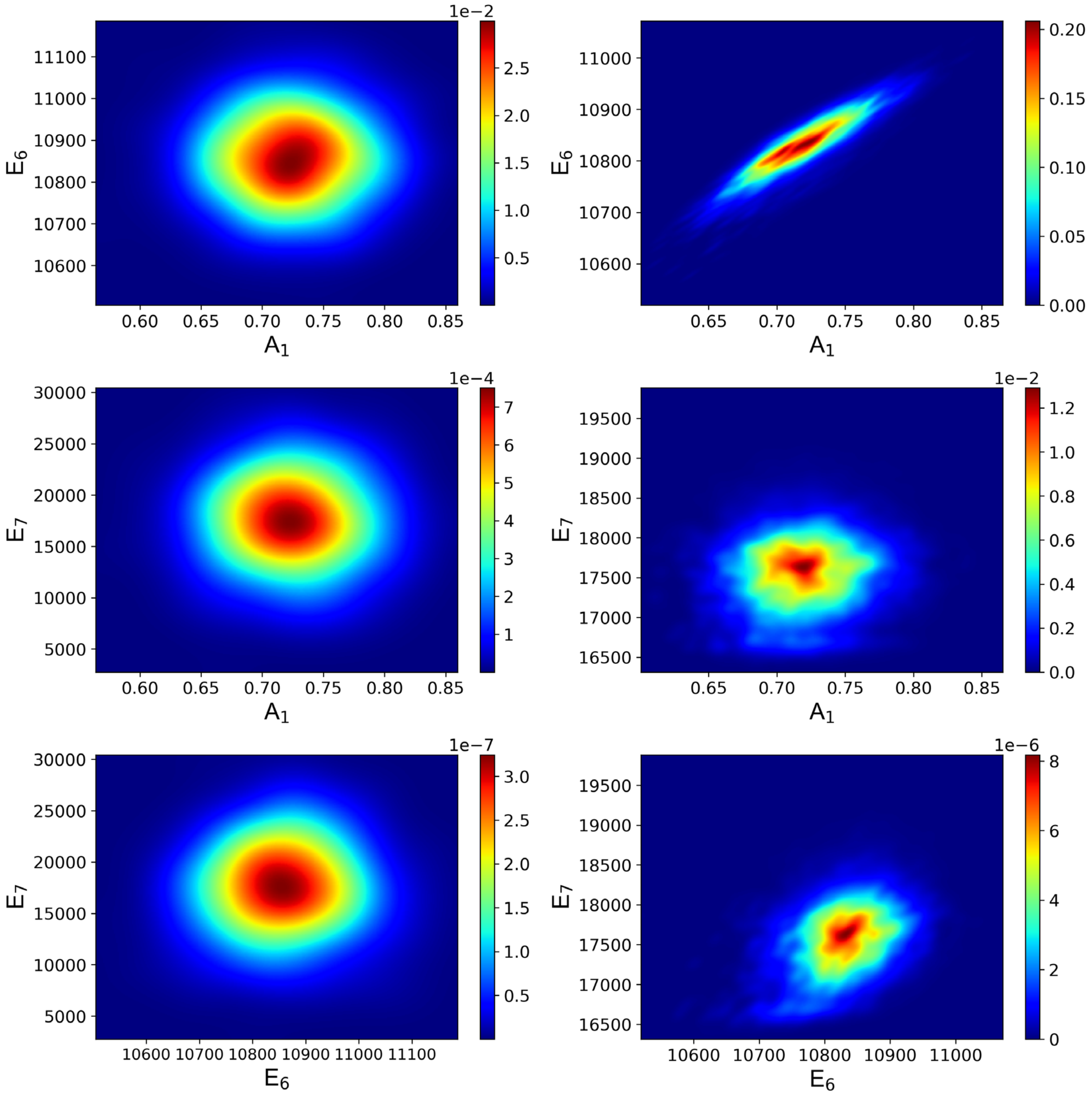

Figure 2.10: Two-parameter prior (left) and posterior (right) probability distributions

Figure 2.9 and Figure 2.10 show the results of the Bayesian inference calculations. Figure 2.9 shows the marginal single-parameter probability density functions for prior and posterior distributions and Figure 2.10 shows the marginal two-parameter prior and posterior distributions. All three parameters show a narrower posterior distribution which indicates a reduction in uncertainty obtained by the Bayesian inference process for these parameters.

2.5.2. Forward UQ using Propagation

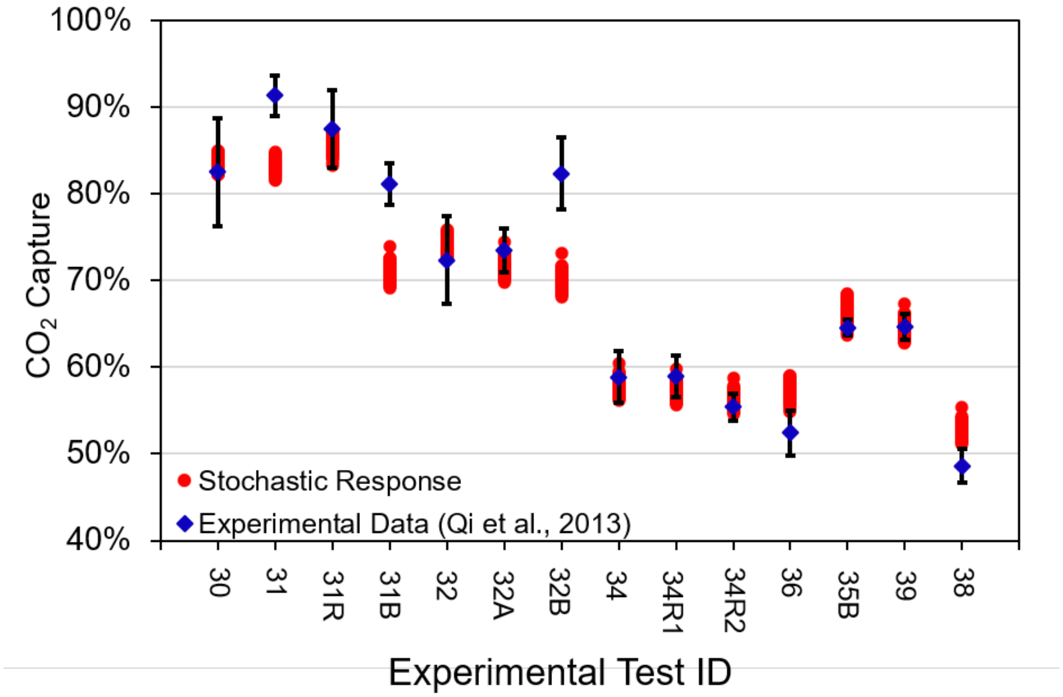

Figure 2.11: Comparison of stochastic model generated using posteriors to experimental data. Experimental data presented with error bars representing ±1 standard deviation included in reporting of the data [14].

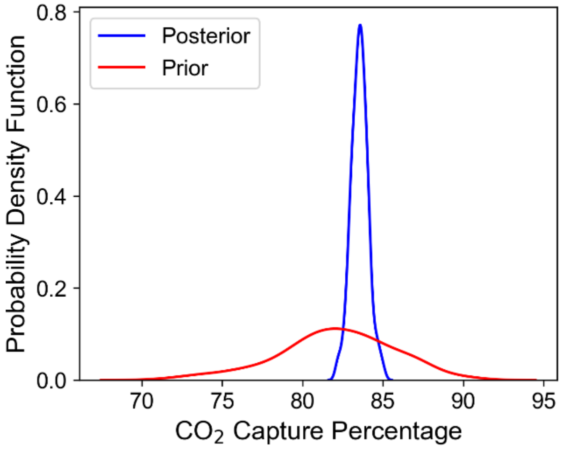

Figure 2.12: Probability density function of CO_2 capture percentage for operating conditions corresponding to experimental test ID 30 (Table A.1)

The effects of parameter uncertainty can better be understood when represented in terms of important process metrics, such as CO_2 capture or energy requirements. To do this, a sample was taken from the joint distributions of the UQ parameters and propagated through the model of interest. Figure 2.11 shows the stochastic response of the posterior distributions for the experimental operating conditions from Qi *et al*. [14] as shown in Table A.1. For the majority of the experimental trials, the experimental data point falls within the range of the stochastic response. Figure 2.12 shows the probability density function for CO_2 capture generated from the stochastic model response for the operating conditions of experimental test ID 30. The width of the 95% confidence interval, which has been previously used in literature to describe the uncertainty of stochastic predictions of process metrics [59], is 13.9 and 2.1 for the prior distribution and posterior distribution, respectively, presented in Figure 2.12. The narrower distribution of the stochastic model generated using the posteriors indicates that the Bayesian inference process results in a reduction in uncertainty when predicting CO_2 capture. The same methodology is applied to the membrane-assisted CAP process model. Figure 2.13 shows the stochastic response of the posteriors and the corresponding 95% confidence intervals for the energy requirements of the CO_2 Stripper Reboiler, NH_3 Stripper Reboiler, and CO_2 Lean Solvent Chiller. Operating conditions corresponding to these results are listed in Table 2.3. It is observed that the Bayesian approach results in a narrow distribution for all three key performance measures- duties of CO_2 stripper reboiler. NH_3 stripper reboiler, and CO_2 lean solvent chiller.

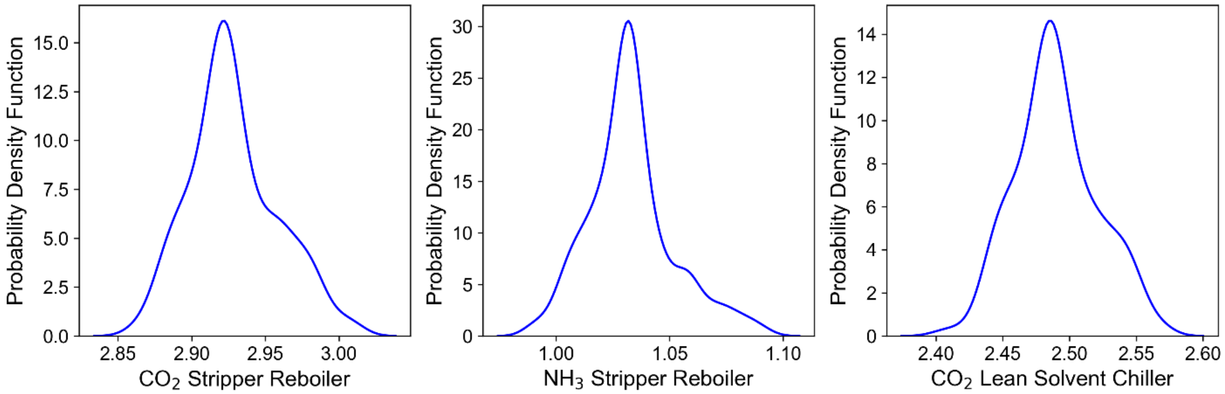

Figure 2.13: Stochastic model results for energy requirements [MJ/kg CO_2] of important equipment in the membrane-assisted CAP process generated using the posteriors. Results also generated considering 60% membrane water removal. 95% Confidence Intervals: [$2.88 \leq CO_2$ Stripper Reboiler ≤ 2.99], [$1.00 \leq NH_3$ Stripper Reboiler ≤ 1.07], [$2.44 \leq CO_2$ Lean Solvent Chiller ≤ 2.55]

2.6. Conclusions

A detailed model of a CAP system was developed with rigorous thermodynamic, transport, kinetic and mass transfer sub-models. Model of a novel CAP system is developed. A simultaneous regression methodology was used for estimating mass transfer and kinetic model parameters utilizing the WWC and pilot-plant data simultaneously. Parameters are estimated using WLS as well as two robust estimation approaches-Hampel's redescending M-estimator and Logistic estimator. Parameters obtained using the WLS estimator resulted in a reduction in RMSE of 10.3% for prediction of the validation data when compared to the literature parameter values. For Hampel's estimator and Logistic estimator, RMSE increased by 9.9% and 4.6% when compared to the literature parameter values, respectively. After downselecting the parameter space and generating priors based on the confidence interval obtained from the WLS and robust estimators, parameter uncertainty was quantified using Bayesian inferences which led to a narrower posterior distribution for all three parameters. For the membrane-assisted CAP system, reboiler, cooler, and condenser duties in the NH_3 abatement section reduces monotonically with increasing water removal by the membrane. However, as the water removal increases, the required membrane area increases with a steeper rise beyond about 60% water removal. Determining the optimal water removal in the membrane would require consideration of the tradeoff between the increasing capital cost due to the increase in the membrane area versus the reduction in the operating cost reboiler, cooler, and condenser duties in the NH_3 abatement section. Nevertheless when 60% water removal is considered, which is considered feasible as it is similar to commercial reverse osmosis applications, the NH_3 stripper reboiler energy requirement reduces by 45% compared to the base case. Moreover, the combined duties of the condenser and cooler decreases by 52% when compared to the base case. The membrane shows promise for reducing energy costs, but future work should focus on identifying any potential drawbacks such as operability or the possibility of solids precipitation deteriorating performance. Posterior distribution of parameters obtained from the Bayesian inference were propagated through the process model corresponding to the pilot plant operating conditions available in the public domain and it was observed that most of the experimental data are within the estimated uncertainty of model predictions. Additional methods such as simultaneous data reconciliation can be used to investigate data outliers and is a possible area of future work. The

UQ performed in this work pertains to only parametric uncertainty, expanding upon this to include more rigorous handling of the measurement and experimental uncertainty in order to obtain a better stochastic response to the data is a possible future area of work. It is also observed that the Bayesian inference results in a nearly 7x reduction in the prediction uncertainty of key variables such as the CO_2 capture compared to the base case. When the posteriors are propagated through the membrane-assisted CAP system, it is observed that there is low uncertainty in the duties of the CO_2 Stripper Reboiler, NH_3 Stripper Reboiler, and CO_2 Lean Solvent Chiller. In future, this model can be utilized for rigorous process optimization or control studies of ammonia-based capture systems. Currently the costs of the commercial membrane for the target application are not available to the best of the author's knowledge. If these costs are available, one desired future work would be to determine the optimal water removal in the membrane. Even though solids precipitation wasn't predicted by the model for the operating conditions in this work, this has been identified as a potential issue and investigating this using other research methods is an area of interest. Nevertheless, the study shows that the membrane-assisted CAP has a high potential for reducing the energy penalty of ammonia-based post-combustion CO_2 capture systems.

3. Isotherm and Kinetic Models for dmpn–Mg_2(dobpdc) and Mg_2(dobpdc)(3-4-3)

Accurate modeling of the adsorption equilibrium is vital to the development of contactor models and subsequent process models which can be utilized for process evaluation. Due to the unique step shaped isotherms exhibited by this class of amine-appended MOFs, traditional isotherms are not applicable. In this chapter, the development of isotherm models for dmpn–Mg_2(dobpdc) and Mg_2(dobpdc)(3-4-3) are presented which can predict the CO_2 adsorption equilibrium with varying temperature and pressure. Two models are developed for **dmpn–Mg_2(dobpdc)**, a **weighted dual-site Langmuir** model and a **dual-site Sips** model. For **Mg_2(dobpdc)(3-4-3)**, an **extended weighted Langmuir** model is developed. A kinetic model is also developed in this chapter using experimental data for **dmpn-Mg_2(dobpdc)** to address the current lack in literature studies which either do no account for kinetic limitations or use models developed for other sorbents.

Portions of this Chapter are published in the following peer-reviewed journal article:

Hughes, R.; Kotamreddy, G.; Ostace, A.; Bhattacharyya, D.; Siegelman, R. L.; Parker, S. T.; Didas, S. A.; Long, J. R.; Omell, B.; Matuszewski, M. Isotherm, Kinetic, Process Modeling, and Techno-Economic Analysis of a Diamine-Appended Metal–Organic Framework for CO_2 Capture Using Fixed Bed Contactors. *Energy Fuels* **2021**, *35* (7), 6040–6055. https://doi.org/10.1021/acs.energyfuels.0c04359.

3.1. Introduction

Traditional isotherm models are unable to predict the step shaped isotherms exhibited by this class of MOFs. The fit of many traditional isotherm models to dmpn-Mg_2(dobpdc) can be seen in the Appendix of this work. However, in some cases these models have been adapted or new models developed to account for the stepped adsorption. In the first study of a previous MOF variant, mmen–M_2(dobpdc) (mmen = *N*,*N*′-dimethylethylenediamine), CO_2 uptake was modeled using three separate equations before, at, and after the adsorption step [25], but the discontinuity of this approach renders it unacceptable for use in process modeling and optimization. Notably, the weighted dual-site Langmuir model used by Hefti *et al.* [60] was able to accurately predict the complete adsorption profile for mmen–M_2(dobpdc). Kundu *et al.* [61] presented a model for CO_2 uptake in mmen–M_2(dobpdc) derived from quantum and statistical mechanics that was able to predict the position of the isotherm step but poorly reproduced adsorption behavior after the step. Pai *et al.* [62] separately modeled chemisorption and physisorption of CO_2 in mmen–M_2(dobpdc) and used both single-site and dual-site Langmuir models to fully describe the adsorption data. The two-step isotherm data exhibited by Mg_2(dobpdc) will only increase the difficulty of developing models which can predict step shaped behavior. To the best of the author's knowledge, Ga *et. al.* [63] presents the only model available in literature for multistep adsorption isotherms applied to amine-appended MOFs. The model uses rectified constant units to apply traditional isotherm models to subregions in the pressure range of the experimental data and is applied to 2-ampd-Mg_2(dobpdc). The current literature focuses on the modeling and evaluation of mmen-M_2(dobpdc) and 2-ampd-Mg_2(dobpdc), but models developed for a certain diamine variant may not be suitable for other variants. Specifically, the presence of different diamines altering the shape of the isotherm curves make it difficult to apply existing models to new variants. To apply these models to our MOFs of interest, dmpn–Mg_2(dobpdc) and Mg_2(dobpdc)(3-4-3), model parameters would need to be re-estimated and even with these re-estimated parameters, the models may be inadequate.

The current literature also lacks kinetic models that are developed using experimental data for diamine-appended MOFs. They instead rely on mass transfer coefficients that are developed using generalized correlations or estimated from experimental data for other solid sorbents [60,62,64–66]. These models also have also exclusively focused on mmen–M_2(dobpdc). Hefti *et al.* [60] ignore kinetics and assume equilibrium in their shortcut based modeling of a TSA system. In later work by the same researchers [64], a kinetic model is used which considers a constant mass transfer coefficient for CO_2 that was estimated using experiments with activated carbons [65,66]. Pai *et al.*[62] assume macropore molecular diffusion to be the controlling mass transfer mechanism and the properties of a commercial zeolite were used to calculate the mass transfer coefficient.

Herein, a modified weighted dual-site Langmuir isotherm model and a dual-site Sips isotherm model is used to fit CO_2 adsorption data for dmpn–Mg_2(dobpdc) for the first time. Additionally, an extension of the weighted Langmuir model is use to fit CO_2 adsorption data for Mg_2(dobpdc)(3-4-3) for the first time. A kinetic model for CO_2 adsorption in dmpn–Mg_2(dobpdc) is also developed from thermogravimetric analysis data and used with the Sips adsorption model which is validated using experimental breakthrough data.

3.2. Isotherm Model Development

3.2.1. Weighted Dual-Site Langmuir Model. The first isotherm model investigated is a weighted dual-site Langmuir model similar to that developed by Hefti *et al.* [60] for predicting the CO_2 adsorption equilibrium of mmen–M_2(dobpdc).

$$q_{CO_2}^* = n_L(p,T)\big(1-\omega(p,T)\big) + n_U(p,T)\omega(p,T) \tag{3.1}$$

Here, $q_{CO_2}^*$ represents the equilibrium loading of CO_2 predicted by the model, p is the CO_2 pressure, and n_L and n_U describe the lower and upper portions of the isotherm before and after the adsorption step. The term $\omega(P,T)$ (Eq. (3.5)) is a weighting function that shifts the predicted equilibrium loading from the lower to the upper region of the isotherm model as the pressure increases, which enables the modeling of stepped behavior [60]. While it is difficult to find a rigorous physical interpretation of the weighting function, it helps to retain the characteristics of the underlying isotherm, offer flexibility, and have been used in the literature for modeling complex isotherm characteristics of some MOFs [60,67]. The terms n_L and n_U are given by Eqs. (3.2) and (3.3):

$$n_L = \frac{n_L^\infty d_L p}{1 + d_L p} + d_B p \tag{3.2}$$

$$n_U = \frac{n_U^\infty d_U p}{1 + d_U p} + d_H p \tag{3.3}$$

$$d_\propto = d_\propto^\infty \exp\left(\frac{E_\propto}{RT}\right); \quad \propto \in [L,B,U,H] \tag{3.4}$$

$$\omega(P,T) = \left(\frac{\exp\left(\frac{\ln(p) - \ln(p_{step}(T))}{\sigma(T)}\right)}{1 + \exp\left(\frac{\ln(p) - \ln(p_{step}(T))}{\sigma(T)}\right)} \right)^{\gamma} \tag{3.5}$$

$$\sigma(T) = X_1 \exp\left(X_2 \left(\frac{1}{T_0} - \frac{1}{T} \right) \right) \tag{3.6}$$

$$p_{step}(T) = p_{step,0} \exp\left(\frac{-H_{step}}{R} \left(\frac{1}{T_0} - \frac{1}{T} \right) \right) \tag{3.7}$$

We note that in Hefti *et al.* [60], the n_L parameter contains only the first term shown in Eq. (3.2); however, our initial results with this form showed poor model performance at pressures before the adsorption step. Accordingly, in this work n_L was altered to include the heuristic linear $d_B p$ term to improve the model, analogous to the form of upper isotherm parameter n_U. In Eq. (3.5), the parameters p_{step} and γ determine the position of the step and σ determines the step width (here, pressure range). The parameters n_L^{∞}, n_U^{∞}, $d_{\propto}^{\infty}$, $E_{\propto}$, γ, X_1, X_2, p, $P_{step,0}$, and H_{step} (a total of 15 parameters) are determined from fits to the experimental data.

3.2.2. Dual-site Sips Model. Previous characterization of various diamine-appended M_2(dobpdc) frameworks via ^{13}C solid-state NMR spectroscopy [30] revealed that a small amount of CO_2 is physisorbed in the materials in addition to the major chemisorption product. Accordingly, a dual-site Sips isotherm model was also used to model the equilibrium of chemisorbed and physisorbed CO_2 in dmpn–Mg_2(dobpdc). This model is used to predict adsorption in heterogeneous systems and has been used previously to describe CO_2 and methane uptake in Mg_2(dobdc) (dobdc^{4-} = 2,5-dioxido-1,4-benzenedicarboxylate) [68], while a single-site Sips equation with added temperature dependent terms has been used to model adsorption of N_2, methane, ethane, and propane on commercial activated carbons and polyvinyl chloride [69]. The dual-site Sips model used in this work is given in Eqs. (3.8) and (3.9) and is a modified version of the model developed by Bao *et al.* [68], with the introduction of temperature dependence in the terms q_{chem}^{∞}, q_{phys}^{∞}, and n_{chem}.

$$q_{CO_2}^* = q_{chem}^* + q_{phys}^* \tag{3.8}$$

$$q_{CO_2}^* = q_{chem}^{\infty}\left[\frac{(b_{chem}p)^{1/n_{chem}}}{1 + (b_{chem}p)^{1/n_{chem}}}\right] + q_{phys}^{\infty}\left[\frac{\left(b_{phys}p\right)^{1/n_{phys}}}{1 + \left(b_{phys}p\right)^{1/n_{phys}}}\right] \tag{3.9}$$

Here, $q_{CO_2}^*$ is the total CO_2 equilibrium loading predicted by the model, p is the equilibrium pressure, and n_{chem} and n_{phys} are fit parameters that account for surface inhomogeneity [68]. The term n_{chem} varies as a function of temperature according to Eq. (3.10):

$$n_{chem} = n_{chem,0} exp\left[\frac{E_n}{RT_0}\left(\frac{T_0}{T} - 1\right)\right] \tag{3.10}$$

Here, R is the ideal gas constant, T_0 is a reference temperature (318 K), and $n_{chem,0}$ and E_n are parameters determined from the fit. The terms q_{chem}^{∞} and q_{phys}^{∞} in Eq. (3.9) describe the maximum loading at chemisorption and physisorption sites, respectively, and are given by:

$$q_{chem}^{\infty} = N_{chem}\left[\frac{exp\left(K_a + {}^{K_b}\!/_{T}\right)}{1 + exp\left(K_a + {}^{K_b}\!/_{T}\right)}\right] \tag{3.11}$$

$$q_{phys}^{\infty} = N_{phys}\left[\frac{exp\left(K_c + {}^{K_d}\!/_{T}\right)}{1 + exp\left(K_c + {}^{K_d}\!/_{T}\right)}\right] \tag{3.12}$$

Here, N_{chem} is the diamine loading in the MOF (determined experimentally to be 3.82 mmol/g [3]) and K_a, K_b, K_c, K_d, and N_{phys} are fit parameters. Eq. (3.11) was first derived for the chemisorption sites under the assumption that there is a 1:1 ratio of diamine to chemisorbed CO_2, and Eq. (3.12) was adopted for the physisorption sites and is analogous to the form of Eq. (3.11). Parameters b_{chem} and b_{phys} in Eq. (9) are adsorption equilibrium constants for the two adsorption sites, defined by Eq. (3.13).

$$b_{\propto} = b_{\propto,0}\exp\left[\frac{Q_{st,\propto}}{RT_0}\left(\frac{T_0}{T} - 1\right)\right], \propto \in [chem, phys] \tag{3.13}$$

Here, $Q_{st,j}$ are the isosteric heats of adsorption at zero loading [68] at each adsorption site that are also determined from the fit, and R is the ideal gas constant. Overall, the dual-site Sips model has 12 parameters that are estimated using the experimental data.

3.2.3. Extended weighted Langmuir Model. To model the two step transitions for Mg2(dobpdc)(3-4-3), the weighted dual-site Langmuir model presented by Hefti *et al.* [60] is extended by adding a second weighting function, as shown in Eq. (3.14).

$$q_{CO_2}^* = (1 - \omega_1)q_1^* + (\omega_1 - \omega_2)q_2^* + \omega_2 q_3^* \tag{3.14}$$

Here, q_1^*, q_2^*, q_3^* are the Langmuir type isotherm models which represent the three main sections of the isotherm. q_1^* represents the section before the first step transition, q_2^* represents the section between the first and second transition, and q_3^* represents the section after the second transition. ω_1 and ω_2 are the weighting functions which follow the same functional form as the dual-Site Langmuir model presented above. A complete list of the isotherm equations for the extended weighted Langmuir model is shown below.

$$q_1^* = q_1^\infty \frac{d_1 P}{1 + d_1 P} \tag{3.15}$$

$$q_2^* = q_2^\infty \frac{d_2 P}{1 + d_2 P} \tag{3.16}$$

$$q_3^* = q_3^\infty \frac{d_3 P}{1 + d_3 P} + d_4 P \tag{3.17}$$

$$d_\alpha = d_\alpha^\infty exp\left(\frac{-E_\alpha}{RT_0}\left(\frac{T_0}{T} - 1\right)\right); \quad \alpha \in [1,2,3,4] \tag{3.18}$$

$$\omega_1 = \left[\frac{exp\left(\frac{ln(P) - ln\left(P_{step,1}\right)}{\sigma_1}\right)}{1 + exp\left(\frac{ln(P) - ln\left(P_{step,1}\right)}{\sigma_1}\right)}\right]^{\gamma_1} \tag{3.19}$$

$$\omega_2 = \left[\frac{exp\left(\frac{ln(P) - ln\left(P_{step,2}\right)}{\sigma_2}\right)}{1 + exp\left(\frac{ln(P) - ln\left(P_{step,2}\right)}{\sigma_2}\right)}\right]^{\gamma_2} \tag{3.20}$$

$$\sigma_\alpha = X_{1,\alpha} exp\left[X_{2,\alpha}\left(\frac{1}{T_0} - \frac{1}{T}\right)\right]; \quad \alpha \in [1,2] \tag{3.21}$$

$$P_{step,\alpha} = P_{0,\alpha} exp\left[\frac{-H_{step,\alpha}}{R}\left(\frac{1}{T_0} - \frac{1}{T}\right)\right]; \quad \alpha \in [1,2] \tag{3.22}$$

As before, the weighting functions vary with temperature and pressure and are naturally bounded between 0 and 1. At low pressures, both weighting functions are near zero which results in the total CO_2 loading consisting of the first Langmuir model. As the pressure increases above the first step pressure, the first weighting function reaches a value of 1 and the second Langmuir term is the dominant contributor to the total loading. Finally, as the pressure increases above both step pressures, both weighting functions go to values of 1 and the third Langmuir term is the main contributor.

3.2.4. Parameter Estimation. Model parameters were estimated using the 'fmincon' routine in MATLAB, which uses a sequential quadratic programming algorithm to solve the following optimization problem:

$$\min_{\theta} \left(\frac{q^*_{CO_2,exp} - q^*_{CO_2,model}}{q^*_{CO_2,exp}}\right)' \Sigma^{-1} \left(\frac{q^*_{CO_2,exp} - q^*_{CO_2,model}}{q^*_{CO_2,exp}}\right)$$

$$s.t. \tag{3.23}$$

$$f(\theta) = 0$$
$$g(\theta) \leq 0$$

where $q^*_{CO_2,exp}$ represents the experimental equilibrium loading data, $q^*_{CO_2,model}$ represents the model prediction, θ represents the vector of estimated parameters, and $f(\theta)$ and $g(\theta)$ represent the equality and inequality constraints, respectively. For this problem, the equality constraints consist of the isotherm equations for the model of interest listed above, and the inequality constraints consist of upper and lower bounds for the model parameters. The objective function uses a normalized least squares method with a weighting matrix Σ^{-1}. Because a larger number of experimental data points were available at lower pressures than at higher pressure, a weighted objective function was used where the weight for each data point was set to be inversely proportional to the number of data points that are in the same neighborhood of partial pressure as the data point that is being evaluated. Accordingly, the data were divided up into intervals, or bins, of equal length with respect to partial pressure. The bin size was chosen so that every bin contained at least one data point. The weight of a specific data point is then equal to the inverse of the number of data points in the bin where the data point of interest resides.

3.2.5. dmpn-Mg_2(dobpdc) Isotherm Model Results. As noted earlier, 15 and 12 parameters are estimated for the dual-site Langmuir model and dual-site Sips model, respectively. For estimating these parameters, more than 500 isotherm data showing variation in loading with respect to temperature and pressure have been used. About 100 isotherm data are used for model validation. Various initial guesses were investigated, and the optimizer converged to the same optimal estimates.

Experimental adsorption data for dmpn–Mg_2(dobpdc) [3] and corresponding fits derived using the dual-site Sips and weighted dual-site Langmuir isotherm models are shown in Figure 3.1. Table 3.1 and Table 3.2 shows the estimated model parameters (see Figure A.4 in the Appendix for residual plots for the isotherm model development). To better visualize the fits to the data, the results shown in Figure 3.1 are also presented on a linear scale with respect to partial pressure in the Appendix in Figure A.5 and Figure A.6. Both models are able to accurately predict the step locations at all temperatures. The Sips model also provides a good fit to the data before the step transition, but the goodness of the fit diminishes at low temperatures and high pressures. In contrast, the weighted Langmuir model provides a better fit to the data beyond the adsorption step but does not adequately fit the upper region of the adsorption step, particularly at 60 and 75 °C. However, both models show good agreement with the experimental data under conditions relevant to a typical post-combustion TSA process, namely adsorption between 25 and 50 °C at partial pressures between 0.01 and 0.15 bar and desorption between 75 and 120 °C at partial pressures that encompass the range of experimental partial pressures.

During a TSA cycle, the temperatures and partial pressures within the bed can reach values that are between the boundary conditions for adsorption and desorption. Models developed using only experimental data pertaining to those conditions may therefore perform poorly under intermediate conditions. Considering this, additional adsorption data were collected at 80 and 90 °C and used for model validation for both isotherm models (Figure 3.2). At 80 °C, the dual-site Sips model predicts a less abrupt step than is present in the experimental data, whereas there is no clear step in the weighted dual-site Langmuir model at the same temperature. At 90 °C, both models predict slightly higher loadings than are observed experimentally, although it is clear that the Sips model performs better overall. Based on the above results and the root mean squared error for each model (Table 3.3), the dual-site Sips model was selected to predict subsequent adsorption equilibria.

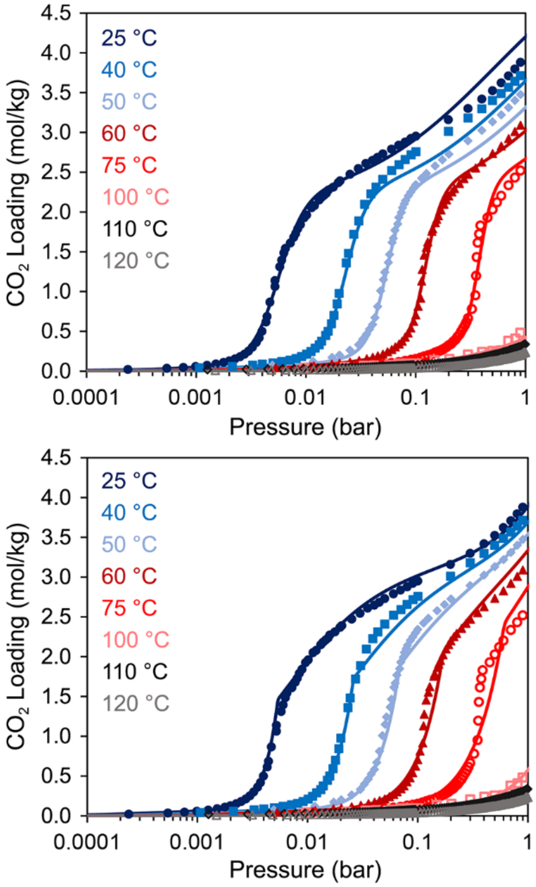

Figure 3.1: Experimental CO_2 adsorption isotherms for dmpn–Mg_2(dobpdc) at the indicated temperatures (colored symbols) and fits (colored lines) using a dual-site Sips isotherm model (upper) and a weighted dual-site Langmuir isotherm model (lower).

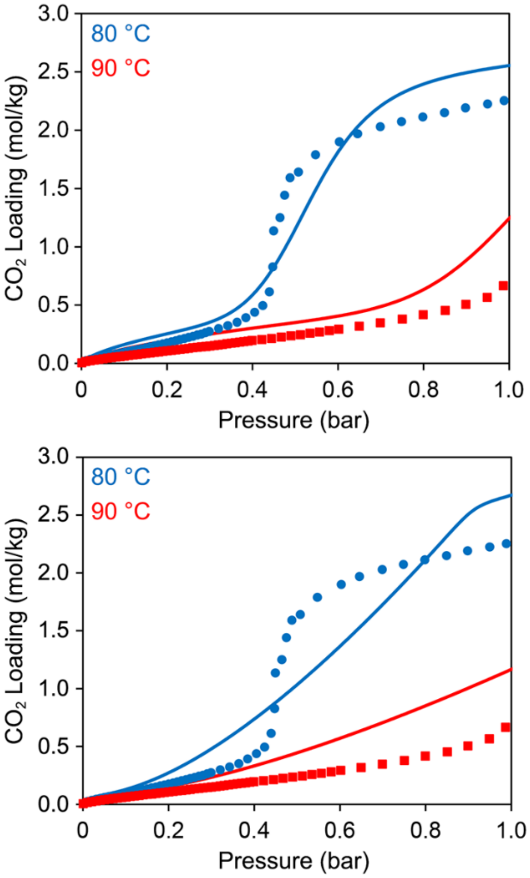

Figure 3.2: Model validation results for the dual-site Sips model (upper) and weighted dual-site Langmuir model (lower). Experimental CO_2 adsorption data for dmpn–Mg_2(dobpdc) at 80 and 90 °C are shown as colored symbols and fits to the data are shown as colored lines.

Table 3.1: Fit parameters determined using the weighted dual-site Langmuir model for CO_2 adsorption in dmpn–Mg_2(dobpdc).

Parameter	Value	Units
$p_{step,0}$	0.027	[bar]
H_{step}	−81.70	[kJ/mol]
n_L^{∞}	0.0895	[mmol/g]
b_L^{∞}	2.05×10^{-6}	[bar^{-1}]
E_L	51.1	[kJ/mol]
b_b^{∞}	4.19×10^{-4}	[mmol/g/bar]
E_b	13.6	[kJ/mol]
n_U^{∞}	3.12	[mmol/g]
b_U^{∞}	6.17×10^{-10}	[bar^{-1}]
E_U	65.2	[kJ/mol]
b_H^{∞}	0.00862	[mmol/g/bar]
E_H	11.2	[kJ/mol]
X_1	0.0100	[dimensionless]
X_2	1767.5	[K^{-1}]
γ	0.0223	[dimensionless]

Table 3.2: Fit parameters determined using the dual-site Sips model for CO_2 adsorption in dmpn–Mg_2(dobpdc)

Parameter	Value	Units
$b_{chem,0}$	28.56	[bar^{-1}]
$Q_{st,chem}$	72.56	[kJ/mol]
$n_{chem,0}$	0.21	[dimensionless]
$b_{phys,0}$	0.62	[bar^{-1}]
$Q_{st,phys}$	43.83	[kJ/mol]
n_{phys}	1.46	[dimensionless]
N_{phys}	3.52	[mmol/g]
K_a	−0.92	[dimensionless]
K_b	324.86	[K]
E_n	11.29	[kJ/mol]
K_c	−71.14	[dimensionless]
K_d	2.84×10^{4}	[K]

Table 3.3: Root mean squared errors determined for the dual-site Sips and weighted dual-site Langmuir model fits.

	dual-site Sips	weighted dual-site Langmuir
Estimation data	0.050	0.137
Validation data	0.163	0.190

3.2.6. Mg_2(dobpdc)(3-4-3) Isotherm Model Results. In total, 21 parameters are estimated for extended weighted Langmuir model. Isotherm data is taken from Kim *et al.* [29] and includes 232 data points for pressures ranging from 0.5 mbar to 1000 mbar and 4 temperature sets (90 °C, 100 °C, 110 °C, and 120 °C). Figure 3.3 shows the results of the parameter estimation and the fit of the extended weighted Langmuir model to the isotherm data. It can be seen that the model shows excellent prediction of the data at all temperatures and pressures and notably is able to accurately predict both step positions for all temperatures (RMSE=0.18 [dimensionless]).

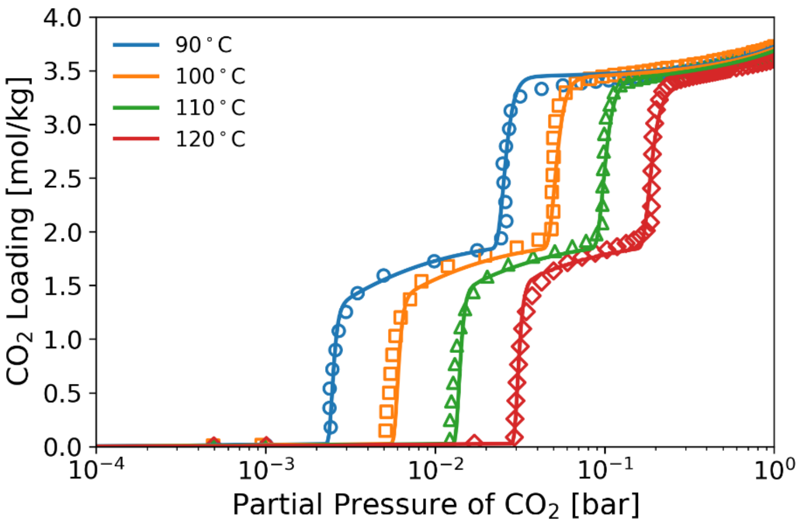

Figure 3.3: Experimental CO_2 adsorption isotherms for Mg_2(dobpdc)(3-4-3) at the indicated temperatures (colored symbols) and fits (colored lines) using the extended weighted Langmuir model.

Table 3.4: Fit parameters determined using the extended weighted Langmuir model for CO_2 adsorption in Mg_2(dobpdc)(3-4-3).

Parameter	Estimated Value	Units
q_1^∞	2.87E-02	[mol/kg]
q_2^∞	1.95	[mol/kg]
q_3^∞	3.45	[mol/kg]
d_1^∞	1670.31	[bar^{-1}]
d_2^∞	789.01	[bar^{-1}]
d_3^∞	10990.67	[bar^{-1}]
d_4^∞	0.28	[bar^{-1}]
E_1	-76.15	[kJ/mol]
E_2	-77.44	[kJ/mol]
E_3	-194.48	[kJ/mol]
E_4	-6.76	[kJ/mol]
$X_{1,1}$	4.20E-02	[dimensionless]
$X_{2,1}$	2.97	[K^{-1}]
$X_{1,2}$	7.74E-02	[dimensionless]
$X_{2,2}$	1.66	[K^{-1}]
$P_{0,1}$	1.85E-03	[bar]
$H_{step,1}$	-99.64	[kJ/mol]
$P_{0,2}$	1.78E-02	[bar]
$H_{step,2}$	-78.19	[kJ/mol]
γ_1	894.67	[dimensionless]
γ_2	95.22	[dimensionless]

3.3. Kinetic Model Development

The kinetics of CO_2 adsorption in powdered dmpn–Mg_2(dobpdc) were characterized using thermogravimetric analysis. Time-dependent uptake data were collected at temperatures of 35, 40, 45, and 50 °C using a pure CO_2 gas stream at atmospheric pressure, following the experimental protocol in Martell *et al.* [70]. The total CO_2 adsorption rate was modeled as the sum of the chemisorption and physisorption rates, and a linear driving force was used to model the kinetics as shown in Eqs. (3.24)-(3.26). Due to a lack of experimental data, a kinetic model for Mg_2(dobpdc)(3-4-3) was not developed.

$$\frac{dq_{CO_2}}{dt} = \frac{dq_{chem}}{dt} + \frac{dq_{phys}}{dt} = k_{chem}(q^*_{chem} - q_{chem}) + k_{phys}\left(q^*_{phys} - q_{phys}\right) \tag{3.24}$$

$$k_{chem} = k_{chem,0} exp\left[\frac{-E_{chem}}{RT_0}\left(\frac{T_0}{T} - 1\right)\right] \tag{3.25}$$

$$k_{phys} = k_{phys,0} exp\left[\frac{-E_{phys}}{RT_0}\left(\frac{T_0}{T} - 1\right)\right] \tag{3.26}$$

Here, q_{chem} and q_{phys} are the loadings of the chemisorption and physisorption products, respectively, and q^*_{chem} and q^*_{phys} are the predicted equilibrium loadings as defined above for the dual-site Sips isotherm model. The parameters k_{chem} and k_{phys} are mass transfer coefficients modeled using a standard Arrhenius equation, and $k_{chem,0}$, $k_{phys,0}$, E_{chem}, and E_{phys} are parameters determined from fitting the model to the experimental data. Model parameters were estimated using the fmincon routine in MATLAB and a sequential quadratic programming algorithm to solve the following optimization problem:

$$\begin{gathered}\min_{\theta} \left(\frac{q_{CO_2,exp} - q_{CO_2,model}}{q_{CO_2,exp}}\right)' \Sigma^{-1} \left(\frac{q_{CO_2,exp} - q_{CO_2,model}}{q_{CO_2,exp}}\right) \\ s.t. \\ f(\theta) = 0 \\ g(\theta) \leq 0\end{gathered} \tag{3.27}$$

where $q_{CO_2,exp}$ represents the experimental loading data, $q_{CO_2,model}$ represents the model prediction, θ represents the vector of estimated parameters, and $f(\theta)$ and $g(\theta)$ represent the equality and inequality constraints, respectively. For this problem, the equality constraints consist of the kinetic equations listed above, and the inequality constraints consist of upper and lower bounds for the model parameters.

As seen in Figure 3.4, the linear driving force kinetic model is able to accurately describe the kinetics of CO_2 uptake in dmpn–Mg_2(dobpdc). Estimated parameters are shown in Table 3.5

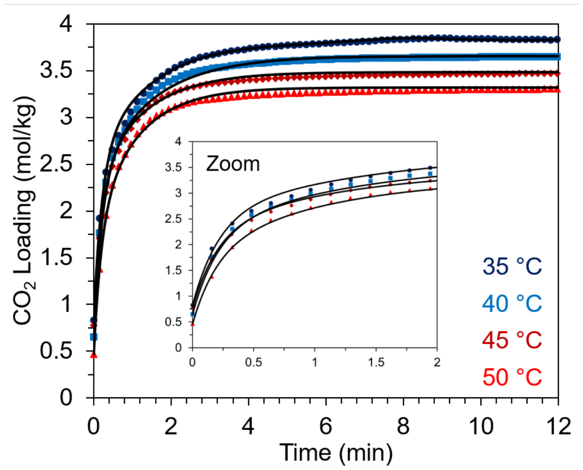

Figure 3.4: Experimental data for time-dependent CO_2 adsorption in dmpn−Mg_2(dobdc) (colored symbols) and fits obtained using the linear driving force kinetic model (RMSE = 0.025).

Table 3.5: Fitted parameters for linear driving force kinetic model

Parameter	**Value**	**Units**
$k_{chem,0}$	0.0136	[s^{-1}]
E_{chem}	23.21	[kJ/mol]
$k_{phys,0}$	0.0823	[s^{-1}]
E_{phys}	7.18	[kJ/mol]

3.4. Conclusions

In this chapter, isotherm models for two amine-appended metal-organic frameworks, dmpn-Mg_2(dobpdc) and Mg_2(dobpdc)(3-4-3), are developed. A Sips isotherm model and weighted dual-site Langmuir isotherm model were developed that are able to accurately describe the adsorption of pure CO_2 in dmpn–Mg_2(dobpdc). The resulting models and parameters were also able to model validation data collected at additional temperatures that were not included in the initial parameter estimation. The sips isotherm model showed less error for the estimation data (-64%) and the validation data (-14%) when compared to the weighted dual-site Langmuir model. An extended weighted Langmuir model was developed to predict the two step adsorption isotherms for pure CO_2 in Mg_2(dobpdc)(3-4-3). The model is able to accurately predict the isotherm data yielding a RMSE of 0.18 [dimensionless]. The kinetic model developed in this chapter was also able to accurately describe experimental data for dmpn-Mg_2(dobpdc) obtained from thermogravimetric analysis. These models were developed considering adsorption of pure CO_2, which is suitable for a base case analysis given that the CO_2 adsorption capacity of dmpn–Mg_2(dobpdc) and kinetics of CO_2 adsorption in the material are not significantly affected in the presence of water. However, the development of more rigorous models will necessitate including an analysis of the effects of water co-adsorption on overall process performance.

4. Chemistry-based Modeling for Functionalized Solid Sorbents

In this chapter, a chemistry-based model for a diamine-appended MOF [**dmpn-Mg_2(dobpdc)**] is developed for the first time. Since the chemistry and reaction pathways of dmpn-Mg_2(dobpdc) is still relatively unknown, optimal reaction set selection from a proposed candidate set is performed. Estimation of the chemistry model parameters is performed using isotherm data, and the chemistry model is found to reduce prediction error by nearly a factor of 6 and the AIC by 42% when compared to heuristic models. The model also implements a constraint on the heat of adsorption prediction into model development via an inequality constraint in the parameter estimation problem which is not typically done for chemistry-based models. Profiles for the total CO_2 loading as well as the chemisorption species are presented and discussed in this chapter.

4.1. Introduction

The prediction of adsorption equilibrium for solid sorbents is typically done using traditional "off the shelf" isotherm models. As many of these traditional isotherm models have been historically developed for non-functionalized sorbents, they may not adequately represent the complicated isotherm behavior of the functionalized sorbents. Traditional isotherm models can be altered and expanded upon to allow for more accurate prediction of the isotherm data of the functionalized sorbents, similar to the methodology used in previous chapters of this work and in literature [25,60,62]. The result of this workflow is isotherm models which are heuristic and may give good fits to experimental data, but do not give any insight into the underlying adsorption mechanisms. Additionally, many of the isotherm models are developed for physisorption mechanisms and are incapable of capturing underlying chemisorption mechanisms which can give important insight into process performance and behavior. Development of chemistry-based models for functionalized solid sorbents can be extremely beneficial for understanding the reaction mechanisms which may not be well known or well understood for novel sorbents, especially because of impracticality of identifying species formed and measuring their evolving concentration with operating conditions at the interior of solids. A chemistry-based model also can improve modeling fidelity and accuracy by predicting CO_2 adsorption capacity, quantifying interactions of other species present in flue gas, specifically water, and calculating a more accurate estimate of heat of adsorption. Additionally, a chemistry model also has the possibility of aiding in the development of new sorbent technologies. The products that are formed during adsorption are nearly impossible to measure, and a chemistry model which can predict adsorption equilibrium, adsorption products, and heats of adsorption can reduce the need for complex experimental work and reduce the time it takes to identify new possible sorbent variants and aid in the development of new technologies.

Currently, there are few chemistry-based models for solid sorbents present in the literature which include adsorbate-adsorbent reactions. Lee *et al.* [71] present a model for the chemisorption of CO_2 on potassium-carbonate-promoted hydrotalcite. The model considers two reactions, initial chemisorption of CO_2 onto an empty surface site and a coupling reaction in which gaseous CO_2 reacts with the initial chemisorption product to form a large surface complex. Using an additional site balance equations and a simple kinetic formulation, an analytical solution of the reaction system at equilibrium was obtained, and parameter estimation shows that the chemisorption model is able to accurately predict the unique isotherm shape of the potassium-carbonate-promoted hydrotalcite. The same researchers also exhibit that this chemisorption model, with re-estimated parameters, is able to accurately predict CO_2 adsorption equilibrium on sodium oxide promoted alumina [72,73]. Additionally, the model is used to predict the isosteric heat of adsorption and shows good prediction when compared to available literature data but isn't used in any model development purposes. For this model, parameter estimation is done for each respective temperature that data is available which results in a different set of parameters for each temperature. This method isn't suitable for use of the model in rigorous process simulators which consider adiabatic systems with varying temperatures along the length of an adsorption bed. Abdollahi-Govar *et al.* [74] developed semi-empirical kinetic models for the reversible adsorption and desorption of CO_2 in a solid amine sorbent composed of polyethylenimine (PEI) immobilized on a silica support. The authors investigate multiple candidate sets of CO_2 reactions with different amine sites within PEI and perform optimal reaction set selection based on the fit of each set to time dependent TGA data. Model parameters for each candidate set are simultaneously estimated using data for multiple temperatures and CO_2 concentrations, and the authors find that their semi-empirical mechanistic model is able to accurately predict the kinetic experiments. The authors also predict heat of adsorption using their model but do not consider it in any stage of model development. Other sources [75,76] present chemisorption models that follow a very similar structure: formulation of reactions specific to the system of interest, kinetic equation formulation for the reactions of interest, and solutions of the model for either kinetic or equilibrium conditions.

These chemistry-based models do an adequate job at predicting either the kinetic or equilibrium data for their respective sorbents, but the adsorption equilibrium behavior of amine-appended MOFs is significantly different than the sorbents for which these chemistry models were developed, specifically their sensitivity to temperature and pressure. Potassium-carbonate-promoted hydrotalcite and sodium oxide promoted alumina, which the Lee *et al*. [71–73] model was applied to, exhibits Langmuir behavior in the low pressure region with deviation at higher pressure, but does not show a sensitivity to pressure as steep as the step shaped isotherms of the amine-appended MOFs. Additionally, only a small number of temperatures are used to develop the models with the shape of the isotherm staying relatively similar for each which is unlike many of the amine-appended MOFs. For example, the dmpn-Mg_2(dobpdc) stepped isotherm shape completely disappears at high temperatures which is a behavior that must be accounted for by any prospective adsorption equilibrium model. Abdollahi-Govar *et al.* [74] developed their chemistry-based model for polyethylenimine (PEI) immobilized on a silica support which exhibits Langmuir type equilibrium curves which are not as sensitive to pressure and temperature as the isotherm curves for many of the amine-appended MOFs. For the chemistry-based models discussed here, significant additions would be required for them to accurately predict the adsorption equilibrium behavior of amine-appended MOFs being considered for carbon capture. Reaction mechanisms of the amine-appended MOFs are complex, and their isotherm characteristics are unique due to the chain formation-which has not been modeled in the literature. Furthermore, none of the works noted above have considered heat of adsorption as a constraint while developing the chemistry models and estimating the kinetic parameters. However, as the equilibrium (i.e., isotherm) and heat of adsorption are thermodynamically related, heat of adsorption should be considered as a constraint while estimating the parameters of the chemistry model for thermodynamic consistency.

In this work, a chemistry model for dmpn-Mg_2(dobpdc) is developed for the first time. The reaction mechanisms of amine-appended MOFs are still not fully understood, so optimal selection of a reaction set from a group of candidates is performed. The parameters for each reaction set are optimally estimated using least-squares fitting to available isotherm data. Additionally, the isosteric heat of adsorption is implemented as an inequality constraint in the parameter estimation problem which is not typically done for chemistry-based model development. The framework for the chemistry model developed in this work is also generic and the approach can be applied to other chemisorbents by incorporating suitable reaction pathways.

4.2. Chemistry Model Equations

In this section, the equations for a chemistry-based model to describe the equilibrium behavior for dmpn-Mg_2(dobpdc) are presented. The reactions first proceed through an adsorbed phase "free" CO_2 which is in equilibrium with the vapor phase CO_2. This adsorbed phase CO_2 then reacts to form the adsorption products whose relative concentrations are determined by the set of equilibrium relationships for each reaction that is being considered. Additionally, balance equations such as the mole fraction summation and amine site balance are used to calculate the loadings of each participating species and importantly the total loading of CO_2. A simple Langmuir model is also considered to predict the adsorption of the physisorbed CO_2 product. The isosteric heat of adsorption is calculated as a part of the model and is implemented as an inequality constraint during the parameter estimation. While some chemistry models use the heat of adsorption for qualitative evaluation and validation, none use it during estimation of the model parameters or in the development stage of the model. Optimal selection of the reaction set is done using an information criterion to avoid overparameterization of the model. The framework for the chemistry model developed in this work is also generic and can be applied to any chemisorbent. Modeling and parameter estimation is done in an equation-oriented framework and solved as a nonlinear programming problem which allows for the adsorption reactions to be changed without the need for a complex and a time-consuming analytical solution if one even exists. The solid-vapor equilibrium equation is independent of the sorbent chemistry and the additional equations, such as mole fraction summation and site balance, are only dependent on the stoichiometry of the adsorption reactions. Additionally, since models to predict the heat of adsorption for chemisorbents is still not well understood or defined in the literature, the isosteric heat of adsorption equation used in this work is considered an approximation of the true heat of adsorption. However, this framework is generic, and this equation can be easily updated.

4.2.1. Solid-Vapor Equilibrium and Activity Coefficient Modeling. The relationship between the gas phase CO_2 and free CO_2 is determined by equating the fugacity of the solid-phase and the vapor-phase, shown in Eqs. (4.1) and (4.2).

$$\hat{f}^{v}_{CO_2} = \hat{f}^{s}_{CO_2} \tag{4.1}$$

$$y_{CO_2}\hat{\phi}_{CO_2}P = \gamma_{CO_2} z_{CO_2^*} f^{0}_{CO_2} \tag{4.2}$$

Vapor-phase fugacity is calculated using the partial-pressure of CO_2 and the vapor-phase fugacity coefficient ($\hat{\phi}_{CO_2}$). In this work, it is assumed that the vapor phase behaves ideally ($\hat{\phi}_{CO_2} = 1$). The solid-phase fugacity is calculated using the CO_2 activity coefficient (γ_{CO_2}), the mole fraction of free CO_2 $\left(z_{CO_2^*}\right)$, and a reference state CO_2 fugacity ($f^{0}_{CO_2}$). The activity coefficient is modeled using a multicomponent Margules equation [77] shown in Eq. (4.3). which is derived from the excess Gibbs energy for a multicomponent nonideal mixture. Only binary interaction parameters for free CO_2 and amine which hasn't reacted yet, simply denoted as *Am*, are considered.

$$\ln\left(\gamma_{CO_2}\right) = z_{Am}\left[\tau_A - \tau_B\left(z_{Am} - 2z_{CO_2^*}\right)\right] - z_{CO_2^*} z_{Am}\left[\tau_A + 2\tau_B\left(z_{CO_2^*} - z_{Am}\right)\right] \tag{4.3}$$

τ_A and τ_B are interaction parameters for free CO_2 and DMPN and vary with temperature with the following correlations.

$$\tau_A = \tau_{A,0} + \frac{\tau_{A,1}}{T} \tag{4.4}$$

$$\tau_B = \tau_{B,0} + \frac{\tau_{B,1}}{T} \tag{4.5}$$

The reference state fugacity is modeled using Henry's Law as shown in Eqs. (4.6) and (4.7) [39].

$$f^{0}_{CO_2} = k_{H,CO_2} \tag{4.6}$$

$$\ln\left(k_{H,CO_2}\right) = a_H + \frac{b_H}{T} \tag{4.7}$$

4.2.2. dmpn-Mg2(dobpdc) Chemistry and Reaction Modeling. The reaction mechanisms for this class of amine-appended MOFs are still not fully understood. The main mechanism is theorized to be what is referred to as a cooperative adsorption mechanism in which CO_2 gets inserted into the amine-metal bond to form well-ordered product chains along the axis of the MOF channels [26]. Additionally, Kundu *et al*. [61] use a combination of quantum chemistry and statistical mechanics which supports the presence of this chain formation mechanism. Forse *et al.* [30] perform NMR spectroscopy that attempts to characterize which species form during CO_2 adsorption for multiple amine-appended MOFs. One of the main products of CO_2 adsorption on dmpn-Mg_2(dobpdc) is carbamate chains which form via this cooperative adsorption mechanism. One of the products that is unique to dmpn-Mg_2(dobpdc) is a carbamate-carbamic acid pair, referred to as a mixed product, that forms across the channel of the MOF. Carbamate chains and the mixed structure are shown in Figure 4.1.

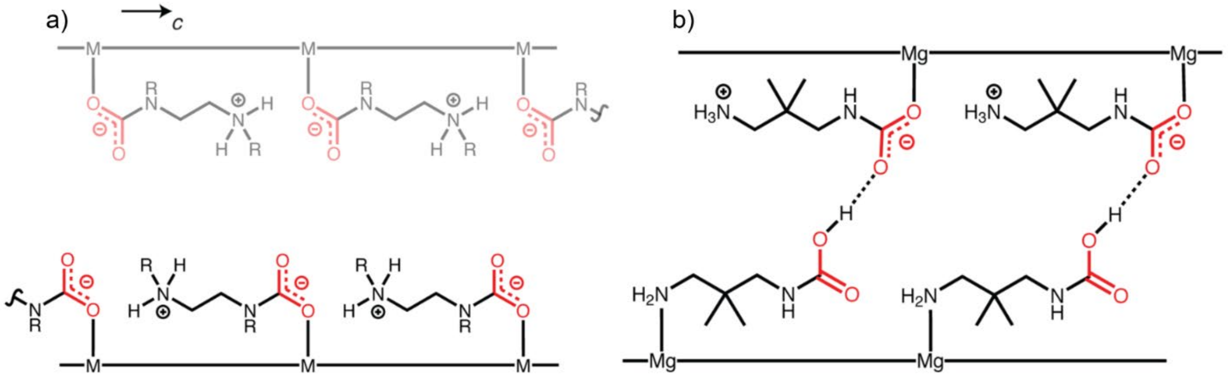

Figure 4.1: Structure of ammonium carbamate chains (a) and mixed product of carbamate and carbamic acid (b). Carbamate chain formation shown using generic diamine and dmpn-Mg_2(dobpdc) shown in mixed structure figure [30].

Forse *et al*. [30] also state that the mixed structure product is the dominant product at all partial pressures of CO_2 while carbamate chains are primarily only present in small amounts at low partial pressures in dmpn-Mg_2(dobpdc). Additionally, the presence of a physisorbed CO_2 species is confirmed in these NMR studies.

Here, it is proposed that the cooperative adsorption mechanism proceeds in multiple steps. The first step is an initiation reaction in which CO_2 reacts with unreacted amine sites to form the initial product chain. Then, a series of propagation reactions can occur in which additional CO_2 is adsorbed to increase the chain length. The stochiometric amounts of CO_2 in these reactions as well as the number of reactions needed to accurately predict the adsorption behavior are unknown and determining this is one of the main goals of this work.

A generalized series of reactions used to describe the cooperative adsorption mechanism are shown below.

$$n_1 CO_2^* + n_1 Am \rightleftharpoons B_1 \tag{R1}$$

$$n_2 CO_2^* + n_2 Am + B_1 \rightleftharpoons B_2 \tag{R2}$$

$$\vdots$$

$$n_N CO_2^* + n_N Am + B_{N-1} \rightleftharpoons B_N \tag{R3}$$

$$m_1 CO_2^* + m_1 Am \rightleftharpoons C_1 \tag{R4}$$

$$m_2 CO_2^* + m_2 Am + C_1 \rightleftharpoons C_2 \tag{R5}$$

$$\vdots$$

$$m_M CO_2^* + m_M Am + C_{M-1} \rightleftharpoons C_M \tag{R6}$$

Eq. (R1) is the initial formation reaction which forms the chemisorption product chain (B_1) of length n_1. Here, chain length is defined as the number of moles of CO_2 contained in the chemisorption product. Reactions (R2) and (R3) are propagation reactions in which the product chain formed in the previous step grows by stochiometric coefficient *n*. Here, N corresponds to the maximum number of chains considered for the formation of a cooperatively adsorbed species and therefore the number of reactions considered as well. These reactions are also developed assuming a 1:1 stochiometric ratio between moles of CO_2 and moles of diamine which has been used in previous studies [3,26]. This work considers the presence of two cooperatively adsorbed species with the second species being denoted by C with stochiometric coefficients *m* and maximum number of formation reactions *M*.

The equilibrium relationship for the reactions considered in this work along with the temperature dependency of the equilibrium coefficient is shown in Eqs. (4.8) and (4.9).

$$K_{eq,j} = \prod_{i=1}^{J} {z_i}^{v_i} \tag{4.8}$$

$$ln\left(K_{eq,j}\right) = k_{0,j} + \frac{k_{1,j}}{T} \tag{4.9}$$

Here, K_{eq} is a dimensionless, mole fraction-based equilibrium coefficient developed assuming an elementary relationship in which the exponent for each species is equal to the stochiometric coefficient. The equilibrium coefficient varies with temperature according to the correlation in Eq. (4.9).

4.2.3. Component and Site Balances. The mole fraction of each species is related by the mole fraction summation as shown in Eq. (4.10).

$$z_{Am} + z_{CO_2^*} + \sum_{j=1}^{N} z_{B_j} + \sum_{j=1}^{M} z_{C_j} = 1 \tag{4.10}$$

The loading (q_i^*) for each product and species predicted by the chemistry model can be calculated using Eq. (4.11).

$$q_i^* = Qz_i \tag{4.11}$$

Here, Q is the total loading of the system which can be determined by solving an amine site balance shown in Eq. (4.12). The amine site balance relates the number of amine sites contained in the chemisorption reactants and products (LHS of equation) to the total number of amine sites present on the MOF (RHS of equation) which is a value that has been determined experimentally to be 3.82 mol/kg [3].

$$q_{Am}^* + \sum_{j=1}^{N} \delta_{B_j} * q_{B_j}^* + \sum_{j=1}^{N} \delta_{C_j} * q_{C_j}^* = Q_{Am} \tag{4.12}$$

Here, δ is defined as the number of amine sites in the chemisorption product of interest. This value can be determined by taking the sum of the stochiometric coefficients for the formation reaction of the product of interest as well as all preceding reactions, as shown in Eqs. (4.13) and (4.14).

$$\delta_{B_j} = \sum_{i=1}^{j} n_i \tag{4.13}$$

$$\delta_{C_j} = \sum_{i=1}^{j} m_i \tag{4.14}$$

The loading of chemisorbed CO2 can be determined in a similar manner using a CO2 balance, shown in Eq. (4.15). Since the stochiometric ratio between CO2 and amine is 1:1, the number of CO2 molecules contained in a chemisorption product is equal to the number of amine sites and can therefore also be represented by δ.

$$q_{chem}^{*} = \sum_{j=1}^{N} \delta_{B_j} * q_{B_j}^{*} + \sum_{j=1}^{N} \delta_{C_j} * q_{C_j}^{*} \tag{4.15}$$

As previously mentioned, the model also considers physisorption represented by the Langmuir isotherm equation, shown in Eqs. (4.16) and (4.17) [78].

$$q_{phys}^{*} = N_{phys} \left(\frac{K_L * y_{CO_2} P}{1 + K_L * y_{CO_2} P} \right) \tag{4.16}$$

$$K_L = k_{phys,0} * \exp\left[\frac{-E_{phys}}{RT_0} \left(\frac{T_0}{T} - 1 \right) \right] \tag{4.17}$$

Finally, the total amount of CO2 adsorbed can be calculated by summing the loading of free CO2, chemisorbed CO2, and physisorbed CO2.

$$q_{CO_2}^{*} = q_{CO_2^*}^{*} + q_{chem}^{*} + q_{phys}^{*} \tag{4.18}$$

4.2.4. Heat of Adsorption. Additionally, the heat of adsorption can be estimated using the isosteric heat of adsorption equation [71] for each loading of interest.

$$\left.\frac{\partial[\ln(P)]}{\partial T}\right|_{q^*_{CO_2}} = \frac{\Delta H_{ads}}{RT^2} \tag{4.19}$$

4.3. Reaction Set Selection and Parameter Estimation

Parameters N and M, which correspond to the number of chain formation reactions, are integer variables which in turn make this reaction set selection and parameter estimation problem a mixed integer programming (MINLP) problem. However, the number of equations, variables, constraints, and the overall structure of the model will change as the N and M variables change. Therefore, relaxation of these integer variables to continuous variables for obtaining bound as is done in many MINLP algorithms are not acceptable. While the MINLP problem can be solved by many algorithms including variants of Branch and Bound algorithms as well as meta-heuristic algorithms, as values of N and M are expected to be low for this problem, exhaustive enumeration is used to obtain globally optimal solution for N and M. The corresponding nonlinear programming (NLP) subproblem is solved for each combination. The NLP subproblem is shown below:

$$\begin{aligned} &\min_{\theta} \quad \left(q^*_{CO_2,exp} - q^*_{CO_2,model}\right)' \Sigma^{-1} \left(q^*_{CO_2,exp} - q^*_{CO_2,model}\right) \\ &s.t. \\ &f(\mu,\eta,\theta) = 0 \\ &g(\mu,\eta,\theta) \le 0 \end{aligned} \tag{4.20}$$

Here, $q^*_{CO_2,exp}$ represents the experimental equilibrium loading of CO_2, $q^*_{CO_2,model}$ represents the equilibrium loading of CO_2 predicted by the chemistry model, θ represents the vector of estimated parameters, and $f(\mu,\eta,\theta)$ and $g(\mu,\eta,\theta)$ represent the equality constraints and inequality constraints of the model, respectively. Additionally, μ represents model inputs such as temperature and pressure and η represents model variables such as mole fractions. In this problem, the equality constraints consist of the chemistry model equations, and the inequality constraints consist of variable bounds along with any additional constraints. This parameter estimation problem uses a least-squares type estimator with weighting function Σ^{-1} which takes into account the uneven number of data points at low partial pressures of CO_2 and temperatures, similar to that described in Section 3.2. The model is implemented in Pyomo [79], a python-based software developed for optimization, and is solved using a the interior point optimization algorithm IPOPT [80].

To evaluate the optimal combination of N and M, an information criterion is used to evaluate the tradeoff between the increasing model size and decreasing error. Here, the Akaike Information Criterion (AIC) [81] is used, shown in Eq. (4.21).

$$\mathrm{AIC} = 2p + N_D * \ln\left(\frac{obj}{N_D}\right) \tag{4.21}$$

Here, p is the total number of parameters and N_D is the total number of data points used for estimation.

4.3.1. Model Reformulation. The chemistry model, as written above, contains several structural issues that present problems in the optimization solver and can result in poor convergence. First, the highly nonlinear solid-vapor equilibrium and reaction equilibrium equations can be difficult to converge. Second, the mole fraction variables for the chemisorption products are bounded between 0 and 1 and the value of these variables are expected to be at the lower bound when low loadings of CO_2 are exhibited which can cause issues with convergence of NLP solvers, especially interior points solvers. In an attempt to address this, a log transformation of the model is performed.

First, the natural log was applied to the solid-vapor equilibrium equation.

$$ln\left(y_{CO_2}\hat{\phi}_{CO_2}P\right) = ln\left(\gamma_{CO_2}\right) + ln\left(z_{CO_2^*}\right) + ln\left(f^0_{CO_2}\right) \tag{4.22}$$

Substituting $\hat{\phi}_{CO_2} = 1$ and $f^0_{CO_2} = k_{H,CO_2}$, Eq. (4.22) becomes:

$$ln\left(y_{CO_2}P\right) = ln\left(\gamma_{CO_2}\right) + ln\left(z_{CO_2^*}\right) + ln(k_{H,CO_2}) \tag{4.23}$$

Next, the natural log is applied to the reaction equilibrium equation.

$$ln\left(K_{eq}\right) = \sum_{i=1}^{J} v_i ln(z_i) \tag{4.24}$$

This transformation results in new linear equations, but additional steps must be taken to avoid calculating the natural log in an equation-oriented framework. The LHS of the transformed SVE equation can be handled by a preprocessing of the experimental data and is simply a fixed input into the parameter estimation problem. The correlations for the activity coefficient of CO_2, Henry's constant, and the reaction equilibrium constant are already written for the natural log of each term and can simply be substituted into the equations. To address the natural log of mole fractions, a new transformed mole fraction variable, $\mathbb{Z}$, is introduced in Eq. (4.25). Bound transformation for this new variable is also performed and shown in Eq. (4.26).

$$z_i = exp(\mathbb{Z}_i) \tag{4.25}$$

$$\mathbb{Z}_i \in [-\infty, 0] \tag{4.26}$$

Substituting this new variable into Eqs. (4.23) and (4.24) yields the linear equations shown below.

$$ln\left(y_{CO_2} P\right) = ln\left(\gamma_{CO_2}\right) + \mathbb{Z}_{CO_2^*} + ln\left(k_{H,CO_2}\right) \tag{4.27}$$

$$ln\left(K_{eq}\right) = \sum_{i=1}^{J} v_i \mathbb{Z}_i \tag{4.28}$$

Substitution can also be performed for the remaining chemistry model equations in which mole fractions appear and are shown below for clarity.

$$\begin{aligned} \ln\left(\gamma_{CO_2}\right) = exp(\mathbb{Z}_{Am}) \left[\tau_A - \tau_B \left(exp(\mathbb{Z}_{Am}) - 2exp\left(\mathbb{Z}_{CO_2^*}\right)\right)\right] \\ - exp\left(\mathbb{Z}_{CO_2^*}\right) exp(\mathbb{Z}_{Am}) \left[\tau_A + 2\tau_B \left(exp\left(\mathbb{Z}_{CO_2^*}\right) - exp(\mathbb{Z}_{Am})\right)\right] \end{aligned} \tag{4.29}$$

$$exp(\mathbb{Z}_{Am}) + exp\left(\mathbb{Z}_{CO_2^*}\right) + \sum_{j=1}^{N} exp\left(\mathbb{Z}_{B_j}\right) + \sum_{j=1}^{M} exp\left(\mathbb{Z}_{C_j}\right) = 1 \tag{4.30}$$

$$q_i^* = Q * exp(\mathbb{Z}_i) \tag{4.31}$$

To summarize, the improvements to the model structure when a log transformation is performed are two-fold. First, the highly nonlinear SVE and reaction equilibrium equations are replaced by linear equations. Second, mole fraction variables in the transformed model are replaced by the new variable $\mathbb{Z}_i$ which does not need to satisfy the lower bound. This bound removal reduces the number inequality constraints in the NLP problem bust most importantly removes the issue of the mole fraction variables converging near the lower bound of 0.

4.4. Results

4.4.1. Reaction Set Selection. The results for the reaction set selection and parameter estimation problems are presented in this section. The optimal set of formation reactions is determined by solving the parameter estimation subproblem for multiple reaction sets and evaluating which combination minimizes the AIC, which is shown in Figure 4.2.

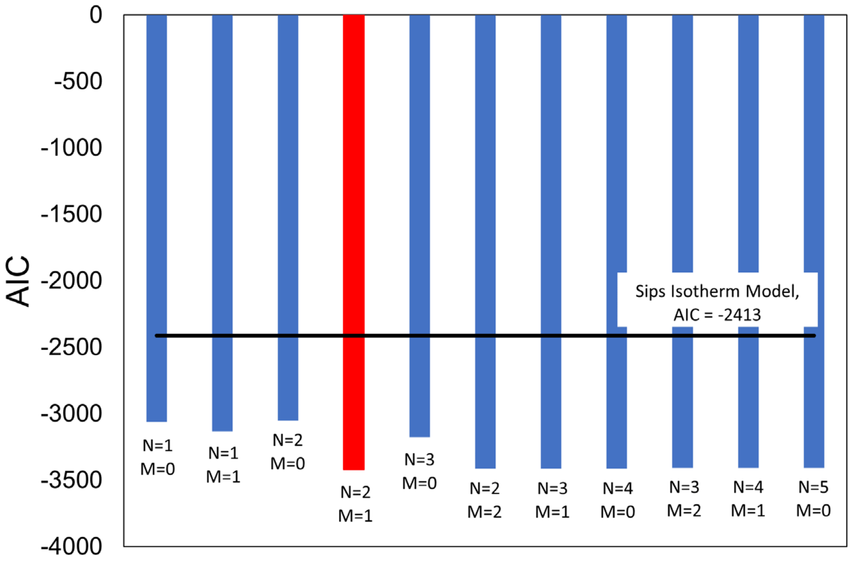

Figure 4.2: Integer sensitivity results for model selection. AIC for varying combinations of chain formation reactions. Minimal AIC (-3418) is at *N*=2, *M*=1 (red bar).

Figure 4.2 shows that the reaction combination of *N*=2 and *M*=1 gives the minimal AIC value of -3418. The reaction sets are generated by taking possible combinations of *N* and *M* and start with the smallest possible model with the least number of parameters, a single cooperatively adsorbed species with only a single formation reaction. As previously mentioned, NMR work supports the presence of two cooperatively adsorbed species but models which only consider a single species are still investigated here for thoroughness. It should also be noted that since formation reactions are equivalent for each cooperatively adsorbed species, models with reversed values for N and M are equivalent. That is, a model with N=1 and M=0 is equivalent to a model with N=0 and M=1. The left side of Figure 4.2 shows smaller models with a reduced number of parameters, but the fit to the experimental data is poor and gives a higher AIC value than the optimal combination. The right side of Figure 4.2 shows larger models with an increased number of parameters which give good fits to the experimental data, but the increase in the number of parameters give AIC values higher than the optimal. Importantly, the optimal reaction set shows a near 42% reduction in AIC when compared to the Sips isotherm model. It is also interesting to note that for all combinations of N and M shown in Figure 4.2, AIC values are superior to the dual-site Sips isotherm model. A complete list of the number of parameters, objective function value, and AIC for each model presented in Figure 4.2 is shown in the Appendix.

4.4.2. Parameter Estimation and Validation

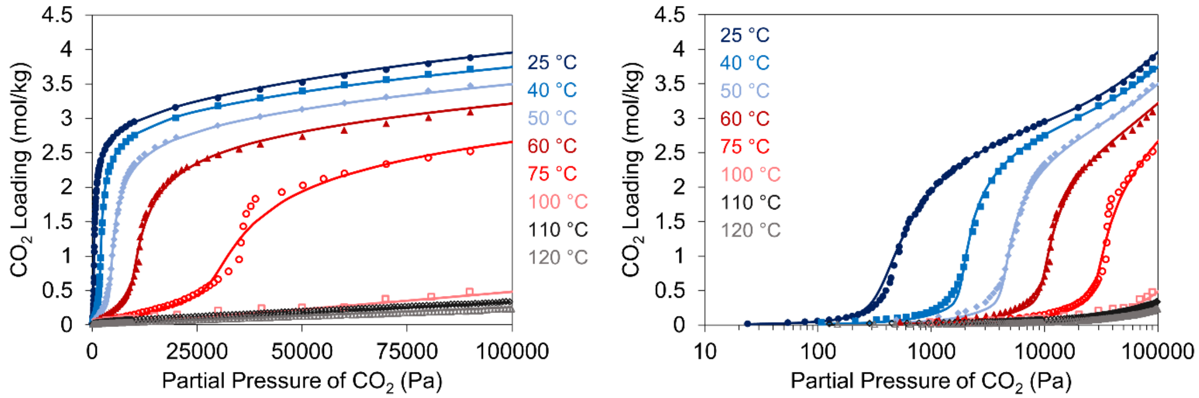

Figure 4.3: Parameter estimation results for *N*=2 and *M*=1 for linear pressure scale (left) and logarithmic pressure scale (right). Symbols represent experimental data and lines represent model prediction.

Table 4.1: Estimated parameters for *N*=2 and *M*=1

Parameter	Estimated Value	Units	Lower Bound	Upper Bound
k_{0,N_1}	67.62	-	-1000	10000
k_{0,N_2}	214.95	-	-1000	10000
k_{0,M_1}	23.56	-	-1000	10000
$k_{phys,0}$	3.31E-06	Pa^{-1}	-50	100
k_{1,N_1}	160.07	K	-10000	10000
k_{1,N_2}	69.65	K	-10000	10000
k_{1,M_1}	92.14	K	-10000	10000
E_{phys}	16.85	kJ/mol	5	500
n_1	2.85	-	1	15
n_2	8.19	-	1	15
m_1	1	-	1	15
N_{phys}	2.59	mol/kg	0	1000
a_H	206.16	Pa	-	-
b_H	-114.18	K	-	-
$\tau_{A,0}$	-385.03	-	-	-
$\tau_{B,0}$	-204.70	-	-	-
$\tau_{A,1}$	254.09	K	-	-
$\tau_{B,0}$	132.67	K	-	-
Objective Function	1.692	$(mol/kg)^2$		

Figure 4.3 shows the fit of the optimal reaction model to the experimental data for dmpn-Mg_2(dobpdc). The figure shows that the chemistry model is able to accurately represent the experimental data at all temperatures and across the experimental pressure range. When

compared to the Sips isotherm model developed in Section 3.2, the optimal chemistry model predicts the isotherm data much better at high partial pressures and exhibits an objective function value, as calculated by Eq. (4.20), which is nearly 6x lower (Sips = 9.48 $(\text{mol/kg})^2$). A complete list of the estimated parameters for the optimal chemistry model can be found in Table 4.1.

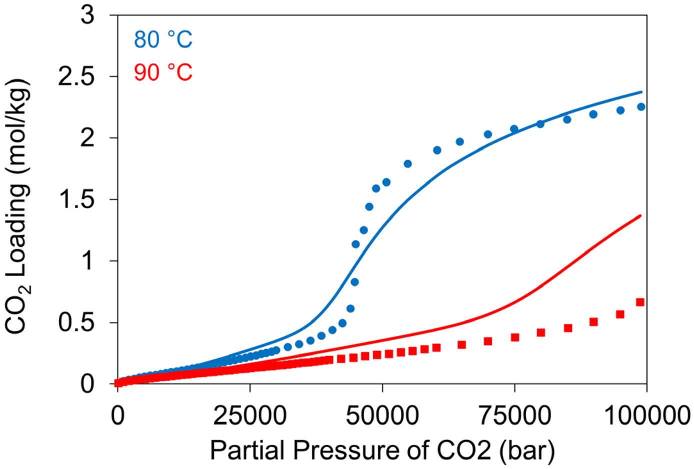

Figure 4.4: Optimal chemistry model (*N*=2, *M*=1) prediction of validation data. Symbols represent experimental data and lines represent model prediction.

The chemistry model is also evaluated by investigating the prediction to validation data that was not a part of the parameter estimation data set. Figure 4.4 shows that the chemistry model is able to predict the validation data reasonably well. At 80 °C, the model predicts a less abrupt step than the experimental data, and at 90 °C the model overpredicts the data slightly at low pressures and more significantly at higher pressures. The RMSE of the validation data prediction is 0.166 which is only a slight 0.81% larger than the RMSE of the Sips Isotherm model.

4.4.3. Heat of Adsorption Constraint

The heat of adsorption, calculated by Eq. (4.19), is included as an inequality constraint in the model. Experimental data for the heat of adsorption is currently unavailable in the literature, so the heat of adsorption calculated using the Clausius-Clapeyron equation in Milner *et al*. [3] is treated as a baseline. Using this, a constraint which ensures that the heat of adsorption predicted by the model is withing +/- 50% of the baseline data from Milner *et al.* [3] is included. To avoid adding a large number of equations to the NLP parameter estimation problem, the heat of adsorption is calculated only at a few representative CO_2 loadings for each temperature rather than every experimental isotherm data point. Figure 4.5 shows the heat of adsorption predicted by the chemistry model and its comparison to the Milner *et al.* data. For most temperatures, the predicted heat of adsorption lies near the baseline value. The 25 °C prediction shows a large discrepancy from the baseline with it overpredicting at low loadings and underpredicting at high loadings. The predictions at 75 °C and 100 °C are also lower than the baseline. The dashed lines in Figure 4.5 correspond to the upper and lower bound implemented as an inequality constraint with all points evaluated falling well within the bounds except for 25 °C and 3.1 mol/kg which lies on the lower bound. It should also be noted that the baseline from Milner *et al.* [3] is calculated by averaging the heat of adsorption over each experimental temperature so variations when examining a single temperature can be expected. Still, ensuring that the heat of adsorption is within a practical and expected range for the MOF system can help avoid overfitting to experimental data.

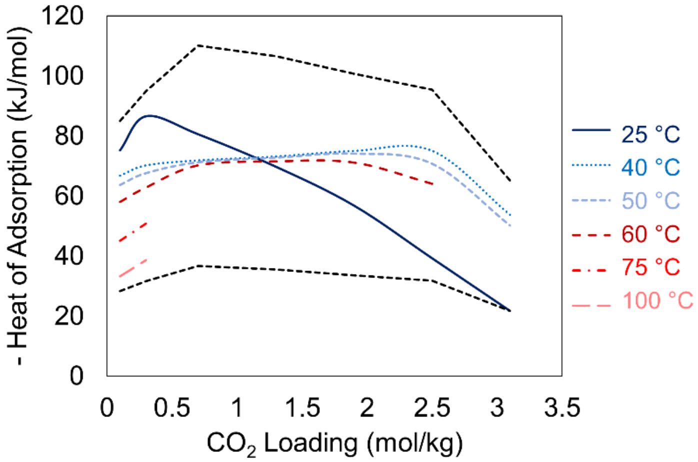

Figure 4.5: Chemistry model heat of adsorption as a function of loading and temperature.

4.4.4. Chemisorption reactant and product loadings. Results presented so far in this section have focused prediction of the total CO_2 loading of the system. However, analyzing the contribution of individual species is valuable and can be important in identifying species or reaction pathways, but this is impossible for many of the heuristic-based isotherm models as they do not model these species or go into this type of resolution. In this section, the profiles for the optimal chemistry-based model are presented and analyzed.

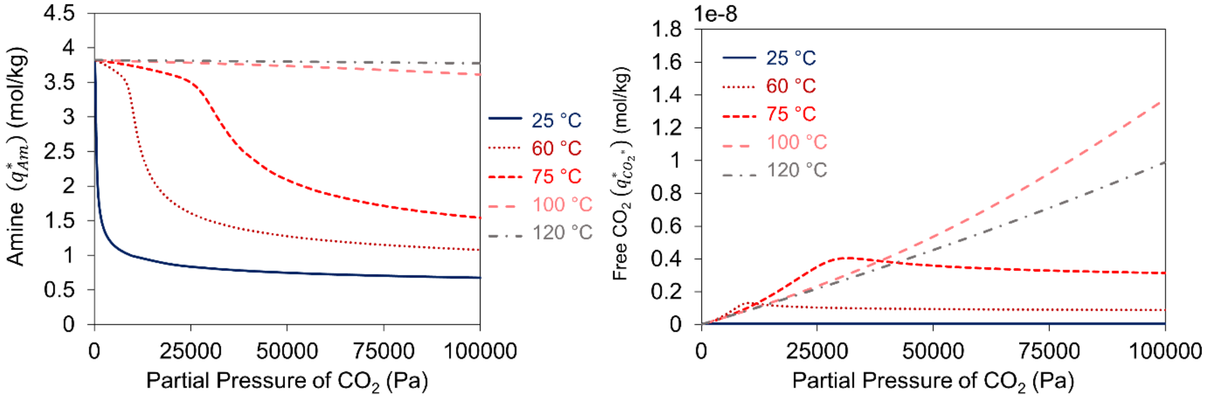

Figure 4.6: Loadings [mol/kg] of the species present in the optimal chemistry model (*N*=2, *M*=1). Left) Unreacted diamine (*Am*). Right) Adsorbed phase free CO_2 ($\boldsymbol{CO_2^*}$).

Figure 4.6 shows the loadings for the two main reactants in the chemisorption reactions, the unreacted diamine and free CO_2. At very low partial pressures of CO_2 nearing zero, the loading of amine converges to the total amine loading in the MOF (Q_{Am}) which is 3.82 mol/kg and is expected since no CO_2 will be adsorbed as the partial pressure nears zero. The step-shaped profile with respect to partial pressure is present for the unreacted amine loading as well. Figure 4.6 shows that the free CO_2 loading is only present in very small amounts and only acts as an intermediate step in the adsorption process, not significantly contributing to the total loading of CO_2.

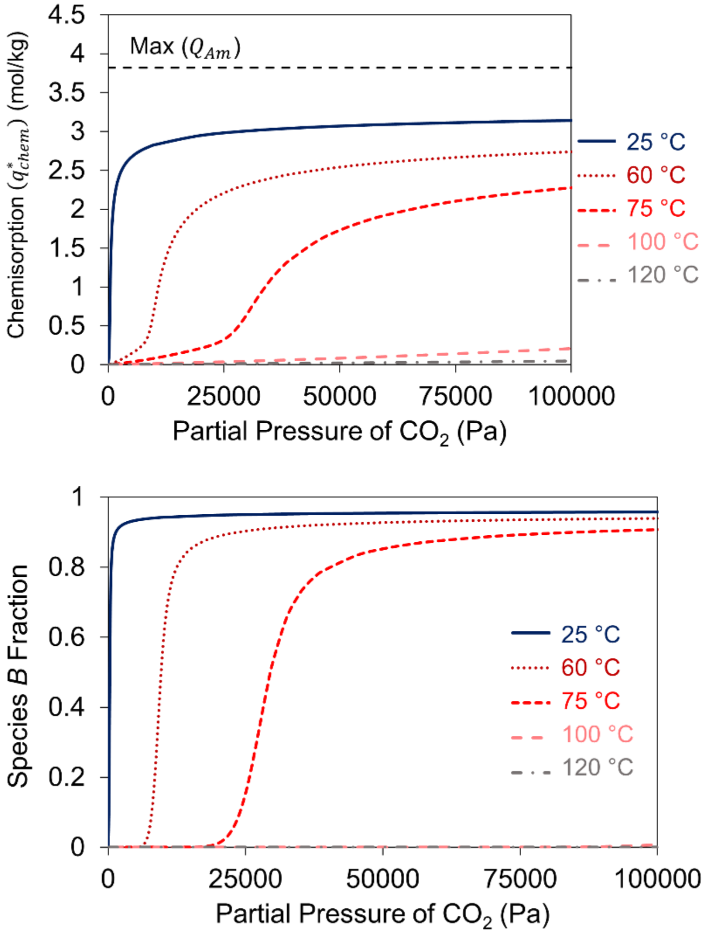

Figure 4.7: Prediction of chemisorbed CO_2 loading and chemisorbed product distribution. Top) Total chemisorbed CO_2 loading. Dashed line represents the maximum achievable loading ($\boldsymbol{Q_{Am}}$). Bottom) Fraction of chemisorbed CO_2 contained in cooperatively adsorbed species *B*.

Figure 4.7 shows the total amount of chemisorbed CO_2 predicted by the optimal chemistry model for the experimental range of temperatures and partial pressures. The figure shows that the step-shaped profile is present for the chemisorption product which indicates that the chemisorption product is the main contributor to the step-shape adsorption profile for the total CO_2 loading. Similar to the experimental isotherm data, the step disappears after 75 °C and negligible uptake is seen for the higher temperatures. Figure 4.7 also shows the percentage of chemisorbed CO_2 which is contained in a single cooperatively adsorbed species. The figure shows that the majority (~90%) of the chemisorbed CO_2 is contained in a single species (chain) at most temperatures and partial pressures. The second cooperatively adsorbed species is only the dominant species at very low partial pressures, usually before the step occurs for a specific temperature. However, the second species does contain nearly all the chemisorbed CO_2 for the higher temperatures which do not experience a step transition.

4.4.5. Chain Lengths. The length of each cooperatively adsorbed product chain is estimated as part of the parameter estimation problem presented in Section 4.3. McDonald *et al.* [26] have previously used the Hill equation [82], which was first developed to estimate the number of ligand molecules needed to bind to a receptor to achieve a functional effect as a method to estimate the cooperativity of amine-appended MOFs. Table 4.2 gives a comparison of the chain length estimated by this work for dmpn-Mg_2(dobpdc) and the Hill coefficients calculated for mmen-M_2(dobpdc). The value presented for this work is calculated by taking the sum of n_1 and n_2, and the Hill coefficients are calculated using only 25 °C isotherm data. Table 4.2 shows that the chain lengths estimated by this work are similar to those estimated previously for similar solid sorbents.

Table 4.2: Comparison of chain length estimations for varying MOFs and methods.

MOF	**Value**	**Method**	**Source**
dmpn-Mg_2(dobpdc)	11.0	Chemistry Model	This work
mmen-Mg_2(dobpdc)	10.6	Hill Coefficient	McDonald *et al.* [26]
mmen-Mn_2(dobpdc)	5.6	Hill Coefficient	McDonald *et al.* [26]
mmen-Fe_2(dobpdc)	7.5	Hill Coefficient	McDonald *et al.* [26]
mmen-Co_2(dobpdc)	11.5	Hill Coefficient	McDonald *et al.* [26]
mmen-Zn_2(dobpdc)	6.0	Hill Coefficient	McDonald *et al.* [26]

4.4.6. Physisorbed Loading. Figure 4.8 shows the predicted physisorbed CO_2 loading for the temperature and pressure range of the experimental isotherm data. The physical adsorption is modeled using a standard Langmuir isotherm equation therefore does not exhibit any step transitions which are seen with the chemisorption species. Figure 4.8 also shows the percentage of CO_2 which is physisorbed compared to the total amount of adsorbed CO_2. For the lower temperatures (25 °C - 75 °C) which exhibit a step transition of total CO_2 loading, the fraction of physisorbed CO_2 remains relatively low while the majority of adsorbed CO_2 for the higher temperatures is physisorbed.

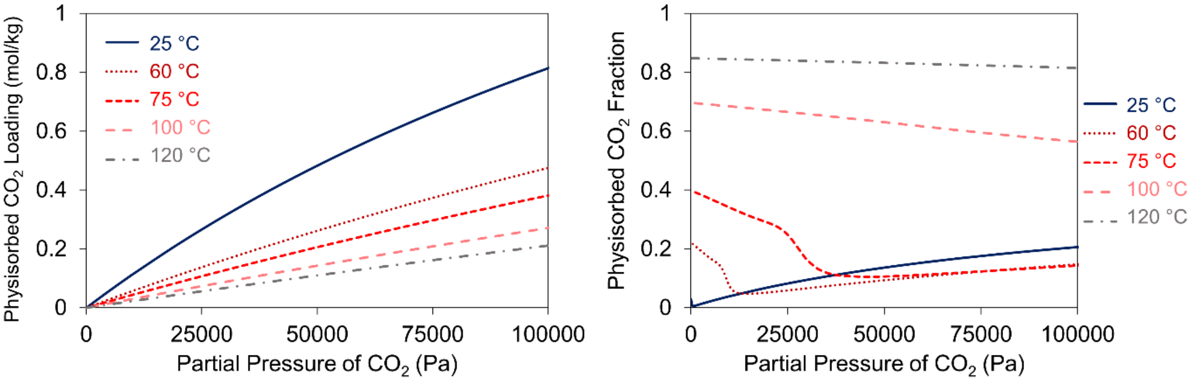

Figure 4.8: Left) Prediction of physisorbed CO_2 loading and right) fraction of total loading which is physisorbed.

4.5. Conclusions

In this Chapter, a chemistry-based model is developed to describe the adsorption equilibrium of an amine-appended MOF, specifically dmpn-Mg_2(dobpdc), for the first time. The model considers an equilibrium between gas phase CO_2 and an adsorbed phase CO_2, referred to as free CO_2, which then reacts with empty diamine sites in a series of reactions formulated as part of this work for a cooperatively adsorbed species. Results from NMR studies support the presence of two cooperatively adsorbed species, but little information is known about the number of reactions needed to accurately describe each species. Reaction set selection is performed based on exhaustive enumeration of combination of integer variables for minimizing the AIC. The optimal reaction set is found to be: N=2 and M=1 which gives an AIC value of -3418 and is a reduction of nearly 42% when compared to the Sips isotherm model developed earlier in this work. The optimal reaction combination also gives an excellent fit to the experimental isotherm data, showing a nearly 6x reduction of the weighted least squares objective function used in this work when compared to the Sips isotherm model. The performance of the chemistry model is also investigated by evaluating the prediction of a validation data set which consists of experimental isotherm data for 80 °C and 90 °C that was not included in the parameter estimation. The chemistry model predicts this validation set reasonably well but exhibits a higher RMSE (+0.81%) than the Sips isotherm model. However, this increase is almost negligible, and the chemistry model is still considered to be a good predictor of the validation data. The heat of adsorption predicted by the model is also used as an inequality constraint in the parameter estimation NLP problem. The constraint ensures that prediction for varying temperatures and loadings is within +/-50% of the baseline value published in the literature. The product chain length in this work also compares well to chain lengths estimated for other amine-appended MOFs. Overall, this model gives better prediction of the experimental data while giving an insightful look into the compositions of cooperatively adsorbed species and how they change with varying temperatures and pressures which has not been done for previous amine-appended isotherm models. In future, this model can be enhanced to provide a much better framework for incorporating interactions with other species, mainly water. The model can also be expanded to include enthalpy models which will give a better prediction of the heat of adsorption if experimental data becomes available. Evaluation of new materials by identifying limiting pathways can also be a focus of future work.

5. Fixed Bed Contactor Modeling

In this chapter, a fixed bed model is presented to be used in simulation studies of dmpn–Mg_2(dobpdc) and Mg_2(dobpdc)(3-4-3). The first-principles model is dynamic, non-isothermal and considers 1-D axial variation of important transport properties such as concentration, temperature, and loading. For **dmpn-Mg_2(dobpdc)**, the **dual-site Sips isotherm** model and kinetic model developed in Chapter 3 are used to predict the mass transfer rate. For **Mg_2(dobpdc)(3-4-3)**, the **extended weighted Langmuir** model developed in Chapter 3 is used in the prediction of the mass transfer rate. Both models are validated using experimental fixed bed breakthrough data. The model is then scaled up and used for thermal management studies to investigate the impact of heat removal on adsorption performance.

Portions of this Chapter are published in the following peer-reviewed journal article:

Hughes, R.; Kotamreddy, G.; Ostace, A.; Bhattacharyya, D.; Siegelman, R. L.; Parker, S. T.; Didas, S. A.; Long, J. R.; Omell, B.; Matuszewski, M. Isotherm, Kinetic, Process Modeling, and Techno-Economic Analysis of a Diamine-Appended Metal–Organic Framework for CO_2 Capture Using Fixed Bed Contactors. *Energy Fuels* **2021**, *35* (7), 6040–6055. https://doi.org/10.1021/acs.energyfuels.0c04359.

5.1. Introduction

Fixed beds are well studied in literature [83] and the amine-appended MOF models that currently exist in literature all consider fixed bed contactors. Hefti *et al.* [60] simulate a fixed bed TSA cycle using mmen-Mg_2(dobpdc) which does not consider axial variation in the bed and assumes an isothermal adsorption step. In a later work by the same researchers [64], a partial differential equation model was used to optimize their TSA process with respect to various performance indicators using a constant mass transfer coefficient for CO_2 that was estimated using experiments with activated carbons [65,66]. Pai *et al.* [62] use a fixed bed model to simulate a pressure swing adsorption cycle using mmen-Mg_2(dobpdc), and assume mass transfer properties of a commercial zeolite. Recently, Ga *et. al.* [63] use a first principles, 1-D partial differential equation to simulate isothermal breakthrough curves for 2-ampd-Mg_2(dobpdc) but no process simulation is performed. These previous studies laid valuable groundwork for exploring the practical performance of amine-appended Mg_2(dobpdc) materials but given that the structure of the appended amine can significantly alter the shape of the CO_2 adsorption curves, it is challenging to directly apply existing models to new framework variants such as dmpn–Mg_2(dobpdc) or Mg_2(dobpdc)(3-4-3). This work adds to these literature studies by developing models for dmpn–Mg_2(dobpdc) and Mg_2(dobpdc)(3-4-3) for the first time.

5.2. Fixed Bed Modeling Equations

In this work, an axial-flow fixed bed is modeled using Aspen Adsorption V9, which contains a framework that simultaneously solves sets of equations comprising mass, momentum, and energy conservation. For cooling during CO_2 capture and heating during desorption, the fixed bed reactors were modeled with an embedded heat exchanger with a configuration similar to a shell-and-tube heat exchanger. In this configuration, multiple tubes are located inside the reactor, with the heat transfer fluid located in the tube side and the shaped adsorbent particles located in the shell side surrounding the tubes (see Figure 5.1). For this work, a reactor is defined as the equipment that contains the bed of adsorbent particles and the embedded heat exchanger. The key assumptions of our model include:

(1) one-dimensional axial variation of the transport variables (i.e., concentration, temperature, velocity, and pressure) and

(2) negligible spatial variation of the temperature within individual particles.

Axial dispersion is neglected since in the velocity range considered in this study and due to the reasonably fast kinetic and mass transfer rates, convective flux is found to be the dominating mechanism. It can be noted that consideration of the axial dispersion term can considerably add to the computational expense. Several studies were conducted, and it was observed that if axial dispersion is considered, the cycle time differs by less than 0.1% while the CPU time for the simulation increases by more than 20% when compared to the model with no axial dispersion.

Therefore, the axial dispersion term is not considered. The model also accounts for external and internal mass transfer limitations and heat transfer between the gas and solid phase as well as the gas phase and embedded exchanger. For both MOFs investigated using the fixed bed model, the current version considers that CO_2 is the only adsorbed species, and that the presence of O_2, N_2, and H_2O does not affect the adsorption equilibrium or mass transfer of CO_2. For dmpn-Mg_2(dobpdc), this simplifying assumption is made given that O_2 and N_2 isotherms for dmpn-Mg_2(dobpdc) show adsorption of these species is negligible while maintaining a high selectivity of CO_2 [3], and dry and humid breakthrough data for dmpn–Mg_2(dobpdc) using 15% CO_2 in N_2 are nearly identical [3]. O_2 and N_2 are also likely to have a negligible effect on the purity of the regenerated CO_2 stream. Milner *et al*. [3] show that at compositions typical for coal flue gas, CO_2 will make up greater than 99% of the total adsorbed content of CO_2, O_2, and N_2 based on non-competitive adsorption equilibrium data. The energy released by these species is also expected to be negligible due to the small amounts adsorbed when compared to CO_2. Additionally, although the underlying mechanism of adsorption has been shown to change in the presence of water, the CO_2 capacity remains the same as that under dry conditions [30]. Additionally, extensive experimental work was completed for Mg_2(dobpdc)(3-4-3), which includes breakthrough and cycling data, to demonstrate the maintained performance under humid conditions [29].

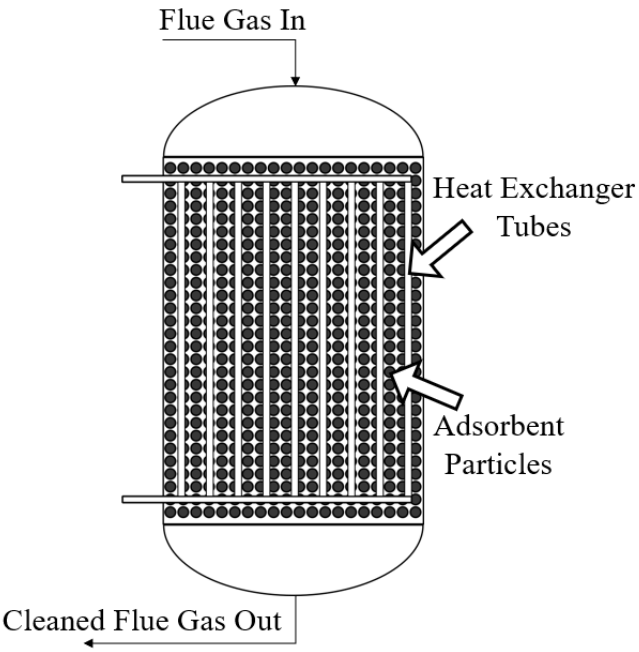

Figure 5.1: Diagram of a fixed bed reactor

5.2.1 Bulk Gas Phase Species Balance.

$$\varepsilon_b \frac{\partial C_{g,i}}{\partial t} = -\frac{\partial (v_g C_{g,i})}{\partial z} - (1-\varepsilon_b)\frac{6k_{f,i}}{d_p}(C_{g,i} - C_{surf,i}) \tag{5.1}$$

The gas phase species balance given in Eq. (5.1) relates the accumulation of gaseous species i to the axial convection and also the mass transfer of the gas to the solid phase. In this equation, ε_b represents the voidage in the bed, $C_{g,i}$ represents the bulk gas phase concentration of species i, v_g is the superficial gas phase velocity, $k_{f,i}$ is the gas-phase film mass transfer coefficient, d_p is the diameter of the particle, and $C_{surf,i}$ is the concentration of species i at the surface of the particle. The difference between the bulk gas phase concentration and the gas phase concentration at the particle surface determines the driving force for gas phase mass transfer.

5.2.2 Mass Transfer. Due to differences in available data to develop reaction kinetics models and differences in the forms of the isotherm models, different mass transfer models are used for dmpn-Mg_2(dobpdc) and Mg_2(dobpdc)(3-4-3). Each model is described below.

dmpn-Mg$_2$(dobpdc) Mass Transfer Model:

For shaped particles that are used in a fixed bed contactor, the mass transfer mechanisms captured in the kinetic model developed in Section 3.3 will still be present, with the addition of particle diffusion. To account for this additional mechanism, the mass transfer coefficients used in the fixed bed reactor model include particle diffusion and reaction kinetics. The overall mass transfer resistance from the shaped particles was modeled as the sum of the mass transfer resistances due to macropore particle diffusion [83] and the reaction kinetics for both the chemisorption and physisorption products, as given in Eqs. (5.2) and (5.3).

$$\frac{1}{k_{OC}}=\frac{r_p^2}{15\varepsilon_p D_{eff}}+\frac{1}{k_{chem}} \tag{5.2}$$

$$\frac{1}{k_{OP}}=\frac{r_p^2}{15\varepsilon_p D_{eff}}+\frac{1}{k_{phys}} \tag{5.3}$$

k_{OC} and k_{OP} are the overall mass transfer coefficients for the physisorbed and chemisorbed products, respectively, and k_{chem} and k_{phys} are defined in Eqs. (3.25) and (3.26). D_{eff} is the effective particle diffusion given by:

$$D_{eff}=C_1(T_s)^{0.5} \tag{5.4}$$

The parameter C_1 encapsulates all particle diffusion mechanisms and is estimated using fixed bed experimental breakthrough data for each amine-appended MOF of interest. Additionally, experimental data for parameter estimation of the effective diffusion model is only available for a single temperature, so the model assumes that the effective diffusion will vary with a square root relationship to temperature, which is common for Knudsen type diffusion [78]. These coefficients are then used in a similar linear driving force model which, for clarity, is given in Eq. (5.5).

$$\frac{dq_{CO_2}}{dt}=\frac{dq_{chem}}{dt}+\frac{dq_{phys}}{dt}=k_{OC}(q_{chem}^*-q_{chem})+k_{OP}\left(q_{phys}^*-q_{phys}\right) \tag{5.5}$$

The rate of adsorption/desorption in an adsorbent particle is calculated assuming a linear driving force:

$$R_i = \frac{6k_{f,i}}{d_p}\left(C_{g,i} - C_{surf,i}\right) = \rho_s \frac{\partial q_i}{\partial t} \tag{5.6}$$

where $k_{f,i}$ is the external (gas film) mass transfer coefficient and $C_{surf,i}$ is the concentration of the gas at the particle surface. Eq. (5.6) determines $C_{surf,i}$ and accounts for any external mass transfer resistance across the gas film that surrounds the particle.

Mg_2(dobpdc)(3-4-3) Mass Transfer Model:

As previously mentioned, a kinetic model for Mg_2(dobpdc)(3-4-3) was not developed due to the lack of experimental data. Therefore, k_{chem} and k_{phys} are removed from the mass transfer coefficient model and the dominant mass transfer mechanism is considered to be due to particle diffusion. Additionally, the extended weighted Langmuir isotherm model doesn't distinguish between chemisorbed CO_2 and physisorbed CO_2. Therefore, the mass transfer rate is calculated using a LDF equation for the total adsorbed CO_2. The equations for the Mg_2(dobpdc)(3-4-3) mass transfer model are shown below.

$$\frac{dq_{CO_2}}{dt} = k_O\left(q^*_{CO_2} - q_{CO_2}\right) \tag{5.7}$$

$$k_O = \frac{15\varepsilon_p D_{eff}}{r_p^2} \tag{5.8}$$

$$D_{eff} = C_1(T_s)^{0.5} \tag{5.9}$$

$$R_i = \frac{6k_{f,i}}{d_p}\left(C_{g,i} - C_{surf,i}\right) = \rho_s \frac{\partial q_i}{\partial t} \tag{5.10}$$

5.2.3 Gas and Solid Phase Energy Balances. The bulk gas phase energy balance is given in Eq. (5.11) and relates the change in temperature of the gas to axial heat convection, gas expansion or compression, heat transfer between the gas and solid phase, and heat transfer to the embedded heat exchanger.

$$\begin{aligned}\varepsilon_b\rho_g C_{v,g}\frac{\partial T_g}{\partial t} = -\rho_g C_{v,g} v_g \frac{\partial T_g}{\partial z} - P\frac{\partial v_g}{\partial z} - (1-\varepsilon_b)a_p h_f\left(T_g - T_s\right) \\ - a_{HX}h_{HX}\left(T_g - T_t\right)\end{aligned} \tag{5.11}$$

Here, ρ_g is the density of the gas, $C_{v,g}$ is the constant volume heat capacity of the gas, a_p is the specific surface area of the particle, h_f is the heat transfer coefficient for gas and solid phase heat transfer, a_{HX} is the specific surface area for heat transfer with the embedded heat exchanger, h_{HX} is the heat transfer coefficient for the embedded heat exchanger, and T_t is the temperature of the heat exchange medium in the tube.

The solid phase energy balance is given by:

$$\rho_s C_{p,s} \frac{\partial T_s}{\partial t} = \rho_s(-\Delta H_{CO_2}) \frac{dq_{CO_2}}{dt} + a_p h_f \left(T_g - T_s\right) \tag{5.12}$$

The solid phase energy balance relates the change in the temperature of the adsorbent to the heat of adsorption and the heat transfer with the gas phase. Here, ρ_s is the solid density, $C_{p,s}$ is the heat capacity of the solid, and $-\Delta H_{CO_2}$ is the heat of adsorption. Here, $-\Delta H_{CO_2}$ is the isosteric heat of adsorption. For many sorbent-based capture studies in literature, the heat of adsorption is assumed to be a constant value [60,62,64]. For the dmpn-Mg_2(dobpdc) model in this work, a constant value is used (see Table 5.1) which is shown to be a reasonable simplifying assumption when examining the heat of adsorption data shown in Milner *et. al.* [3]. For Mg_2(dobpdc)(3-4-3), heat of adsorption data generated using the Clausius-Clapeyron equation shows 3 distinct loading regions with different values for heat of adsorption [29]. To capture this heat of adsorption behavior, a surrogate model is used and shown in Eq. (5.13). A more rigorous method to estimate the heat of adsorption would be to solve the isosteric heat of adsorption differential equation within the fixed bed model, but this can lead to a significant increase in the computation complexity of the model.

$$-\Delta H_{CO_2} = \Delta H_1 - (\Delta H_1 - \Delta H_2) \frac{exp\left[a_1\left(q^*_{CO_2} - b_1\right)\right]}{1 + exp\left[a_1\left(q^*_{CO_2} - b_1\right)\right]} - (\Delta H_2 - \Delta H_3) \frac{exp\left[a_2\left(q^*_{CO_2} - b_2\right)\right]}{1 + exp\left[a_2\left(q^*_{CO_2} - b_2\right)\right]} \tag{5.13}$$

Here, ΔH_i represent the heats of adsorption for the three specific regions, and a_i and b_i are shape and position parameters used to shift the prediction between the three regions. These parameters are optimally estimated using the heat of adsorption data from Kim *et. al.* [29].

5.2.4 Embedded Heat Exchanger. The embedded exchanger was designed considering a triangular pitch tube arrangement and the configuration of the exchanger was determined using Eqs. (5.14) and (5.15) [84].

$$N_t = (CTP)\frac{\pi D_x^2}{4A_1} \tag{5.14}$$

$$A_1 = (CL)P_t^2 \tag{5.15}$$

Here, D_x is the reactor diameter, N_t is the total number of tubes present in the reactor, A_1 is the cross-sectional area of a repeating unit in the reactor that contains a single tube, and P_t is the tube pitch. CTP and CL are the tube count calculation constant and the tube layout constant, respectively; for one tube pass, CTP = 0.93 and CL = 0.87 for 30 and 60 equilateral tri pitch. Similar configurations can be found in the modeling studies performed by Kim *et al.* [85] and Kotamreddy *et al.* [86].

The heat transfer coefficient between the gas phase and the embedded heat exchanger (h_{HX}) was calculated using correlations from Penny *et al.* [87].

$$Nu_{HX} = \frac{h_{HX}d_t}{k_{eff}} = \left(0.333 + 0.26Re_{d_t}^{0.533}\right)Pr^{0.33}\left(\frac{d_t}{d_p}\right)^{0.1} \tag{5.16}$$

Here, Re_{d_t} is the Reynolds number as a function of the heat exchanger tube diameter, d_t:

$$Re_{d_t} = \frac{d_t\rho_g v_g}{\mu_g} \tag{5.17}$$

The parameter *Pr* is the Prandtl number given by:

$$Pr = \frac{C_{p,g}\mu_g}{k_g} \tag{5.18}$$

and k_{eff} is the effective thermal conductivity and is a function of the gas thermal conductivity, solid thermal conductivity, and void fraction of the bed.

$$k_{eff} = k_g\left\{1 - \sqrt{(1-\varepsilon_b)} + \frac{2\sqrt{(1-\varepsilon_b)}}{1-\lambda\beta} * \left[\frac{(1-\lambda)\beta}{(1-\lambda\beta)^2}\ln\left(\frac{1}{\lambda\beta}\right) - \frac{\beta+1}{2} - \frac{\beta-1}{1-\lambda\beta}\right]\right\} \tag{5.19}$$

$$\lambda = \frac{k_g}{k_s} \tag{5.20}$$

$$\beta = 1.25\left[\frac{1-\varepsilon_b}{\varepsilon_b}\right]^{\frac{10}{9}} \tag{5.21}$$

5.2.5 Pressure Drop. The pressure drop across the bed was modeled using the Ergun equation [83] (Eq. (5.22)), which relates the change in pressure to the gas superficial velocity, gas viscosity, as well as other bed properties such as bed voidage and particle diameter.

$$-\frac{\partial P_g}{\partial z} = \frac{150\,\mu_g(1-\varepsilon_b)^2 v_g}{{\varepsilon_b}^3\,{d_p}^2} + \frac{1.75(1-\varepsilon_b)\rho_g|v_g|v_g}{{\varepsilon_b}^3\,d_p} \tag{5.22}$$

5.2.6 External Heat and Mass Transfer Coefficients. The gas-to-solid heat transfer coefficient was modeled using correlations from Cavenati *et al*. [88] as follows:

$$Nu_f = 2 + 1.1Re^{0.6}Pr^{1/3} = \frac{h_f d_p}{k_g} \tag{5.23}$$

Similarly, the gas-to-solid mass transfer coefficient is given by:

$$Sh = 2 + 1.1Re^{0.6}Sc^{1/3} = \frac{k_f d_p}{D_g} \tag{5.24}$$

where *Sc* is the Schmidt number given by:

$$Sc = \frac{\mu_g}{\rho_g D_g} \tag{5.25}$$

5.2.7 Breakthrough Time. The breakthrough time for a fixed bed adsorption system is commonly used to describe when the solid particles are saturated with CO_2 and adsorption is effectively finished. In this work, the breakthrough time is defined as the maximum allowable time in which the integral CO_2 slip, or CO_2 that exits the bed, is equal to 10% of the total CO_2 that has been fed to the bed during the current adsorption step (i.e., 90% integral CO_2 capture) [86]. This scenario is described by Eq. (5.26).

$$0.1 * \int_{t_0}^{t_0+t_b} F_{in}\, y_{CO_2,in} dt = \int_{t_0}^{t_0+t_b} F_{out}\, y_{CO_2,out} dt \tag{5.26}$$

Table 5.1 lists model parameters that were set as constants for the dmpn-Mg_2(dobpdc). As previously discussed, the heat of CO_2 adsorption was kept constant and averaged over the range of experimental loading data found in Milner *et al.* [3]. Similarly, the adsorbent heat capacity is based on experimental measurements performed by Milner *et al.* [3]. Model parameters which correspond to the configuration of a shaped particle and its arrangement in a contactor (ε_b, ρ_s, and d_p) are based on the lab-scale fixed-bed experimental setup of Milner *et al.* [3] for compressed, semi-spherical pellets of dmpn–Mg_2(dobpdc). Heat exchanger design variables (d_t and P_t) are similar to the literature and result in a specific heat exchange area of 53 m^2/m^3 which is similar to other studies found in literature [86].

Table 5.1: dmpn-Mg_2(dobpdc) fixed bed reactor model constants

Parameter	Value	Units
Heat of CO_2 Adsorption (ΔH_{CO_2})	-65	[kJ/mol]
Adsorbent Heat Capacity ($C_{p,s}$)	1.457	[$kJ \cdot kg^{-1} \cdot K^{-1}$]
Bed Voidage (ε_b)	0.68	[m^3 void/m^3 bed]
Density of adsorbent particle (ρ_s)	1000	[kg/m^3]
Particle diameter (d_p)	525	[µm]
Diameter of heat exchanger tubes (d_t)	1	[inches]
Heat exchanger tube pitch (P_t)	0.04	[m]

Table 5.2 shows the fixed bed model constants for Mg_2(dobpdc)(3-4-3). The adsorbent heat capacity is taken to be the same as dmpn-Mg_2(dobpdc) due to a lack of data. The bed voidage, particle density, and particle diameter are taken from the experimental breakthrough data from Kim *et. al.* [29]. For the Mg_2(dobpdc)(3-4-3) model, the heat of adsorption is predicted using a surrogate model (see Eq. (5.13)) and the configuration of the heat exchanger is optimized and therefore are not considered model constants.

Table 5.2: Mg_2(dobpdc)(3-4-3) fixed bed reactor model constants

Parameter	Value	Units
Adsorbent Heat Capacity ($C_{p,s}$)	1.457	[$kJ \cdot kg^{-1} \cdot K^{-1}$]
Bed Voidage (ε_b)	0.73	[m^3 void/m^3 bed]
Density of adsorbent particle (ρ_s)	986	[kg/m^3]
Particle diameter (d_p)	525	[µm]

5.3. Fixed Bed Model Validation and Parameter Estimation

The fixed bed models presented in this Chapter are validated using experimental breakthrough data. Additionally, the lumped mass transfer parameter, C_1, is estimated for compressed, semi-spherical pellets of each amine-appended MOF. Breakthrough experiment details can be found in the corresponding publication for each MOF (Milner *et. al.* [3] for dmpn-Mg_2(dobpdc) and Kim *et. al.* [29] for Mg_2(dobpdc)(3-4-3)). Both breakthrough experiments are assumed to operate isothermally so thermal fronts are expected to be negligible. The isothermal assumption is also corroborated with temperature measurements of the outlet gas which show almost no change (<1 °C) from the design/bed temperature throughout the entire length of the experiment. The results for the parameter estimation of the Mg_2(dobpdc)(3-4-3) heat of adsorption surrogate model is also presented in this section.

5.3.1. dmpn-Mg_2(dobpdc) Results. Experimental breakthrough conditions for dmpn-Mg_2(dobpdc) are shown inTable 5.3. The effective diffusion, D_{eff}, for the framework particles was calculated using Eq. (5.4) and a value of $C_1 = 4.11\times10^{-12}$ $m^2\cdot K^{-0.5}\cdot s^{-1}$, which was determined using a least squares estimator and a quasi-Newton based algorithm available in Aspen Adsorption. As shown in Figure 5.2, the fixed bed model reproduces both the breakthrough time and the shape of the breakthrough curve, confirming that the bed adsorption capacity and the kinetics of the system under these conditions are well predicted by the model.

Table 5.3: Experimental breakthrough conditions used to collect data to validate the dmpn-Mg_2(dobpdc) fixed bed model.

Variable	**Value**	**Units**
Bed Length	13.34	[cm]
Bed Diameter	0.46	[cm]
Temperature	40	[°C]
Pressure	1	[bar]
Volumetric Flow Rate	10	[sccm]
y_{CO2}	0.15	[mol fraction]
y_{N2}	0.85	[mol fraction]

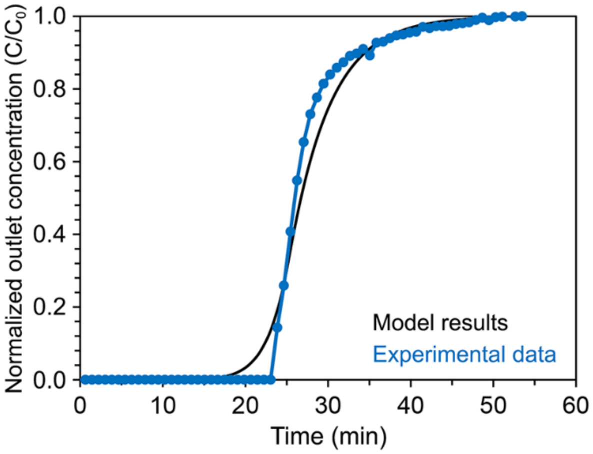

Figure 5.2: Comparison of breakthrough model prediction (black trace) and experimental breakthrough data (blue trace). The normalized outlet concentration, C/C$_0$, represents the concentration of gas phase CO_2 exiting the bed relative to gas phase CO_2 entering the bed (root mean squared error = 0.051).

5.3.2. Mg$_2$(dobpdc)(3-4-3) Results. Figure 5.3 shows the prediction of the heat of adsorption surrogate model for Mg$_2$(dobpdc)(3-4-3) to data from Kim *et. al.* [29]. Parameter estimation was performed using the parmest package [89] available in Pyomo [79], and the estimated parameters are shown in Table 5.4.

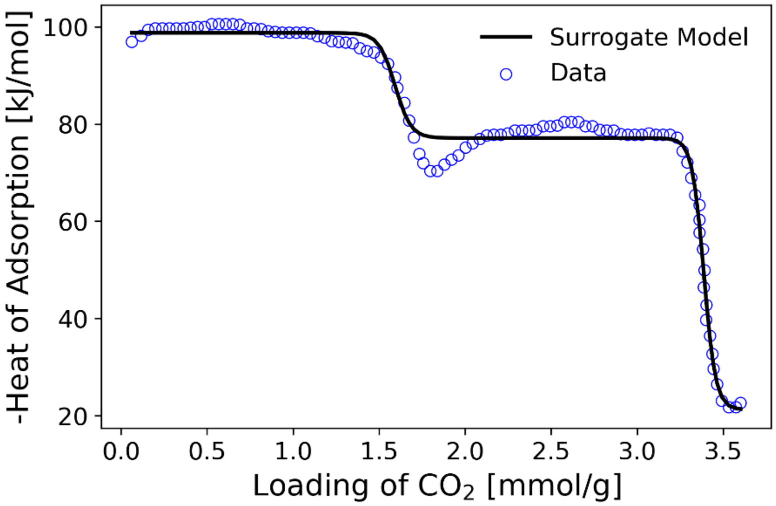

Figure 5.3: Fit of the Mg$_2$(dobpdc)(3-4-3) heat of adsorption surrogate model. Open circles represent fitting data and solid line represents model prediction.

Table 5.4: Estimated parameters for $Mg_2(dobpdc)(3\text{-}4\text{-}3)$ heat of adsorption surrogate model.

Parameter	**Estimated Value**	**Units**
a_1	21.68	[g/mmol]
a_2	29.10	[g/mmol]
b_1	1.59	[mmol/g]
b_2	3.39	[mmol/g]
ΔH_1	98.76	[kJ/mol]
ΔH_2	77.11	[kJ/mol]
ΔH_3	21.25	[kJ/mol]

Experimental breakthrough conditions for $Mg_2(dobpdc)(3\text{-}4\text{-}3)$ are shown in Table 5.5, and Figure 5.4 shows that the fixed bed model is able to accurately predict the experimental data. The results for the parameter estimation problem are shown in Table 5.6. In addition to C_1, the inlet CO_2 mole fraction of the simulated flue gas was estimated to better match the prediction of the breakthrough position to the experimental data as that is dominated by the capacity of the adsorbent rather than the kinetics. Observed and initial values are also shown in Table 5.6. The estimated inlet CO_2 mole fraction shows only a small change from the observed value, 4% to 3.3%. For $Mg_2(dobpdc)(3\text{-}4\text{-}3)$, the initial C_1 value used in the optimization problem is the estimated value for dmpn-$Mg_2(dobpdc)$ and the estimated values for both of these sorbents are within the same order of magnitude which improve our confidence in the estimates. Again, the parameter estimation problem was solved using a least squares estimator and a quasi-Newton based algorithm available in Aspen Adsorption.

Table 5.5: Experimental breakthrough conditions used to collect data to validate the $Mg_2(dobpdc)(3\text{-}4\text{-}3)$ fixed bed model.

Variable	**Value**	**Units**
Bed Length	15.24	cm
Bed Diameter	0.46	cm
Temperature	100	°C
Pressure	1.02	bar
Volumetric Flow Rate	30	sccm

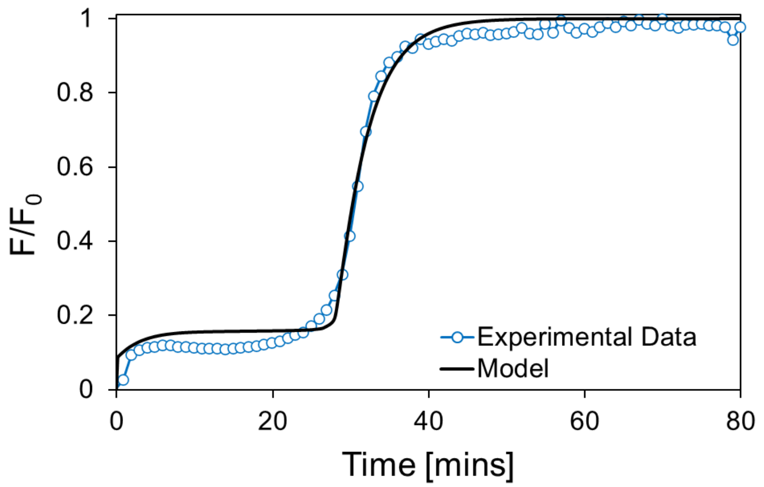

Figure 5.4: Comparison of Mg_2(dobpdc)(3-4-3) breakthrough model prediction (black trace) and experimental breakthrough data (blue trace). The normalized outlet concentration, F/F_0, represents the concentration of gas phase CO_2 exiting the bed relative to gas phase CO_2 entering the bed.

Table 5.6: Mg_2(dobpdc)(3-4-3) fixed bed parameter estimation results

Variable	**Observed/Initial**	**Estimated Value**
$y_{CO_2,inlet}$	0.04	0.033
C_1 $[m^2K^{-0.5}s^{-1}]$	$4.11*10^{-12}$	$3.42*10^{-12}$

5.4. Thermal Management Studies

In this section, thermal management studies using the **dmpn-Mg_2(dobpdc) fixed bed model** are performed. Adsorption of CO_2 in dmpn–Mg_2(dobpdc) is highly exothermic, and the heat released upon CO_2 uptake, coupled with the low material heat capacity, is expected to result in large temperature spikes during the adsorption step. Additionally, CO_2 adsorption isobars for dmpn–Mg_2(dobpdc) [3] indicate that the breakthrough curves will be highly sensitive to temperature. In order to investigate the effects of temperature in greater detail, we simulated isothermal and adiabatic cases using the process conditions outlined in Table 5.7. The isothermal case study assumes perfect removal of the heat generated during adsorption, whereas no heat removal is considered for the adiabatic case study. As shown in Figure 5.5, the breakthrough time in the isothermal scenario is much higher than in the more realistic adiabatic case (80.4 versus 22.7 min, respectively); in other words, achieving perfect heat removal would increase the amount of captured CO_2 by nearly a factor of four. The reduced performance in the adiabatic case can be understood by examining the bed temperature and loading as a function of time (Figure 5.6). Here, large temperature spikes of ~40 °C lead to poor CO_2 loading throughout the majority of the bed. For example, at the bed entrance, initial rapid loading of CO_2 causes a temperature spike that results in a much slower continued rate of CO_2 uptake. Incoming flue gas serves to gradually cool the entrance after this spike, but the uptake rate never achieves the initial value. Similarly, temperature spikes at the middle and end of the bed result in a complete plateau in CO_2 uptake at a low loading. These results indicate that efficient heat removal during adsorption would be critical for realizing the potential of dmpn–Mg_2(dobpdc) in a real-world process.

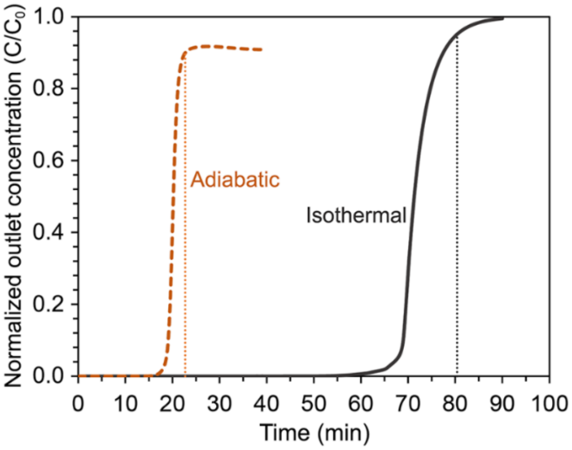

Figure 5.5: Modeled breakthrough curves for isothermal and adiabatic case studies discussed in the text. The normalized outlet concentration C/C_0 represents the concentration of gas phase CO_2 exiting the bed relative to gas phase CO_2 entering the bed. Vertical lines correspond to the breakthrough times for each scenario.

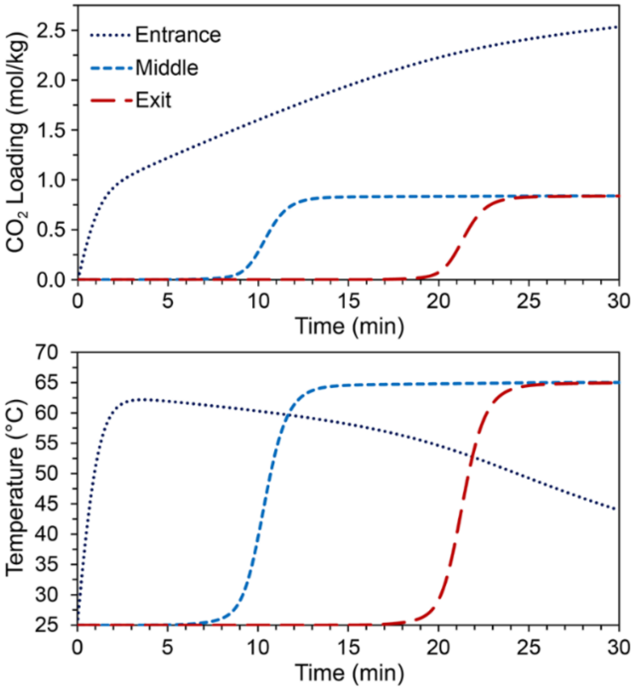

Figure 5.6: Dynamic loading (upper) and temperature (lower) profiles at the entrance, middle, and exit of the bed for the adiabatic case study.

Table 5.7: Process conditions for thermal management case studies.

Variable	Value	Units
Flue Gas Pressure	1.1	[bar]
Flue Gas Temperature	25	[°C]
Flue Gas Flow rate	120	[mol/s]
Flue Gas Composition		
y_{CO2}	0.132	[mol fraction]
y_{H2O}	0.055	[mol fraction]
y_{N2}	0.813	[mol fraction]
Bed Length	10	[m]
Bed Diameter	3	[m]
Initial Bed Temperature	25	[°C]
Initial Bed Loading	0	[mol/kg]

5.5. Conclusions

A detailed, dynamic axial-flow fixed bed model for two amine-appended MOFs, dmpn–Mg_2(dobpdc) and Mg_2(dobpdc)(3-4-3), was developed and validated against experimental breakthrough data. Using this model, isothermal and adiabatic systems were analyzed to investigate how temperature effects and effective heat removal will impact the adsorption performance. The results indicate that effective removal of the heat generated during adsorption can reduce the number of adsorbent beds and subsequently the capital costs of the system by a factor of four. The fixed bed model developed in this Chapter can be used to simulate and analyze industrial scale capture processes.

6. Moving Bed Contactor Modeling

In this chapter, a moving bed contactor model is presented to be used in simulation studies of **dmpn-Mg_2(dobpdc)**. The first-principles model is dynamic, non-isothermal and considers 1-D axial variation of important transport properties such as concentration, temperature, and loading. Two versions of the model are developed. **Version 1** uses the **dual-site Sips isotherm** model developed in Chapter 3 to calculate the adsorption equilibrium, and **Version 2** uses the **chemistry-based isotherm** model developed in Chapter 4. Both versions use the mass transfer model for spherical pellets which has been developed and validated using fixed bed experimental data, as shown in Chapter 5. Steady-state and dynamic sensitivity studies are then performed to better understand the behavior of the moving bed system.

6.1. Introduction

Contactor technology plays a key role in obtaining the maximal performance of solid sorbents [4]. While the contactor technology for solvent-based capture is often absorber/stripper, selection of the appropriate contactor technology for solid-based capture is not straightforward. Optimal selection of the contactor technology among the potential technologies- such as fixed beds of various types, moving beds and fluidized beds- not only requires consideration of material characteristics such as attrition resistance but also satisfactory evaluation of performance characteristics of the contactor [4]. Therefore, detailed modeling of the contactor technology is extremely important when designing and evaluating novel capture processes. Few models exist in literature for the contactors for the amine-appended MOF capture processes [60,62–64]. All of these studies consider fixed bed processes which can suffer from drawbacks which include complicated cyclic control and operation, and lower driving forces for mass and heat transfer. As highlighted in the thermal management studies presented in Section 5.4, efficient thermal management is critical. Efficient heat removal/addition is challenging in fixed beds due to limiting heat transfer coefficient between the gas phase and stagnant solid phase in a fixed bed. The thermal management studies also show that a considerable amount of the bed may be underutilized when the breakthrough happens in a fixed bed design. Obviously, underutilization of the bed material will lead to higher capital cost. Furthermore, recovery of the residual heat from the solids at the end of desorption and utilization of that heat for pre-heating the solids at the end of adsorption step before solids undergo desorption are crucial for reducing the energy penalty. Moving beds can address, to a great extent, many of the drawbacks of the fixed beds processes mentioned above. First and foremost, as moving beds (MBs) operate under much milder flow regime compared to the fluidized beds, MBs have great potential for MOFs, that generally, cannot withstand strong attrition. MBs continuously operate with solid particles entering at the top of the bed while gas enters at the bottom and flows upward through the moving solid particles (see Figure 6.1). This counter-current flow pattern results in large driving forces for mass and heat transfer. The MB technology was initially used in drying processes, but has garnered attention in many industries, most notably in the petrochemical industry [90]. Experimental studies exist in literature which demonstrate the application of the MB technology to carbon capture [91,92]. Ku *et al.* [91] studied the MB process for methane combustion by performing experiments in a lab-scale reactor. Okumura *et al*. [92] performed pilot scale tests to capture CO_2 from the exhaust gas of a 7800 kW gas engine and demonstrated the feasibility of the MB technology. Some of the earliest mathematical models of the MBs were developed for coal gasifiers [93–96]. There exist others works in the literature, experimental and computational, that have demonstrated the potential of the MB process for carbon capture directly such as by using a sorbent or indirectly such as through chemical looping combustion [85,97–102]. To the best of our knowledge, there is no paper in the open literature on the modeling of the MB-based CO_2 capture process using amine-appended MOFs. Furthermore, the existing literature for the MB-based CO_2 capture processes has mainly evaluated energetics, recovery, and efficiency, but not the complete economic analysis considering capital and operating costs. Techno-economic process analysis is necessary for evaluating the critical tradeoff between capital and operating expenditures.

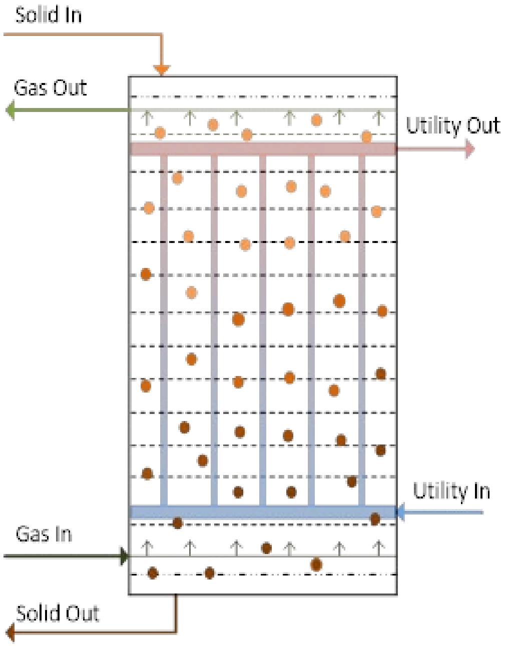

Figure 6.1: Diagram of a moving bed reactor (Kim *et al.*, 2016) [85]

In this work, two versions of the moving bed model are developed. Both versions contain the same mass balances, energy balances, momentum balances, and auxiliary equations but differ in the submodel used to predict the adsorption equilibrium of dmpn-Mg_2(dobpdc). In the first version of the model, referred to simply as "**Version 1**", the **dual-site Sips model** presented in Chapter 3 is used, and in the second version of the model, referred to simply as "**Version 2**", the **chemistry-based isotherm** model presented in Chapter 4 is used.

6.2. Moving Bed Modeling Equations

The moving bed model developed in this work closely follows the model developed by Kim *et al.* [85] and is implemented in Aspen Custom Modeler which contains a framework that simultaneously solves the set of equations comprising mass, momentum, and energy conservation. Similar to the fixed bed contactor, the moving bed contactor considers a shell-and-tube type embedded heat exchanger to supply/remove heat from the system. The key assumptions considered in the modeling of moving bed reactor are as follows:

- Only axial distribution of the process variables is considered.
- Particles flow uniformly throughout the bed with constant voidage and velocity.

- Radial variation due to particle distribution is ignored.
- Temperature variation within the particle is neglected.
- Particle attrition is negligible.

Similar to the fixed bed model developed in this work, it is assumed that the presence of other species typically found in flue gas will not affect the mass transfer or equilibrium of CO_2 on dmpn-Mg_2(dobpdc).

6.2.1 Bulk Gas Phase Species Balance

$$\varepsilon_b \frac{\partial C_{g,i}}{\partial t} = \varepsilon_b D_z \frac{\partial^2 C_{g,i}}{\partial z^2} - \frac{\partial\left(v_g C_{g,i}\right)}{\partial z} - (1-\varepsilon_b)\rho_p \frac{\partial Q_i}{\partial t} \tag{6.1}$$

In the gas phase species balance presented in Eq. (6.1), ε_b represents the voidage in the bed, $C_{g,i}$ represents the concentration of species *i,* D_z is the effective axial dispersion coefficient, v_g is the superficial gas velocity, ρ_p is the particle density, and $\partial Q_i/\partial t$ is the rate of mass transfer between the gas phase and solid particles.

In this work, the Peclet number (Pe') is used for calculating the effective axial dispersion coefficient (Eq. (6.2)).

$$\frac{1}{Pe'} = \frac{D_z}{v d_p} = \frac{20}{Re_p Sc_p} + \frac{1}{2} \tag{6.2}$$

Here, v is the particle velocity and Re_p and Sc_p are the particle Reynolds and Schmidt numbers, respectively.

6.2.2 Solid Phase Species Balance.

$$(1-\varepsilon_b)\rho_p \frac{\partial q_i}{\partial t} = J_s \frac{\partial q_i}{\partial z} + (1-\varepsilon_b)\rho_p \frac{\partial Q_i}{\partial t} \tag{6.3}$$

The solid phase species balance is given by Eq. (6.3) where q_i is the particle loading of species i and J_s is the solid flux which is assumed constant in this work.

6.2.3 Mass Transfer. The rate of the molar amount of CO2 (Q_{CO2}) transferred between the gas and solid phases is assumed to be the sum of the molar amount of chemisorbed species (q_{chem}) and phyisorbed species (q_{phys}) and is given below:

$$\frac{dQ_{CO2}}{dt} = \frac{dq_{chem}}{dt} + \frac{dq_{phys}}{dt} \tag{6.4}$$

$$\frac{dq_{chem}}{dt} = k_{OC}[q^*_{chem} - q_{chem}] \tag{6.5}$$

$$\frac{dq_{phys}}{dt} = k_{OP}\left[q^*_{phys} - q_{phys}\right] \tag{6.6}$$

Here, k_{OC} and k_{OP} are the overall mass transfer coefficients that are previously used for the fixed bed contactor model in Chapter 5 and described in Eqs. (5.2) and (5.3).

Version 1:

In Version 1 of the moving bed model, q^*_{chem} and q^*_{phys} are the equilibrium loadings predicted by the **dual-site Sips model** developed in Chapter 3.2 and shown in Eqs. (3.8) and (3.9).

Version 2:

In Version 2 of the moving bed model, q^*_{chem} and q^*_{phys} are the equilibrium loadings predicted by the **chemistry-based model** developed in Chapter 4.2 and shown in Equations (4.15) and (4.16), respectively.

Similar to the fixed bed model, the rate of adsorption/desorption in an adsorbent particle is calculated assuming a linear driving force:

$$R_i = \frac{6k_{f,i}}{d_p}\left(C_{g,i} - C_{surf,i}\right) = \rho_p \frac{\partial Q_i}{\partial t} \tag{6.7}$$

where $k_{f,i}$ is the external (gas film) mass transfer coefficient and $C_{surf,i}$ is the concentration of the gas at the particle surface. Eq. (6.7) determines $C_{surf,i}$ and accounts for any external mass transfer resistance across the gas film that surrounds the particle.

6.2.4 Energy Balances

$$\varepsilon_b \rho_g C_{p,g} \frac{\partial T_g}{\partial t} = -\rho_g C_{p,g} v_g \frac{\partial T_g}{\partial z} - P \frac{\partial v_g}{\partial z} - (1-\varepsilon_b) a_p h_{gs} (T_g - T_s) \tag{6.8}$$

The gas phase energy balance is given in Eq. (6.8). Here, T_g represents the temperature of the gas phase, $C_{p,g}$ is the heat capacity of the gas phase, a_p is the specific particle surface area, and h_{gs} is the heat transfer coefficient between the gas phase and the solid phase.

$$\begin{aligned}(1-\varepsilon_b)\rho_s C_{p,s} \frac{\partial T_s}{\partial t} &= C_{p,s} J_s \frac{\partial T_s}{\partial z} + (1-\varepsilon_b) a_p h_{gs} (T_g - T_s) \\ &+ \frac{\pi D_t N_{tube}}{A_{bed}} h_t (T_w - T_s) + \Delta \mathrm{H}_{CO_2} \rho_s \frac{\partial Q_{CO_2}}{\partial t}\end{aligned} \tag{6.9}$$

The solid phase energy balance is given in Eq. (6.9). Here, N_{tube} is the number of heat exchanger tubes in the moving bed reactor, h_t is the heat transfer coefficient between the solid phase and heat exchanger tube wall, and T_w is the temperature of the tube wall. The last term in the solid phase energy balance accounts for the adsorption heat where $\Delta \mathrm{H}_{CO_2}$ is the heat of adsorption.

The energy balance across the tube wall gives the following equation:

$$\pi(d_t - 2w_{thx}) N_{tube} h_{wgt} (T_w - T_{tube}) - \pi d_t N_{tube} h_t (T_w - T_s) = 0 \tag{6.10}$$

The energy balance for the tube side fluid is written in terms of enthalpy and is shown in Eq. (6.11).

$$F_t \frac{\partial H_t}{\partial z} - \pi(d_t - 2w_{thx}) N_{tube} h_{wgt} (T_w - T_{tube}) = 0 \tag{6.11}$$

Here, F_t is the flow of the tube side fluid, H_t is the enthalpy of the tube side fluid, and h_{wgt} is the heat transfer coefficient between the tube fluid and the inner side of the tube.

6.2.5 Heat Transfer Coefficients. Heat transfer coefficients used are taken from Kim *et al.* [85] and are based on fluidized bed correlations found in literature [78,103,104]. The gas-to-solid h_{gs}, wall-to-gas h_{wg}, wall-to-solid h_{ws}, and steam-wall h_t heat transfer coefficients are described in the equations below:

$$Nu = \frac{h_{wg} d_p}{k_g} = 0.009 Ar^{1/2} Pr^{1/3} \tag{6.12}$$

$$Nu_p = \frac{h_{gs} d_p}{k_g} = 2.0 + 1.1 Pr^{1/3} Re_p^{3/5} \tag{6.13}$$

$$k_{pa} \ = \ (3.58 - 2.5e) k_g \left({k_s}/{k_g} \right)^{0.46(1-e)} \tag{6.14}$$

$$h_{ws} \ = \ 2 \left(k_{pa} \rho_s C_{p,s} \frac{1-e}{\pi \tau} \right)^{1/2} \tag{6.15}$$

$$h_t \ = \ f_b \, h_{ws} + (1 - \ f_b \ ) \, h_{wg} \tag{6.16}$$

where k_g and k_s denote the gas and sorbent thermal conductivities, respectively, Ar is the Archimedes number, Pr is the Prandtl number, k_{pa} is the bed's thermal conductivity at minimum fluidization velocity, f_b is the fraction of time that the heat exchanger surface contacts the solids, and τ is the average residence time of the solids contacting the heat exchanger surface. The parameters f_b and τ are given by the following relations:

$$f_b = 0.33 \left[v_{mf}^2 \left(\frac{(f_n - a_h)^2}{9.8 d_p} \right)^{0.14} \right] \tag{6.17}$$

$$f_n = \frac{v_g}{v_{mf}} \tag{6.18}$$

$$\tau = 0.44 \left[\left(\frac{9.8 d_p}{v_{mf}^2 (f_n - a_h)^2} \right)^{0.14} \left(\frac{d_p}{d_o} \right)^{0.225} \right] \tag{6.19}$$

6.2.6 Auxiliary Equations. The behavior of a falling particle in the moving bed can be estimated by analogy to a fluidized bed. For maintaining the bed in the moving bed region, the internal gas velocity through the bed should be less than the minimum fluidization velocity, v_{mf}, given by the equation below from Kunii and Levenspiel [105].

$$\frac{1.75}{\psi\varepsilon_{mf}^{3}}\left(\frac{d_p u_{mf}\rho_g}{\mu_g}\right)^2+\frac{150\left(1-\varepsilon_{mf}\right)}{\psi^2\varepsilon_{mf}^{3}}\left(\frac{d_p u_{mf}\rho_g}{\mu_g}\right)=\frac{d_p^3\rho_g\left(\rho_s-\rho_g\right)g}{\mu_g^2} \tag{6.20}$$

Therefore, the following constraint is satisfied at all positions in the bed.

$$v_g < v_{mf} \tag{6.21}$$

The embedded exchanger configuration and equations used in the moving bed model are the same that are used in the fixed bed model in Chapter 5 and are given in Eqs. (5.14) and (5.15).

6.3. Modeling Results

All results in this Section are generated using **Version 1** of the moving bed model which uses the **dual-site Sips model** to calculate the adsorption equilibrium.

6.3.1 Steady-State Behavior. To analyze the behavior of many important process variables, sensitivity studies for important operating conditions are performed in this section. Base case operating and design conditions are listed in Table 6.1.

Table 6.1: Base case design and operating conditions for moving bed modeling studies

Process Condition	**Value**	**Units**
Adsorber		
Lean Solids Temperature	25	°C
Lean Solids Flow	91,266	[kg/hr]
Flue Gas Composition (mol fraction)		
CO_2	0.147	[-]
H_2O	0.026	[-]
N_2	0.827	[-]
Flue Gas Flow	1669	[kmol/hr]
Cooling Water Temperature	20	°C
Cooling Water Flow	20,000	[kmol/hr]
Desorber		
Rich Solids Temperature	110	°C
Rich Solids Flow	588,914	[kg/hr]
Direct Steam Temperature	110	°C
Direct Steam Flow	182	[kmol/hr]
Indirect Steam Temperature	139	°C
Design Conditions		
CO_2 Capture	90%	[-]
Lean Solids Loading	0.3	[mol/kg]
Cooling water temperature change	10	°C
Maximum gas velocity relative to minimum fluidization velocity	90%	[-]

Figure 6.2 shows how the loading and gas CO_2 composition profiles in a moving bed adsorber change with a decrease in solids flow. It should be noted that operating conditions are kept at the base case value unless otherwise specified which results in the design conditions not being constantly maintained for the single variable sensitivity studies performed in this section. For the base case, solids flow was set so CO_2 capture was 90% so a decrease in solids flow would result in a decrease in CO_2 capture, which is shown in the figure. For a 50% decrease in solids flow, CO_2 capture decreases to 38%. Also as expected, a smaller amount of solids flowing through the adsorber would result in a sharper rise in solids loading, which is shown in Figure 6.2. Similar to the base case, adsorption for the new case mainly occurs in the top section of the bed and again results in solids exiting the bed that are in equilibrium with the bed temperature and flue gas composition at the bottom of the bed. Additional base case profiles can be found in the Appendix.

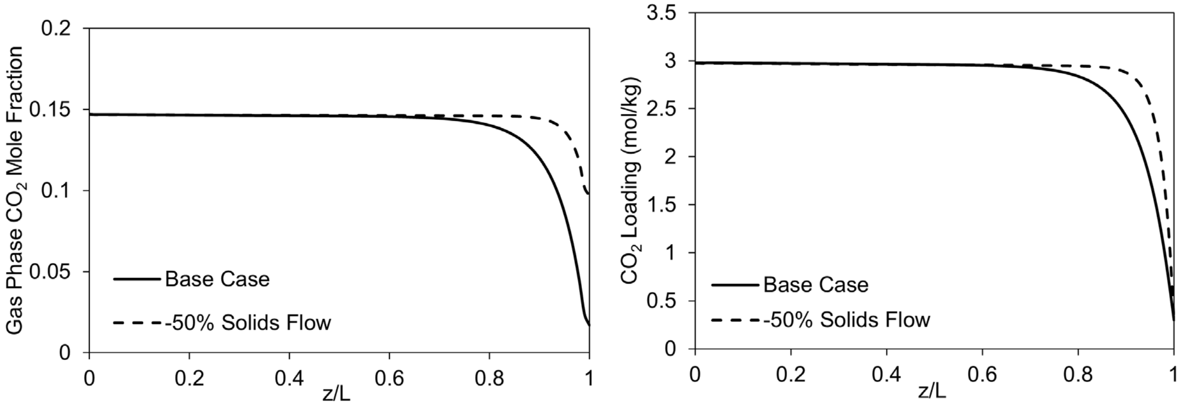

Figure 6.2: Adsorber steady-state response to a 50% decrease in solids flow. z/L represents the normalized length of the bed with 0 corresponding to the bottom of the bed.

Figure 6.3 shows a similar analysis for a moving bed desorber. For a larger flow of solids, residence time decreases which results in a smaller loading change when compared to the base case. However, a larger flow of solids results in more CO_2 being released which in turn results in a higher composition of CO_2 in the gas phase. The opposite is true for a decrease in solids flow. A longer residence time results in a larger change in solids loading but a smaller amount of CO_2 being regenerated into the gas phase. The lean loading for the base case is 0.3 mol/kg while the lean loading for the 50% increase and the 50% decrease is 0.61 mol/kg and 0.04 mol/kg, respectively. Additional base case profiles can be found in the Appendix.

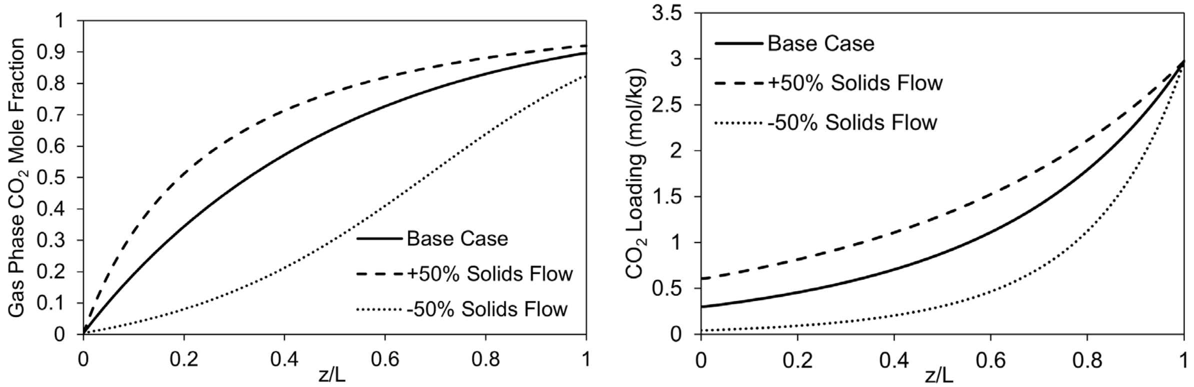

Figure 6.3: Desorber steady-state response to a +/-50% change in solids flow. z/L represents the normalized length of the bed with 0 corresponding to the bottom of the bed.

6.3.2 Dynamic Behavior. Dynamic responses of the adsorber and desorber to an input disturbance are shown in the section below. To simulate the response, the model was solved for the steady-state conditions listed in Table 6.1 and then the input disturbance of interest was introduced as a 30 second ramp change.

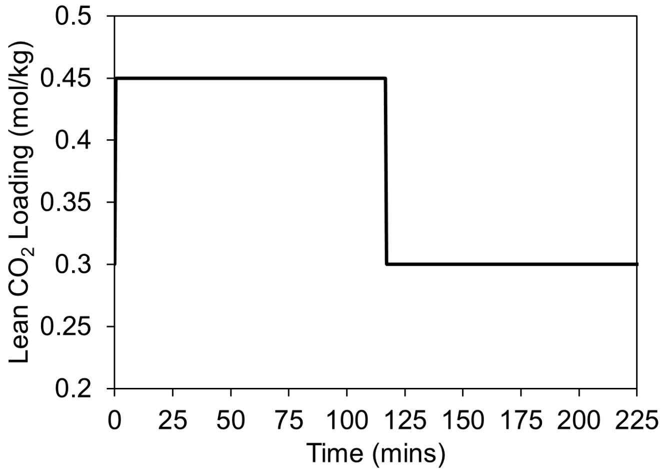

Figure 6.4: Adsorber lean loading input disturbance.

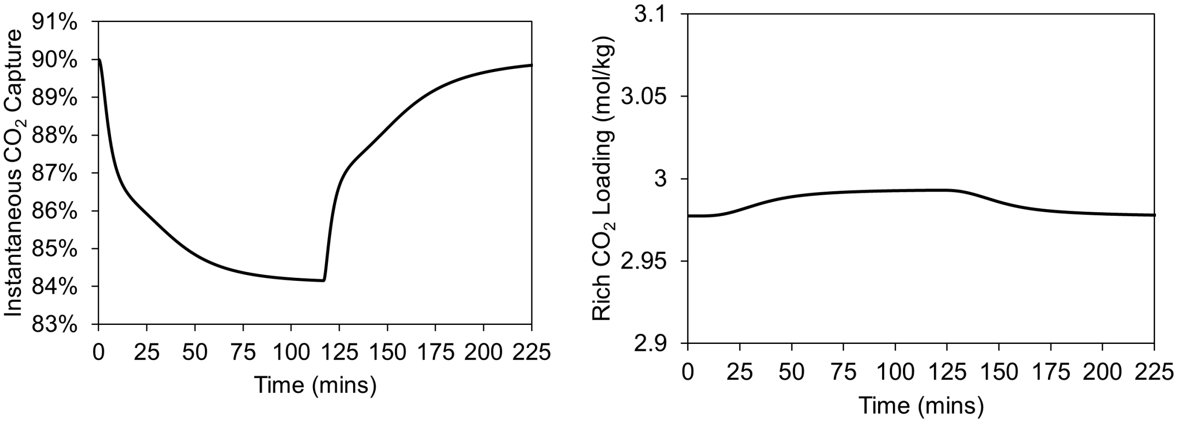

Figure 6.5: Dynamic adsorber response of instantaneous CO_2 capture (left) and rich CO_2 loading (right).

Figure 6.4 shows the lean loading input disturbance used for the adsorber dynamic analysis. The lean loading increases to a value of 0.45 mol/kg, a 50% increase from the base case, then, once the process reaches the new steady-state, is returned to the base case value. Figure 6.5 shows the dynamic response of the CO_2 capture and rich loading. Due to long solids residence times, the adsorber takes ~125 mins to reach a new steady-state. The increase in lean loading causes a decrease in capture due to the reduction of CO_2 capacity in the solids. For the 50% increase in lean loading, the capture percentage approaches a new steady-state value around 84%. When the loading returns to the base case value, the capture percentage returns to its base case value of 90%. The rich loading of the solids shows very little change during this dynamic case. This can be attributed to the effective cooling from the embedded exchanger and residence times that are long enough so that the solids reach equilibrium before they exit the bed.

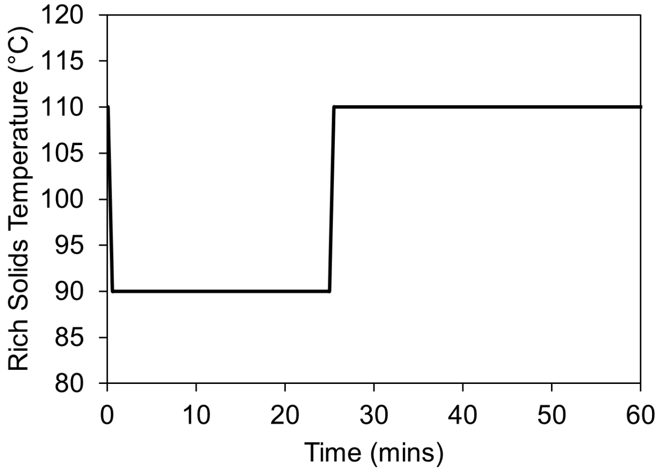

Figure 6.6: Desorber rich solids temperature input disturbance.

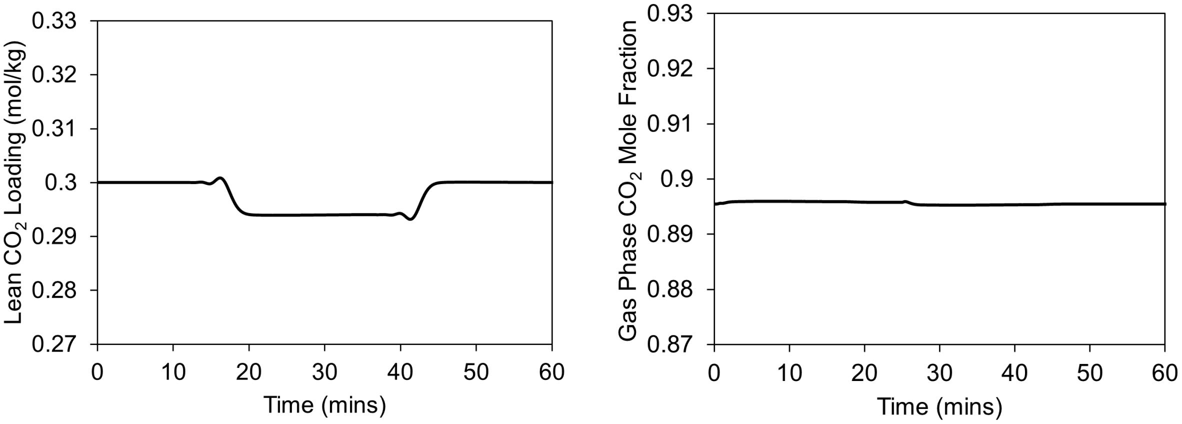

Figure 6.7: Dynamic desorber response of lean CO_2 loading (left) and gas phase CO_2 mole fraction of the exit gas (right).

Figure 6.6 shows the input disturbance of the rich solids temperature. The temperature decreases from its base case value of 110°C by to 90°C, then, once the process reaches the new steady-state, is returned to the base case value. As shown in Figure 6.7, the change in temperature elicits very little response from the lean loading and exiting gas phase composition. This lack of response can be attributed to two factors, the small difference of the CO_2 capacity of the adsorbent from 90°C to 110°C and the dominating heat transfer from the embedded exchanger. The low CO_2 capacity of the adsorbent over 90°C results in small changes in the driving force for mass transfer, and the large amount of heat transferred from condensing steam in the embedded exchanger means that the solids still reach high temperatures before exiting the bed.

6.4. Conclusions

A detailed, dynamic, pressure driven moving bed contactor model with axial variation for dmpn-Mg_2(dobpdc) was developed in this Chapter. Two version of the model exist, Version 1 uses the Sips isotherm model developed in Chapter 3.2 and Version 2 uses the chemistry-based model developed in Chapter 4 to calculate the CO_2 adsorption capacity as a function of temperature and pressure. Steady-state and dynamic sensitivity studies are performed to better understand the behavior of the moving bed process. The model developed here can be used to simulate and analyze industrial scale capture processes.

7. Techno-economic Analysis and Optimization of Amine-Appended MOF Capture Processes

In this Chapter, techno-economic analysis and optimization of industrial scale capture processes using amine-appended MOFs is performed. Two cost models are developed. The first uses an equivalent annual operating cost (EAOC) to evaluate the tradeoff between capital and operating costs. The second cost model is used for Mg_2(dobpdc)(3-4-3) studies and is developed to be more in line with NETL standards. Analysis of dmpn-Mg_2(dobpdc) capture processes for coal-based flue gas is then performed using the fixed bed and moving bed models developed in this work. The fixed bed model is also used for analysis of a TSA capture process using Mg2(dobpdc)(3-4-3) for NGCC flue gas. Sensitivity studies are also performed to evaluate the effect of important design variables as well as uncertain costing parameters on process economics.

Portions of this Chapter are published in the following peer-reviewed journal article:

Hughes, R.; Kotamreddy, G.; Ostace, A.; Bhattacharyya, D.; Siegelman, R. L.; Parker, S. T.; Didas, S. A.; Long, J. R.; Omell, B.; Matuszewski, M. Isotherm, Kinetic, Process Modeling, and Techno-Economic Analysis of a Diamine-Appended Metal–Organic Framework for CO_2 Capture Using Fixed Bed Contactors. *Energy Fuels* **2021**, *35* (7), 6040–6055. https://doi.org/10.1021/acs.energyfuels.0c04359.

7.1. Analysis of dmpn-Mg_2(dobpdc) for Coal-based Capture

Techno-economic optimization and analysis of coal-based capture processes utilizing dmpn-Mg_2(dobpdc) are presented in this section. In total, three separate TSA models are used here. The contactor type and isotherm model used are summarized below:

1. Fixed bed contactor with **dual-site Sips** isotherm model
2. Moving bed contactor with **dual-site Sips** isotherm model, referred to as **Version 1**
3. Moving bed contactor with **chemistry-based** isotherm model, referred to as **Version 2**

7.1.1. Cost Model

The costs for equipment items used in the process models were determined using the Aspen Process Economic Analyzer (APEA). The reactors and compressors were considered to be the dominant capital costs. The reactors modeled here are very similar in configuration to shell and tube heat exchangers and were priced using APEA. However, the heat transfer area for the reactors considered in the basic and modified processes exceeds the maximum heat transfer area that can be priced in APEA, so the estimated cost for a reactor size of interest was calculated using the following equation [106]:

$$\text{Esimated cost} = \text{Base cost}\left(\frac{\text{required area}}{\text{base area}}\right)^{0.6} \tag{7.1}$$

Here, the base area is the maximum heat exchange area that can be priced in APEA, the base cost is the cost associated with the base area, and the required area is the area for the reactor of interest. The capital costs considered in this work are bare module costs which are obtained using correlations from Turton *et al.* [106]. The bare module method of costing uses the purchased cost of equipment, which is obtained from APEA and Eq. (7.1) in this work, and multiplies it by a factor to account for additional expenses due to labor, installation, overhead, and transportation [106]. The capital costs were then amortized over the projected plant life. The discount rate (or interest rate) was assumed to be 10% and the lifespan of the reactors and compressors was set at 10 years. The other major costs considered in this work are the operating costs due to steam, cooling water, and electricity. These costs are calculated based on the amount used, which is obtained from simulations, and utility prices (see Table 7.1) obtained from Turton *et al.* [106]. The equivalent annual operating cost (EAOC) was then calculated using Eq. (7.2).

$$\begin{aligned}\text{EAOC} = {} & \text{Capital cost}\frac{\text{Discount rate}}{\left(1-(1+\text{Discount rate})^{-\text{Number of years}}\right)} \\ & + \text{Yearly Operating Costs}\end{aligned} \tag{7.2}$$

We also determined the EAOC of a conventional post-combustion capture system using monoethanolamine (MEA) for comparison. Capital and operating costs for the MEA system were obtained from a study published by the National Energy Technology Laboratory [107].

Table 7.1: Utility prices used in dmpn-Mg_2(dobpdc) costing model

Utility	Price
Steam	29.29 \$/(1000 kg)
Electricity	0.06 \$/kWh
Cooling Water	0.354 \$/GJ

7.1.2. Fixed Bed TSA Process

A commercial-scale post-combustion temperature swing adsorption (TSA) process model was developed. The cycle begins by flowing the flue gas through a regenerated bed until the bed reaches its breakthrough time (see Eq. (5.26)) which ensures 90% integral CO_2 capture. Once the bed reaches its breakthrough time, it is effectively saturated and therefore the flow of flue gas to the bed is stopped and desorption (regeneration) begins.

Two different configurations for the TSA cycle were considered as shown in Figure 7.1. The basic configuration (top of Figure 7.1) uses condensing steam as the heating medium in the embedded heat exchanger during desorption: steam is introduced into both the embedded exchanger (indirect steam) as well as directly injected into the bed (direct steam). The direct steam provides much less heat than the indirect steam because it is not condensed in the bed, and its primary purpose is to lower the partial pressure of CO_2 in the bed and thereby aid in desorption. The modified configuration (bottom of Figure 7.1) utilizes cooling water in the embedded exchanger during the adsorption step to aid in the removal of heat generated upon adsorption and therefore improve bed performance. Note that the use of steam for desorption in this configuration would require that the cooling water first be completely removed from the heat exchanger (for example, using pressured air) to prevent hydraulic shock and potential mechanical damage. In order to avoid the time and cost penalties associated with this added step, hot water (generated in an external heat exchanger by condensing steam) is used as the indirect heating medium during desorption. The use of hot water instead of steam leads to a lower internal heat transfer coefficient for the embedded heat exchanger. However, assuming heuristic heat transfer coefficient values [106] of 850 $W \cdot m^{-2} \cdot K^{-1}$ for condensing steam, 560 $W \cdot m^{-2} \cdot K^{-1}$ for liquid-to-solid, and 60 $W \cdot m^{-2} \cdot K^{-1}$ for gas-to-solid, a quick estimation of the overall heat transfer coefficient ($1/U = 1/h_1 + 1/h_2$) results in 56 and 54 $W \cdot m^{-2} \cdot K^{-1}$, a less than 5% difference and shows that the external heat transfer coefficient between the tube wall and flowing gas is limiting for this system. The driving force for desorption is lower when using hot water, given that the temperature of the water will decrease along its flow direction. However, this effect can be compensated by increasing the inlet water temperature. Finally, similar to the basic TSA process, direct steam is also introduced into the bed during desorption. For both configurations, the desorption step continues until the average particle loading throughout the bed reaches a desired value. Then, the bed is cooled to the desired initial temperature for the next adsorption step. This adsorption–desorption cycle is repeated several times until the differences between loading and temperature profiles for successive cycles are below a minimum convergence value, achieving a cyclic steady state [108]. The results presented below are cyclic steady state results.

In both models, a sufficient number of adsorbent beds were configured in parallel in order to continuously process large amounts of flue gas, with the assumption that adsorption and desorption are occurring simultaneously in different beds. The total number of beds needed for the TSA process was calculated by solving a scheduling problem that guarantees enough parallel beds are available to continuously process the flue gas. A simplified diagram of the parallel configuration developed for the basic TSA cycle is shown in Figure 7.2.

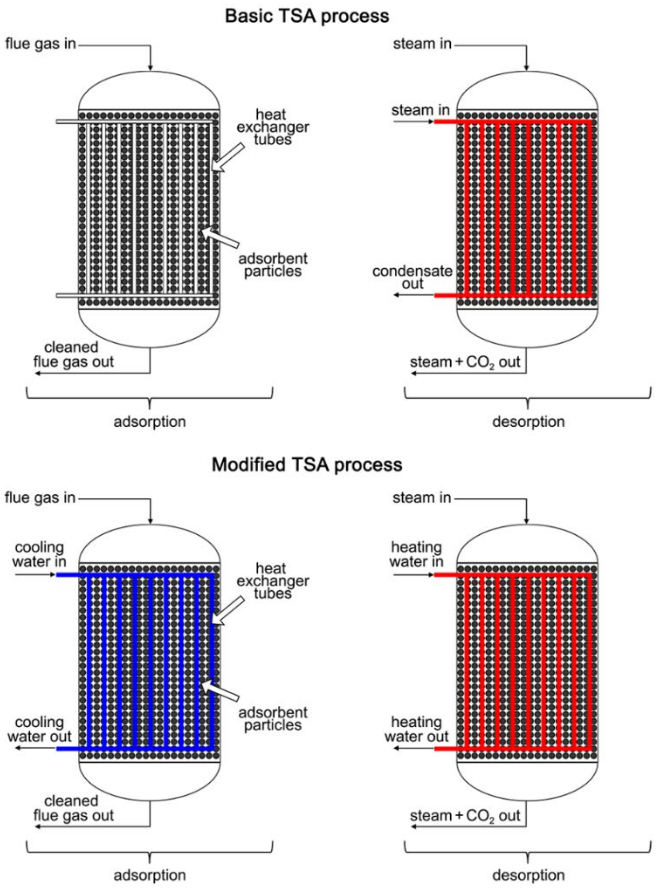
Basic TSA process
flue gas in
steam in
heat exchanger tubes
steam in
adsorbent particles
condensate out
cleaned flue gas out
steam + CO_2 out
adsorption
desorption
Modified TSA process
flue gas in
steam in
cooling water in
heat exchanger tubes
heating water in
adsorbent particles
cooling water out
heating water out
cleaned flue gas out
steam + CO_2 out
adsorption
desorption

Figure 7.1: Configuration steps for the basic TSA process (upper) and the modified TSA process (lower).

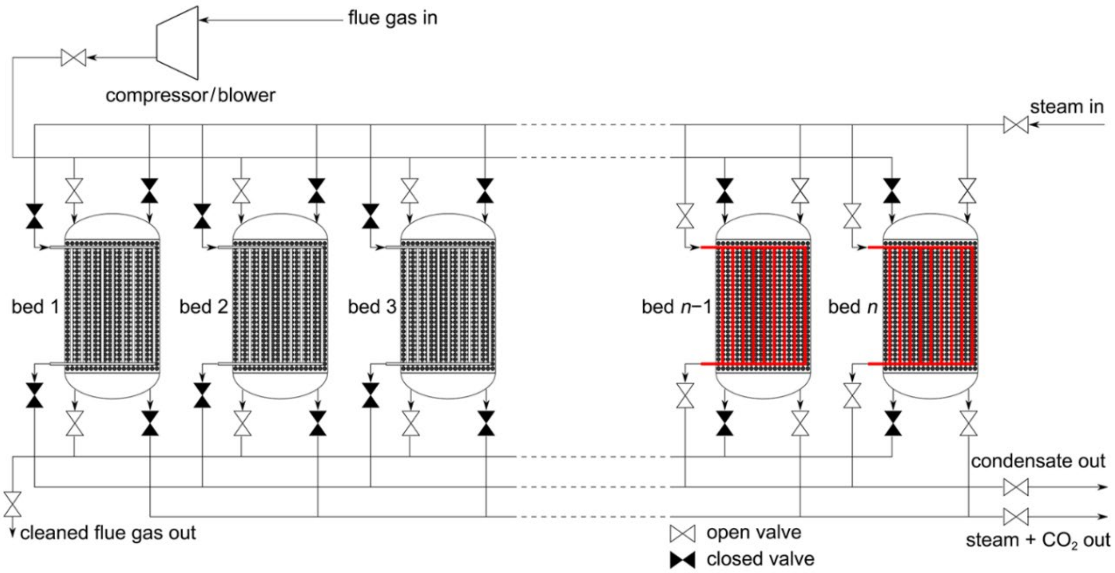
flue gas in
compressor/blower
steam in
bed 1
bed 2
bed 3
bed *n*−1
bed *n*
condensate out
cleaned flue gas out
open valve
closed valve
steam + CO_2 out

Figure 7.2: Simplified diagram of the parallel bed configuration used in modeling the basic TSA cycle. A process that uses *n* beds is shown, with dashed lines representing the possibility of introducing more beds.

7.1.2.1 Impact of Operating Conditions on Process Economics. In this section, an analysis of process economics sensitivity to the residence time of flue gas in the bed and the bed temperature at the onset of adsorption is presented. Flue gas residence time—which is determined from the volumetric flow of the gas to a single bed, bed length, and bed diameter—directly impacts the number of beds required in the process and therefore the capital costs. For example, increasing the volumetric flow of the flue gas can decrease the residence time and therefore the number of adsorption beds required to simultaneously process a given amount of flue gas. Conversely, an increase in residence time will generally lead to an increase in the breakthrough time and reduce the cycling rate of the beds but will result in a monotonic increase in the number of required adsorption beds. The importance of temperature and its relation to adsorption capacity and performance has been highlighted in previous chapters of this work. It is relevant to note that the pre-adsorption cooling step can add to the total cycle time and increase the number of beds required and therefore the capital costs. However, this time can be considerably reduced by using a large flowrate of a gas for cooling like air from the forced draft fan in a pulverized coal plant. In addition, for the modified process, the embedded cooler rapidly cools the sorbent therefore adding an embedded cooler in the pre-adsorption step can further reduce the time for cooling. Therefore, it is assumed that the cooling time is insignificant when compared to the time required for adsorption/desorption and it is therefore not considered in the cycle time evaluation.

Given the importance of these parameters, we analyzed the sensitivity of the TSA process economics to residence times ranging from 13.9 to 46.5 s at bed temperatures of 25, 35, and 40 °C. For this analysis, it is assumed that the flue gas is available at the same temperature as the initial adsorption temperature. The flue gas conditions used for this analysis correspond to case 11B in the National Energy Technology Laboratory baseline study [107]. The gas was assumed to be generated from a 644 MWe gross power subcritical pulverized coal power plant and to enter the adsorption bed at water saturation for each examined temperature, due to the typical presence of a scrubber before the capture system [107]. Important process variables are shown in

Table 7.2, and the results of the cost analyses are given in Figure 7.3 for the basic and modified TSA process scenarios. For the basic process, the EAOC decreases with decreasing residence time down to ~20 s, reflecting the fact that fewer adsorption beds are required to treat a given quantity of flue gas. However, as the residence time decreases, the superficial velocity of the flue gas in the bed correspondingly increases, resulting in a larger pressure drop across the bed. In order to maintain a required outlet pressure of 1 bar, compressors become necessary below a certain residence time to achieve an inlet pressure that is no longer accessible with a traditional blower. As residence times continue to decrease, the operating and capital costs associated with the compressors begin to outweigh the cost savings achieved from reducing the number of adsorption beds, leading to an increase in the EAOC. This balance between adsorbent bed and compressor cost leads to a minimum EAOC for residence times of 16.1, 18.7, and 18.4 s for bed temperatures of 25, 35, and 40 °C, respectively.

Table 7.2: Important variables for the fixed bed TSA process configuration.

Variable	**Value**	**Units**
Bed length	10	[m]
Bed diameter	10	[m]
Outlet gas pressure	1.05	[bar]
Specific area for heating/cooling	53.3	[m^2/m^3]
Average bed loading at the end of the cycle	0.25	[mol/kg]
Basic TSA Process		
Inlet steam temperature	130	[°C]
Direct steam residence time	100	[s]
Modified TSA Process		
Cooling water approach ΔT	5	[°C]
Cooling water flow	175	[kg/s]
Hot water inlet temperature	130	[°C]
Hot water flow	275	[kg/s]

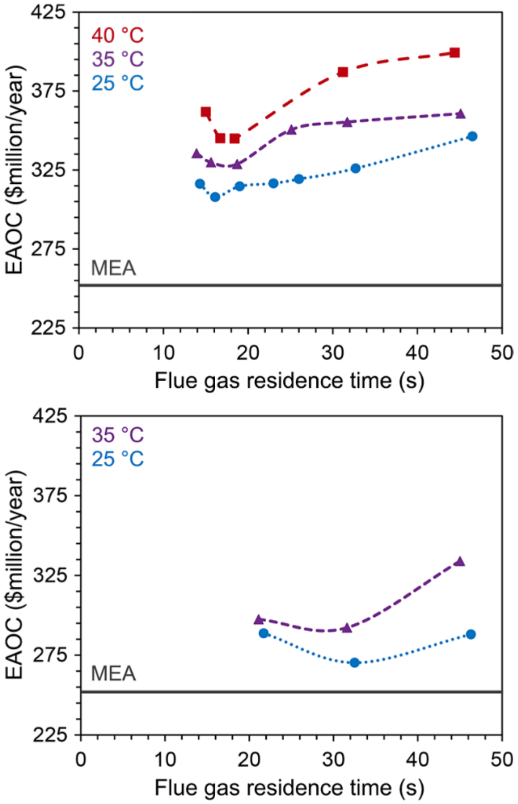

Figure 7.3: Equivalent annual operating cost (EAOC) versus flue gas residence time for the basic dmpn-Mg_2(dobpdc) TSA process (upper) and the modified dmpn-Mg_2(dobpdc) TSA process (lower). Different colored data points indicate cost variations resulting from changing the bed temperature and flue gas temperature at the beginning of the adsorption step. The horizontal line in both plots represents the EAOC for the state-of-the-art MEA system as discussed in the text.

For the modified TSA process, a similar phenomenon is observed, and a minimum in cost occurs at residence times of 32.5 and 31.6 s for bed temperatures of 25 and 35 °C, respectively. In this scenario, the increase in EAOC to the left of the minimum (low residence times) is also associated with the heat generated upon adsorption, which cannot be efficiently removed by the embedded cooler and therefore diminishes the improved adsorption performance that is expected for the modified process. The adsorption performance improves with higher residence times, however, as seen with the basic process, the number of parallel adsorption beds required to process the entire amount of the flue gas increases, driving up the EAOC. Figure 7.4 shows how the breakthrough time (or adsorption time) changes with respect to flue gas residence time for the modified TSA process and the basic TSA process. Results shown here were generated considering an initial adsorption temperature of 25 °C for both processes. The profiles show that an increase in breakthrough time (representative of improved adsorption performance) of the modified process is much larger than that for the basic process at higher residence times (207% greater at a residence time of 47 seconds). At low residence times, the heat generated during adsorption cannot be efficiently removed, and the modified process begins to show breakthrough times similar to the basic process (31% greater at a residence time of 12 seconds). Due to the different nature of the systems and improved adsorption performance at higher residence times for the modified process, the optimum EAOC for the modified process is at a higher residence time than that for the basic process.

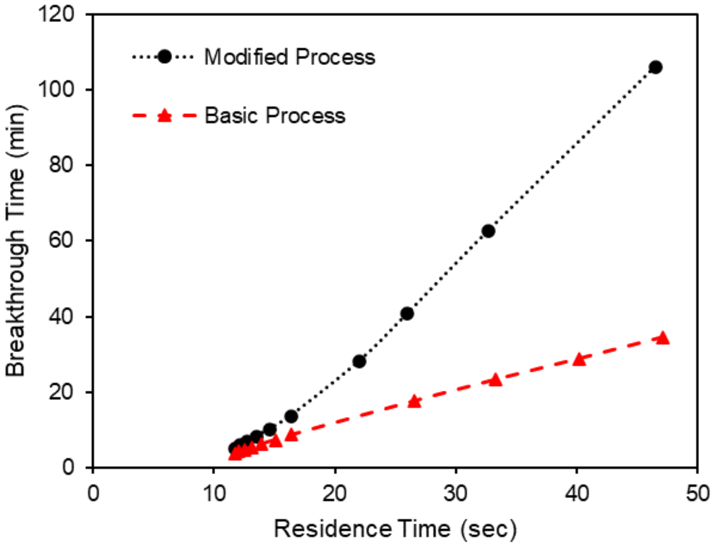

Figure 7.4: Profiles for breakthrough time vs. residence time for the modified TSA process and basic TSA process for dmpn-Mg_2(dobpdc).

As the initial bed temperature (and correspondingly, the flue gas inlet temperature) is decreased, the EAOC also decreases, given that the framework exhibits a higher loading capacity at lower temperatures. The lowest initial bed temperature considered was 25 °C, with the assumption that cooling water is available at 20 °C. While it is possible to lower the initial bed temperature below 25 °C using chilled water or refrigerant, this process would drastically increase the operating costs of the system. For the basic and modified TSA processes, the conditions that result in the lowest EAOC are initial bed temperatures of 25 °C and flue gas residence times of 16.1 and 32.5 s, respectively. Table 7.3 shows times for the adsorption and desorption cycles for a single bed as well as the total number of beds for the minimum EAOC scenarios of the basic and modified process.

Table 7.3: Breakdown of step times and number of beds of the optimal scenarios for the basic and modified dmpn-Mg_2(dobpdc) TSA processes.

	Basic TSA Process	**Modified TSA Process**
Flue gas residence time (s)	16.1	32.5
Adsorption cycle time (s)	546	3607
Desorption cycle time (s)	1372	3551
Number of beds undergoing adsorption	12	32
Total number of beds	43	64

Additionally, dynamic profiles of the loading and temperature of the bed for these scenarios are shown in Figure 7.5 and Figure 7.6.

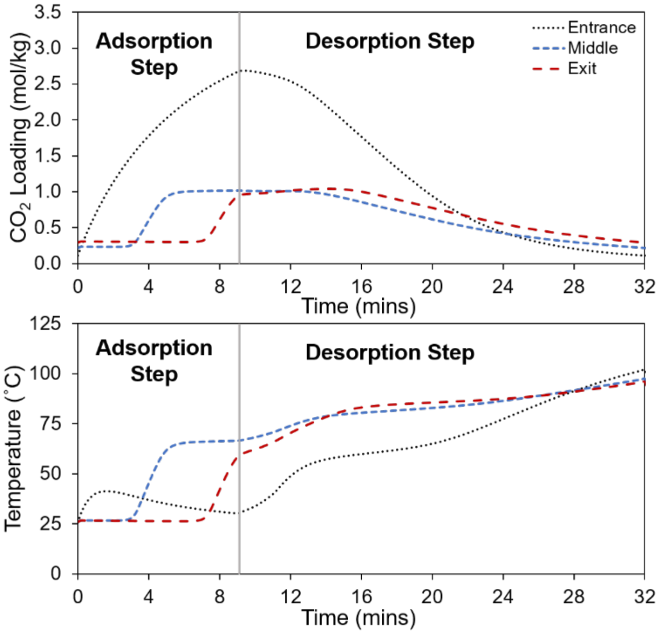

Figure 7.5: Basic dmpn-Mg_2(dobpdc) fixed bed TSA dynamic profiles

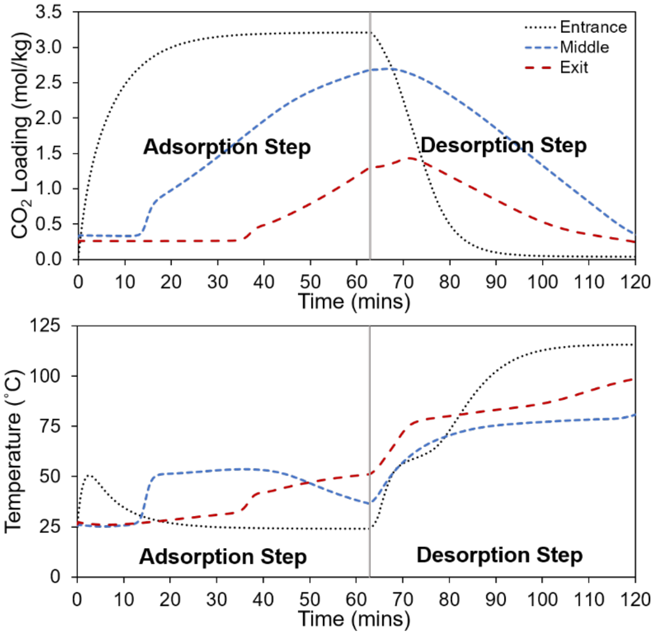

Figure 7.6: Modified dmpn-Mg_2(dobpdc) fixed bed TSA dynamic profiles

The breakdown of costs contributing to the minimum EAOC in each scenario is given in Table 7.4. For the basic process, an inlet pressure of 1.8 bar is required, and the amortized capital costs of the compressors along with the electricity and cooling water required to operate them is reflected in Table 7.4. For the modified process, the high residence time does not require compression of the flue gas and therefore these respective costs are not included. The EAOC for the optimal modified process configuration is about \$37 million/year less expensive than the basic fixed bed configuration, while the EAOCs for the basic and modified processes are approximately \$55 million/year (+21.8%) and \$18 million/year (+7.3%) higher than for the MEA system (EAOC of \$252 million/year), respectively.

Table 7.4: Breakdown of contributing costs to the equivalent annual operating cost (\$Million/year) of the optimal scenarios for the basic and modified dmpn-Mg_2(dobpdc) TSA processes.

	Basic TSA Process	*Modified TSA Process*
Amortized Capital	**84.6**	**99.9**
Reactor	69.8	99.9
Compressor	14.8	–
Yearly Operating Costs	**223.2**	**170.5**
Steam	206.4	167.9
Electricity	16.4	–
Cooling Water	0.4	2.6
EAOC	**307.8**	**270.4**

7.1.2.2 Impact of Heat Recovery on Process Economics. During a typical TSA process, the regenerated bed contains a large amount of sensible heat that can in principle be recycled and used as a heat source elsewhere in the process (e.g., to reduce the amount of steam used for regeneration). In this section, rigorous modeling of a complicated heat recovery section is not performed, but rather the possible improvement of the process economics due to heat recovery is investigated considering two discrete values for recovery efficiencies. For a conventional MEA capture system, a lean/rich amine heat exchanger is used to extract heat from the regenerated solvent stream, with recovery efficiencies as high as 80 to 90% [109]. However, these efficiencies are not likely to feasible with a fixed bed gas–solid system as evaluated here. A practical estimate for the percent heat that could be recovered in the basic and modified TSA processes was determined based on the temperature profile in the respective beds at the end of desorption and the initial adsorption temperature. The calculated percent heat recovered varied based on the given process conditions but was found to be ~35% for the basic and modified TSA process scenarios studied here (See the Appendix for additional information on how the estimated heat recovery is calculated). Notably, with this moderate amount of heat recovery, the estimated annual operating cost for the modified TSA process approaches that of the state-of-the-art MEA system and is approximately \$26 million/year lower than the cost of the basic process (Figure 7.7). In a scenario with 85% heat recovery, the modified process is only about \$4 million/year less expensive than the basic process, while both processes achieve a cost savings of more than \$20 million/year when compared to the MEA system (see Table 7.5 for EAOC breakdowns for each heat recovery case). Thus, exploring strategies to enhance and optimize heat recovery in adsorbent-based systems stands as a crucial goal toward making their process economics competitive with solvent capture systems.

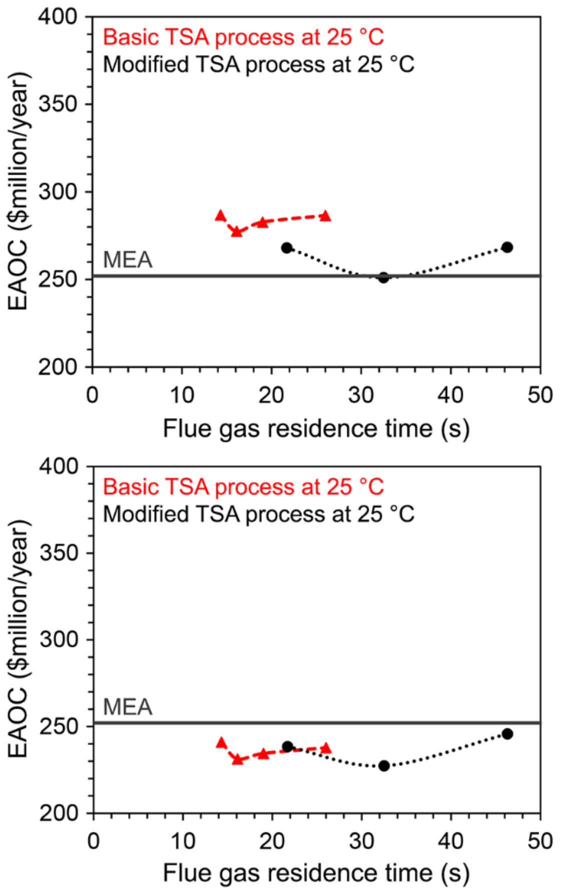

Figure 7.7: EAOC versus flue gas residence time for the basic dmpn-Mg_2(dobpdc) TSA process (red) and modified dmpn-Mg_2(dobpdc) TSA process (black) assuming 35% practical heat recovery (upper) and 85% heat recovery (lower). The horizontal line represents the EAOC for the state-of-the-art MEA system.

Table 7.5: Breakdown of contributing costs to the EAOC ($Million/year) for the heat recoveries considered in this work. Cases presented correspond to the optimal scenarios for the basic and modified TSA processes.

	Basic TSA Process		***Modified TSA Process***	
	35% Heat Recovery	*85% Heat Recovery*	*35% Heat Recovery*	*85% Heat Recovery*
Amortized Capital	**84.6**	**84.6**	**99.9**	**99.9**
Reactor	69.8	69.8	99.9	99.9
Compressor	14.8	14.8	–	–
Yearly Operating Costs	**193.0**	**146.7**	**151.1**	**127.4**
Steam	176.2	129.9	148.5	124.8
Electricity	16.4	16.4	–	–
Cooling Water	0.4	0.4	2.6	2.6
EAOC	**277.6**	**231.3**	**251.0**	**227.3**

7.1.2.3 Particle Cost Uncertainty Analysis. For the analyses completed in preceding sections of this Chapter, the cost of the MOF particles was ignored due to a lack of accurate costing information. However, the cost of these particles will more than likely be a significant cost of the TSA process and should be accounted for. To perform this analysis, the cost of the MOF particle on a per kg basis was varied within a feasible range to investigate how the overall process economics will change. The feasible range of MOF particle costs were determined using a review performed by Liu *et al.* [110] which states that these costs can vary between 1 – 35 $/kg. The cost of zeolite 13x was estimated at $6/kg [111] and is used in this uncertainty analysis as a comparison to costs for a traditional solid sorbent. Based on the total mass of the MOF particles in the cycle and the particle cost of interest, the amortized capital cost of the particles is calculated using the same method as the other equipment as described in Eq. (7.2) with the life span of the MOF particles assumed to be 2 years. Figure 7.8 shows the results for EAOC versus flue gas residence time with varying MOF particle costs for the modified process with practical heat recovery. The baseline curve ($0/kg) corresponds to the results shown in Figure 7.7 (upper). When a particle cost is considered that is similar to that of a traditional solid sorbent ($6/kg), process economics increase by $36 million/year (+14%) when compared to the economics when no particle cost is considered. At the upper value of the uncertainty considered in this work ($30/kg), process economics increase by $175 million/year (+70%).

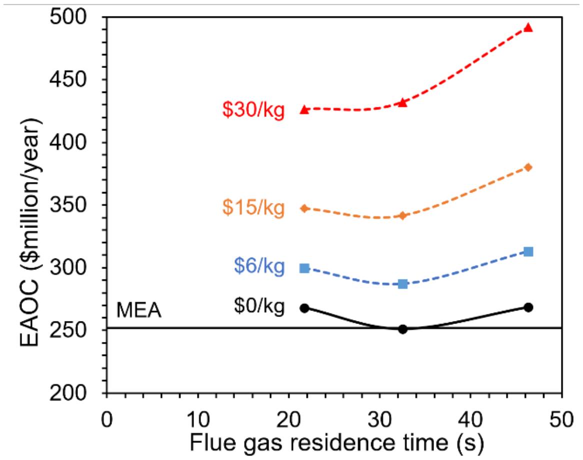

Figure 7.8: EAOC versus flue gas residence time for varying costs of MOF particles ($/kg) of the modified process with practical heat recovery.

7.1.2.4 Evaluation of Energy Requirements. To further understand the techno-economic analysis results, we examined the bed temperature and loading profiles (Figure 7.9) and energy requirements for the optimal basic and modified TSA process scenarios. As discussed in Section 5.4, the adsorption performance of dmpn–Mg_2(dobpdc) is highly sensitive to temperature. As seen in Figure 7.9, the average bed loading for the modified process is about 130% higher than that for the basic process, due to bed cooling. The thermal energy requirements for the basic and modified processes were found to be 3.97 and 3.23 MJ/kg CO_2, respectively, calculated based on the integral steam usage and integral CO_2 captured during a single cycle, assuming the minimum EAOC scenario conditions discussed in previous sections. Note that these values are higher than the regeneration energy of 2.1 MJ/kg CO_2 reported by Milner *et al.* [3], which was calculated assuming a theoretical working capacity that is difficult to achieve in practice due to bed temperature effects discussed in this work. Regeneration energies reported for MEA systems vary in the literature. Theoretical values based on thermodynamic analysis have been reported as low as 3.4 MJ/kg CO_2 [112], while process simulations of a traditional configuration have reported values as low as 3.6 MJ/kg CO_2[51]. Thus, the regeneration energy required for the modified TSA process is 19% and 10% less than that for the basic TSA and MEA processes, respectively. The lower regeneration energy required for the modified process relative to the basic process is a direct consequence of the higher loadings achieved with the former configuration (Figure 7.9, lower). In particular, for modified process, a single bed remains in line longer for adsorption, decreasing the number of cycles and therefore parasitic loss associated with each cycle.

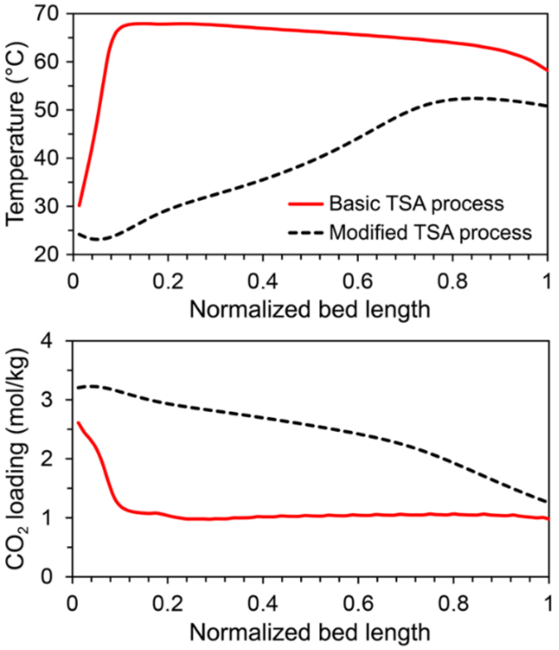

Figure 7.9: Temperature and loading axial profiles at the end of the adsorption step for the basic and modified TSA processes.

7.1.2.5 Conclusions. The fixed bed model developed in previous sections of this work was scaled-up to simulate two different TSA systems processing flue gas from an industrial scale power plant, one that uses condensing steam as the heating medium for regeneration (basic TSA process) and one that uses cooling water for heat removal during adsorption and hot water as well as steam for regeneration (modified TSA process). A techno-economic analysis revealed that the modified process is about $37 million/year less costly and requires 19% less energy than the basic process. These results reiterate the conclusions drawn from the isothermal and adiabatic case studies, that thermal management of this adsorbent system is a key design consideration. When factoring in a practical heat recovery of ~35%, the EAOC of the modified TSA process is further reduced by $18 million/year and approaches that of a state-of-the-art MEA capture system. Further improving heat recovery to 85% could lower the modified process EAOC by an additional $25 million/year, bringing it below that of the MEA system. An uncertainty analysis was performed to investigate the sensitivity of the total process economics to varying values of costs of the MOF particles. This study showed that the modified process EAOC would increase by a modest 14% if the cost of the MOF particles are similar to that of other solid sorbents, but economics have the possibility of increasing by nearly 70% for larger particle costs.

In this study, two discrete values of heat recovery are evaluated. In reality, heat recovery can increase the cycle time due to the increase in the desorption step as a result of pre-heating the bed with a lower temperature fluid than steam as well as increase in the adsorption step as a result of pre-cooling the bed with a higher temperature fluid than the cooling water. Obviously, an increase in the cycle time might lead to higher number of beds. Furthermore, for high driving force, pre-heating a bed might need heat exchange with several beds undergoing cooling arranged in order of their temperature profile thus leading to complex operating schedule. Thus, both economic and practical considerations would be desired for setting the extent of heat recovery. Nevertheless, the results of this study highlight that the successful commercial implementation of this MOF technology will require efficient addition and rejection of heat during adsorption and desorption, as well as heat recovery. Given the limitations of the fixed beds for heat recovery, future work will benefit from examining other types of contactor technologies, such as moving beds and rotary packed beds. The inherently better heat transfer properties of these beds will also provide better opportunities for efficient thermal management during adsorption and desorption. Due to circulating solids, those beds can reduce the amount of solids inventory, which is a critical component of the capital cost. Rigorous optimization of operating variables and contactor configuration will also serve to lower the capital and operating costs. Furthermore, this class of materials is highly tunable. Therefore, for improving the economics further, isotherm step locations and their characteristics as well as adsorption energetics can be considerably altered by varying the diamine.

7.1.3. Moving Bed TSA Process

A full moving bed CO_2 adsorption/desorption process (see Figure 7.10) model was developed in Aspen Custom Modeler v9. In the post combustion process, the MOF adsorbs CO_2 at near ambient conditions in the adsorber. As highlighted in the thermal management studies in Chapter 5.4, the heat of adsorption can significantly deteriorate the performance of the MOF if not properly removed. Therefore, cooling water is used in the embedded heat exchanger of the moving bed adsorber to reduce the temperature rise. The cleaned flue gas is then vented to the atmosphere and the CO_2 rich MOF particles are sent to the desorber. Before the particles enter the desorber, they are heated in the pre-heat exchanger which uses sensible heat from the lean sorbent to heat the particles to regeneration conditions. This sensible heat recovery is an additional advantage of the moving bed process. Steam is inputted at the bottom of the desorber to aid in the removal of CO_2 from the reactor as well as reduce the partial pressure of CO_2 in the bed to aid in the driving force for mass transfer. Once the particles are regenerated in the desorber, they pass through the opposite side of the pre-heat exchanger to recover the heat and then are sent back to adsorber.

A key assumption in the process is that a single desorber did not necessarily have to process the same amount of solids that pass through a single adsorber. For reactors of the same size and configuration, the desorber is frequently able to process more solids than the adsorber mainly because of higher operating temperature that enhances reaction rate constants and mass and heat transfer coefficients thus resulting in a lower number of desorber beds needed for the system. Here, the solids flow to each contactor is set to achieve design conditions for CO_2 capture (adsorber solids flow) and lean loading (desorber solids flow). Due to limitation in the maximum gas velocity in MBs to avoid transitioning into fluidized bed regimes and due to max size limitation of a single MB reactor, often more than one MB is needed to process the flue gas from commercial scale power plants. To size the process for industrial capture, the moving bed adsorbers are assumed to operate in parallel with the number of required beds calculated based on the total flue gas flow rate from the power generation source and the design flow rate to a single bed. Similarly, the desorbers operate in parallel, as needed, to regenerate the total amount of solids used in the adsorbers.

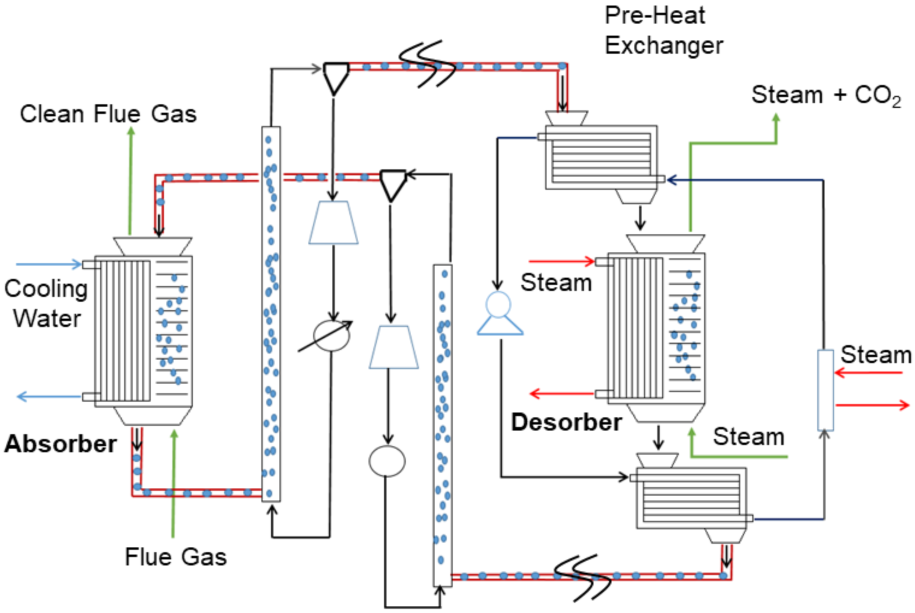

Figure 7.10: Moving bed TSA process

7.1.3.1. *Moving Bed Analysis Results: Version 1*

The results presented in this subsection are for **Version 1** of the dmpn-Mg_2(dobpdc) moving bed TSA process which uses the **dual-site Sips** isotherm model to predict the adsorption equilibrium.

Impact of Operating Conditions on Process Economics: Figure 7.11 shows the results for the sensitivity of the moving bed process economics to changes in the lean sorbent loading and lean sorbent temperature. The lean sorbent loading, i.e. the loading of the sorbent particles that enter the top of the adsorber, was varied for different bed temperatures and the EAOC was evaluated for each case. The lean loadings investigated in these studies span the range of the tradeoff between solid circulation rate and solids residence time in the desorber. At low lean loadings, increased capacity in the adsorber results in low solid circulation rates but longer residence time (and/or higher direct steam injection) in the desorber which are needed to achieve these lean loadings and can result in high capital/operating costs. At high lean loadings, the energy associated with a higher solids circulation rate can become a dominating cost. Again, 25°C was the lowest temperature studied due to the fact that any cooling below this temperature would require a refrigerated coolant which would drastically increase costs. This tradeoff between increased desorption residence time and solids circulations rate leads to a minimum EAOC of

$273 million/year at a lean loading of 0.45 mol/kg and 25 °C. The optimal EAOC values for the moving bed are similar to the optimal alternative fixed bed process with both cooling and heating options. One area where this improvement can be attributed to is the increase of sorbent loading at the end of adsorption which increases the working capacity of the system. The use of cooling water in the embedded heat exchanger in the adsorber aids in removing some of the heat generated during adsorption and therefore increases the working capacity. For the moving bed, working capacity is over twice as large when compared to the working capacity obtained in the fixed bed system without cooling and 25% higher than the fixed bed system with cooling. The inherent counter-current flows that occur in the moving bed contactors greatly increase mass transfer and can also be attributed to the improvement over the fixed bed system. However, one of the issues with the moving bed system is the required low superficial velocity to avoid transition of the bed in the fluidized bed regime. This leads to large number of parallel contactors increasing the capital cost.

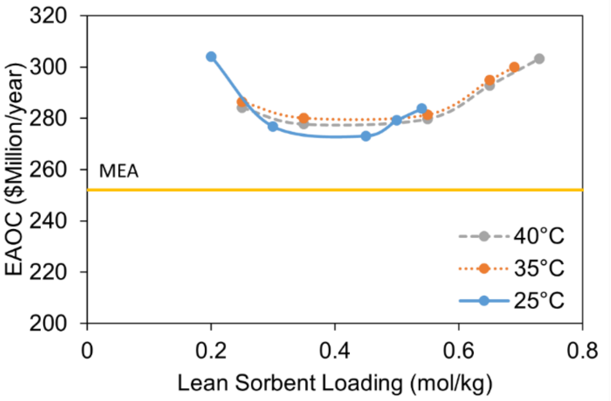

Figure 7.11: Moving bed EAOC versus lean sorbent loading.

Impact of Heat Recovery on Process Economics: Figure 7.11 shows that the best-case results for the moving bed system are not an improvement over the traditional MEA system. One area where the MEA systems save on energy costs is the heat integration between the cold, rich solvent that exits the absorber and the hot, lean solvent that exits the bottom of the desorber. For the moving bed system, the same type of heat integration between the hot, lean sorbent stream and cold, rich sorbent stream can be helpful. The results using a heat recovery of 85%, which is similar to the extent of heat recovery in MEA systems [109], are shown below in Figure 7.12. It should be noted that a value of 85% may not be possible for this system and was chosen to showcase a best-case scenario. More extensive complete process studies need to be completed to evaluate the heat recovery potential. When considering 85% heat recovery, the minimum EAOC is 217.3 $million/year and still occurs at a lean loading of 0.45 mol/kg and 25 °C.

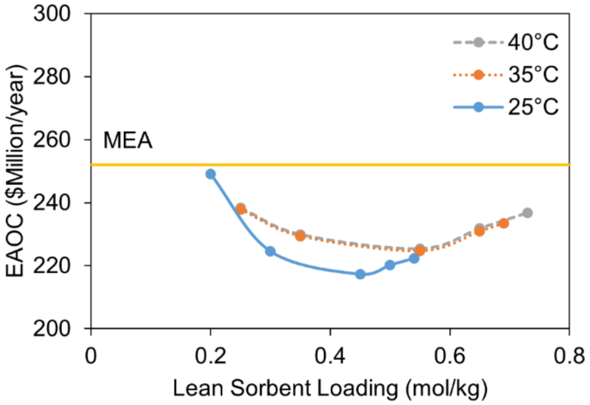

Figure 7.12: Moving Bed EAOC versus lean sorbent loading for 85% heat recovery between lean/rich sorbent stream.

Table 7.6 gives a breakdown of the EAOC for the minimal cases found in the sensitivity studies when considering no heat recovery and when considering 85% heat recovery. Heat recovery decreases the EAOC by $55.7 million/year (-20.4%). When compared to a traditional MEA capture system, the case with no heat recovery is $21 million/year (+8.3%) more expensive and the heat recovery case is $34.7 million/year cheaper (-13.8%).

Table 7.6: Best case EAOC ($Million/year) breakdown for best moving bed cases with different heat recoveries.

	No Heat Recovery	**85% Heat Recovery**
Amortized Capital	**85.7**	**85.7**
Reactor	85.7	85.7
Compressor	-	-
Yearly Operating Costs	**187.3**	**131.6**
Steam	185.1	129.4
Electricity	-	-
Cooling Water	2.2	2.2
EAOC	**273.0**	**217.3**

Capital Cost Uncertainty of the Moving Bed TSA Process: The costing model considers only the reactors and compressors when evaluating equipment costs, but the real-life system would require other balance of the plant. Furthermore, there is high uncertainty in the cost model for the moving bed reactors. In addition, it is not clear at this moment what would be the rate of makeup MOF to the system and how much it would cost. Therefore, in Figure 7.13, the amortized capital costs were varied by +/-50% to evaluate its impact on the EAOC. The +50% uncertainty in the capital cost brings the EAOC for the moving bed above the EAOC of the MEA system. However, a -50% uncertainty in the capital cost can results in 30% lower EAOC in comparison to the MEA system.

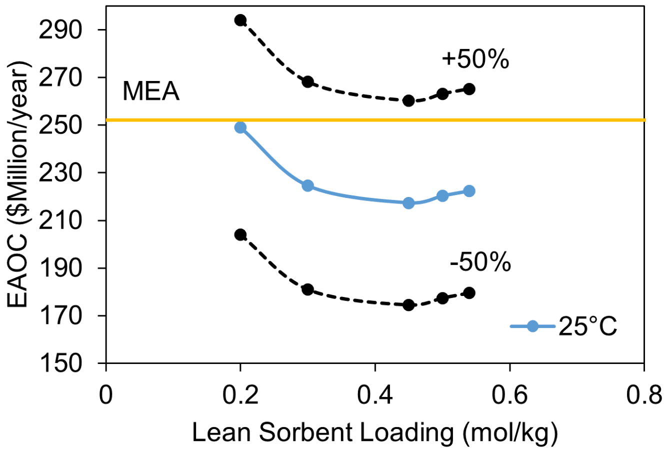

Figure 7.13: Capital cost uncertainty effect on moving bed EAOC. The base case (solid blue line) corresponds to a lean solids temperature of 25 °C and 85% heat recovery.

Impact of the Operating Pressure on Moving Bed TSA Economics: The EAOC values shown above show promise for the moving bed system, but these systems still require large numbers of adsorbers to process the flue gas due to the constraint that the flue gas velocity in the adsorber must remain below the minimum fluidization velocity. One way of increasing the flowrate through a single bed without violating the constraint is to increase the pressure, which can then result in lower number of beds. A study was conducted by fixing the pressure at the top of the bed, i.e., at the flue gas outlet, at 2 bar. For the previous moving bed cases, pressure at the top of the bed was fixed at 1 bar. Figure 7.14 shows the change in the EAOC with the lean sorbent loading for no heat recovery and 85% heat recovery as the bed outlet pressure is changed to 2 bar. Table 7.7 provides a comparison between the no heat recovery and 85% heat recovery cases, both at a pressure of 2 bar.

Table 7.8 compares the number of reactors. As expected, the number of adsorbers required to process the flue gas decreases for the higher-pressure cases. When compared to the previous optimal moving bed case, the total amortized capital costs also decrease for the high-pressure cases even when considering the capital cost of the compressors needed to pressurize the flue gas. However, the electricity required by the compressors marginally increases the total EAOC when compared to the previous best case. It should be noted that 2 bar was chosen to investigate the potential of increased adsorber pressures and that further investigation of intermediate pressures may result in decreased EAOC values.

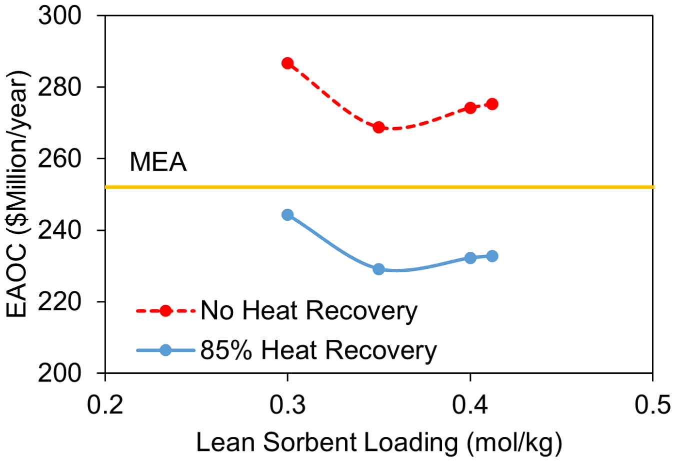

Figure 7.14: Moving bed EAOC versus lean sorbent loading for high pressure adsorber scenarios at 25°C lean sorbent temperature.

Table 7.7: EAOC ($Million/year) breakdown for optimal high-pressure cases with different heat recoveries.

	No Heat Recovery	**85% Heat Recovery**
Amortized Capital	**73.6**	**73.6**
Reactor	55.0	55.0
Compressor	18.6	18.6
Yearly Operating Costs	**204.8**	**157.0**
Steam	173.0	125.2
Electricity	28.8	28.8
Cooling Water	3.0	3.0
EAOC	**278.4**	**230.6**

Table 7.8: Reactor breakdown for the best moving bed cases with different adsorber pressures

	1 bar	**2 bar**
Number of Adsorbers	47	26
Number of Desorbers	7	7
Total Number of Reactors	**54**	**33**

Particle Cost Uncertainty: In the economic studies completed for the moving bed process in this section, the cost of the MOF particles is ignored due to lack of accurate costing information. Similar to the study performed for the fixed bed process in Section 7.1.2, discrete values of 6, 15, and 30 dollars per kilogram are used in the sensitivity study based on the results of the literature review described in that section. Figure 7.15 shows the results of the particle cost sensitivity study for the moving bed process. The base case ($0/kg) corresponds to the moving bed process with an inlet sorbent temperature of 25 °C and 85% heat recovery. When a particle cost is considered similar to that of a traditional solid sorbent ($6/kg), economics increase by a modest $18 million/year and still are an improvement over a traditional MEA system. At the upper end of the feasible range considered for this study ($30/kg), the economics increase by $92 million/year.

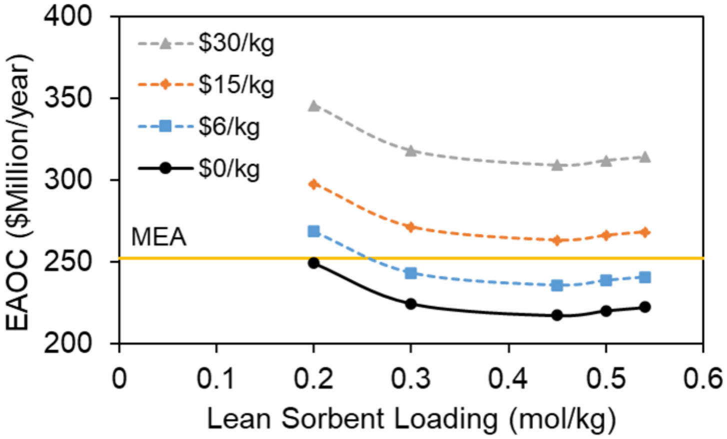

Figure 7.15: Effect of MOF particle cost uncertainty on moving bed process economics

7.1.3.2. Moving Bed Analysis Results: Version 2

In this section, **Version 2** of the moving bed model, which uses the **chemistry-based** isotherm model to predict the adsorption equilibrium, is used to expand upon the sensitivity analyses performed in the preceding section. Here, techno-economic optimization of the moving bed process is performed using derivative free optimization (DFO) algorithms available as part of the FOQUS toolset [58]. In addition to the costing components described in the preceding cost model, three components are included in this section which include the capital cost of the distributors, capital cost of the cross heat exchanger, and the power required to circulate the solids using bucket elevators. The equations for these components along with the costing constants are taken from Kotamreddy [113] and are given in Eqs. (7.3)-(7.5).

$$A_{CEX} = \frac{Q_{CEX}}{U_{CEX}\Delta T_{LM}} \tag{7.3}$$

$$Cost_{dist} = 125(\pi/4)(3.281 * D_b)^2 \tag{7.4}$$

$$P_{BE} = 6.88e^{-4} * \dot{V}_{BE} * (3.28 * D_H + 10) * DSF \tag{7.5}$$

Here, the capital cost of the cross exchanger is determined by its required heat transfer area (A_{CEX}). The cross exchanger is not rigorously simulated, and the heat transfer area is estimated using Eq. (7.3) which is then used to cost the exchanger using the same method as the moving bed reactors. The cost of a distributor for a single reactor is shown in Eq. (7.4) and calculated based on the diameter of the reactor. The power required by the bucket elevators (P_{BE}) is calculated using Eq. (7.5). The power is given in kW and is a function of the solids volumetric flowrate in m^3/hr, the discharge height in meters, and the drive safety factor (DSF) which varies depending on the class of the drive and is taken at the upper bound of 2 in this work. Additionally, the costing values for compression of the inlet flue gas are made suitable for optimization by use of a surrogate model to allow for continuous prediction of the compression work and blower equipment costs as a function of the required inlet pressure of the moving bed. These surrogate models along with their fit to the data obtained from Aspen Plus and APEA can be found in the Appendix (see Figure A.9 and Figure A.10).

Techno-economic Optimization:

$$\begin{aligned} &\min_{x} \; f(x) = EAOC \\ &s.t. \\ &h(x) = 0 \\ &g(x) \leq 0 \\ &x^L \leq x \leq x^U \end{aligned} \tag{7.6}$$

The moving bed techno-economic optimization problem is shown in Eq. (7.6). The goal of the optimization problem is to minimize our economic objective function, $EAOC$, by optimizing the set of decision variables, denoted as x, which include design variables and operating conditions of the moving bed capture process. The optimization problem is subject to equality and inequality constraints, denoted as $h(x)$ and $g(x)$, respectively. Here, the equality constraints consist of the rigorous, first-principles model equations of the moving bed process. The optimization problem is solved with the use of the FOQUS toolset [58] which has the capability to connect modeling platforms to numerous mathematical tools, including derivative free optimization algorithms. At each iteration of the DFO algorithm, the FOQUS toolset will input the decision variables to the moving bed process model in ACM, run the model, and collect the results needed to calculate the economic objective function. This is a feasible path approach where the equality constraints of the optimization problem are satisfied at every iteration. In this work, the BOBYQA algorithm [114] is used to solve the optimization problem. Since derivative free algorithms are not able to guarantee global optimality, multi-start methods were used to help in avoiding local minima and improve confidence that the optimal is found.

Eqs. (7.7)-(7.11) show design constraints and inequality constraints implemented in the moving bed optimization problem. The lean solids flow rate to the adsorber is calculated to achieve 90% capture of the CO_2 in flue gas feed, as shown in Eq. (7.7). The desorber solids inlet temperature is calculated based on the temperature approach design constraint shown in Eq. (7.8). Additionally, no trim heaters or coolers are considered, and the adsorber solids inlet temperature is calculated by solving the energy balance around the cross exchanger. For both the adsorber and desorber, the maximum gas velocity is constrained to be less than or equal to 85% of the minimum fluidization velocity as shown in Eqs. (7.9)-(7.10). As the velocity is calculated at every axial position, this constraint is ensured along the entire length of the reactor. Lastly, the purity of the regenerated CO_2 stream leaving the top of the desorber was constrained to be greater than 95%.

$$CO_2\ Capture = 90\% \tag{7.7}$$

Cross Exchanger Temperature Approach = 10 °C (7.8)

$$v_{g,ads} \leq 0.85 * u_{mf,ads} \tag{7.9}$$

$$v_{g,des} \leq 0.85 * u_{mf,des} \tag{7.10}$$

CO_2 Product Purity (mole basis) ≥ 95% (7.11)

As mentioned in previous sections of this work, the cost to produce MOF particles on an industrial scale is still not well known and therefore multiple optimization runs are carried out for different values of MOF price and particle lifespan. MOF prices of 0.5, 15, and 30 $/kg are used based on the literature review performed in earlier sections of this Chapter. For particle lifespan, values of 0.5 and 2 years are used. There is little data available to support this assumption for lifespan range, but this is similar to values used in a solid sorbent direct air capture report published by NETL [115]. Typical particle deactivation in fixed bed systems is due to negative reaction with contaminants in the flue gas but moving bed systems are subject to additional attrition due to the circulation of the solids which can reduce the lifespan of the particles even further. In all, 6 optimization cases are carried out with differing combinations of MOF price and lifespan which are shown in Table 7.9.

Table 7.9: MOF price and particle lifespan for moving bed optimization cases

	MOF Price [$/kg]	Particle Lifespan [years]
Case 1	0.5	0.5
Case 2	15	0.5
Case 3	30	0.5
Case 4	0.5	2
Case 5	15	2
Case 6	30	2

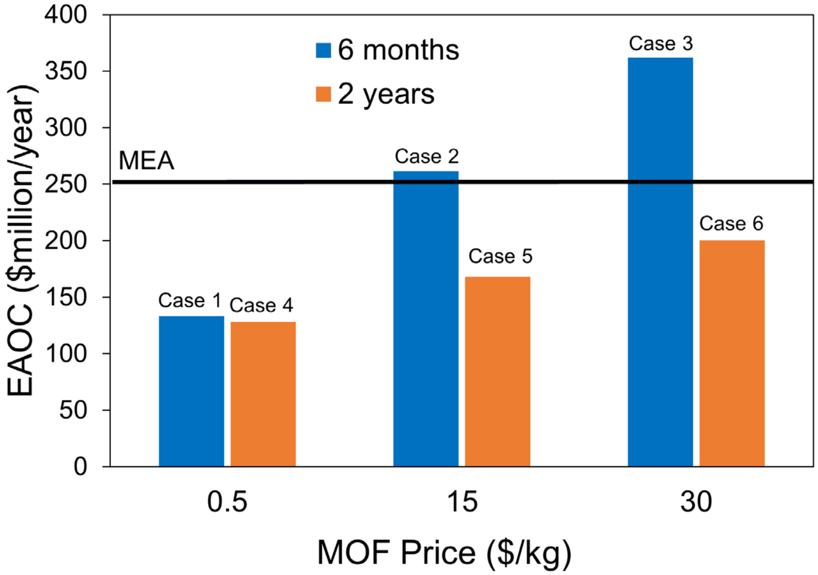

Figure 7.16: Moving bed optimization results for varying MOF price and lifespan

Figure 7.16 shows the results for the optimal EAOC of the moving bed process for varying combinations MOF price and particle lifespan. Case 4 is shown to have the lowest EAOC (128 $million/year) of the cases studied here and shows a 49% improvement over the MEA process. Two cases show economics higher than the MEA process, Case 2 and Case 3. Case 2 is only slightly higher while Case 3 shows an EAOC of 362 $million/year which is 44% higher than the MEA baseline. It is strongly believed that Case 3, where the MOF price is $30/kg and life span is just 6 months, is very unlikely and is considered to be an extreme case. Table 7.10 shows the results of the moving bed optimization problem for all 6 cases. It gives the design and operating variables that were considered as decision variables, their optimized value, and their lower and upper bounds. Table 7.11 shows the costing breakdown for all cases.

Table 7.10: Moving bed optimization results for each particle cost uncertainty case.

Decision Variable	Case 1	Case 2	Case 3	Case 4	Case 5	Case 6	Lower Bound	Upper Bound	Units
Adsorber Height	3.63	2.51	2.05	4.01	2.38	2.14	1	20	[m]
Adsorber Diameter	10.0	10.0	10.0	10.0	10.0	10.0	1	10	[m]
Adsorber Tube Pitch	0.082	0.065	0.052	0.086	0.059	0.054	0.035	0.5	[m]
Desorber Height	13.2	12.3	11.7	14.2	11.3	11.6	1	20	[m]
Desorber Diameter	10.0	10.0	10.0	10.0	10.0	10.0	1	10	[m]
Desorber Tube Pitch	0.114	0.084	0.061	0.122	0.073	0.065	0.035	0.5	[m]
Lean sorbent loading	0.388	0.513	0.553	0.369	0.540	0.518	0.025	1	[mol/kg]
Adsorber Outlet Pressure	1.010	1.010	1.012	1.010	1.010	1.012	1.01	2	[bar]
Flue Gas Flowrate	2122.6	1983.5	1826.5	2149.4	1934.5	1867.8	0	-	[kmol/hr]
Direct Steam Flowrate	97.6	110.1	107.4	97.5	133.0	106.2	0	-	[kmol/hr]

Table 7.11: Cost breakdown [$million/year] for each moving bed optimization case.

	Case 1	Case 2	Case 3	Case 4	Case 5	Case 6
Amortized Capital	**30.4**	**34.6**	**42.6**	**29.8**	**37.6**	**40.5**
Reactors	20.8	23.5	29.9	20.5	26.2	28.4
Blowers	0.931	0.931	0.931	0.931	0.931	0.931
Cross Exchanger	8.7	10.2	11.7	8.4	10.5	11.1
Yearly Operating Costs	**102.8**	**226.9**	**319.4**	**98.6**	**130.5**	**159.8**
Steam	93.8	96.1	97.8	93.5	96.1	96.7
Electricity	2.97	2.53	2.38	3.12	2.44	2.41
Cooling Water	0.275	0.278	0.283	0.276	0.276	0.281
Sorbent	5.79	128.0	219.0	1.70	31.7	60.4
EAOC	**133.3**	**261.5**	**362.0**	**128.4**	**168.1**	**200.3**

Moving Bed Profiles:

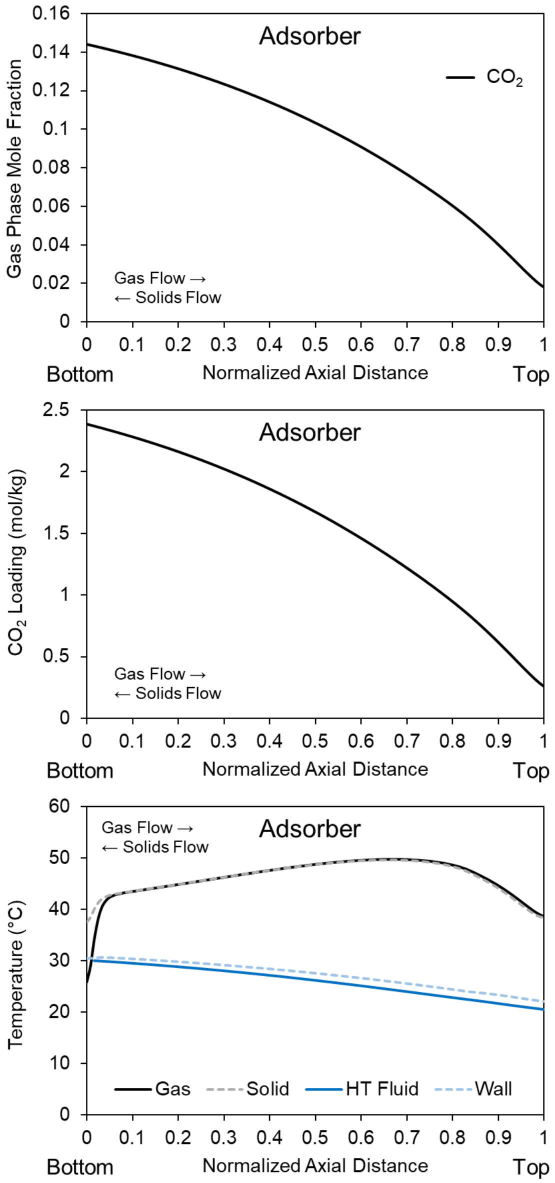

Figure 7.17: Adsorber Moving Bed Profile Plots. Top) Gas phase CO2 mole fraction. Middle) Solids phase CO2 loading. Bottom) Temperature profiles for gas phase, solid phase, heat transfer fluid, and tube wall. X axis is normalized axial distance along the reactor with 0 being the bottom of the moving bed and 1 being the top.

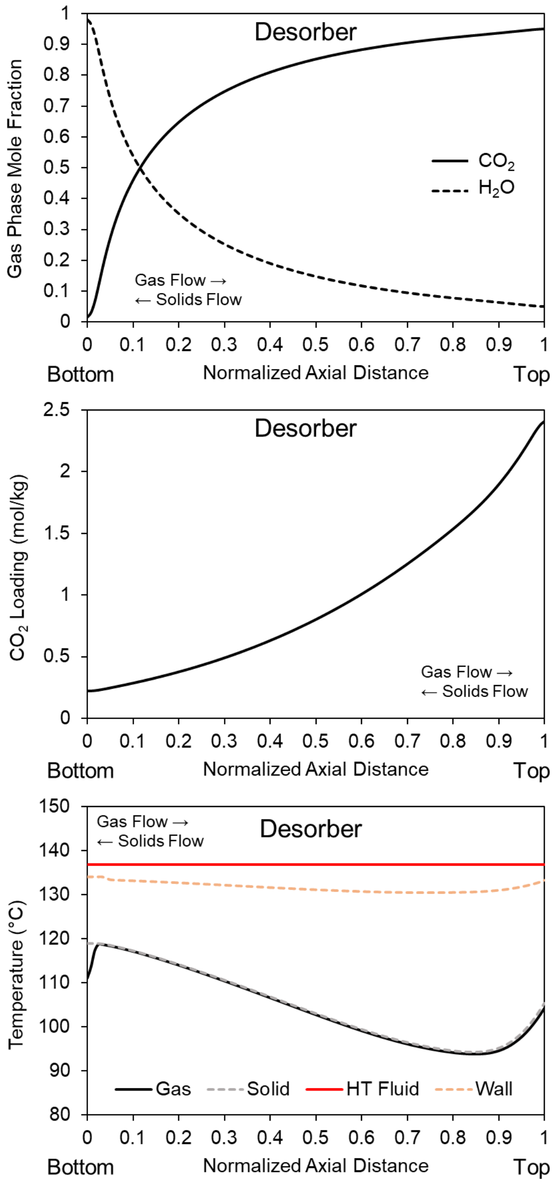

Figure 7.18: Desorber Moving Bed Profile Plots. Top) Gas phase CO2 mole fraction. Middle) Solids phase CO2 loading. Bottom) Temperature profiles for gas phase, solid phase, heat transfer fluid, and tube wall.

Figure 7.17 shows the axial profiles for important process variables which includes gas phase composition, solids loading, and temperature. Flue gas enters the bed at a CO_2 composition of 14.6% and the mole fraction of CO_2 steadily decreases as the gas travels upwards through the bed and CO_2 is captured. Similarly, the solids loading of CO_2 monotonically increases as it travels downward through the bed and captures CO_2. Figure 7.17 also shows the axial profile of the cooling water as it flows co-currently with the solids, downward through the embedded heat exchanger, and increases in temperature as it removes heat from the bed. Solids temperature increases near the top of the bed as fresh, lean sorbent begins to quickly adsorb CO_2 and generate heat but remains somewhat constant in the remainder of the bed as the embedded exchanger and the cooling water are able to effectively remove the heat generated from adsorption. Additionally, since the dominating heat transfer occurs between the solid phase and the tube wall, gas phase temperature quickly approaches the solid phase temperature and the two are nearly the same throughout the length of the bed.

Similarly, Figure 7.18 shows the same axial profiles for the moving bed desorber. For the desorber, pure steam is fed to the bottom of the bed to aid in mass transfer by reducing the partial pressure of CO_2. However, the gas phase composition profile in Figure 7.18 shows that the desorbed CO_2 quickly becomes the primary species in the gas phase and the composition at the top of the desorber is 95% CO_2, which was included as a constraint in the techno-economic optimization problem. Figure 7.18 shows the solids CO_2 loading profile and how the loading decreases as the solids flow downwards through the bed and CO_2 is desorbed. Almost inversely to the behavior seen in the adsorber, the solids temperature decreases at the top of the desorber due to the heat consumed to regenerate the solids and then slowly increases in the rest of the bed as the steam and embedded heat exchanger is able to effectively supply heat to the bed.

Capital Cost Uncertainty Analysis: Similar to studies completed in previous sections, a sensitivity study for the effect of capital cost uncertainty on overall process economics is performed. Here, a factor of -50% up to +50% is used to evaluate the effect on process economics with results shown in Figure 7.19. Overall, the change is relatively small for each case with the largest change occurring for Case 4 which shows a change of 7% when this capital cost uncertainty is considered.

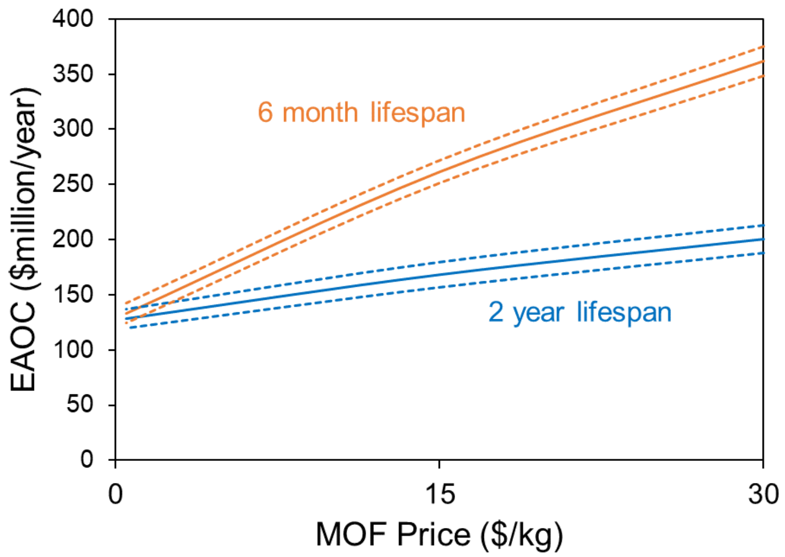

Figure 7.19: Capital cost uncertainty analysis for optimal Version 2 moving bed cases. Dashed lines represent a +/- 50% change in capital costs

Comparison to Fixed Bed Process: In this section, the moving bed economics are compared to the fixed bed process presented earlier in this work. Table 7.12 shows a comparison of the results for that study to the optimized moving bed TSA process in this work. When the same lifespan and price is considered, the moving bed process significantly outperforms the fixed bed process. Even when a lifespan of 6 months is considered, the moving bed process shows lower economics when compared to the fixed bed process with equivalent MOF prices. It should be noted that one of the areas investigated in the fixed bed study is the extent of heat recovery and how it will affect process economics. Table 7.12 only shows results for what was deemed a practical heat recovery, but a detailed design of the heat recovery process may yield an improvement to the economics. Additionally, the economics for the fixed bed process are investigated using single variable sensitivity studies and if rigorous optimization of the process is performed the economics can improve.

Table 7.12: EAOC values for varying MOF capture processes, lifespans, and prices.

dmpn-Mg_2(dobpdc) Capture Process	MOF Lifespan	MOF Price ($/kg)	EAOC ($million/year)
Fixed Bed TSA, Practical Heat Recovery	2 years	0	251
		15	341.6
		30	427
Moving Bed TSA	2 years	0.5	128.4
		15	168.1
		30	200.3
Moving Bed TSA	6 months	0.5	133.3
		15	261.5
		30	362

7.1.3.3. Conclusions

The moving bed contactor model developed earlier in this work is scaled up to simulate CO_2 capture from an industrial scale coal fired power plant. The capture process uses a moving bed contactor for both the adsorber and regenerator with cooling water used in the adsorber to remove the heat generated during adsorption and condensing steam in the regenerator to supply the heat needed for desorption. In Version 1 of the model, which uses the Sips isotherm model to predict adsorption equilibrium, sensitivity studies are performed to investigate the effect of lean loading and adsorption temperature on the overall process economics. For the base case, the EAOC is similar to that of the modified fixed bed process and nearly 8% higher than the MEA baseline. When heat recovery is considered, the economics are about 14% lower than the MEA baseline. When a +/-50% uncertainty in the capital costs is considered, the EAOC ranges from a value higher than the MEA baseline to nearly 30% lower. An uncertainty analysis for the price of the MOF particle is also performed with a range of values taken from a literature review. At the upper end of the MOF price, the EAOC increases by 43% and is higher than the MEA baseline.

Rigorous optimization of the moving bed process is performed using a second version of the model which uses the chemistry-based model developed in this work to predict the adsorption equilibrium. The goal of the optimization problem is to minimize the EAOC while satisfying the moving bed process model equations and satisfying additional design constraints. In total, 6 cases are optimized for different values of MOF price and particle lifespan. The optimization results in a moving bed process with economics that are nearly 49% lower than the MEA baseline process when a MOF price of 0.5 $/kg and lifespan of 2 years is considered. At the higher end of the uncertainty range, the economics increase to 362 $million/year which is 44% higher than the MEA baseline process. It is believed that the extreme values considered in the uncertainty analysis especially where cost of MOF is $30/kg with a life span of 6 months is unlikely. With considerable advances being made in the manufacturing of the functionalized MOF sorbents and with large scale utilization of these materials, MOF particle lifespan is expected to go up and cost is expected to go down. If we consider the cost of MOF to be $15/kg and life span of 2 years (i.e., Case 5), which is the most likely scenario in the near future, EAOC offered by the diamine-appended MOF is about 33% lower than MEA. A +/-50% uncertainty in the capital costs is also considered for the optimized cases which shows only a small change from the nominal values for each process, a maximum of 7%.

The studies completed in this work provide insight into the possible improvement in process economics that a moving bed process can provide when compared to a traditional solvent process and even other type of sorbent contactors for sorbent-based processes. Future work should focus on better understanding some of the areas of uncertainty that were investigated in this work, specifically the price of the MOF sorbent and lifespan of the particle as they have been shown to have a significant effect on the process economics. Additionally, the increased attrition of the moving bed process due to the circulation of the particles can decrease particle lifespan below the range which is even considered here. The gas velocity constraint required to keep the process in the moving bed regime results in a large number of adsorbers needed to process the flue gas due to the low volumetric flow rate to a single bed. An area of future would be investigating hybrid systems which use a moving bed contactor for regeneration and another type of solid contactor for adsorption, such as a fluidized bed.

7.2. Analysis of Mg_2(dobpdc)(3-4-3) for NGCC-based Capture

Techno-economic optimization and analysis of a fixed bed TSA process for NGCC-based capture utilizing Mg_2(dobpdc)(3-4-3) are presented in this section. The fixed bed contactor model uses the **extended weighted Langmuir** isotherm model to predict the adsorption equilibrium.

7.2.1. Cost Model

The cost modeling approach is similar to that for dmpn-Mg_2(dobpdc). The main equipment considered in the costing model are the reactors, blowers, and condensers as they are assumed to be the dominating costs in the process. Equipment costing methodology for these three equipment types have been described in the previous sections of this work (for reactors see Eq. (7.1), for blowers see Figure A.9, for condensers see Eq. (7.3)). However, the model used in this section differs from the previous model as it is developed to closely follow the quality guidelines for costing energy systems developed by NETL [116]. The annualized capital cost is calculated using the equations below.

$$BMC = F_{BM} * \frac{CEPCI_{2019}}{CEPCI_{2013}} * C_E \tag{7.12}$$

$$TPC = TBMC + engineering\ fee + process/project\ contingencies = 1.5 * TBMC \tag{7.13}$$

$$TOC\ = TPC + Owner's\ cost = 1.22 * TPC \tag{7.14}$$

$$TASC = TOC\ * 1.093 \tag{7.15}$$

$$Annualized\ Cost\ = 0.0707\ * TASC \tag{7.16}$$

Here, BMC is the bare module cost of the equipment in which the equipment cost is multiplied by a factor to account for additional expenses such as labor, installation, overhead, and transportation. F_{BM} is the bare module factor (=3.29) taken from Turton *et al*. [106]. APEA cost estimates are generated using 2013 $ so a factor is also included bring these costs into a more recent time index. TPC corresponds to the total plant cost and is calculated considering the total bare module cost (TBMC), engineering fees, project contingencies, and process contingencies. In this work, the engineering fees and contingencies are assumed to be 50% of the TBMC. This value is at the higher range of values recommended by the NETL costing methodology but is in line for processes utilizing new concepts with limited data. TOC is the total overnight cost which is the sum of the TPC and owner's cost. The owner's cost percentage is technology specific and is assumed to be 22% in this work. Finally, the total as spent cost (TASC) and annualized cost are calculated by multiplying by factors which are based on economic assumptions recommended by NETL.

The fixed O&M costs, which included things such as labor costs from multiple sources, property taxes, and insurance. The calculations for these costs are shown in Eqs. (7.17)-(7.20).

$$Annual\ Operating\ Labor = 8 * 38.50 * 8760\ \ * (1 + 0.3) \tag{7.17}$$

$$Maintenance\ Labor = 0.4 * 0.019 * TPC \tag{7.18}$$

$$Administration\ \&\ Support\ Labor = 0.25 * (Annual\ Op.\ Labor + Maint.\ Labor) \tag{7.19}$$

$$Property\ Taxes\ \&\ Insurance = 0.02 * TPC \tag{7.20}$$

The variable O&M costs will have a large impact on the overall cost since they include the price of the operating utilities such as steam and auxiliary power. The main utilities considered in this process are auxiliary power for the blowers, cooling water from embedded heat exchangers and condenser, and steam for the embedded heat exchanger and the direct contact steam during desorption. The utility costs are calculated by obtaining the duties from the process simulations and multiplying by the prices in Table 7.13. It should be noted that these utility prices are the same as used in the previous costing model except for the steam price which is taken from an updated textbook source. The sorbent price and lifespan have been discussed in previous sections and a baseline of 0.5 \$/kg and 0.5 years are taken as the baseline values for MOF price and MOF lifespan. The maintenance material cost is also considered and is calculated using Eq. (X).

$$Maintenance\ Material\ Cost = TPC * 0.6 * 0.019/0.85 * Capacity\ Factor \tag{7.21}$$

Table 7.13: Utility prices used in Mg_2(dobpdc)(3-4-3) costing model

Utility	Price	Source
Auxiliary Power	0.06 [$/kWh]	Turton *et. al*. [106]
Cooling Water	0.354 [$/GJ]	Turton *et. al*. [106]
Steam	7.33 [$/1000kg]	Seider *et. al.* [117]
Sorbent Price	0.5 [$/kg]	Susarla *et. al.* [118]
Sorbent Lifespan	0.5 [years]	NETL Report [115]

Finally, the total annualized cost is calculated by summing the annualized capital cost, fixed O&M costs, and variable O&M costs.

$$Total\ Annualized\ Cost\ = Annualized\ Capital\ Cost + Fixed\ O\&M + Variable\ O\&M \tag{7.22}$$

7.2.2. Fixed Bed TSA Process

The fixed bed model developed in this work is then scaled up to simulate a commercial scale TSA cycle from a NGCC flue gas source. Flue gas conditions are taken from Case B31B of the NETL baseline study for fossil fuel energy plants [119]. The cycle consists of three main steps and is shown in Figure 7.20. The first step in the cycle is ramping the flue gas flow from no flow to its full design flow rate and passing cooling water to the embedded exchanger. This step allows the bed to cool from the desorption temperature to adsorption conditions before taking on the full flue gas load. Other TSA cycles achieve this cooling in a separate step, but this can add significant time to the overall cycle time which will increase the total number of beds in the process and therefore increase the capital costs. The second step is adsorption under the full flue gas design flow rate. The length of this step can be defined in many ways, such as a fixed time value or event-driven where the step will continue until a certain criterion is met. In this work, the adsorption step proceeds until a design value for the averaged CO_2 loading is met. Once this loading criterion is met, the heating/desorption step begins. In this step, heating water is introduced to the embedded heat exchanger to supply the heat needed to regenerate the MOF. It should be noted that the use of steam in this step would require an additional step to fully remove the cooling water from the exchanger to avoid any mechanical issues which would add to the total cycle time and therefore the capital costs of the system. The design of cooling water/heating water versus steam and no cooling during adsorption was investigated in earlier sections of this work and was shown to drastically increase performance and economics of the process. Therefore, a similar configuration is used here. Steam is also introduced directly to the bed during desorption, referred to as direct steam. The purpose of this steam is not to supply the heat needed for desorption but to lower the partial pressure of CO_2 in the bed to improve the mass transfer driving force. Similar to the adsorption step, the desorption step continues until the CO_2 loading in the bed reaches a design value. This cycle is repeated several times until the difference between the loading and temperature profiles for successive cycles are below a convergence value, achieving a cyclic stead state (CSS). The results presented in this work are CSS results.

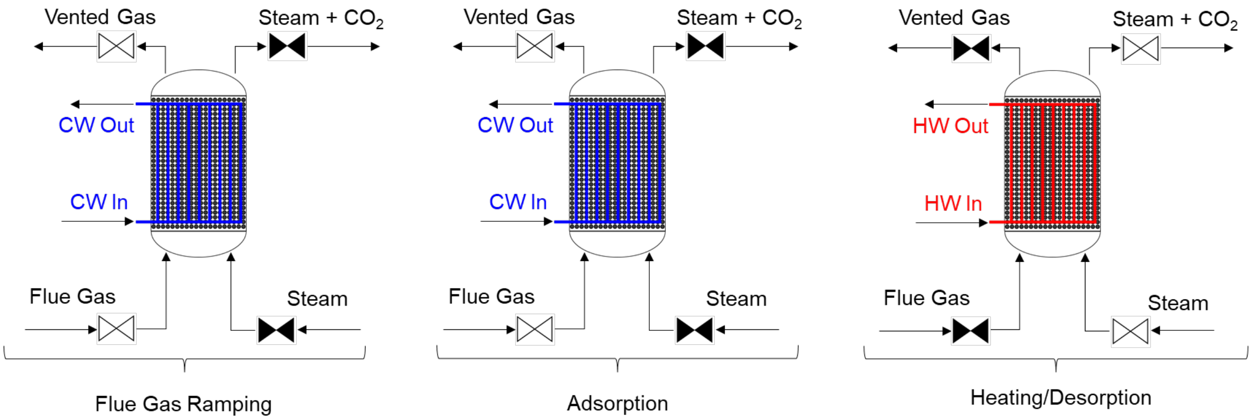

Figure 7.20: Configuration and steps of the TSA process for the Mg_2(dobpdc)(3-4-3)

In this process, a sufficient number of beds are present and organized in a parallel configuration in order to continuously process the flue gas. Adsorption and desorption are occurring simultaneously, and the total number of beds required is calculated by solving a scheduling problem.

A simplified TSA process diagram is shown in Figure 7.21. The flue gas is available at ambient pressure and blowers are used to increase the flue gas to a sufficient pressure to overcome the pressure drop in the bed. Additionally, the pressurization of the inlet flue gas is not rigorously simulated, and a surrogate model is used to calculate the required compression work based on the inlet flue gas pressure (see Figure A.10). To increase the purity of the regeneration product, a condenser is used. The condenser duty and composition of exit streams are evaluated by solving a flash problem using property calls available in Aspen Adsorption.

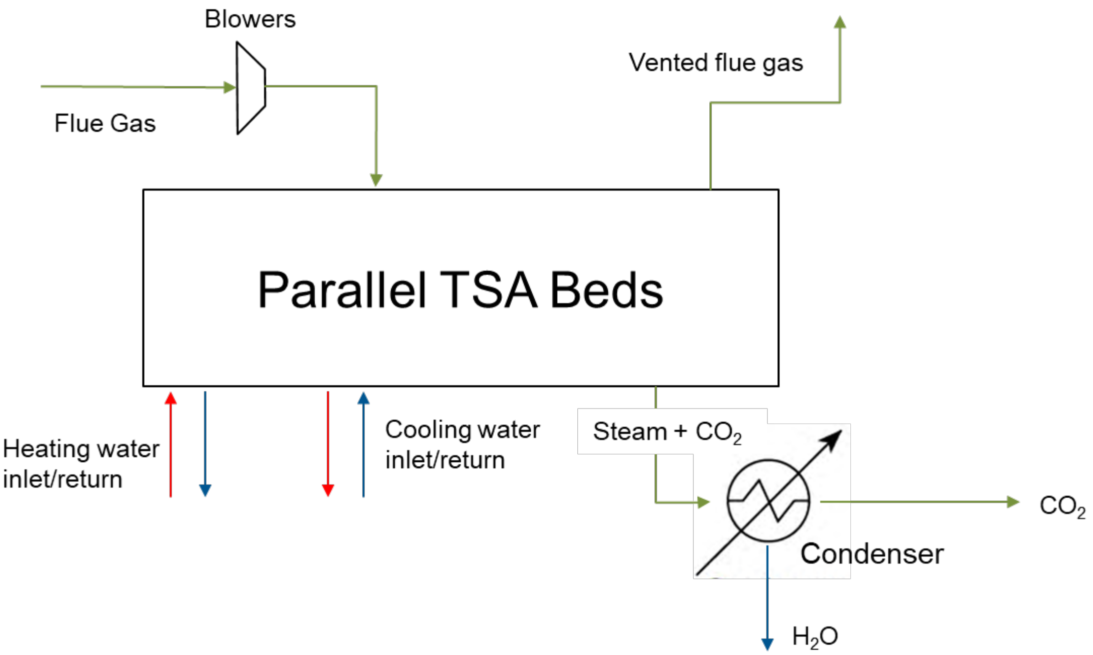

Figure 7.21: Simplified diagram of the Mg_2(dobpdc)(3-4-3) TSA capture process.

7.2.2.1. Optimization Framework. Fixed bed cycle simulations present an interesting optimization challenge due to the inherently dynamic nature of these processes. There are several ways that this problem has been addressed, each with their own advantages and disadvantages. One way is to discretize the model in the time domain and solve in an equation-oriented framework. This results in an extremely large model which can take significant time and effort to develop and obtain convergence. Similarly, the discretization in the spatial domain can be eliminated to obtain 0-D models which are discretized in the time domain and can then be solved in an equation-oriented framework [120]. These models will be drastically reduced in size, but at the sacrifice of accuracy. In this work, the fixed bed cycle model is connected to derivative free optimizers in FOQUS [58]. Microsoft excel is also used to perform the cost calculations and aid in the transfer of information between FOQUS and Aspen Adsorption. A simple diagram of the optimization framework is shown in Figure 7.22 and the fixed bed optimization problem formulation is shown in Eq. (7.23).

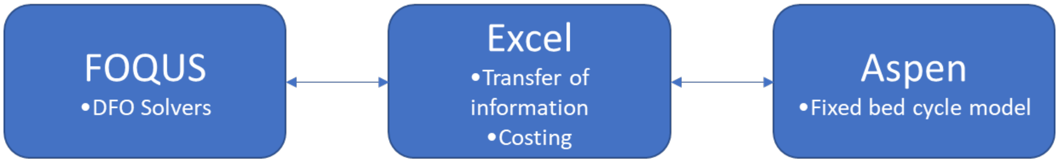

Figure 7.22: Simplified diagram for $Mg_2(dobpdc)(3\text{-}4\text{-}3)$ optimization framework

$$
\begin{aligned}
&\min_{x} \quad f(x) = Total\ Annualized\ Cost\ (\$MM/y) \\
&s.t. \\
&h(x) = 0 \\
&g(x) \leq 0 \\
&x^L \leq x \leq x^U
\end{aligned}
\tag{7.23}
$$

Here, the goal of the optimization problem is to minimize our objective function which is the total annualized cost of the process using the decision variables, denoted by x, while being subjected to the listed constraints. $h(x)$ are the equality constraints which consist of the fixed bed modeling equations (mass transfer, heat transfer, etc.). $g(x)$ are the inequality constraints and the decision variables are contained between an upper and lower bound. In this work, the CO_2 capture is constrained to be >=90%.

7.2.2.2. Results. The results of the fixed bed optimization problem are presented in Table 7.14, Table 7.15, and Figure 7.23. Table 7.14 presents the optimized value for the decision variables considered in the optimization problem. Decision variables for the fixed bed optimization problem include the lean loading target and working capacity which set the CO_2 loading at the end of the desorption and adsorption step, and significantly affect the time for each of these steps. The time for the flue gas ramping step is also included. The flue gas flow during adsorption and steam flow during desorption are also included as decision variables. The flue gas flow directly determines the number of adsorption beds that are required to continuously process the total amount of flue gas from the NGCC plant. Increasing this flow can reduce the total number of beds but will increase the velocity in the bed and therefore increase the pressure drop and the work required by the inlet blowers. Inversely, a small flow can reduce the pressure drop across the bed but will require more adsorption beds and increase the capital costs of the system. The steam flow corresponds to the direct steam injected into the bed during desorption which is designed to keep the partial pressure of CO_2 low to improve driving forces during desorption. A large steam flow will increase the operating costs but improve mass transfer and decrease the time it takes to regenerate the solvent, decreasing the number of beds and capital costs. The reactor dimensions (tube pitch, height, and diameter) are also included as decision variables. Since adsorption equilibrium data only exists for temperatures from 90 °C to 120 °C, the adsorption and regeneration step temperatures are fixed at these two values to avoid simulation outside of the temperature ranges for which data is available. That is, the temperature of the flue gas and cooling water are 90 °C, and the heating water and direct steam temperatures are 120 °C.

The optimized values along with the bounds included in the optimization problem are shown in Table 7.14. It can be observed that the fixed bed diameter is at its upper bound due to larger diameters allowing for a larger amount of flue gas to be processed. An upper diameter of 10 meters is considered as fabrication and on-road transportation of cylindrical vessels larger than this can be difficult, if not impractical.

Table 7.14: Mg_2(dobpdc)(3-4-3) fixed bed TSA optimization results: Decision Variables

Decision Variable	Units	Initial Value	Optimized Value	Lower Bound	Upper Bound
Lean loading target	[mol/kg]	0.226	0.249	0.05	1
Working capacity	[mol/kg]	2.5	2.43	1	3.1
Flue gas ramp time	[min]	146.7	19.88	15	600
Tube pitch	[m]	0.0426	0.0478	0.035	0.15
Flue gas flow	[kmol/s]	0.774	0.925	0.1	1.2
Steam Flow	[kmol/s]	0.306	0.567	0.05	1
Height	[m]	10	11.89	3	20
Diameter	[m]	10	9.95	3	10

Table 7.15 and Figure 7.23 shows the breakdown of the costing variables for the initial and optimized decision variables. It can be seen that the optimized case reduces the Total Annualized Cost from 421.5 to 363.3 $MM/y, a reduction of 14%. The largest reduction in costs occurs in the annualized capital costs, specifically the fixed bed columns. This also reduces the fixed O&M cost as it is related to the annualized capital cost. Two amine-based solvent systems are used for comparison in this work. The NETL baseline study [119] reports a value of 79.6 $/tonne, and Du *et. al.* [121] report a capture cost of 73.9 $/tonne for a state-of-the-art MEA system. When compared to these two systems, the tetraamine MOF cost of capture is 157% and 177% higher, respectively.

Table 7.15: Mg_2(dobpdc)(3-4-3) fixed bed TSA optimization results: Costing Variables

Costing Components	**Initial Value**	**Optimized Value**
Inlet flue gas blowers [$MM/y]	0.81	0.83
Columns [$MM/y]	150.0	96.1
Condenser [$MM/y]	1.8	2.0
Maintenance material [$MM/y]	18.4	12.0
Auxiliary power [$MM/y]	7.4	9.6
Cooling water [$MM/y]	15.6	17.4
Indirect steam [$MM/y]	22.5	19.8
Direct steam [$MM/y]	132.3	153.5
Sorbent makeup [$MM/y]	20.7	16.9
Total Capital, Fixed and Variable O&M costs		
Annualized capital cost [$MM/y]	152.5	98.9
Fixed O&M cost [$MM/y]	52.1	35.3
Variable O&M cost [$MM/y]	216.9	229.0
Key Metrics		
Capture [-]	0.9	0.9
Total annualized cost [$MM/y]	421.5	363.3
Cost of CO_2 capture [$/tonne CO_2]	234.6	205.5

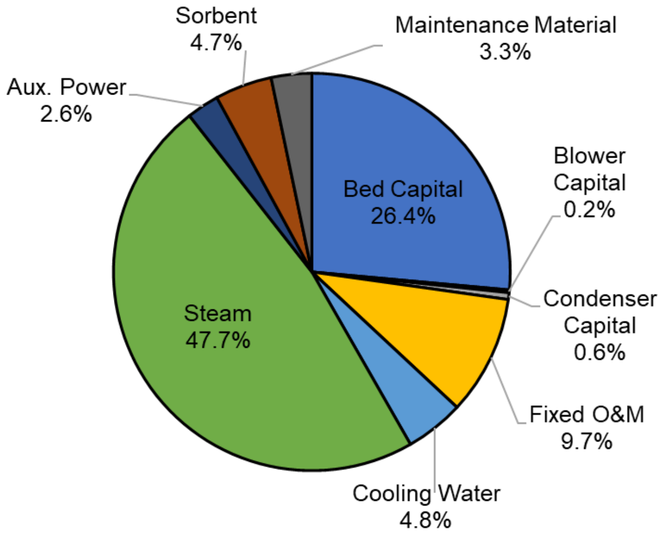

Figure 7.23: Mg_2(dobpdc)(3-4-3) fixed bed TSA optimization results: Costing Breakdown

7.2.2.3. Impact of Heat Recovery. TSA processes present many possible opportunities for heat integration and heat recovery due to the large amount of sensible heat that remains in the bed at the end of desorption. The TSA process in this work also contains additional opportunities for heat recovery due to the regeneration stream of steam and CO_2. Results for a sensitivity study which investigates the possible improvement in process economics due to heat recovery is presented in Figure 7.24. The cost for each case is calculated by reducing the steam OPEX by the heat recovery fraction. The extent of heat recovery that is feasible depends on the type of system. Aqueous solvent systems can typically reach recoveries of 85% and it has been shown earlier in this work that a feasible value for fixed bed systems is around 35%. At a 35% heat recovery, the tetraamine MOF cost of capture is 175.9 \$/tonne which is around 130% higher than the amine-based solvent processes.

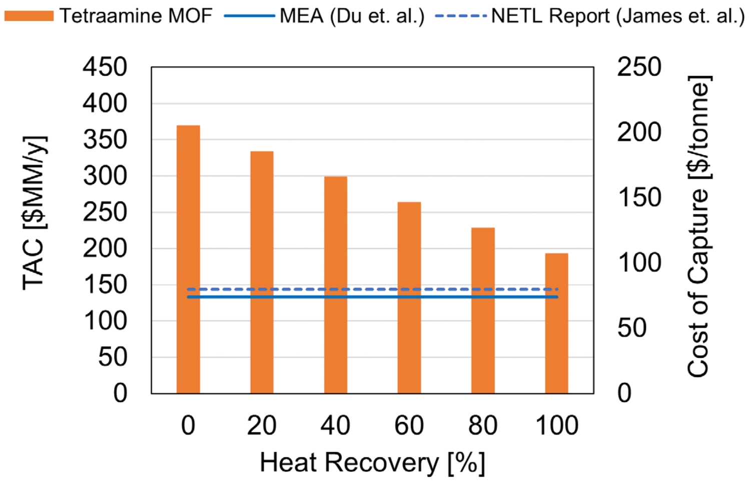

Figure 7.24: Impact of heat recovery for Mg_2(dobpdc)(3-4-3) TSA Process. MEA value taken from Du *et. al.* [121] and NETL report value taken from James *et. al.* [119].

7.2.2.4. Sensitivity to MOF Price. Figure 7.25 presents a sensitivity analysis of the MOF cost to evaluate its impact on the total annualized cost and cost of capture. The lack of knowledge for the price of amine-appended MOFs has been discussed extensively in previous sections of this work and this sensitivity study uses values for MOF prices which have also been used in previous sections. The MOF price varies from the baseline value of 0.5 \$/kg up to 30 \$/kg and the results show that the total process economics are extremely sensitive to the price of the MOF. It should be noted that the results presented in Figure 7.25 correspond to the operating conditions and contactor size for the optimized case which considers the baseline MOF price. Re-optimizing for each MOF price will only serve to lower the cost. For a MOF price of \$30/kg, the cost of CO_2 capture reaches nearly \$800/tonne which is roughly 10x larger than the amine-based solvent systems.

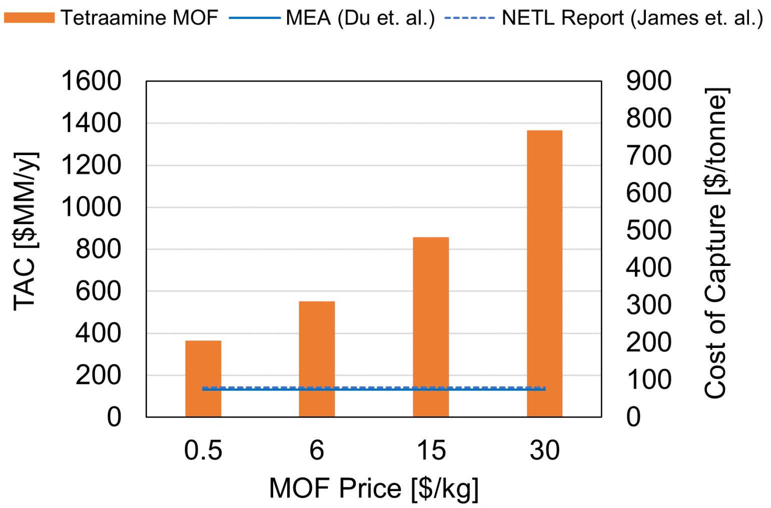

Figure 7.25: Sensitivity of Mg_2(dobpdc)(3-4-3) TSA economics to MOF price. MEA value taken from Du *et. al.* [121] and NETL report value taken from James *et. al.* [119].

7.2.2.5. High Temperature Regeneration Extrapolation. As previously stated, the regeneration temperature for the fixed bed TSA process is fixed at 120 °C since that is the highest temperature that data is available. However, the steam extracted from the NGCC system to supply heat to the TSA system is available at higher temperatures, and therefore the regeneration could be operated at this increased temperature with no increase in the price of the steam. Operation at higher temperatures will increase the driving force for mass transfer and reduce direct steam needed for regeneration which contributed to nearly half of the total annualized cost for the 120 °C regeneration process. The results in this section aim to investigate this possible reduction in costs when operating the regeneration step at 160 °C.

Table 7.16 shows the optimization results for the two fixed bed processes studied in this work. The most significant difference between the decision variables for both processes is the steam flow which decreases by nearly a factor of 2 for the higher temperature desorption process. The reduced adsorption capacity at 160 °C also results in a lower lean loading target determined during the optimization. The reactor configuration determined for the 160 °C regeneration also results in slightly smaller reactors which reduce the cost per column.

Table 7.16: High temperature optimization results for Mg_2(dobpdc)(3-4-3) TSA process: Decision Variables

Decision Variable	Units	120 °C Regeneration	160 °C Regeneration
Lean loading target	[mol/kg]	0.249	0.109
Working capacity	[mol/kg]	2.43	2.23
Flue gas ramp time	[min]	19.88	32.02
Tube pitch	[m]	0.0478	0.0497
Flue gas flow	[kmol/s]	0.925	1.056
Steam Flow	[kmol/s]	0.567	0.332
Height	[m]	11.89	10.52
Diameter	[m]	9.95	9.80

Table 7.17 gives a comparison of the costing variables for both fixed bed processes. As expected, the cost of CO_2 capture is almost cut in half and decreases to $109.4/tonne (-47%). Figure 7.26 gives the costing breakdown for the high temperature process. When examining the contributing costs, the largest decrease when comparing these two processes is the direct steam cost which is nearly 69% lower for the 160 °C regeneration process. The second largest decrease in costs is for the reactors which is nearly 35% lower for the 160 °C regeneration process. However, this higher temperature process is still 48% more expensive than the MEA process from Du *et. al.* [121] and 37% higher than the NETL Report [119].

Table 7.17: High temperature optimization results for Mg_2(dobpdc)(3-4-3) TSA process: Costing Variables

Costing Components	**120 °C Regeneration**	**160 °C Regeneration**
Inlet flue gas blowers [$MM/y]	0.83	0.83
Columns [$MM/y]	96.1	61.7
Condenser [$MM/y]	2.0	1.01
Maintenance material [$MM/y]	12.0	7.68
Auxiliary power [$MM/y]	9.6	10.2
Cooling water [$MM/y]	17.4	7.49
Indirect steam [$MM/y]	19.8	21.7
Direct steam [$MM/y]	153.5	47.6
Sorbent makeup [$MM/y]	16.9	10.5
Total Capital, Fixed and Variable O&M costs		
Annualized capital cost [$MM/y]	98.9	63.5
Fixed O&M cost [$MM/y]	35.3	24.3
Variable O&M cost [$MM/y]	229.0	105.3
Key Metrics		
Capture [-]	0.9	0.9
Total annualized cost [$MM/y]	363.3	193.1
Cost of CO_2 capture [$/tonne CO_2]	205.5	109.4

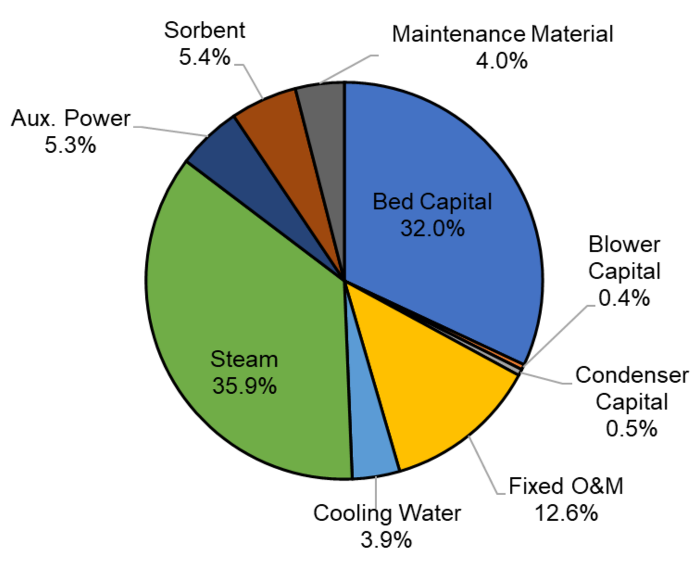

Figure 7.26: High temperature optimization results for Mg_2(dobpdc)(3-4-3) TSA process: Costing Breakdown

The sensitivity studies for heat recovery and MOF price were also performed for the high temperature regeneration process, and these results are shown in Figure 7.27 and Figure 7.28. Similar to the 120 °C process, a MOF price of \$30/kg, which is at the upper end of the range investigated in this work, increases the cost of CO_2 capture by over a factor of 4. When a practical heat recovery value of ~35% is considered, the cost of CO_2 capture is \$95.4/tonne which is 29% larger than the MEA system [121] and 20% larger than the NETL report [119].

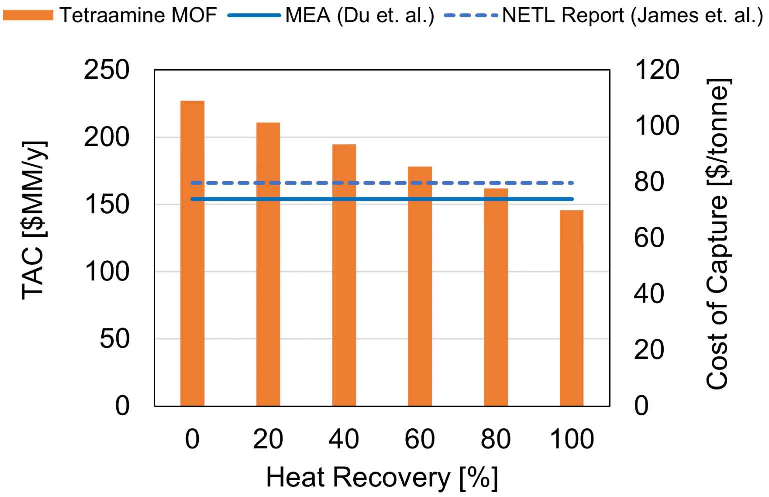

Figure 7.27: Heat recovery sensitivity for high temperature Mg_2(dobpdc)(3-4-3) TSA process. MEA value taken from Du *et. al.* [121] and NETL report value taken from James *et. al.* [119].

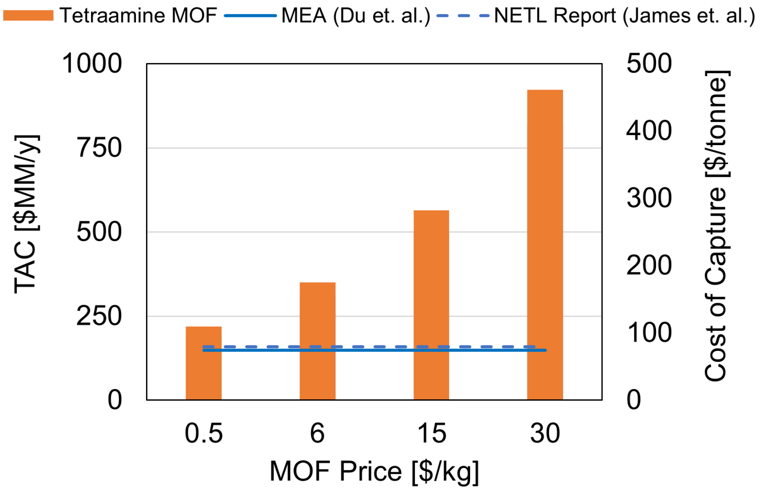

Figure 7.28: MOF price sensitivity for high temperature Mg_2(dobpdc)(3-4-3) TSA process. MEA value taken from Du *et. al.* [121] and NETL report value taken from James *et. al.* [119].

7.2.3. Conclusions

A fixed bed TSA process model is developed utilizing Mg_2(dobpdc)(3-4-3) to capture CO_2 from a NGCC flue gas source. Techno-economic optimization of the TSA process is then performed, and it is found that the cost of CO_2 capture for the optimized case is \$205/tonne which is ~177% larger than a state-of-the-art MEA capture process [121] and 157% higher than the amine-based solvent system reported in the NETL baseline study [119]. The possible reduction in costs due to heat recovery of the fixed bed process were also investigated, and when a practical heat recovery percentage of 35% is considered the tetraamine MOF process is nearly 130% higher than both of the amine-based solvent processes. Accurate costing of the MOF sorbent is still lacking in the open literature, so a sensitivity study was performed to investigate the change in process economics for a range of possible MOF prices. When a price at the upper range is considered, the economics for the fixed bed system increase to nearly 10x when compared to the amine-based processes. A second fixed bed process was also simulated in which the desorption step operates at 160 °C. This temperature is outside of the range of adsorption equilibrium data used to develop the models in this work, so these results should be viewed cautiously. For this higher temperature regeneration case, the cost of capture is still 48% and 37% more expensive than the MEA system and NETL report, respectively. When a practical heat recovery of ~35% is considered, the cost of capture for the higher regeneration temperature reduces to \$95.4/tonne, 29% and 20% higher than the MEA system and NETL report, respectively. Uncertainty analysis for the price of the MOF is again performed and it is found that the economics increase to around 6x when compared to the amine-based solvent systems.

The studies completed in this section show valuable insight into the behavior of Mg_2(dobpdc)(3-4-3) for NGCC based capture, but also show that a fixed bed TSA process may not be economically favorable. The direct injected steam usage in the TSA process is one of the dominating costs and future studies should focus on processes which can reduce this cost. Specifically, a vacuum assisted TSA process will lower the partial pressure of CO_2 along the length of the reactor and reduce the amount of steam needed to maintain high driving forces for mass transfer. The CAPEX and OPEX of the vacuum pump will need to be calculated to evaluate the tradeoff between these costs and the lower steam usage. Additional heat recovery designs such as recycling of the latent heat of the steam and CO_2 regeneration product have the potential to lower the cost of the system also. As mentioned for dmpn-Mg_2(dobpdc) studies, the contactor which will minimize the economics of the process is still not well agreed upon and should be an area of future work for Mg_2(dobpdc)(3-4-3) processes.

8. Final Remarks and Future Work

This work features investigation into two types of alternative post combustion CO_2 capture processes. The first is a traditional solvent capture process which uses chilled ammonia (CAP) as the working solvent which has been identified as a possible alternative to the current industry standard MEA. A detailed model of a novel CAP system was developed using a simultaneous regression methodology and was found to be more accurate in predicting pilot plant data than parameters found in literature. A limited number of pilot plant data was used in development and validation of the mass transfer model as very few publicly available sources of ammonia pilot plant exist. Additional data from multiple sources would serve to avoid any experimental error or bias from a single data source and improve the estimate of the mass transfer parameters. Still, the integrated mass transfer regression approach used here is an excellent tool for developing accurate process models while relying on data from multiple scales. Using the integrated mass transfer model, a novel CAP process model was developed which considered an NH_3 abatement section to reduce ammonia emissions to acceptable levels. The energetics of the process were found to be higher than that reported for MEA processes in the literature, but this analysis was done using design variables and operating conditions taken from multiple literature sources found using a variety of methods. Rigorous optimization of the novel CAP process would serve to lower the energetics and provide a better comparison to MEA. Additionally, a techno-economic analysis would need to be performed to evaluate the optimal water removal percentage of the water wash membrane to balance the capital and operating costs. Solids precipitation of the CAP process has also been reported and discussed thoroughly in the literature and should be investigated in any future work in this area.

The second alternative process that is a focus of this work is amine-appended metal organics frameworks, or simply referred to as MOFs. These amine-appended MOFs are a novel class of solid sorbents which have also been identified as a possible alternative to solvent-based capture processes. Specifically, the diamine-appended MOF dmpn-Mg_2(dobpdc) has been identified as a good candidate for post-combustion capture from coal-based flue gas sources and the tetramine-appended MOF Mg_2(dobpdc)(3-4-3) has been identified as a promising candidate for NGCC flue gas capture. Due to the novelty of these sorbents, mathematical modeling studies and simulations using these sorbents are very slim in the literature, and none exist that focus on dmpn-Mg_2(dobpdc) or Mg_2(dobpdc)(3-4-3). In this work, mathematical models for post-combustion capture using these amine-appended MOFs are developed. Three isotherm models are developed, all of which are heuristic in nature and do a good job at predicting the available isotherm data over the range of temperatures and partial pressures of CO_2 which are expected for post-combustion CO_2 capture process. A mass transfer model is also developed assuming a linear driving force with a mass transfer coefficient that incorporates adsorption reaction kinetics and particle diffusion kinetics. Parameter estimation for each respective MOF is performed, and this linear driving force kinetic model gives good prediction to experimental TGA data (only dmpn-Mg_2(dobpdc)) and lab-scale fixed bed breakthrough data. The kinetic models developed in this work use real life data and diffusion limitation within the MOF channels are assumed to be captured by this, but a multiscale model will do a better job at accounting for these limitations by modeling the concentrations within the channels and is a possible area of future work. These isotherm and kinetic models are extremely useful as they give accurate prediction of the mass transfer phenomena for these MOFs and can be used in process simulations, but significant improvement in prediction as well as the physical understanding of the system can be obtained with more physically meaningful models. This is the motivation for the chemistry-based model for functionalized solid sorbents developed in this work. The chemistry model attempts to account for the adsorption products of dmpn-Mg_2(dobpdc) and how they change with temperature and pressure. Specifically, the adsorption products formed through the cooperative adsorption mechanism which is theorized to be the main mechanism for the majority of this class of MOFs. The reaction pathways for this mechanism are still not well understood so optimal reaction set selection from a group of proposed candidates is performed. For each candidate set investigated, parameter estimation is performed by solving a nonlinear programming problem, and the optimal candidate set is selected using the AIC criterion. The heat of adsorption predicted by the chemistry model is incorporated into the parameter estimation, which typically is not done for chemistry-based models in the literature, by constraining the prediction to be within a certain range of predetermined values. In this work, experimental heat of adsorption data for dmpn-Mg_2(dobpdc) is not available and values calculated using the Clausius-Clapeyron equation are used, but when experimental data becomes available, the model can be easily updated using these new values. The model has also been developed to be generic and applicable to any solid sorbent. This model is the first chemistry-based model for amine-appended MOFs and will be useful for process simulations and aid in development of new materials by identifying limiting pathways. Future work for the chemistry-based model will focus on application to other solid sorbents with significant attention being paid to other amine-appended MOFs. Improvements to the model can focus on thermodynamic consistency across the reaction equilibrium constants and the activity coefficient models. This will lay the foundation for more rigorous modeling of important thermodynamic properties such as enthalpy and subsequently the heat of adsorption. Future work will also heavily focus on incorporating the interaction between other species found in flue gas, mainly water. The chemistry model is better suited to perform this modeling as the effects of water can be accounted for in the reaction set while heuristic-based models must include correlation type adjustment factors which are not theoretically sound and can require significant data for development.

The second part of the MOF work pertains to contactor modeling, process simulation, and techno-economic analysis of post-combustion capture processes. Two contactor models have been developed in this work, a fixed bed contactor and moving bed contactor. Currently, no contactor models exist in literature for dmpn-Mg_2(dobpdc) or Mg_2(dobpdc)(3-4-3) while few exist for fixed bed contactors using other amine-appended MOFs. One of the major assumptions in these models is that CO_2 is the only adsorbing species, and the other species present in flue gas do not alter the adsorption behavior of CO_2. Experimental work has shown that the effect of water on mass transfer is minimal, but future work should focus on incorporating these interactions in the model. This will rely heavily on the updated chemistry model which predicts how these interactions will affect the adsorption equilibrium and kinetics of the MOF system. TSA processes are developed for each contactor model and techno-economic analysis is performed for each system. Analysis of the dmpn-Mg_2(dobpdc) fixed bed TSA system shows that heat management and recovery is important in reducing the economics of the process and making it competitive with a traditional MEA baseline process. Minimal economics of this process are found using sensitivity studies for a small number of operating variables and rigorous optimization will only serve to lower the economics of the process. For the moving bed TSA process, two versions are developed with the first version using the heuristic isotherm models developed as a part of this work. Techno-economic analysis of this version is performed by evaluating the sensitivity of the process economics to important operating variables. The second version of the model uses the chemistry-based adsorption equilibrium for dmpn-Mg_2(dobpdc). Using this version of the moving bed TSA model, rigorous optimization is performed to minimize the economics of the process using operating and design conditions as decision variables. The optimized moving bed process shows considerably lower economics than the MEA baseline system, but uncertainty analyses show that the economics of the process are extremely sensitive to the lifespan and price of the MOF particle and feasible values of these two uncertain parameters can result in economics above that above that of the MEA system. In addition to this uncertainty, capital cost uncertainty for moving bed reactors is also considered, and the costing framework for these systems should be updated whenever updated information for these sources of uncertainty becomes available. For Mg_2(dobpdc)(3-4-3), optimization of the fixed bed operating and design variables are performed and it is found that only when extrapolating to high temperatures and assuming large values for heat recovery can the process be competitive with an MEA based NGCC capture process. Validating the models at these higher temperatures and investigating other fixed bed type cycles such as a vacuum assisted TSA should be an area of future work. Additionally, the effect of SOx and NOx has only recently been experimentally evaluated and incorporating such effects in the model should be an area of future work. As the optimal contactor technology for amine-appended MOFs is still uncertain, future work should focus on the development of other contactor technologies that may alleviate some of the limitations of the contactors studied in this work. This could include but is not limited to rotary packed beds, radial flow beds, and fluidized beds.

Appendix

Appendix A: CAP Process Modeling

Table A.1: Pilot plant regression and validation cases (Data from Qi *et al.*, 2013)

Regression Cases

Test ID	30	31R	31B	32A	32B	34	34R2	36	35B	39	38
Flue Gas Flow Rate [kg/h]	646	632	750	760	821	906	916	799	799	898	912
Flue Gas Composition [vol %]											
CO_2	8.62	9.76	7.58	10.78	8.05	10.09	9.45	9.81	9.37	10.13	11.66
NH_3	0.52	0.47	0.21	0.09	0.07	0.25	0.28	0.03	0.13	0.24	0.08
H_2O	2.21	3.04	1.39	1.35	1.44	1.58	1.56	1.21	1.82	1.48	1.65
Liquid-to-Gas Ratio [mass basis]	12.3	12.6	10.7	10.5	9.7	4.4	4.4	10.0	9.9	8.9	8.8
Lean Solvent NH_3 content [wt %]	4.91	4.21	3.8	4.19	3.98	4.37	4.00	4.97	5.82	4.49	1.92
Lean Solvent CO_2 Loading [mol CO_2/mol NH_3]	0.24	0.23	0.25	0.26	0.22	0.22	0.22	0.41	0.36	0.28	0.22
Experimental CO_2 Capture Percentage	82.5	87.5	81.2	73.4	82.3	58.8	55.4	52.4	64.6	64.6	48.6

Validation Cases

Test ID	31	32	34R1
Flue Gas Flow Rate [kg/h]	646	780	915
Flue Gas Composition [vol %]			
CO_2	9.40	8.85	9.45
NH_3	0.43	0.42	0.28
H_2O	3.22	2.55	1.56
Liquid-to-Gas Ratio [mass basis]	12.3	10.2	4.4
Lean Solvent NH_3 content [wt %]	4.08	3.56	4.37
Lean Solvent CO_2 Loading [mol CO_2/mol NH_3]	0.24	0.25	0.23
Experimental CO_2 Capture Percentage	91.3	72.4	59.0

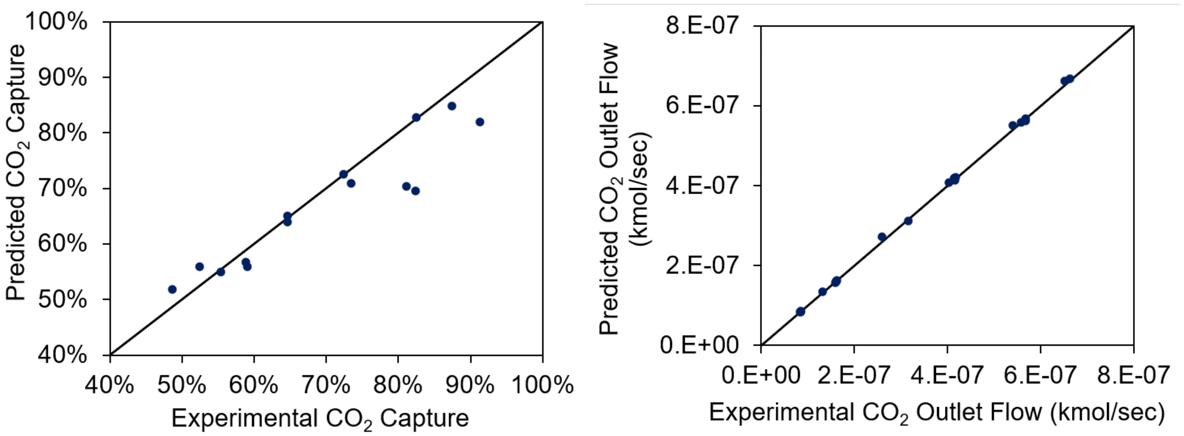

Figure A.1: Model performance using regressed parameters obtained from Hampel's estimator vs. experimental data for (left) packed absorber columns (Qi *et al.,* 2013) and (right) WWC (Puxty *et al.,* 2010)

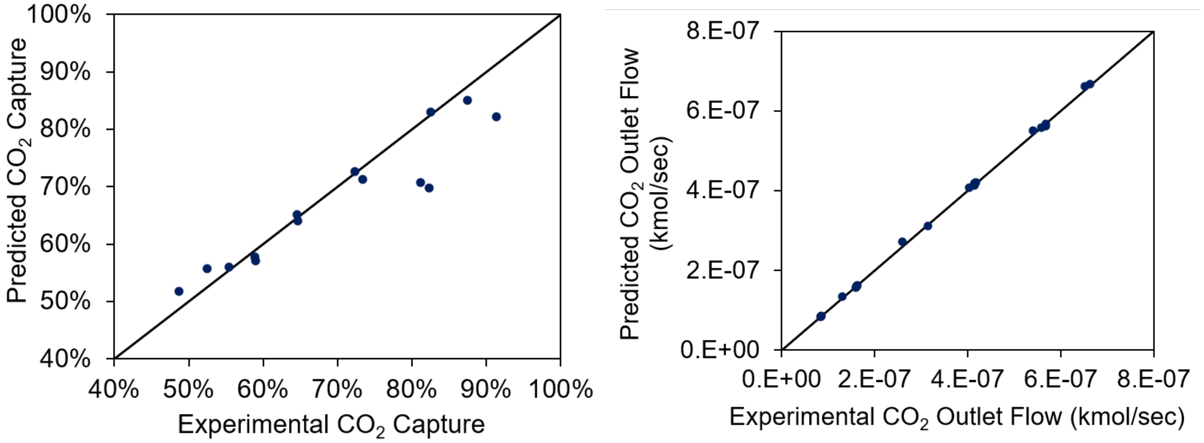

Figure A.2: Model performance using regressed parameters obtained from Logistic estimator vs. experimental data for (left) packed absorber columns (Qi *et al.,* 2013) and (right) WWC (Puxty *et al.,* 2010)

Chilled Ammonia Process Membrane Modeling

The model of a reverse osmosis membrane was developed using Aspen Custom Modeler. The model was developed for a membrane that follows the solution diffusion mechanism. Figure A.3 shows a simplified diagram for the flow directions of the feed, permeate, and mass transport.

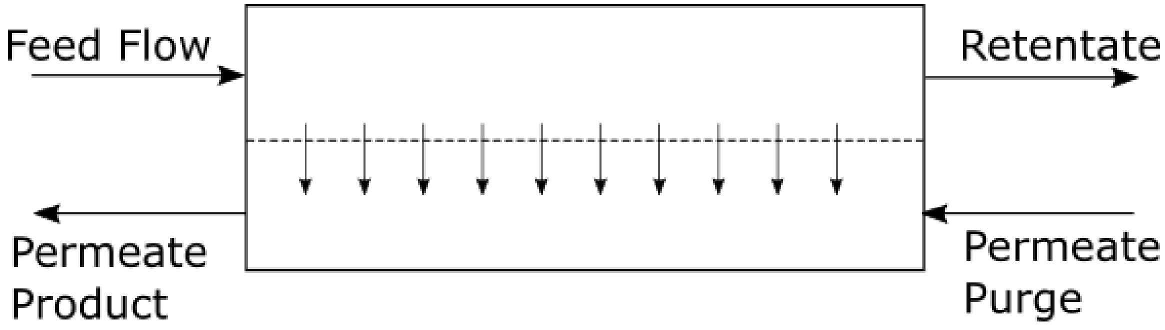

Figure A.3: Simplified diagram of the RO membrane

The following equations are used to model the membrane to predict the permeate flow rate and concentration profiles along the membrane:

$$J_w = A_w(\Delta P - \Delta\pi) \tag{A.1}$$

$$J_s = B_s\left(C_{ret} - C_{per}\right) \tag{A.2}$$

$$\Delta P = \psi(C_{ret} - C_{per}) \tag{A.3}$$

$$\frac{dF_{ret}}{dz} = -J_w - J_{ts} \tag{A.4}$$

$$F_{ret}\frac{dx_{ret,water}}{dz} = -J_w + x_{ret,water}\left(J_w + J_{ts}\right) \tag{A.5}$$

$$F_{ret}\frac{dx_{ret,solute}}{dz} = -J_s + x_{ret,solute}\left(J_w + J_{ts}\right) \tag{A.6}$$

$$F_{per}\frac{dx_{per,water}}{dz} = -J_w + x_{per,water}\left(J_w + J_{ts}\right) \tag{A.7}$$

$$F_{per}\frac{dx_{per,solute}}{dz} = -J_s + x_{per,solute}\left(J_w + J_{ts}\right) \tag{A.8}$$

$$J_{ts} = \sum_{i=1}^{N_s} J_{s,i} \tag{A.9}$$

The area for the RO membrane is calculated by:

$$A_M = \pi N_e D_f L \tag{A.10}$$

Where N_e is the number of elements in the RO membrane, D_f is the diameter of the fiber, and L is the length of the membrane. The diameter of a cellulose acetate RO membrane for high flux brackish water is 2.86 cm [122]. While the fiber diameter can vary based on a particular manufacturer and can be possibly optimized for the CAP system, in this work it is set at 2.86 cm due to lack of availability of more information in the open literature.

The feed to the RO membrane contains the ions and molecular components present for the NH_3-CO_2-H_2O system which includes H_2O, CO_2, NH_3, NH_4^+, HCO_3^-, CO_3^{2-}, NH_2COO^-, OH^-, H_3O^+, N_2. The ion solute permeability through the membrane, which is specified via parameter B_s, is not available in the literature for most of these components. This permeability depends on many factors and generally decreases with increases in degree of dissociation, ionic charge, molecular weight, non-polarity, degree of hydration, and degree of molecular branching [123]. The permeability can also be related to the ion selectivity and physical properties of ions such as ionic radius and hydrated ionic radius [124–126]. The order of salt permeability across the membrane is better explained using hydrated ionic radii instead of ionic radii [125]. The solvation or hydration occurs when an ion is introduced in a polar solvent. The cation transport across the membrane is slow when the hydrated radii is large. For smaller ionic radii and larger charge, the hydration radii are larger. Ghiu [125] showed that irrespective of membrane type, membrane configuration, the salt permeabilities are inversely proportional to the hydrated ionic radii of the cations studied for a common anion. The hydrated ionic radii for the species of interest in this study are given in Table A.2. It is also reported that the rejection of low molecular weight organics and small uncharged species is moderate for reverse osmosis membranes [127].

Table A.2: Hydrated ionic radius

Species	**Hydrated ionic radius [pm]**	**Reference**
NH_4^+	[250, 331]	(Dean, 1998; Kielland, 1937)[128,129]
OH^-	[300, 350]	(Dean, 1998; Kielland, 1937)[128,129]
H_3O^+	280	(Volkov *et al.,* 1997)[130]
CO_3^{2-}	450	(Dean, 1998)[128]
HCO_3^-	400	(Dean, 1998)[128]
NH_2COO^-	-	

In this work, the B_s values which are not available in the literature are estimated based on their relative relationships of molecular weight and hydrated ionic radius to the ionic species for which values are available in the literature. Using the trends described below along with the molecular weight of each species, the order of magnitude of the B_s values are assumed and given in Table A.3.

The order of hydrated ionic radius for the species is:

$CO_3^{2-}>HCO_3^->OH^->H_3O^+> NH_4^+$

Therefore, the proposed order of salt permeability based on hydrated ionic radius is:

$CO_3^{2-}<HCO_3^-$-$<OH^-<H_3O^+< NH_4^+$

Overall, the order of permeability can be:

$CO_3^{2-}<HCO_3^-$- $<NH_2COO^-<OH^-< H_3O^+<NH_4^+<N_2<CO_2< NH_3$

Table A.3: Solute permeability constants

Molecular Weight Grouping				
[< 20]	[20 < 40 < 60]	[> 60]	$\boldsymbol{B_s}$ **[m/h]**	**Reference**
NH_3	-	-	$(2.8\text{-}12.2)\times10^{-3}$	(Salon *et al.,* 1996; Zeuthen *et al.,* 2006)[131,132]
NH_4^+	-	-	0.421×10^{-3}	(Bódalo *et al.,* 2005)[133]
OH^-	-	-	$\sim 10^{-4}$	Assumed
H_3O^+	-	-	$\sim 10^{-4}$	Assumed
-	N_2	-	$\sim 10^{-4}$	Assumed
-	CO_2	-	$\sim 10^{-4}$	Assumed
-	-	CO_3^{2-}	$\sim 10^{-5}$	Assumed
-	-	HCO_3^-	$\sim 10^{-5}$	Assumed
-	-	NH_2COO^-	$\sim 10^{-5}$	Assumed

The osmotic pressure coefficient ψ can be calculated by using the equation $\psi = \varphi RT$ where φ is Van't Hoff factor or osmotic coefficient, R is universal gas constant and T is temperature [K] [134]. φ is not available for the species in the RO feed. An approximation of φ is required for all the other species to calculate ψ. Generally φ will be less than one for electrolyte components [134]. The osmotic coefficient depends on the concentration and type of electrolytes in the system [135]. As the data for the components in Table A.3 is not available, in this study φ is normalized to the total concentrations of the solute components.

One of the important performance measures for the membrane is the recovery rate, which is defined as the ratio of permeate flow to feed water flow thus indicating the overall water removal from the system. Large systems typically have recovery rates between 40% and 60% [53,54]. If experimental data, such as recovery rate, is available then parameter estimation for model parameters such as B_s and φ could be performed and model accuracy could be investigated.

Appendix B: Isotherm and Kinetic Modeling of dmpn-Mg2(dobpdc)

Table A.4: Fit of traditional isotherms to dmpn-Mg$_2$(dobpdc) data

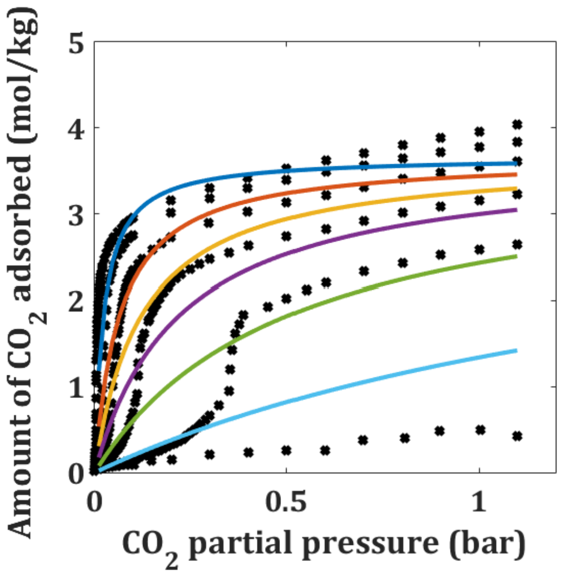

Langmuir Isotherm 1 fit to experimental data.

Langmuir isotherm 1

$$q = q_{max}\frac{KP}{1+KP}$$

$$q_{max} = 3.663$$

$$K = 2.167\times10^{-8}\exp\left(\frac{6380}{T}\right)$$

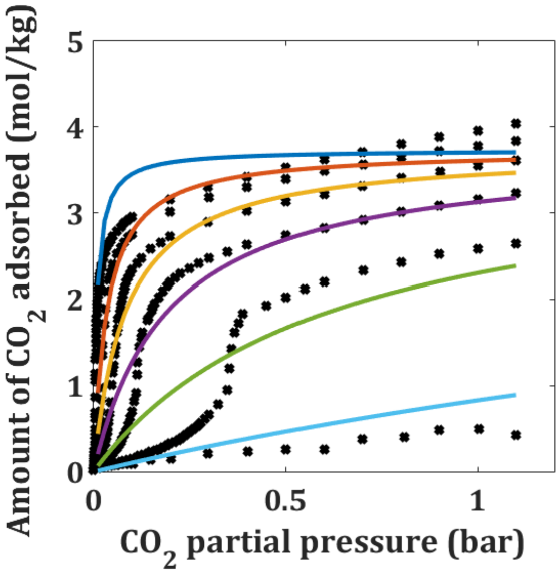

Dual-site Langmuir Isotherm fit to experimental data.

Dual-site Langmuir

$$q = q_{max1}\frac{K_1P}{1+K_1P} + q_{max2}\frac{K_2P}{1+K_2P}$$

$$K_i = \exp\left(\frac{\Delta S_i}{R}\right)\exp\left(\frac{-\Delta H_i}{RT}\right)$$

i	ΔH_i (J/mol)	ΔS_i(J/mol·K)	$q_{max,i}$ (mol/kg)
1	1585	−163.6	31.27
2	−74810	−210.9	3.731

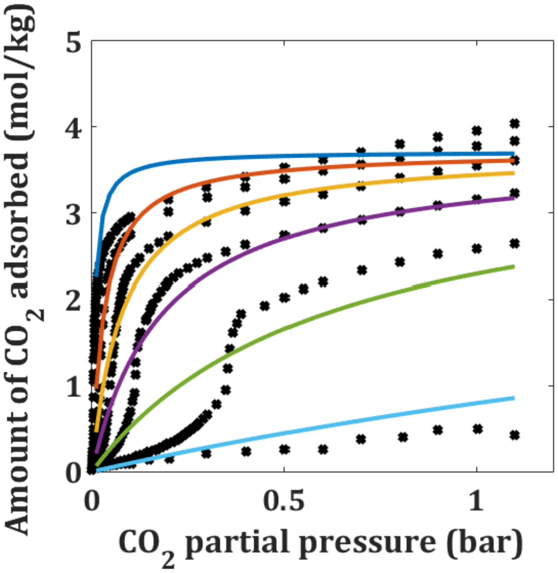

Langmuir Isotherm 2 fit to experimental data.

Langmuir isotherm 2

$$q = q_{max} \frac{KP}{1 + KP}$$

$$q_{max} = 7.403 - \frac{1143}{T}$$

$$K = 1.244 \times 10^{-8} \exp\left(\frac{6497}{T}\right)$$

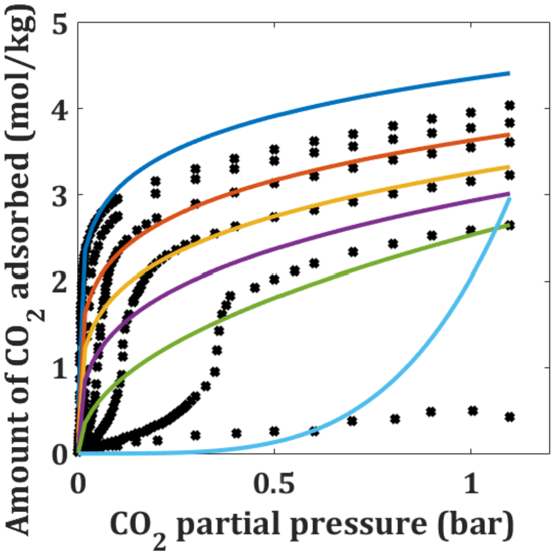

Freundlich Isotherm fit to experimental data.

Freundlich isotherm

$$q = KP^{1/n}$$

$$n = -24.86 - \frac{9382}{T}$$

$$K = 0.09995 \exp\left(\frac{1125}{T}\right)$$

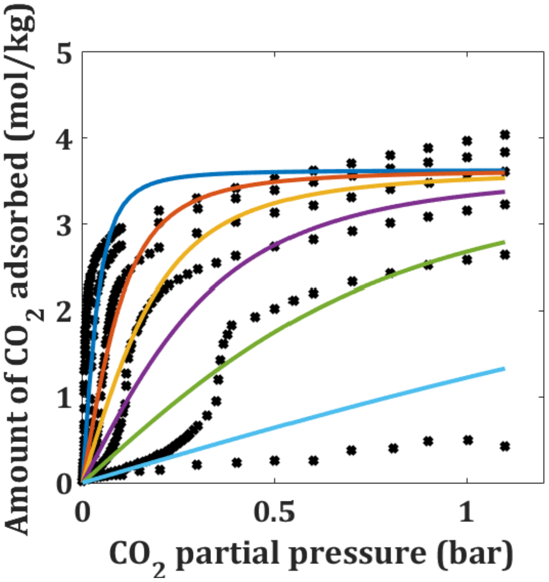

Toth Isotherm 1 fit to experimental data.

Toth isotherm 1

$$q = q_{max}\frac{KP}{(1+(KP)^{b})^{1/b}}$$

$$q_{max} = 3.627$$

$$K = 5.604\times 10^{-8}\exp\left(\frac{48630}{RT}\right)$$

$$b = 3.627$$

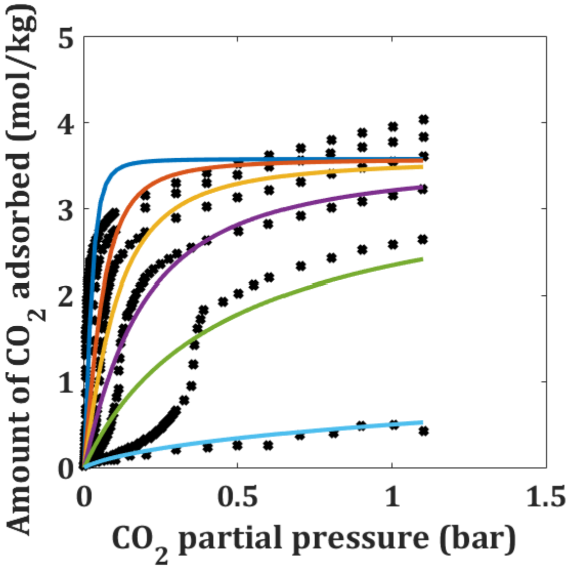

Toth Isotherm 2 fit to experimental data.

Toth isotherm 2

$$q = q_{max}\frac{KP}{(1+(KP)^{b})^{1/b}}$$

$$q_{max} = 3.579$$

$$K = 7.26\times 10^{-7}\exp\left(\frac{5203}{T}\right)$$

$$b = -7.264+\frac{2849}{T}$$

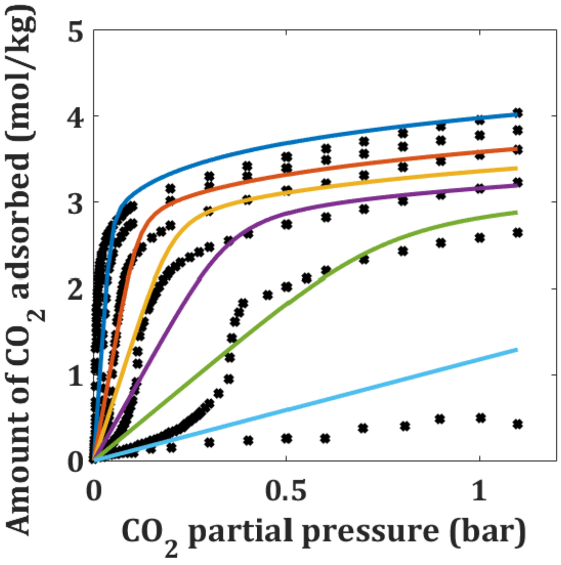

Toth Isotherm 3 fit to experimental data.

Toth isotherm 3

$$q = q_{max}\frac{KP}{(1+(KP)^b)^{1/a}}$$

$$q_{max} = 2.82$$

$$K = 5.282\times10^{-8}\exp\left(\frac{49280}{RT}\right)$$

$$b = 5.623, a = 6.319$$

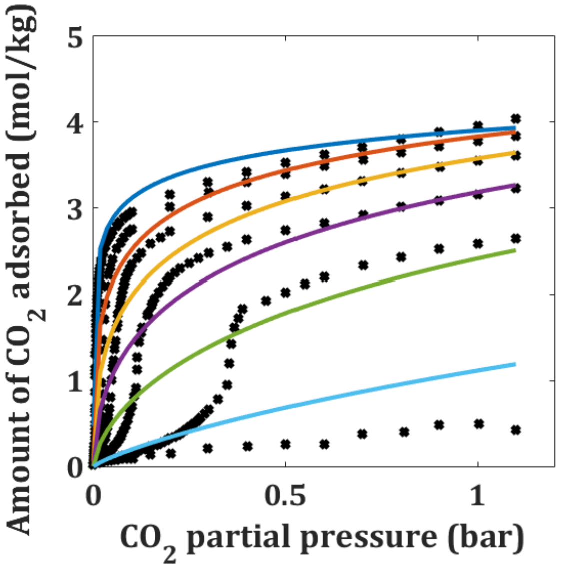

Langmuir-Freundlich Isotherm fit to experimental data

Langmuir-Freundlich isotherm

$$q = q_{max}\frac{(KP)^n}{1+(KP)^n}$$

$$q_{max} = 6.446$$

$$K = 2.814\times10^{-8}\exp\left(\frac{48030}{RT}\right)$$

$$n = 3.226 - \frac{897.8}{T}$$

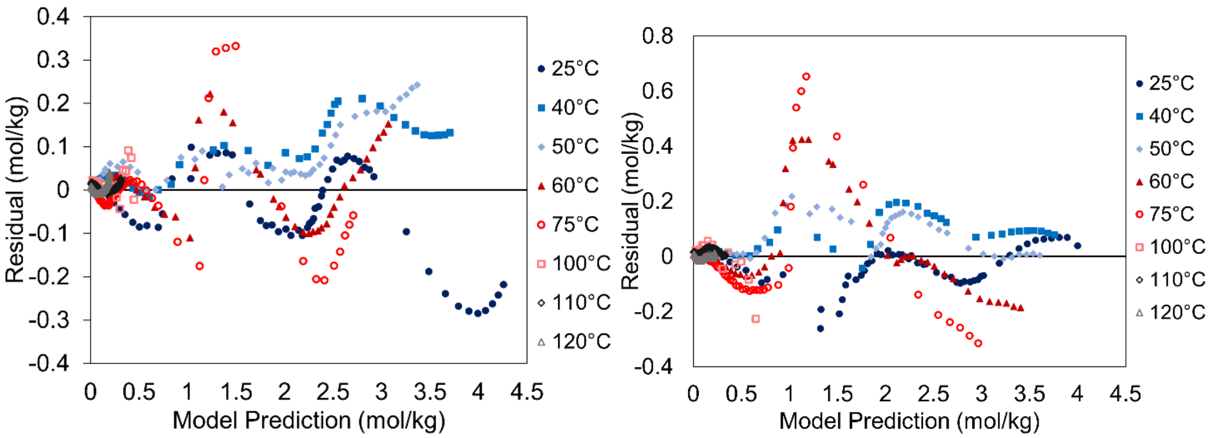

Figure A.4: Residual Plots for the dual-site Sips isotherm model (left) and weighted dual-site Langmuir isotherm model (right).

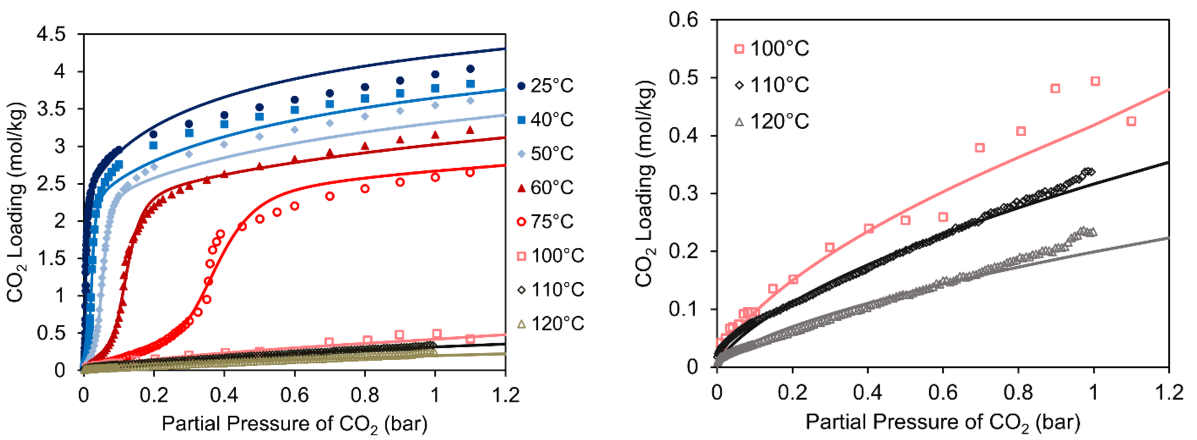

Figure A.5: Experimental CO_2 adsorption isotherms for dmpn–Mg_2(dobpdc) at the indicated temperatures (colored symbols) and fits using a dual-site Sips isotherm model (colored lines). Pressure is shown on a linear scale. The right plot shows an expanded view of the experimental and fit data at 100, 110, and 120 °C.

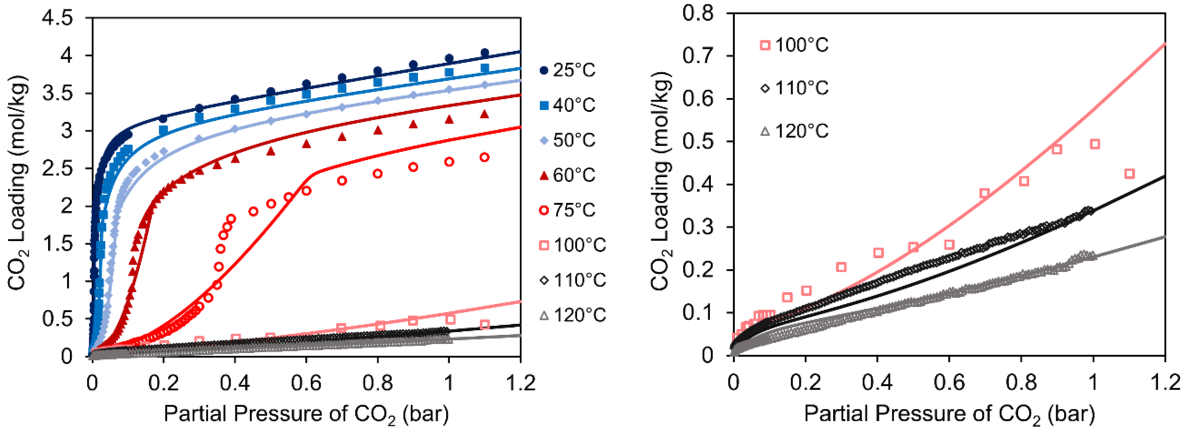

Figure A.6: Experimental CO_2 adsorption isotherms for dmpn–Mg_2(dobpdc) at the indicated temperatures (colored symbols) and fits using a weighted dual-site Langmuir isotherm model (colored lines). Pressure is shown on a linear scale. The right plot shows an expanded view of the experimental and fit data at 100, 110, and 120 °C.

Appendix C: Chemistry-based Modeling for Functionalized Solid Sorbents

Table A.5: Reaction Set Selection Results

Model [*N*,*M*]	# of Parameters	Objective Function	AIC
[1,0]	12	3.170	-3059.65
[1,1]	15	2.773	-3132.53
[2,0]	15	3.170	-3053.65
[2,1]	**18**	**1.692**	**-3417.98**
[3,0]	18	2.547	-3176.63
[2,2]	21	1.692	-3411.98
[3,1]	21	1.692	-3411.98
[4,0]	21	2.547	-3170.63
[3,2]	24	1.692	-3405.98
[4,1]	24	1.692	-3405.98
[5,0]	24	2.547	-3164.63

Appendix D: Contactor and Process Modeling

E*stimation of Heat Recovery for Fixed Bed TSA Process*

The total heat that is able to be recovered from the fixed bed at the end of desorption is calculated using Equation (A.11).

$$HR_{available} = \int_{z=0}^{z=L} C_{p,s} m_s [T_s(z, t = End\ of\ Desorption) - T_s(z, t = Start\ of\ Adsorption)] \tag{A.11}$$

This equation calculates the sensible heat using the temperature difference between the solids at the end of desorption and the beginning of adsorption and then integrates over the length of the bed. The heat that can be practically recovered from the fixed bed reactor at the end of desorption was estimated using Equation (8.12). This equation was derived assuming a 10 °C temperature approach for the heat recovery medium and estimated that only half of that heat could be recovered.

$$HR_{prac} = \int_{z=0}^{z=L} \frac{1}{2} C_{p,s} m_s [T_s(z, t = End\ of\ Desorption) - T_s(z, t = Start\ of\ Adsorption) - 10] \tag{A.12}$$

The percentage heat recovery is then calculated by taking the ratio of the practical heat recovered to the total heat available, Equation (8.13).

$$\%\ Heat\ Recovery = \frac{HR_{prac}}{HR_{available}} * 100\% \tag{A.13}$$

Version 1 Moving Bed Modeling Studies

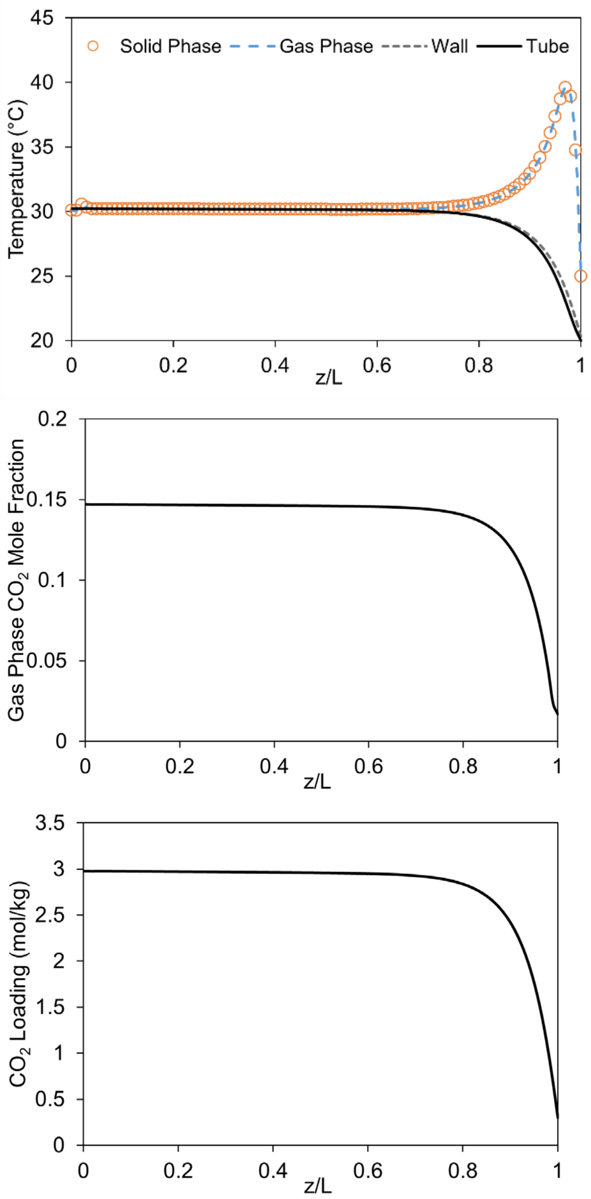

Figure A.7: Steady-state moving bed adsorber profiles for base case operating conditions.

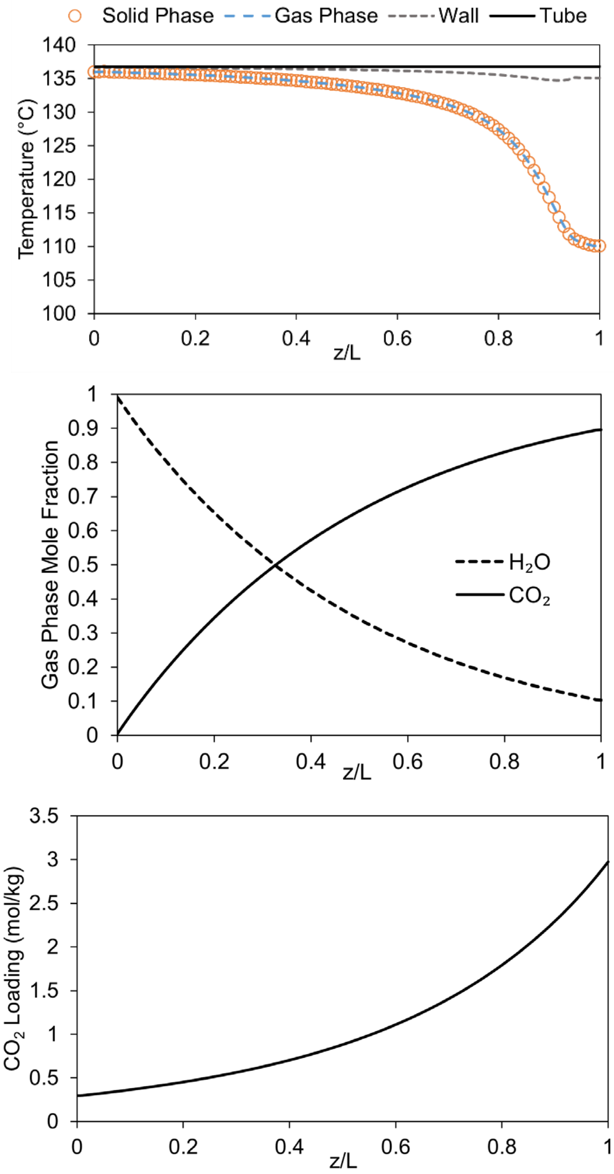

Figure A.8: Steady-state moving bed desorber profiles for base case operating conditions.

Surrogate Models for Inlet Flue Gas Pressurization

A unit model for pressurization of the flue gas feed was not included in the process models as a part of this work. Instead, a surrogate model was developed using simulations from Aspen Plus and APEA for the blower cost and compression work. To generate data to build the surrogate model, simulations were performed for compression from 1 bar (flue gas feed pressure) to a range of pressures which were thought to be possible for these processes. In APEA, there is a maximum flow rate for blower costing. Aspen Plus simulations were performed using this maximum flow rate, and equipment cost scaling was performed using the following equation:

$$C_{Blower} = Base\ cost\ \left(\frac{required\ flow}{base\ flow}\right)^{0.6} \tag{x}$$

Where the base cost and base flow are for the maximum flow rate in APEA and the required flow is the total flue gas flow rate. The sizing exponent is obtained from Turton *et al.* [106]. The blower equipment cost surrogate is presented in Figure A.9 and it can be seen that cost is relatively constant for the pressure range considered here. Nevertheless, the surrogate model is able to predict the data very well.

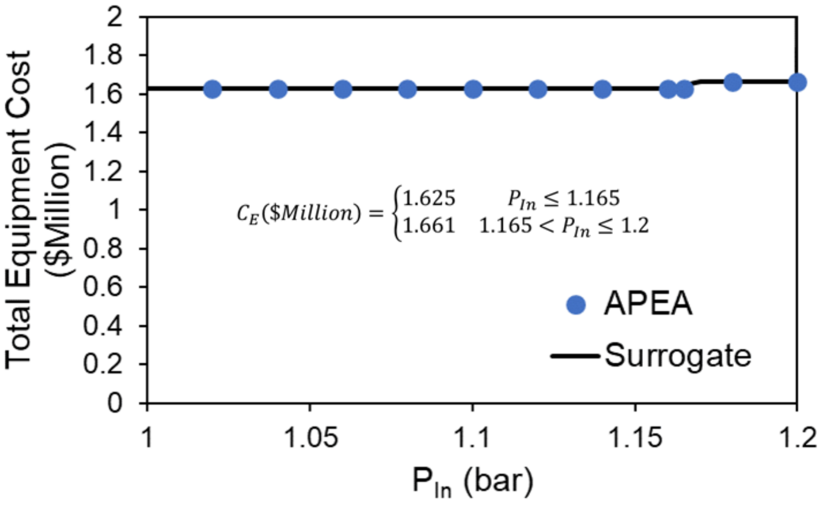

Figure A.9: Surrogate model for Blower Equipment Costs.

A surrogate model for the work required to increase the flue gas pressure was also developed in this work. Simulations from Aspen Plus were used to generate values for the work required for varying pressure differences. The results of this surrogate model are shown in Figure A.10 in which the black dots represent data from Aspen Plus simulations and the dotted line represents the trendline. The surrogate model equation and R^2 value is also given in Figure A.10.

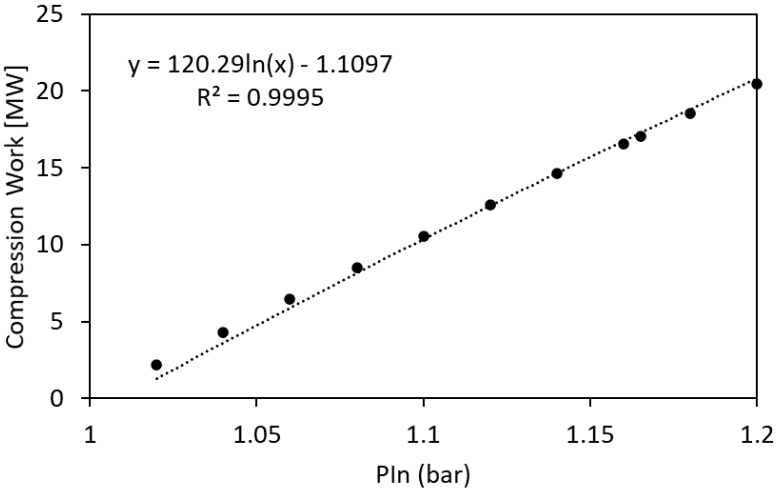

Figure A.10: Surrogate model for inlet flue gas compression work.

Appendix E: Presentations and Publications

Selected Presentations

- Ryan Hughes, Daison Caballero, Miguel Zamarripa, Benjamin Omell, Michael Matuszewski, Debangsu Bhattacharyya, *"Isotherm Modeling and Techno-Economic Analysis of Contactor Technologies for New Tetraamine-Appended MOF for NGCC Applications".* AICHE Annual Meeting. Phoenix, AZ. 2022
- Ryan Hughes, Goutham Kotamreddy, Debangsu Bhattacharyya, Surya Parker, Stephanie Didas, Jeffrey Long, Benjamin Omell, Michael Matuszewski, *"Process Modeling and Techno-Economic Optimization of a Moving Bed Contactor for* CO_2 *Capture Using a Diamine-Appended Metal-Organic Framework".* AICHE Annual Meeting. Phoenix, AZ. 2022
- Ryan Hughes, Chinmay Arias, Goutham Kotamreddy, Debangsu Bhattacharyya, *"Elucidating the Optimal Reaction Pathway of a Functionalized Metal-Organic Framework for Post-Combustion* CO_2 *Capture".* AICHE Annual Meeting. 2021

- Ryan Hughes, Chinmay Arias, Goutham Kotamreddy, Debangsu Bhattacharyya, *"Identifying Optimal Kinetic Pathways of a Functionalized Solid Sorbent for CO_2 Capture through Mathematical Programming"*. AICHE Annual Meeting. 2020
- Ryan Hughes, Goutham Kotamreddy, Debangsu Bhattacharyya, Chinyere Ezeobinwune, Ana Monteiro, Jeffrey Long, Surya Parker, Stephanie Didas, Benjamin Omell, Michael Matuszewski, *"Process Modeling and Techno-Economic Analysis of a Diamine-Appended Metal-Organic Framework for CO_2 Capture"*. AICHE Annual Meeting. 2020
- Ryan Hughes, Goutham Kotamreddy, Debangsu Bhattacharyya, Rebecca Siegelman, Surya Parker, Stephanie Didas, Jeffrey Long, Benjamin Omell, Michael Matuszewski, *"Process Modeling and Optimal Synthesis of a Fixed Bed System for CO_2 Capture using a Diamine-Appended Metal-Organic Framework"*. AICHE Annual Meeting. Orlando, FL. 2019
- Ryan Hughes, Goutham Kotamreddy, Debangsu Bhattacharyya, Rebecca Siegelman, Surya Parker, Stephanie Didas, Jeffrey Long, Benjamin Omell, Michael Matuszewski, *"Modeling and Optimization of a Moving Bed Process for Post-Combustion CO_2 Capture Using a Diamine-Appended Metal-Organic Framework"*. AICHE Annual Meeting. Orlando, FL. 2019
- Ryan Hughes, Goutham Kotamreddy, Debangsu Bhattacharyya, Rebecca Siegelman, Jeffrey Long, Michael Matuszewski, *"Process Modeling and Experimental Studies of a Diamine-Appended Metal-Organic Framework for CO_2 Capture".* AICHE Annual Meeting. Pittsburgh, PA. 2018
- Ryan Hughes, Goutham Kotamreddy, Debangsu Bhattacharyya, Michael Matuszewski, "*Process Modeling and Optimization of a Novel Membrane-Assisted Chilled Ammonia Process for CO_2 Capture*". AICHE Annual Meeting. Minneapolis, MN. 2017

Publications

- Caballero, D.; Hughes, R.; Zamarripa, M.; Bhatacharyya, D.; Matuszewski, M.; Omell, B. Isotherm and Process Modeling of a Tetraamine-Appended Metal-Organic Framework for NGCC Capture using Moving Bed Contactors. Internal Review
- Hughes, R.; Caballero, D.; Zamarripa, M.; Bhatacharyya, D.; Matuszewski, M.; Omell, B. Isotherm and Process Modeling of a Tetraamine-Appended Metal-Organic Framework for NGCC Capture using Fixed Bed Contactors. Internal Review
- Hughes, R.; Kotamreddy, G.; Bhatacharyya, D.; Parker, S.; Dods, M.; Long, J.; Matuszewski, M.; Omell, B. Development of a Chemistry-Based Isotherm Model and Techno-Economic Optimization of a Moving Bed Process for CO_2 Capture Using a Functionalized Metal-Organic Framework. Internal Review
- Kotamreddy, G.; Hughes, R.; Bhatacharyya, D.; Matuszewski, M.; Omell, B. Multi-Scale Dynamic Modeling and Techno-Economic Optimization of a CO_2 Capture Process Using Microencapsulated Carbon Sorbents in a Moving Bed Contactors. Submitted, International Journal of Greenhouse Gas Control.
- Yancy Caballero, Daison and Hughes, Ryan and Zamarripa, Miguel and Omell, Benjamin and Matuszewski, Michael and Bhattacharyya, Debangsu, Isotherm Modeling and Techno-Economic Analysis of Contactor Technologies for New Tetraamine-Appended Mof for Ngcc Applications (November 8, 2022). Available at SSRN: https://ssrn.com/abstract=4271570 or http://dx.doi.org/10.2139/ssrn.4271570
- Hughes, R.; Kotamreddy, G.; Bhattacharyya, D.; Omell, B.; Matuszewski, M. Modeling and Bayesian Uncertainty Quantification of a Membrane-Assisted Chilled Ammonia Process for CO_2 Capture. *Ind. Eng. Chem. Res.* **2022**, *61* (11), 4001–4016. https://doi.org/10.1021/acs.iecr.1c04601.
- Hughes, R.; Kotamreddy, G.; Ostace, A.; Bhattacharyya, D.; Siegelman, R. L.; Parker, S. T.; Didas, S. A.; Long, J. R.; Omell, B.; Matuszewski, M. Isotherm, Kinetic, Process Modeling, and Techno-Economic Analysis of a Diamine-Appended Metal–Organic Framework for CO_2 Capture Using Fixed Bed Contactors. *Energy Fuels* **2021**, *35* (7), 6040–6055. https://doi.org/10.1021/acs.energyfuels.0c04359.
- Kotamreddy, G.; Hughes, R.; Bhattacharyya, D.; Stolaroff, J.; Hornbostel, K.; Matuszewski, M.; Omell, B. Process Modeling and Techno-Economic Analysis of a CO2 Capture Process Using Fixed Bed Reactors with a Microencapsulated Solvent. *Energy Fuels* **2019**, *33* (8), 7534–7549. https://doi.org/10.1021/acs.energyfuels.9b01255.

References

[1] Meyer L, Brinkman S, van Kesteren L, Leprince-Ringuet N, van Boxmeer F. Technical Support Unit for the Synthesis Report 2014:169.

[2] Puxty G, Rowland R, Attalla M. Comparison of the rate of CO2 absorption into aqueous ammonia and monoethanolamine. Chemical Engineering Science 2010;65:915–22. https://doi.org/10.1016/j.ces.2009.09.042.

[3] Milner PJ, Siegelman RL, Forse AC, Gonzalez MI, Runčevski T, Martell JD, et al. A Diaminopropane-Appended Metal–Organic Framework Enabling Efficient CO2 Capture from Coal Flue Gas via a Mixed Adsorption Mechanism. J Am Chem Soc 2017;139:13541–53. https://doi.org/10.1021/jacs.7b07612.

[4] Bhattacharyya D, Miller DC. Post-combustion CO2 capture technologies — a review of processes for solvent-based and sorbent-based CO2 capture. Current Opinion in Chemical Engineering 2017;17:78–92. https://doi.org/10.1016/j.coche.2017.06.005.

[5] Rochelle GT. Amine Scrubbing for CO2 Capture. Science 2009;325:1652–4. https://doi.org/10.1126/science.1176731.

[6] Morgan JC, Soares Chinen A, Omell B, Bhattacharyya D, Tong C, Miller DC, et al. Development of a Rigorous Modeling Framework for Solvent-Based CO2 Capture. Part 2: Steady-State Validation and Uncertainty Quantification with Pilot Plant Data. Ind Eng Chem Res 2018;57:10464–81. https://doi.org/10.1021/acs.iecr.8b01472.

[7] Chinen AS, Morgan JC, Omell B, Bhattacharyya D, Miller DC. Dynamic Data Reconciliation and Validation of a Dynamic Model for Solvent-Based CO2 Capture Using Pilot-Plant Data. Ind Eng Chem Res 2019;58:1978–93. https://doi.org/10.1021/acs.iecr.8b04489.

[8] Patrón GD, Ricardez-Sandoval L. An integrated real-time optimization, control, and estimation scheme for post-combustion CO2 capture. Applied Energy 2022;308:118302. https://doi.org/10.1016/j.apenergy.2021.118302.

[9] Darde V, van Well WJM, Stenby EH, Thomsen K. CO2 capture using aqueous ammonia: kinetic study and process simulation. Energy Procedia 2011;4:1443–50. https://doi.org/10.1016/j.egypro.2011.02.010.

[10] Hanak DP, Biliyok C, Manovic V. Rate-based model development, validation and analysis of chilled ammonia process as an alternative CO2 capture technology for coal-fired power plants. International Journal of Greenhouse Gas Control 2015;34:52–62. https://doi.org/10.1016/j.ijggc.2014.12.013.

[11] Jilvero H, Normann F, Andersson K, Johnsson F. The Rate of CO2 Absorption in Ammonia—Implications on Absorber Design. Ind Eng Chem Res 2014;53:6750–8. https://doi.org/10.1021/ie403346a.

[12] Lombardo G, Agarwal R, Askander J. Chilled Ammonia Process at Technology Center Mongstad – First Results. Energy Procedia 2014;51:31–9. https://doi.org/10.1016/j.egypro.2014.07.004.

[13] Niu Z, Guo Y, Zeng Q, Lin W. Experimental Studies and Rate-Based Process Simulations of CO2 Absorption with Aqueous Ammonia Solutions. Ind Eng Chem Res 2012;51:5309–19. https://doi.org/10.1021/ie2030536.

[14] Qi G, Wang S, Yu H, Feron P, Chen C. Rate-Based Modeling of CO2 Absorption in Aqueous NH3 in a Packed Column. Energy Procedia 2013;37:1968–76. https://doi.org/10.1016/j.egypro.2013.06.077.

[15] Telikapalli V, Kozak F, Francois J, Sherrick B, Black J, Muraskin D, et al. CCS with the Alstom chilled ammonia process development program–Field pilot results. Energy Procedia 2011;4:273–81. https://doi.org/10.1016/j.egypro.2011.01.052.

[16] Yu H, Morgan S, Allport A, Cottrell A, Do T, McGregor J, et al. Results from trialling aqueous NH3 based post-combustion capture in a pilot plant at Munmorah power station: Absorption. Chemical Engineering Research and Design 2011;89:1204–15. https://doi.org/10.1016/j.cherd.2011.02.036.

[17] Li K, Yu H, Tade M, Feron P, Yu J, Wang S. Process Modeling of an Advanced NH3 Abatement and Recycling Technology in the Ammonia-Based CO2 Capture Process. Environ Sci Technol 2014;48:7179–86. https://doi.org/10.1021/es501175x.

[18] Mathias PM, Reddy S, O'Connell JP. Quantitative evaluation of the chilled-ammonia process for CO2 capture using thermodynamic analysis and process simulation. International Journal of Greenhouse Gas Control 2010;4:174–9. https://doi.org/10.1016/j.ijggc.2009.09.016.

[19] Niu Z, Guo Y, Zeng Q, Lin W. A novel process for capturing carbon dioxide using aqueous ammonia. Fuel Processing Technology 2013;108:154–62. https://doi.org/10.1016/j.fuproc.2012.05.028.

[20] Zhang M, Guo Y. Process simulations of NH3 abatement system for large-scale CO2 capture using aqueous ammonia solution. International Journal of Greenhouse Gas Control 2013;18:114–27. https://doi.org/10.1016/j.ijggc.2013.07.005.

[21] Muraskin D, Dube S, Baburao B. Improvement of General Electric's Chilled Ammonia Process with the use of Membrane Technology. General Electric Environmental Control Solutions, Knoxville, TN (United States); 2016.

[22] Sumida K, Rogow DL, Mason JA, McDonald TM, Bloch ED, Herm ZR, et al. Carbon Dioxide Capture in Metal–Organic Frameworks. Chem Rev 2012;112:724–81. https://doi.org/10.1021/cr2003272.

[23] Furukawa H, Cordova KE, O'Keeffe M, Yaghi OM. The Chemistry and Applications of Metal-Organic Frameworks. Science 2013;341:1230444–1230444. https://doi.org/10.1126/science.1230444.

[24] Zhou H-C, Long JR, Yaghi OM. Introduction to Metal–Organic Frameworks. Chem Rev 2012;112:673–4. https://doi.org/10.1021/cr300014x.

[25] McDonald TM, Lee WR, Mason JA, Wiers BM, Hong CS, Long JR. Capture of Carbon Dioxide from Air and Flue Gas in the Alkylamine-Appended Metal–Organic Framework mmen-Mg2 (dobpdc). J Am Chem Soc 2012;134:7056–65. https://doi.org/10.1021/ja300034j.

[26] McDonald TM, Mason JA, Kong X, Bloch ED, Gygi D, Dani A, et al. Cooperative insertion of CO2 in diamine-appended metal-organic frameworks. Nature 2015;519:303–8. https://doi.org/10.1038/nature14327.

[27] Siegelman RL, McDonald TM, Gonzalez MI, Martell JD, Milner PJ, Mason JA, et al. Controlling Cooperative CO2 Adsorption in Diamine-Appended Mg2 (dobpdc) Metal–Organic Frameworks. J Am Chem Soc 2017;139:10526–38. https://doi.org/10.1021/jacs.7b05858.

[28] Siegelman RL, Milner PJ, Forse AC, Lee J-H, Colwell KA, Neaton JB, et al. Water Enables Efficient CO2 Capture from Natural Gas Flue Emissions in an Oxidation-Resistant Diamine-Appended Metal–Organic Framework. J Am Chem Soc 2019;141:13171–86. https://doi.org/10.1021/jacs.9b05567.

[29] Kim EJ, Siegelman RL, Jiang HZH, Forse AC, Lee J-H, Martell JD, et al. Cooperative carbon capture and steam regeneration with tetraamine-appended metal–organic frameworks. Science 2020:392–6. https://doi.org/10.1126/science.abb3976.

[30] Forse AC, Milner PJ, Lee J-H, Redfearn HN, Oktawiec J, Siegelman RL, et al. Elucidating CO2 Chemisorption in Diamine-Appended Metal–Organic Frameworks. J Am Chem Soc 2018;140:18016–31. https://doi.org/10.1021/jacs.8b10203.

[31] Pinsent BRW, Pearson L, Roughton FJW. The Kinetics of Combination of Carbon Dioxide with Ammonia. Transactions of the Faraday Society 1956;52:1512–20.

[32] Que H, Chen C-C. Thermodynamic Modeling of the NH3–CO2–H2O System with Electrolyte NRTL Model. Ind Eng Chem Res 2011;50:11406–21. https://doi.org/10.1021/ie201276m.

[33] Jilvero H, Normann F, Andersson K, Johnsson F. The Rate of CO 2 Absorption in Ammonia—Implications on Absorber Design. Ind Eng Chem Res 2014;53:6750–8. https://doi.org/10.1021/ie403346a.

[34] Afkhamipour M, Mofarahi M. Sensitivity analysis of the rate-based CO2 absorber model using amine solutions (MEA, MDEA and AMP) in packed columns. International Journal of Greenhouse Gas Control 2014;25:9–22. https://doi.org/10.1016/j.ijggc.2014.03.005.

[35] Jayarathna SA, Lie B, Melaaen MC. Dynamic modelling of the absorber of a post-combustion CO2 capture plant: Modelling and simulations. Computers & Chemical Engineering 2013;53:178–89. https://doi.org/10.1016/j.compchemeng.2013.03.002.

[36] Khan FM, Krishnamoorthi V, Mahmud T. Modelling reactive absorption of CO2 in packed columns for post-combustion carbon capture applications. Chemical Engineering Research and Design 2011;89:1600–8. https://doi.org/10.1016/j.cherd.2010.09.020.

[37] Chinen AS, Morgan JC, Omell B, Bhattacharyya D, Tong C, Miller DC. Development of a Rigorous Modeling Framework for Solvent-Based CO2 Capture. 1: Hydraulic and Mass Transfer Models and Their Uncertainty Quantification. Ind Eng Chem Res 2018;57:10448–63. https://doi.org/10.1021/acs.iecr.8b01471.

[38] Morgan JC, Bhattacharyya D, Tong C, Miller DC. Uncertainty quantification of property models: Methodology and its application to CO2-loaded aqueous MEA solutions. AIChE J 2015;61:1822–39. https://doi.org/10.1002/aic.14762.

[39] Morgan JC, Chinen AS, Omell B, Bhattacharyya D, Tong C, Miller DC. Thermodynamic modeling and uncertainty quantification of CO2-loaded aqueous MEA solutions. Chemical Engineering Science 2017;168:309–24. https://doi.org/10.1016/j.ces.2017.04.049.

[40] Aspen Tech. Rate-Based Model of the CO2 Capture Process by NH3 using Aspen Plus. Burlington, MA: Aspen Tech.; 2013.

[41] Billet R, Schultes M. Predicting mass transfer in packed columns. Chemical Engineering & Technology 1993;16:1–9. https://doi.org/10.1002/ceat.270160102.

[42] Tsai RE, Rochelle GT, Eldridge RB, Bonnecaze RT, McGlamery GG, Seibert AF, et al. Mass Transfer Area of Structured Packing. The University of Texas at Austin, 2010.

[43] Chilton TH, Colburn AP. Mass Transfer (Absorption) Coefficients Prediction from Data on Heat Transfer and Fluid Friction. Ind Eng Chem 1934;26:1183–7. https://doi.org/10.1021/ie50299a012.

[44] Hampel FR, Ronchetti EM, Rousseeuw PJ, Stahel WA. Robust statistics : the approach based on influence functions. 1st ed. New York: Wiley; 1986.
[45] Huber PJ, Ronchetti Elvezio. Robust statistics. 2nd ed. Hoboken, N.J.: Wiley; 2009.
[46] Maronna RA, Martin RD, Yohai VJ. Robust Statistics: Theory and Methods. Wiley; 2006.
[47] Rousseeuw PJ, Leroy AM. Robust regression and outlier detection. New York: Wiley; 1987.
[48] Özyurt DB, Pike RW. Theory and practice of simultaneous data reconciliation and gross error detection for chemical processes. Computers & Chemical Engineering 2004;28:381–402. https://doi.org/10.1016/j.compchemeng.2003.07.001.
[49] Lagarias JC, Reeds JA, Wright MH, Wright PE. Convergence Properties of the Nelder--Mead Simplex Method in Low Dimensions. SIAM J Optim 1998;9:112–47. https://doi.org/10.1137/S1052623496303470.
[50] Modekurti S, Bhattacharyya D, Zitney SE. Dynamic Modeling and Control Studies of a Two-Stage Bubbling Fluidized Bed Adsorber-Reactor for Solid–Sorbent CO2 Capture. Ind Eng Chem Res 2013;52:10250–60. https://doi.org/10.1021/ie400852k.
[51] Li K, Cousins A, Yu H, Feron P, Tade M, Luo W, et al. Systematic study of aqueous monoethanolamine-based CO2 capture process: model development and process improvement. Energy Sci Eng 2016;4:23–39. https://doi.org/10.1002/ese3.101.
[52] Luis P. Use of monoethanolamine (MEA) for CO2 capture in a global scenario: Consequences and alternatives. Desalination 2016;380:93–9. https://doi.org/10.1016/j.desal.2015.08.004.
[53] Al-Karaghouli A, Kazmerski L. Economic and Technical Analysis of a Reverse-Osmosis Water Desalination Plant using DEEP-3.2 Software. Journal of Environmental Science & Engineering 2012;1:318–31.
[54] McMordie-Stoughton KL, Duan X, Wendel EM. Reverse Osmosis Optimization. 2013. https://doi.org/10.2172/1095449.
[55] Friedman JH. Multivariate Adaptive Regression Splines. The Annals of Statistics 1991;19:1–141.
[56] Kimaev G, Ricardez-Sandoval LA. A comparison of efficient uncertainty quantification techniques for stochastic multiscale systems. AIChE J 2017;63:3361–73. https://doi.org/10.1002/aic.15702.
[57] Kimaev G, Ricardez-Sandoval LA. Multilevel Monte Carlo applied to chemical engineering systems subject to uncertainty. AIChE J 2018;64:1651–61. https://doi.org/10.1002/aic.16045.
[58] Miller DC, Agarwal D, Bhattacharyya D, Boverhof J, Chen Y, Eslick JC, et al. Innovative computational tools and models for the design, optimization and control of carbon capture processes, 2017.
[59] Morgan JC, Chinen AS, Anderson-Cook C, Tong C, Carroll J, Saha C, et al. Development of a framework for sequential Bayesian design of experiments: Application to a pilot-scale solvent-based CO2 capture process. Applied Energy 2020;262:114533. https://doi.org/10.1016/j.apenergy.2020.114533.
[60] Hefti M, Joss L, Bjelobrk Z, Mazzotti M. On the potential of phase-change adsorbents for CO2 capture by temperature swing adsorption. Faraday Discuss 2016;192:153–79. https://doi.org/10.1039/C6FD00040A.

[61] Kundu J, Stilck JF, Lee J-H, Neaton JB, Prendergast D, Whitelam S. Cooperative gas adsorption without a phase transition in metal-organic frameworks. Phys Rev Lett 2018;121:015701. https://doi.org/10.1103/PhysRevLett.121.015701.
[62] Pai KN, Baboolal JD, Sharp DA, Rajendran A. Evaluation of diamine-appended metal-organic frameworks for post-combustion CO2 capture by vacuum swing adsorption. Sep and Pur Tech 2019;211:540–50. https://doi.org/10.1016/j.seppur.2018.10.015.
[63] Ga S, Lee S, Park G, Kim J, Realff M, Lee JH. New model for S-shaped isotherm data and its application to process modeling using IAST. Chemical Engineering Journal 2021;420:127580. https://doi.org/10.1016/j.cej.2020.127580.
[64] Joss L, Hefti M, Bjelobrk Z, Mazzotti M. On the Potential of Phase-change Adsorbents for CO2 Capture by Temperature Swing Adsorption. Energy Procedia 2017;114:2271–8. https://doi.org/10.1016/j.egypro.2017.03.1375.
[65] Casas N, Schell J, Pini R, Mazzotti M. Fixed bed adsorption of CO2/H2 mixtures on activated carbon: experiments and modeling. Adsorption 2012;18:143–61. https://doi.org/10.1007/s10450-012-9389-z.
[66] Casas N, Schell J, Joss L, Mazzotti M. A parametric study of a PSA process for pre-combustion CO2 capture. Separation and Purification Technology 2013;104:183–92. https://doi.org/10.1016/j.seppur.2012.11.018.
[67] Remy T, Baron GV, Denayer JFM. Modeling the Effect of Structural Changes during Dynamic Separation Processes on MOFs. Langmuir 2011;27:13064–71. https://doi.org/10.1021/la203374a.
[68] Bao Z, Yu L, Ren Q, Lu X, Deng S. Adsorption of CO2 and CH4 on a magnesium-based metal organic framework. Journal of Colloid and Interface Science 2011;353:549–56. https://doi.org/10.1016/j.jcis.2010.09.065.
[69] Tzabar N, ter Brake HJM. Adsorption isotherms and Sips models of nitrogen, methane, ethane, and propane on commercial activated carbons and polyvinylidene chloride. Adsorption 2016;22:901–14. https://doi.org/10.1007/s10450-016-9794-9.
[70] Martell JD, Milner PJ, Siegelman RL, Long JR. Kinetics of cooperative CO2 adsorption in diamine-appended variants of the metal–organic framework Mg2 (dobpdc). Chem Sci 2020;11:6457–71. https://doi.org/10.1039/D0SC01087A.
[71] Lee KB, Verdooren A, Caram HS, Sircar S. Chemisorption of carbon dioxide on potassium-carbonate-promoted hydrotalcite. Journal of Colloid and Interface Science 2007;308:30–9. https://doi.org/10.1016/j.jcis.2006.11.011.
[72] Lee KB, Beaver MG, Caram HS, Sircar S. Chemisorption of carbon dioxide on sodium oxide promoted alumina. AIChE J 2007;53:2824–31. https://doi.org/10.1002/aic.11312.
[73] Lee KB, Beaver MG, Caram HugoS, Sircar S. Effect of Reaction Temperature on the Performance of Thermal Swing Sorption-Enhanced Reaction Process for Simultaneous Production of Fuel-Cell-Grade H2 and Compressed CO2 from Synthesis Gas. Ind Eng Chem Res 2008;47:6759–64. https://doi.org/10.1021/ie071372k.
[74] Abdollahi-Govar A, Ebner AD, Ritter JA. New Kinetic Model That Describes the Reversible Adsorption and Desorption Behavior of CO 2 in a Solid Amine Sorbent. Energy Fuels 2015;29:4492–502. https://doi.org/10.1021/acs.energyfuels.5b01119.
[75] Liu S. Cooperative adsorption on solid surfaces. Journal of Colloid and Interface Science 2015;450:224–38. https://doi.org/10.1016/j.jcis.2015.03.013.
[76] Lee A, Road CF, Virginia W. A Model for the Adsorption Kinetics of CO2 on Amine-Impregnated Mesoporous Sorbents in the Presence of Water n.d.:11.

[77] O'Connell JP, Haile JM. Thermodynamics: Fundamentals for Applications. 1st ed. Cambridge University Press; 2005. https://doi.org/10.1017/CBO9780511840234.
[78] Ruthven DM. Principles of Adsorption and Adsorption Processes. John Wiley & Sons; 1984.
[79] Hart WE, Laird CD, Watson J-P, Woodruff DL, Hackebeil GA, Nicholson BL, et al. Pyomo — Optimization Modeling in Python. 2nd ed. Springer International Publishing; 2017. https://doi.org/10.1007/978-3-319-58821-6.
[80] Wächter A, Biegler LT. On the implementation of an interior-point filter line-search algorithm for large-scale nonlinear programming. Math Program 2006;106:25–57. https://doi.org/10.1007/s10107-004-0559-y.
[81] Akaike H. A new look at the statistical model identification. IEEE Trans Automat Contr 1974;19:716–23. https://doi.org/10.1109/TAC.1974.1100705.
[82] Weiss JN. The Hill equation revisited: uses and misuses. FASEB j 1997;11:835–41. https://doi.org/10.1096/fasebj.11.11.9285481.
[83] Shafeeyan MS, Wan Daud WMA, Shamiri A. A review of mathematical modeling of fixed-bed columns for carbon dioxide adsorption. Chemical Engineering Research and Design 2014;92:961–88. https://doi.org/10.1016/j.cherd.2013.08.018.
[84] Kakac S, Liu H, Pramuanjaroenkij A. Heat Exchangers: Selection, Rating, and Thermal Design. 3rd ed. CRC press; 2012.
[85] Kim H, Miller DC, Modekurti S, Omell B, Bhattacharyya D, Zitney SE. Mathematical modeling of a moving bed reactor for post-combustion CO2 capture. AIChE J 2016;62:3899–914. https://doi.org/10.1002/aic.15289.
[86] Kotamreddy G, Hughes R, Bhattacharyya D, Stolaroff J, Hornbostel K, Matuszewski M, et al. Process Modeling and Techno-Economic Analysis of a CO2 Capture Process Using Fixed Bed Reactors with a Microencapsulated Solvent. Energy Fuels 2019;33:7534–49. https://doi.org/10.1021/acs.energyfuels.9b01255.
[87] Penny C, Naylor D, Friedman J. Heat transfer to small cylinders immersed in a packed bed. International Journal of Heat and Mass Transfer 2010;53:5183–9. https://doi.org/10.1016/j.ijheatmasstransfer.2010.07.042.
[88] Cavenati S, Grande CA, Rodrigues AE. Separation of CH4 / CO2 / N2 mixtures by layered pressure swing adsorption for upgrade of natural gas. Chem Eng Sc 2006;61:3893–906. https://doi.org/10.1016/j.ces.2006.01.023.
[89] Klise KA, Nicholson BL, Staid A, Woodruff DL. Parmest: Parameter Estimation Via Pyomo. Computer Aided Chemical Engineering 2019;47:41–6. https://doi.org/10.1016/B978-0-12-818597-1.50007-2.
[90] Shirzad M, Karimi M, Silva JAC, Rodrigues AE. Moving Bed Reactors: Challenges and Progress of Experimental and Theoretical Studies in a Century of Research. Ind Eng Chem Res 2019;58:9179–98. https://doi.org/10.1021/acs.iecr.9b01136.
[91] Ku Y, Wu H-C, Chiu P-C, Tseng Y-H, Kuo Y-L. Methane combustion by moving bed fuel reactor with Fe2O3/Al2O3 oxygen carriers. Applied Energy 2014;113:1909–15. https://doi.org/10.1016/j.apenergy.2013.06.014.
[92] Okumura T, Ogino T, Nishibe S, Nonaka Y, Shoji T, Higashi T. CO2 Capture Test for A Moving-bed System Utilizing Low-temperature Steam. Energy Procedia 2014;63:2249–54. https://doi.org/10.1016/j.egypro.2014.11.243.

[93] Denn MM, Yu W-C, Wei J. Parameter Sensitivity and Kinetics-Free Modeling of Moving Bed Coal Gasifiers. Ind Eng Chem Fund 1979;18:286–8. https://doi.org/10.1021/i160071a016.

[94] Yoon H, Wei J, Denn MM. A model for moving-bed coal gasification reactors. AIChE J 1978;24:885–903. https://doi.org/10.1002/aic.690240515.

[95] Yoon H, Wei J, Denn MM. Transient behavior of moving-bed coal gasification reactors. AIChE J 1979;25:429–39. https://doi.org/10.1002/aic.690250307.

[96] Yoon H, Wei J, Denn MM. Feasible Operating Regions for Moving Bed Coal Gasification Reactors. Ind Eng Chem Proc Des Dev 1979;18:306–12. https://doi.org/10.1021/i260070a023.

[97] Mondino G, Grande CA, Blom R. Effect of Gas Recycling on the Performance of a Moving Bed Temperature-Swing (MBTSA) Process for CO2 Capture in a Coal Fired Power Plant Context. Energies 2017;10:745. https://doi.org/10.3390/en10060745.

[98] Knaebel KS. Temperature Swing Adsorption System. US 7,594,956 B2, 2009.

[99] Kim K, Son Y, Lee WB, Lee KS. Moving bed adsorption process with internal heat integration for carbon dioxide capture. International Journal of Greenhouse Gas Control 2013;17:13–24. https://doi.org/10.1016/j.ijggc.2013.04.005.

[100] Ostace A, Lee A, Okoli CO, Burgard AP, Miller DC, Bhattacharyya D. Mathematical Modeling of a Moving-Bed Reactor for Chemical Looping Combustion of Methane. Computer Aided Chemical Engineering, vol. 44, Elsevier; 2018, p. 325–30. https://doi.org/10.1016/B978-0-444-64241-7.50049-5.

[101] Morales-Ospino R, Santos VN, Lima ARA, Torres AEB, Vilarrasa-García E, Bastos-Neto M, et al. Parametric Analysis of a Moving Bed Temperature Swing Adsorption (MBTSA) Process for Postcombustion CO2 Capture. Ind Eng Chem Res 2021;60:10736–52. https://doi.org/10.1021/acs.iecr.0c05067.

[102] Mondino G, Spjelkavik AI, Didriksen T, Krishnamurthy S, Stensrød RE, Grande CA, et al. Production of MOF Adsorbent Spheres and Comparison of Their Performance with Zeolite 13X in a Moving-Bed TSA Process for Postcombustion CO2 Capture. Ind Eng Chem Res 2020;59:7198–211. https://doi.org/10.1021/acs.iecr.9b06387.

[103] Chen JC, Grace JR, Golriz MR. Heat transfer in fluidized beds: design methods. Powder Technology 2005;150:123–32. https://doi.org/10.1016/j.powtec.2004.11.035.

[104] Baskakov AP, Berg BV, Vitt OK, Filippovsky NF, Kirakosyan VA, Goldobin JM, et al. Heat transfer to objects immersed in fluidized beds. Powder Technology 1973;8:273–82. https://doi.org/10.1016/0032-5910(73)80092-0.

[105] Kunii D, Levenspiel O. Fluidization Engineering. Elsevier; 1991.

[106] Turton R, Shaeiwitz JA, Bhattacharyya D, Whiting WB. Analysis, Synthesis, and Design of Chemical Processes, Fifth Edition. Prentice Hall; 2018.

[107] Fout T, Zoelle A, Keairns D, Pinkerton LL, Turner MJ, Woods M, et al. Cost and Performance Baseline for Fossil Energy Plants Volume 1a: Bituminous Coal (PC) and Natural Gas to Electricity Revision 3. 2015. https://doi.org/10.2172/1480987.

[108] Plaza MG, Rubiera F, Pevida C. Evaluating the Feasibility of a TSA Process Based on Steam Stripping in Combination with Structured Carbon Adsorbents To Capture CO2 from a Coal Power Plant. Energy Fuels 2017;31:9760–75. https://doi.org/10.1021/acs.energyfuels.7b01508.

[109] Raksajati A, Ho MT, Wiley DE. Techno-economic Evaluation of CO2 Capture from Flue Gases Using Encapsulated Solvent. Ind Eng Chem Res 2017;56:1604–20. https://doi.org/10.1021/acs.iecr.6b04095.

[110] Liu J, Thallapally PK, McGrail BP, Brown DR, Liu J. Progress in adsorption-based CO2 capture by metal–organic frameworks. Chem Soc Rev 2012;41:2308–22. https://doi.org/10.1039/C1CS15221A.

[111] Su F, Lu C. CO2 capture from gas stream by zeolite 13X using a dual-column temperature/vacuum swing adsorption. Energy Environ Sci 2012;5:9021. https://doi.org/10.1039/c2ee22647b.

[112] Oyenekan BA. Modeling of Strippers for CO2 Capture using aqueous amines. The University of Texas at Austin, 2007.

[113] Kotamreddy G. Process Modeling and Techno-Economic Analysis of Micro-Encapsulated Carbon Sorbents (MECS) for CO2 capture in a Fixed Bed and Moving Bed Reactors. West Virginia University, 2021.

[114] Powell, M.J.D.: The BOBYQA Algorithm for Bound Constrained Optimization Without Derivatives. Technical report, Department of Applied Mathematics and Theoretical Physics, University of Cambridge (2009).

[115] Valentine J, Zoelle A, Homsy S, Mantripragada H, Woods M, Roy N, et al. Direct Air Capture Case Studies: Sorbent System. 2022. https://doi.org/10.2172/1879535.

[116] Theis J, Gerdes K, Summers W, Wimer J. Quality Guidelines for Energy System Studies: Cost Estimation Methodology for NETL Assessments of Power Plant Performance. 2021. https://doi.org/10.2172/1513278.

[117] Seider WD, Seader JD, Lewin DR, Widagdo S. Product and Process Design Principles: Synthesis, Analysis, and Evaluation. Wiley; 2010.

[118] Susarla N, Haghpanah R, Karimi IA, Farooq S, Rajendran A, Tan LSC, et al. Energy and cost estimates for capturing CO2 from a dry flue gas using pressure/vacuum swing adsorption. Chemical Engineering Research and Design 2015;102:354–67. https://doi.org/10.1016/j.cherd.2015.06.033.

[119] James, III R, Keairns D, Turner M, Woods M, Kuehn N, Zoelle A. Cost and Performance Baseline for Fossil Energy Plants Volume 1: Bituminous Coal and Natural Gas to Electricity. 2019. https://doi.org/10.2172/1569246.

[120] Joss L, Gazzani M, Hefti M, Marx D, Mazzotti M. Temperature Swing Adsorption for the Recovery of the Heavy Component: An Equilibrium-Based Shortcut Model. Ind Eng Chem Res 2015;54:3027–38. https://doi.org/10.1021/ie5048829.

[121] Du Y, Gao T, Rochelle GT, Bhown AS. Zero- and negative-emissions fossil-fired power plants using CO2 capture by conventional aqueous amines. International Journal of Greenhouse Gas Control 2021;111:103473. https://doi.org/10.1016/j.ijggc.2021.103473.

[122] GE Osmonics. https://www.lenntech.com/Data-sheets/GE-Osmonics-CG-L.pdf (accessed January 25, 2021).

[123] FilmTecTM Reverse Osmosis Membranes Technical Manual 2020:207.

[124] Crittenden JC, Trussell RR, Hand DW, Howe KJ, Tchobanoglous G. MWH's Water Treatment: Principles and Design. John Wiley & Sons; 2012.

[125] Ghiu SMS. Mass Transfer of Ionic Species in Direct and Reverse Osmosis Processes. University of South Florida, 2003.

[126] Mukherjee P, SenGupta AK. Ion Exchange Selectivity as a Surrogate Indicator of Relative Permeability of Ions in Reverse Osmosis Processes. Environ Sci Technol 2003;37:1432–40. https://doi.org/10.1021/es0207495.

[127] Bellona C, Drewes JE, Xu P, Amy G. Factors affecting the rejection of organic solutes during NF/RO treatment—a literature review. Water Research 2004;38:2795–809. https://doi.org/10.1016/j.watres.2004.03.034.

[128] Dean JA. Lange’s Handbook of Chemistry. 15th ed. McGraw-Hill Professional Publishing; 1998.

[129] Kielland J. Individual Activity Coefficients of Ions in Aqueous Solutions. J Am Chem Soc 1937;59:1675–8. https://doi.org/10.1021/ja01288a032.

[130] Volkov AG, Paula S, Deamer DW. Two mechanisms of permeation of small neutral molecules and hydrated ions across phospholipid bilayers. Bioelectrochemistry and Bioenergetics 1997;42:153–60. https://doi.org/10.1016/S0302-4598(96)05097-0.

[131] Salon C, Mir NA, Canvin DT. Influx and efflux of inorganic carbon in Synechococcus UTEX625. Plant Cell Environ 1996;19:247–59. https://doi.org/10.1111/j.1365-3040.1996.tb00248.x.

[132] Zeuthen T, Wu B, Pavlovic-Djuranovic S, Holm LM, Uzcategui NL, Duszenko M, et al. Ammonia permeability of the aquaglyceroporins from Plasmodium falciparum, Toxoplasma gondii and Trypansoma brucei. Mol Microbiol 2006;61:1598–608. https://doi.org/10.1111/j.1365-2958.2006.05325.x.

[133] Bódalo A, Gómez J-L, Gómez E, León G, Tejera M. Ammonium removal from aqueous solutions by reverse osmosis using cellulose acetate membranes. Desalination 2005;184:149–55. https://doi.org/10.1016/j.desal.2005.03.062.

[134] Andreoli TE, Brown AM, Fambrough DM, Hoffman JF, Schultz SG, Welsh MJ. Molecular Biology of Membrane Transport Disorders. Springer Science & Business Media; 2013.

[135] Reible DD. Fundamentals of Environmental Engineering. CRC Press; 1998.